Imperial College London

# Development of a multidimensional luminescence microscope and its application to imaging and spectroscopy of luminescent defects in diamond

Daniel Christopher Jones

Photonics Group

Department of Physics

Imperial College London

Thesis submitted in partial fulfilment of the requirements

for the degree of Doctor of Philosophy (Ph.D.)

Imperial College of Science, Technology and Medicine

# Abstract

This thesis concerns the development and characterisation of a novel multidimensional luminescence microscope, and its application to diamond defect luminescence. The instrument can resolve luminescence with respect to excitation and emission wavelength, lifetime, and polarisation, providing co-registered image data to support studies of the underlying photo physics or evaluation of (diamond-based) photonics devices. The thesis provides an overview of luminescent defects that have been reported in synthetic and natural diamond. Defect parameters based on absorption and emission spectra, lifetime, polarisation, and orientation in the lattice have previously been studied using a myriad of different instruments, technologies, and methods, making direct comparisons difficult. The instrumentation developed in this thesis enables a systematic characterisation of diamond luminescence to provide information concerning growth, processing of diamonds, and to support new applications such as quantum optics and sensing.

Spectrally resolved fluorescence lifetime imaging microscopy (FLIM) was implemented using time-correlated-single-photon-counting (TCSPC) with stage scanning. This could be combined with hyperspectral imaging, which also provides a rapid means to identify spectral and spatial regions of interest. A novel electronically tuneable, ultrafast excitation source was developed and utilised for (polarisation-resolved) photoluminescence emission and excitation (PLE) spectroscopy/imaging, and for hyperspectral imaging and FLIM. For the analysis of luminescence lifetime data, both iterative fitting and phasor analysis were used.

The instrument was applied to synthetic diamonds containing nitrogen and silicon vacancies, and to natural diamonds presenting a range of defects. This enabled separation of defects based on their relative concentrations through FLIM, revealed complex decays caused by quenching, and fundamental measurements of the $SiV^-$ defect. These have applications ranging from understanding the photo-physics of defects to better apply them to quantum applications, to determining the origin of diamonds based on their spatial distribution of defects.

## Author declaration

The work presented in thesis is the authors own, unless labelled, with the following exceptions:

- All diamond samples were supplied by De Beers, who also provided all the DiamondView$^{TM}$ images, as indicated.
- The measurement of IR absorption of a natural diamond plate reported in Chapter 7 was undertaken by Dr Phil Diggle (De Beers Technologies), who also provided concentration measurements.
- Dr Ben Green supplied the initial computer code to construct diamond atomic structure graphs for pure diamond and defects, in Chapter 3. He also provided the model for the dipole orientations of the $SiV^-$ defect based on the orientation of the sample.
- Warwick University conducted the UV-Vis absorption measurement in Chapter 6.
- The *FLIMfit* software for the iterative lifetime fitting, was developed by Dr Sean Warren.
- The single point temporally resolved spectrofluorometer was previously developed by Dr Gordon Kennedy and Dr Hugh Manning.

Daniel Christopher Jones

## Copyright

The copyright of this thesis rests with the author. Unless otherwise indicated, its contents are licensed under a Creative Commons Attribution-Non-Commercial 4.0 International Licence (CC BY-NC).

Under this licence, you may copy and redistribute the material in any medium or format. You may also create and distribute modified versions of the work. This is on the condition that: you credit the author and do not use it, or any derivative works, for a commercial purpose.

When reusing or sharing this work, ensure you make the licence terms clear to others by naming the licence and linking to the licence text. Where a work has been adapted, you should indicate that the work has been changed and describe those changes.

Please seek permission from the copyright holder for uses of this work that are not included in this licence or permitted under UK Copyright Law.

# Acknowledgments

I would like to thank the tireless efforts of my supervisors, Paul French, Chris Dunsby and Mark Neil, who shared their knowledge, practical expertise, kindness, and support throughout my PhD. Always ready to help, to discuss, and eager to see the project succeed, I could not ask anymore from these fantastic supervisors.

I will never forget the wonderful members of our Photonics group, whose conversations, laughter, and support made this work possible. To Sunil and Nathan, who were always on hand ready to fix what was broken (or fix until it was broken Sunil!), and whose expertise provided the background for my practical knowledge of instrumentation and *LabVIEW* programming. To Jonathan, who shared the main lab with me and helped to align the instrumentation, discuss optical problem, or "acquire" items for my workbench, thank you. To the rest of the office and group, Hugh, Connor, Edwin, Riccardo, Terry, Yuriy, Sam, Jack, Frederik, and Liuba, you provided a comfortable working environment, and put up with me for far too long!

The instrumentation would not have been possible without the support and efforts of the brilliant Photonics Workshop with Martin and Simon. Thank you for the intelligent designs, time management, and support. I would also like to thank the admin team of Judith and Marcia, who operated in the background, making sure equipment was ordered, and sorting out the funding issues that have occurred.

I would like to thank De Beers in Maidenhead who provided any samples I asked for and the many conversations we have shared over the years. In particular, I would like to thank Peter Lanigan, Colin McGuinness, Matthew Dale, David Fisher, and Philip Martineau.

I would like to acknowledge the Engineering and Physical Sciences Research Council and the Diamond Science and Technology CDT for the funding of this project.

Finally I would like to thank the rock under my feet, my loving and caring family, who have supported me throughout my PhD and every step before.

*To my family*

# Table of contents

**Abstract** ..... 2
**Author declaration** ..... 3
**Copyright** ..... 3
**Acknowledgments** ..... 4
**Table of contents** ..... 6
**List of abbreviations** ..... 11
**Table of figures** ..... 13
**List of tables** ..... 30
**Chapter 1 – Thesis overview** ..... 31
**Chapter 2 – Optical microscopy, spectroscopy, and lifetime** ..... 33
**Outline** ..... 33
**Luminescence** ..... 33
*Absorption, Emission, Stokes shift* ..... 35
*Absorption and PLE spectroscopy* ..... 37
*Luminescence Lifetime* ..... 37
*Polarisation* ..... 39
*Sources of emission* ..... 40
**Optical Microscopy** ..... 41
*Wide-field Transmission* ..... 41
*Fluorescence Microscopy* ..... 42
*Laser Scanning Confocal Microscopy* ..... 43
*Spectral Imaging* ..... 44
*Hyperspectral Imaging* ..... 44
*Luminescence Lifetime Microscopy* ..... 47
***Fluorescence lifetime measurements and FLIM*** ..... 47
***Frequency Domain lifetime measurements*** ..... 48
***Time Domain lifetime measurements – time-gated imaging*** ..... 49
***Time Domain lifetime measurements - TCSPC*** ..... 50
***Instrument response function*** ..... 52
***PLE lifetime spectroscopy*** ..... 53
**Instrumentation** ..... 53

*Excitation sources* ..... *53*
*Detectors* ..... *54*
***Cameras*** ..... ***54***
***Photomultipliers*** ..... ***55***
***Single photon counting avalanche photodiodes (SPADs)*** ..... ***55***
*Filters* ..... *56*
**Conclusion** ..... **56**
**Chapter 3 – Diamond defects and properties: photo-physics, characterisation, and applications** ..... **57**
**Outline** ..... **57**
**Structure** ..... **57**
*Crystallinity* ..... *59*
*Nanodiamond* ..... *60*
**Properties of diamond** ..... **60**
*Mechanical Properties* ..... *60*
*Thermal Properties* ..... *61*
*Optical Properties* ..... *61*
*Birefringence* ..... *62*
*Raman scattering* ..... *63*
*Band structure* ..... *64*
**Growth** ..... **65**
*Natural growth* ..... *66*
*Synthetic growth* ..... *66*
*High Pressure High Temperature (HPHT)* ..... *67*
*Chemical Vapour Deposition (CVD)* ..... *67*
*Detonation nanodiamonds (DNDs)* ..... *69*
**Defects** ..... **69**
*In crystals* ..... *69*
*Diamond defects* ..... *71*
***Nitrogen in diamond*** ..... ***71***
***Diamond classification*** ..... ***71***
***C and A-centres*** ..... ***72***
***NV centres*** ..... ***73***

Manufacture of NV centres ..... 74
Energy level structure of $NV^-$ ..... 75
Charge transfer (Photochromism) ..... 76
***H3 defect ..... 76***
***N3 defects ..... 77***
*Group 4 vacancy defects ..... 78*
***Silicon vacancy ..... 78***
Energy level structure ..... 79
Charge transfer (photochromism) ..... 80
***Germanium and Tin vacancy ..... 81***
*Boron defects ..... 81*
*Hydrogen defects ..... 82*
*Defect incorporation ..... 82*
**Conclusion and outlook ..... 83**
**Chapter 4 - Development and characterisation of instrumentation for multidimensional luminescence microscopy and spectroscopy ..... 84**
**Outline ..... 84**
**Design of a grism-based line scanning hyperspectral microscope ..... 84**
*Illumination and optical elements ..... 85*
*Emission collection and spectral resolution ..... 86*
*Sample mounting ..... 88*
*Application of hyperspectral luminescence microscope to synthetic diamond ..... 89*
*Summary ..... 91*
**Single-point time-resolved spectrofluorometer ..... 92**
*Introduction ..... 92*
*Application of time-resolved spectrofluorometer to synthetic CVD diamond ..... 94*
*Summary ..... 95*
**Multidimensional luminescence microscope ..... 96**
*Introduction ..... 96*
*Supercontinuum excitation laser source and characterisation ..... 98*
*Other excitation laser sources ..... 101*
*Illumination optics and steering mirrors ..... 102*
*Emission optics and imaging spectrograph ..... 102*
***Monochromator port ..... 103***

***Spectrometer imaging port*** ..... ***104***
Spatial Resolution ..... 105
*Linear variable filter* ..... *107*
*Side port colour camera* ..... *108*
*LabVIEW interface and experimental methods* ..... *109*
*Long-lived luminescence measurements* ..... *119*
**Hyperspectral data analysis** ..... **121**
*Median wavelength plots and images* ..... *122*
**Luminescence decay analysis** ..... **123**
*Nonlinear iterative fitting to discrete exponential decay models using FLIMfit* ..... *123*
*Phasor analysis* ..... *125*
***Theory*** ..... ***125***
Universal circle ..... 127
***Background contributions to the measured signals*** ..... ***129***
***Incomplete decays*** ..... ***130***
**Exemplar luminescence data from a synthetic CVD diamond** ..... **135**
*White-light transmission, birefringence, and hyperspectral luminescence imaging* ..... *135*
*Spectrally resolved FLIM* ..... *139*
*Excitation-emission-lifetime matrix* ..... *143*
*Power variation experiment* ..... *146*
**Conclusion and outlook** ..... **147**
**Chapter 5 – Application of multidimensional imaging and spectroscopy to synthetic diamond** ..... **149**
**Outline** ..... **149**
**Introduction** ..... **149**
**Hyperspectral Imaging of a CVD diamond with HPHT substrate** ..... **151**
*Spectrally resolved FLIM on a synthetic CVD diamond with HPHT substrate – 675 nm emission* ..... *154*
*Spectrally resolved FLIM on a synthetic CVD diamond with HPHT substrate – 737 nm emission* ..... *162*
*Single-point spectrally-resolved emission lifetime measurements on a synthetic CVD diamond with HPHT substrate* ..... *171*
*Single-point spectrally-resolved excitation-emission-lifetime measurements of a synthetic CVD diamond with HPHT substrate* ..... *174*

*Conclusion* ..... *182*

**Chapter 6 - Spectroscopic and lifetime analysis of the $SiV^-$ defect in synthetic diamond** ..... **183**

**Outline** ..... **183**

**Introduction** ..... **183**

*$SiV^-$ point-excitation-emission-lifetime matrix and PLE spectra* ..... *183*

*Polarisation resolved PLE spectroscopy of SiV-* ..... *187*

*SiV- spectroscopic and lifetime analysis on a second CVD diamond sample* ..... *197*

*Comparison with absorption data* ..... *202*

**Conclusion and outlook** ..... **203**

**Chapter 7 – Application of multidimensional imaging and spectroscopy to natural diamond** ..... **204**

**Outline** ..... **204**

**Overview** ..... **204**

**Faceted natural diamond** ..... **205**

*Hyperspectral and lifetime imaging* ..... *205*

*Single point-spectrally resolved lifetime* ..... *210*

**Natural diamond plate** ..... **212**

*Hyperspectral imaging* ..... *213*

*Single point-spectrally resolved lifetime* ..... *215*

*Luminescence lifetime imaging* ..... *220*

**Natural diamond plate with mapped varying A-centre concentrations** ..... **226**

*Luminescence lifetime mapping with phasor analysis* ..... *227*

**Conclusion and outlook** ..... **231**

**Chapter 8 – Conclusions and future work** ..... **232**

**Introduction** ..... **232**

**Conclusions** ..... **233**

**Future luminescence studies** ..... **235**

**Future instrument improvements** ..... **236**

**Published work and proceedings** ..... **240**

**References** ..... **241**

# List of abbreviations

| Abbreviation | Meaning |
|---|---|
| ADC | Analogue to digital converter |
| AO | Adaptive optics |
| AOTF | Acousto-optic tuneable filter |
| B&H | Becker and Hickl |
| BP | Band pass |
| CFD | Constant fraction discriminator |
| CoM | Centre of Mass |
| CVD | Chemical vapour deposition |
| CW | Continuous wave |
| DND | Detonation nanodiamonds |
| EE | Excitation-emission |
| EELM | Excitation-emission-lifetime matrix |
| EEM | Excitation-emission matrix |
| FCC | Face-centred-cubic |
| FLIM | Fluorescence lifetime imaging microscopy |
| FOV | Field of view |
| FWHM | Full width half maximum |
| GeV | Germanium Vacancy |
| GOI | Gated optical intensifier |
| HBT | Hanbury-Brown and Twiss |
| HPHT | High pressure high temperature |
| IR | Infrared |
| IRF | Instrument response function |
| LCTF | Liquid crystal tuneable filter |
| LED | Light emitting diode |
| L-$N_2$ | Liquid nitrogen |
| LP | Long pass |
| LVLWP | Linear variation long wave pass |
| MCP | Micro-channel plate |
| MLE | Maximum likelihood estimation |
| ND | Neutral density |

| | |
|---|---|
| NV | Nitrogen vacancy |
| OD | Optical density |
| ODMR | Optically detected magnetic resonance |
| OPO | Optical parametric oscillator |
| PCCVD | Polycrystalline chemical vapour deposition |
| PCD | Polycrystalline diamond |
| PLE | Photoluminescence excitation |
| PMT | Photomultiplier tube |
| RESOLFT | Reversable saturable optical fluorescence transitions |
| ROI | Region of interest |
| sCMOS | Scientific complementary metal oxide semiconductor |
| SDK | Software development kit |
| SIMS | Secondary ion mass spectroscopy |
| SiV | Silicon Vacancy |
| SLM | Spatial light modulator |
| SnV | Tin vacancy |
| SP | Short pass |
| SPAD | Single photon avalanche diode |
| SPD | Spectral power density |
| SQUID | Superconducting quantum interference devices |
| STORM | Stochastic optical reconstruction microscopy |
| TAC | Time to amplitude converter |
| TCSPC | Time correlated single photon counting |
| TRS | Time resolved spectroscopy |
| UV | Ultraviolet |
| ZPL | Zero phonon line |

# Table of figures

*Figure 1 – A Jablonski energy level diagram showing the common electronic transitions in a luminescent species. The exact energy level structure will depend on the emitter. Colour is used here to represent the approximate wavelengths of light (and therefore energy) in each process. Non-radiative relaxation does not involve the emission of light and therefore is coloured grey. ..... 34*

*Figure 2 – A schematic of a conventional wide-field microscope with optional polarisers using white-light transmission illumination. ..... 41*

*Figure 3 – A conventional epi-fluorescence microscope for wide-field excitation. The dichroic beam splitter ensures that the red-shifted emission (red) reaches the detector, whilst the emission filter blocks the reflected excitation light (yellow). Dependant on excitation source, an excitation filter may not be required. ..... 42*

*Figure 4 – An optical diagram of confocal microscopy, which shows how optical sectioning is achieved by blocking the out of focus light from other focal planes. The black lines represent the emission light from the correct focal plane, whilst the red dashed lines are out of focus emission. ..... 43*

*Figure 5 – Three techniques for achieving hyperspectral data sets are shown. The transparent blocks indicate data that is taken in the next step/s, whilst solid-coloured blocks represent the current acquisition. The number of colours (representing wavelengths) gives an indication of the expected spectral resolution of each technique. ..... 46*

*Figure 6 – An example of a frequency domain measurement, showing the excitation modulation (green) and emission modulation (red). The amplitude is given by A and the average intensity B for excitation and emission. The phase difference between the two signals is given by $\phi_\omega$. ..... 48*

*Figure 7 – A diagram of a GOI, showing the emission photons, the detection photocathode, MCP, and phosphor. The photocathode voltage is rapidly switched to block or accelerate the photoelectrons from the photocathode to the MCP to implement the time-gated imaging. ..... 49*

*Figure 8 – An implementation of TCSPC, using a pulsed excitation source with an output signal (laser), and the detected signal (PMT). The TCSPC card contains the CFD, TAC and ADC and outputs the shown decay to the PC. An example fit of the decay is shown in red, with the green bar representing counts in the histogram. ..... 51*

*Figure 9 – Structure of the diamond unit cell showing the two-atom basis. The tetrahedral symmetry is shown, along with other important parameters. All grey atoms are carbon-12 atoms. ..... 58*

*Figure 10 – An example of a monocrystalline faceted natural diamond (left), and a polycrystalline CVD synthetic diamond mounted to a copper block with carbon tape (right). Here the grains in the PCCVD diamond are only visible under a microscope, but regions of black graphitic/non-$SP^3$ carbon are visible to the naked eye. ..... 59*

*Figure 11 – An example of the first order Raman shift at 1332 $cm^{-1}$ from a single crystal natural diamond. The laser source was a 633 nm HeNe laser. This data was acquired by the author on a previous project at Aberystwyth university using a Horiba spectrometer. ..... 63*
*Figure 12 – A carbon phase diagram for diamond showing the stable regions for graphite, diamond, and liquid carbon. The line separating the graphite and diamond stable regions is called the Berman-Simon line. HPHT (with catalyst) and CVD synthesis conditions are shown, with an exaggerated pressure scale for CVD growth. Figure redrawn from[r] ..... 65*
*Figure 13 – This diagram shows a simplified homo-elemental 2D lattice with a selection of defects. a) shows a vacancy, with an exaggerated distortion to the lattice. b) shows a native elemental interstitial atom, slightly distorting the lattice. c) is a substitution of an isotope of the native element. d) represents a larger substitutional atom, and e) a small substitutional atom. Defect f) represents a larger lattice distortion from a much larger element occupying a bond centred site, between two vacancy sites. ..... 70*
*Figure 14 – A structural diagram of the C-centre in diamond a lattice of carbon atoms (grey) surrounding a single substitutional nitrogen atom (yellow)..... 72*
*Figure 15 - A structural diagram of the A-centre in diamond: a lattice of carbon atoms (grey) surrounding a pair of substitutional nitrogen atoms (yellow) next to each other. ..... 73*
*Figure 16 - A structural diagram of the NV centre in diamond: a lattice of carbon atoms (grey) surrounding a single substitutional nitrogen atom (yellow) next to a lattice vacancy (purple)..... 74*
*Figure 17 – This is the currently understood energy level structure of the $NV^-$ defect in diamond. The current location within the band gap has been inferred from excitation wavelength measurements. The defect consists of two primary energy levels, the $^3A_2$ ground state and $^3E$ excited state, which are spin degenerate. A second pair of energy levels are also shown. The black and grey dotted arrows show the likely transitions, and the second decay path allows the $m_s \pm 1$ excited state to decay into the $m_s \pm 0$ ground state. ..... 75*
*Figure 18 - A structural diagram of the H3 centre in diamond: a lattice of carbon atoms (grey) with a pair of substitutional nitrogen atoms (yellow) surrounding a lattice vacancy (purple). ..... 77*
*Figure 19 - A structural diagram of the N3 centre in diamond: a lattice of carbon atoms (grey) with three substitutional nitrogen atoms (yellow) surrounding a lattice vacancy (purple). ..... 78*
*Figure 20 - A structural diagram of the SiV centre in diamond: a lattice of carbon atoms (grey) with a large silicon atom (light purple) at a bond centred site between two vacancies (purple). ..... 79*
*Figure 21 – The diagram on the left depicts the energy level structure of the $SiV^-$ defect in its negative charge state, as currently understood. Recent research on the $SiV^0$ has produced the energy level structure (right), where the side energy level at 1.3 eV is currently not well understood. ..... 80*

*Figure 22 - A structural diagram of a Boron centre in diamond: a lattice of carbon atoms (grey) surrounding a substitutional boron atom (blue).* ..... *81*
*Figure 23 – System diagram of the push-broom hyperspectral imaging microscope. This diagram shows the excitation and emission paths, with exemplar camera images. In the excitation beam path, a beam expander and cylindrical lens are used to achieve an overfilled line on the back focal plane of the objective. This is then imaged to the entrance slit of the 'spectrograph' grism system, and onto the camera.* ..... *85*
*Figure 24 – Left: an example slice from a single hyperspectral data set showing the spatial x-axis and wavelength axis. Centre: a stack of three images showing the spatial y-axis. Right: an example hyperspectral image of diamond and dust (yellow-coloured region), where average wavelength has been converted to colour and modulated by intensity.* ..... *87*
*Figure 25 – (left) The original mounting apparatus, using a glass slide and corresponding summed intensity hyperspectral fluorescence image showing the observed interference pattern resulting from light reflected between a diamond sample and glass slide. (right) A summed intensity hyperspectral fluorescence image with the new mounting method, showing no interference effects.* ..... *88*
*Figure 26 – (left) An intensity modulated median wavelength image of a CVD diamond with HPHT substrate. 520 nm excitation was used. (right) Extracted spectra from four ROIs on the image. Spectral features from* $NV^-$ *(637 nm ZPL) and* $SiV^-$ *(737 nm ZPL) are present.* ..... *89*
*Figure 27 – A set of five images taken using white-light transmission, crossed polarisers, and hyperspectral fluorescence emission at 520 nm excitation. The hyperspectral data is broken into summed fluorescence intensity, median wavelength and intensity modulated median wavelength images. This shows how different features can be related between the different modalities.* ..... *91*
*Figure 28 – A schematic of the spectrofluorometer showing the excitation and emission paths with their optical elements. The tuneable excitation supercontinuum was not used from this system. The excitation polarisation state is adjusted using the Glan Taylor polariser. Vertical is defined as parallel to the entrance slit and a pair of quartz lenses image the sample onto the entrance slit of the monochromator.* ..... *93*
*Figure 29 – Two colour contour plots show the decay information for the horizontal and vertical emission for vertically polarised excitation (375 nm) of a synthetic CVD diamond. Lifetime analysis shows the emission spectra and intensity weighted mean lifetime (tau) as a function of wavelength. A breakdown of the different beta (population fraction) parameters is also shown as a function of wavelength for both polarisation states. This reveals emission from* $NV^0$ *(Beta 1) with a lifetime of 19.6 ns, and two other unknown components.* ..... *95*

*Figure 30 – A schematic of the multidimensional luminescence microscope, showing the various excitation sources, emission paths, and optical elements. Manual flipper mirrors are used to switch between the different excitation sources. A manual mirror/prism inside the microscope frame (blue dashed box) allows the output to be switched from a colour CMOS camera on the side port of the microscope frame to the imaging spectrograph mounted on its left-hand port. An internal mirror switches the output of the spectrograph between the PMT and imaging ports. ..... 97*

*Figure 31 – Measured excitation source wavelengths from the spectrally selected monochromator. This was measured using the spectrograph's monochromator port with 10-micron entrance and exit slits. (right) is the same graph on a log scale. ..... 99*

*Figure 32 – (left) The double exponential fit relating excitation wavelength to stage position. (right) Measured FWHM of a fitted Gaussian function to each spectrally selected output. The power and spectral power density are also shown. This data was collected using a USB2000+ spectrometer (Ocean Optics) and a photodiode power meter (S170C, Thorlabs). ..... 100*

*Figure 33- Two different Gaussian fits showing the monochromator spectral resolution (right), and for comparison, the attainable resolution using the imaging port and an sCMOS camera is shown (left). ..... 103*

*Figure 34 – a) The camera view of the spectrally dispersed mercury emission line. b) A comparison between the pixel based and c) converted wavelength emission line. ..... 105*

*Figure 35 – A graph showing the line profiles through the image of a single TetraSpeck™ bead under 500 nm excitation using a 100x 0.95 NA objective, detected using the sCMOS camera on the imaging port of the spectrograph. The entrance slit was set to 1 mm..... 106*

*Figure 36 – a) is an image showing the linear variable filter. Emission from a fluorescent slide at various cut-on wavelengths is shown in b), with given stage positions in mm. Graph c) shows the linear fit between cut on wavelength and stage position for the linear variable filter. Graph d) is an example set of emission spectra at different excitation wavelengths for the same fluorescent slide. ..... 108*

*Figure 37 – Two colour images showing white-light transmission (left) and birefringence (right - obtained using crossed polarisers) of a monocrystalline diamond sample. In these images, the HPHT diamond is the yellow substrate, and the CVD diamond is the region grown around it. A dark region to the left of the sample shows non-$SP^3$ carbon..... 109*

*Figure 38 – The main LabVIEW interface screen, showing the split sections and multiple tabs. The tabs on the right are used to view acquired data, and the tabs on the left are used to modify settings and start acquisitions..... 110*

*Figure 39 – This shows the interface for controlling the spectrometer and the linear variable filter. Wavelengths can be set for the monochromator, which corresponds to the central wavelength on the imaging port. ..... 111*
*Figure 40 – Images from the imaging port can have ROIs selected through them, and the spectrum can be extracted, as shown on the red plots (right). This allows spectral features to be identified for targeted spectral analysis by hyperspectral imaging or spectrally resolved FLIM..... 112*
*Figure 41 – User interface for the stage controls. This includes step size variations for use in hyperspectral imaging and FLIM, start and end positions for all imaging, and the ability to save and recover spatial positions. The step size for hyperspectral imaging is linked to the magnification and is set by changing the current objective. ..... 113*
*Figure 42 – Control interface for the imaging port of the spectrograph, allowing starting wavelength, hyperspectral re-slicing, and hyperspectral imaging acquisitions to be started. Some options are not used, based on the camera currently in use, which is set on the front panel. Another set of tabs provides information for specific cameras. ..... 114*
*Figure 43 – This panel controls the ROI view from the hyperspectral imaging and PMT images. The hyperspectral slice bar can be used to switch between the different binned spectral channel images. ..... 115*
*Figure 44 – The PMT control tab allows the start wavelength, end wavelength and 'resolution' (practically this is the wavelength step size) to be set, and acquisitions started. There are many experiments, which can be performed using the PMT, and they are broadly split into static and variable excitation wavelength acquisitions. If 'Mapping?' is true, then the acquisition will use the spatial information in the 'Stage Control' tab to acquire an image. If this is not selected, point-spectrally resolved decays are acquired instead. Measurements which involve the variation of excitation wavelength require the 'PLE Acquisition' button in the bottom left section of the interface. ..... 116*
*Figure 45 – This tab controls all the parameters the LabVIEW program can modify for the TCSPC card. The most important options are the TAC range, Collection Time (s), and CFD settings. The SYNC frequency divider setting can be changed from 1 or 2, to switch between measuring one or two periods. ..... 117*
*Figure 46 – Fluorescence decays from the TCSPC card are shown on the top graph, along with the current mapped total intensity from the PMT tiling acquisition. Monitoring the current decay information (using 'monitor decay') is used to measure the IRF for single excitation wavelength applications..... 118*

*Figure 47 – Flow diagram showing the components and signal paths used for long lifetime luminescence measurements. ..... 119*
*Figure 48 – An example long-lived luminescence decay from a natural diamond at 520 nm emission and 405 nm excitation with a fitted triple exponential decay model. The rising part of the data has been removed from these decays. ..... 120*
*Figure 49 – Phasor plot of the real and imaginary components from the converted decay. The semicircle represents a continuum of monoexponential lifetimes from 0 (1,0) to ∞ lifetime (0,0). Several data points are shown, with 1 ns (red), 3 ns (blue) and 10 ns (green) monoexponential decay lifetimes (assuming a 80 MHz laser repetition rate). The yellow point presents an emission decay profile with a mixture between the 1 and 3 ns lifetime components and so should sit along a chord between the two lifetime components on the universal circle. A purple data point representing a mixture of all three lifetime components should sit in a triangle between the 3 component lifetimes on the universal circle. ..... 128*
*Figure 50 – The above figure shows a standard universal circle, and the distorted universal circle which originated from missing decay data in the time period T. The black arrow represents the moving of the ∞ lifetime origin point. ..... 131*
*Figure 51 -A set of four graphs showing the progression of the solution to the missing data. Graph a) shows the two decays, each with a 25 ns period, over the collection time. Note the missing data at the start and near 50 ns due to the limitations of TCSPC electronics. In b) the two decays have been moved to overlap each other over an individual pulse period of 25 ns. The incorrect and missing data is shown at the end of the red decay. In graph c) this missing/incorrect data has been removed and replace with a duplicate from the first blue decay. The decays are summed in d) to produce the green profile..... 133*
*Figure 52 – Figure showing luminescence decay data before and after background subtraction on the left and right respectively from a point spectrally-resolved decay data set. Top: phasor plots. Bottom: exemplar fluorescence decay profiles at selected emission wavelengths. In both top panels the colour of the data points indicates the emission wavelength, as shown by the scale bar which is in nm. The bottom panels curve colours do not correspond to wavelength. This data was collected using a 400 ns laser pulse period. The phasor plot points are distorted due to the missing data. The universal circle has been distorted in accordance with the missing data. ..... 134*
*Figure 53 – Image a) shows a white-light transmission image of the sample, with white dotted lines indicating locations of the new growth layers. Image b) is a crossed polariser view of the same region. An intensity modulated median wavelength luminescence image excited at 475 nm is shown in c) of the same region. Extracted spectra from ROIs in c) are shown in d). Image e) is a larger-scale*

*white-light transmission image. Image f) is a large-scale crossed-polariser image of the same region as e). A fluorescence image from DiamondView™ is shown in g). Scale bar is 250 microns. ..... 136*
*Figure 54 – Extracted spectra from the four ROIs shown in the intensity-modulated median-wavelength images (right). Note the different scale bars on the graph per spectra, where the colour matches the coloured axis. The spectral resolution, spectral range, and spatial resolution are all higher using the sCMOS camera compared to the EMCCD in Figure 53. Data was collected using a 10x 0.3 NA objective and 475 nm excitation. The two intensity-modulated median-wavelength images have different colour scales to enhance contrast. ..... 138*
*Figure 55 – a) is the intensity-modulated median-wavelength luminescence image (from Figure 53) excited at 475 nm, where the colour represents median wavelength in nm (colour scale bar shown in Figure 53). Images b), c) and d) are three intensity-modulated weighted-mean-lifetime FLIM maps acquired for three different emission bands of the red bounded ROI in a), where the colour scale bar represent lifetime in ps. The scale bar is 250 microns. ..... 140*
*Figure 56 – Image a) is a summed intensity map of the FLIM map of Figure 55 b), which is reproduced in b). The colour scale bar in b) represents lifetime in ps. An exemplar decay profile and fitting model with residuals corresponding to the point indicated by the white arrow in b) is shown in c). ..... 141*
*Figure 57 – The images in a) show the variation of the three beta (β) parameters and lifetime (tau, τ) for the 621/25 nm emission band. Lifetimes are measured in ps in all three τ images. Graphs b) and c) show example fits and residuals at the two arrows for the HPHT substrate b), and CVD diamond c). The fitting parameters for those particular decays are also given. ..... 142*
*Figure 58 - The images in a) show the variation of the three beta (β) parameters and lifetime (tau, τ) for the 721/25 nm emission band. Lifetimes are measured in ps in all three τ images. Graphs b) and c) show example fits and residuals at the two arrows for the HPHT substrate b), and CVD diamond c). The fitting parameters for those particular decays are also given. ..... 143*
*Figure 59 – A 3D colour contour map of the excitation-emission-lifetime matrix from a region on the CVD diamond. This is explained in the text. ..... 144*
*Figure 60 – A set of six contour maps of the excitation-emission-lifetime matrix, showing the various extracted parameters from the lifetime fitting, including total count (photons), weighted mean lifetime (ps), $Chi^2$, and all three beta parameters. ..... 145*
*Figure 61 – Two measurements to investigate the validity of laser SPD post experiment normalisation. A detailed account of the setup is discussed in the text. Both constant power (fixed to a minimum power and varied using a polarisation-based setup) and post experiment normalisation data are similar. Power measurement was not taken at the sample plane, which is incorrect for the blue end of the excitation spectrum, but this does not affect the experimental results. ..... 147*

*Figure 62 – Colour image (left) shows a full view of the CVD diamond with HPHT substrate (yellow/orange) using white-light transmission and a 1.25x 0.04 NA objective. The two images (right) show a magnified region using a 10x 0.3 NA objective and show white-light transmission and crossed polariser FOVs. The birefringence indicated that there is strain (brighter regions) around the edge of the sample, particularly around the crack/chip (red arrow). ..... 150*

*Figure 63 - Hyperspectral luminescence intensity image data was collected using a 4x 0.16 NA objective, with luminescence excitation at 500 nm (1.25 nm FWHM), using line illumination and a line acquisition time of 1 s. (a) shows an intensity modulated median wavelength image. The scale bar is 0.5 mm. The intensity contrast has been adjusted to enhance the visibility of signal from the CVD diamond region. The maximum diamond CVD emission was 3x lower than that of the HPHT substrate, across all wavelengths. The spectra in (b) are taken from the four ROIs shown in (a) and show that the CVD diamond and HPHT substrate have different emission spectra, originating from different defects/charge states. The emission spectrum from each ROI is shown using a separate vertical axis that is coloured to match the line colour for that ROI. ..... 153*

*Figure 64 - FLIM data set analysed using spatial phasor analysis and MLE decay fitting. Data collected using a 40x 0.6 NA objective under point illumination at an excitation wavelength of 500 nm (1.25 nm FWHM) and 675/2 nm emission, with a pixel dwell time of 0.275 s. The summed photon count image is shown in (a) showing bright emission from the HPHT substrate (top), and less emission from the CVD diamond (bottom). The scale bar is 0.2 mm. The contrast in this image has been adjusted to enhance visibility of the CVD diamond region. The corresponding spatial phasor plot is shown in (b), which shows three clusters of phasor coordinates. The numbers along the outside of the universal circle are the lifetime scale in ns. The inset to (b) shows the full range of the spatial phasor plot. The colour scale indicates the number of FLIM image pixels that map onto each location on the spatial phasor plot. A modulation lifetime map from the spatial phasor plot is shown in (c), which shows different modulation lifetimes in the CVD and HPHT substrate diamond regions. The intensity-weighted mean lifetime from a four-component MLE fit is shown in d) and shows a similar spatial variation in lifetime as (c). The lifetime maps use the same colour scale, which is in ps. ..... 155*

*Figure 65 - Exemplar decays and MLE quadruple-exponential fits from the FLIM data for an excitation wavelength of 500 nm and detection wavelength of 675 nm. Top graph for each panel: round points, raw data; solid blue line, fit; red line, IRF. Bottom graph of each panel: normalised fit residuals. The modulation lifetime image shows the locations where the decay originated. ..... 157*

*Figure 66 - Population fraction (β) maps of Figure 64(d), showing the spatial distribution of the four fitted lifetime components. The scale bar is 0.2 mm. In (e) the $\chi^2$ shows that the fit is poorer in the HPHT substrate, and close to 1 in the rest of the diamond. ..... 158*

*Figure 67 - FLIM maps for extracted ROIs using phasor segmentation. (a) closer analysis of the spatial phasor plot in Figure 64, with inset showing the triangle of chords formed by the three lifetime components identified by iterative fitting from ROIs in the HPHT substrate. The numbers along the outside of the universal circle are lifetime scale in ns. Three ROIs (red, orange, green), each with different bounds on the false-colour lifetime scale, are shown along with their corresponding calculated modulation lifetime images (b, c, d). Here the colour of the ROI boxes (b, c, d) corresponds to the phasor plot ROIs. ..... 159*

*Figure 68 – a) summed photon count and b) modulation lifetime images from the HPHT substrate. These figures show the variation in structure/composition (bands) of the HPHT substrate. c) modulation lifetime and summed photon count as a function of distance along the yellow arrow shown in a) & b), which does not show a strong correlation between lifetime and photon counts. d) scatter plot of photon count and modulation lifetime values from along the yellow line shown in a) & b) indicating that there is no correlation when moving across the bands. e) modulation lifetime and photon count as a function of distance along the black arrow shown in a) & b), indicating their correlation. f) scatter plot of photon count and modulation lifetime values from along the black arrow in a) & b) that illustrates their correlation. ..... 161*

*Figure 69 - The data for this FLIM map was collected with emission centred at a wavelength of 737/2 nm with excitation at a wavelength of 500 nm (1.25 nm FWHM). Data was collected with a 40x 0.6 NA objective and point illumination with pixel dwell time of 0.275 s. The intensity (summed photon count) image in (a) shows larger than previously measured intensity from the CVD region, caused by emission from $SiV^-$. The scale bar is 0.2 mm. (b) spatial phasor plot with numbers along the outside of the universal circle representing a lifetime scale in ns. The spatial phasor plot shows several distinct regions inside the universal circle, suggesting complex decays are present. The lifetime maps in (c, d, e) show variation in the HPHT substrate as previously shown, but spatial variations in the CVD diamond are now apparent. The lifetime images use the same colour scale which is in ps. ..... 163*

*Figure 70 - Exemplar decays and MLE quadruple-exponential fits from the FLIM data for an excitation wavelength of 500 nm and detection wavelength of 737 nm. Top graph for each panel: round points, raw data; solid blue line, fit; red line, IRF. Bottom graph of each panel: normalised fit residuals. The modulation lifetime image shows the locations where the decay originated. ..... 164*

*Figure 71 - Beta and $\chi^2$ maps of the emission at a wavelength of 737 nm and excitation at a wavelength of 500 nm for the data in Figure 69. Components 1 & 4 are attributed to the CVD region and components 2, 3 & 5 are attributed to the HPHT region. ..... 165*

*Figure 72 - ROI selections from the phasor diagram in Figure 69, showing the variation in modulation lifetime in the CVD diamond and HPHT substrate.* ..... 166
*Figure 73 – These ROI selections operate in reverse to Figure 72, and show data from Figure 69. The images were used to extract the local phasor plots for four ROIs. The phasor plot outlines correspond to the colours of the ROI photon count images. This is a useful capability if a specific region on the sample, as opposed to a lifetime cluster on the phasor plot, is of interest.* ..... 167
*Figure 74 - (a) Integrated photon count image from emission centred at a wavelength of 675/2 nm. The scale bar is 0.2 mm. (b) Integrated photon count image from emission centred at a wavelength of 737/2 nm. (c) Beta map of $NV^0$ from fit shown in Figure 71. The red lines through these images denote the line profile used for panels (e) and (f). (d) A scatter plot of the integrated photon counts of the two emission bands showing regions of linear correlation. (e) A full line profile of images (a)-(c) showing the change in intenisty and beta for $NV^0$. The coloured bars correspond to the colours of the data points in (d). (f) Line profile of counts at emission wavelengths of 675 and 737 nm, and beta of the $\tau_1$ = 19,000 ps component attributed to $NV^0$ showing a strong correlation in the locations of the peaks and troughs.* ..... 169
*Figure 75 – An extension of the analysis shown in Figure 74. Images a) and b) are the summed intensity images from the CVD diamond of 675 and 737 nm emission, respectively. The emission from 675 nm is caused by $NV^0$, whilst the emission at 737 nm is dominated by $SiV^-$. Image c) shows the four ROI regions which were used to plot the scatter graph. The scatter graphs show the relationship of the pixel counts for the two emission bands, where the black line indicated unity gradient. ROI 1 and 2 show similar gradients, but ROI 3 has a decreased gradient. ROI 4 shows a significant change relative to the other ROIs.* ..... 170
*Figure 76 – Point-spectrally resolved TCSPC data recorded using a 40x 0.6 NA objective, with an excitation wavelength of 500 nm (1.25 nm FWHM) using a integration time of 5 s per emission wavelength. (a) Intensity modulated median wavelength image from Figure 63. The scale bar is 0.5 mm. (b) Emission spectra calculated from the integrated photon count of the decay profile acquired at each emission wavelength, with a data point every 0.5 nm. The locations of the two ROIs are shown in (a). (c) population fraction (β) parameters from MLE fitting of the spectrally-resolved decay curves for ROI 1 to a quadruple exponential decay model and a double exponential for ROI 2. (d) Spectrally-resolved phasor plot of ROI 1 demonstrates a linear region between a monoexponential decay of ~19 ns ($NV^0$) for the blue end of the emission spectrum, and a point inside the universal circle for the red end of the emission spectrum. Each data point corresponds to a different emission wavelength (indicated by the colour scale). (e) Spectrally-resolved phasor plot for ROI 2 shows a similar feature as (d) between a monoexponential decay of ~19 ns for the blue end, and a point near*

*a monoexponential decay of ~1.1 ns for the red end of the emission spectrum. Points for an emission wavelength below 700 nm are found on the universal circle at ~19 ns. (f) The phasor modulation lifetime and intensity-weighted mean lifetime from MLE fitting as a function of emission wavelength. ..... 173*

*Figure 77 - a) shows the variation in the spectral power density at the sample plane from the tuneable supercontinuum laser source. b) shows the variation in spectral resolution of the excitation source, as measured by the imaging spectrograph, with an increase in linewidth attributed to the reduced dispersion at longer wavelengths. ..... 175*

*Figure 78 – Phasor analysis of excitation-emission-lifetime data from a location on the HPHT substrate. An intensity modulated median wavelength image is shown in (a) with the marked ROI, from Figure 63. The excitation-emission phasor plot of the excitation-emission-lifetime image is shown in (b), where colour represents the number of pixels with that phasor coordinate. There is a complex region and a linear region extending from a lifetime of ~19 ns on the universal circle. (c) shows the emission intensity (summed photon count) excitation-emission matrix of the ROI in the HPHT substrate. This indicates that the bulk of the emission comes from $NV^-$ emission (>637 nm, yellow region). A log scale plot of (c) is shown in (d). See text for explanation of the coloured arrows. ..... 177*

*Figure 79 - The plot in a) shows the modulation lifetime-excitation-emission matrix corresponding to the phasor plot in Figure 78 b). b) shows the same data as a) plotted on an 11x expanded lifetime scale to enhance the contrast. See text for explanation of arrow. ..... 178*

*Figure 80 - Iteratively fitted excitation-emission-lifetime plots. Plots of (a, b) intensity-weighted mean lifetime and (c, d, e, f) population fraction $\beta_i$ against excitation-emission wavelength for a fit to a quadruple-exponential decay model of luminescence from an ROI in the HPHT substrate, indicated in Figure 78 a). ..... 179*

*Figure 81 - The EELM weighted mean lifetime plot shows a green and two red lines corresponding to three different wavelength measurements which are extracted in the bordered graphs. The beta corresponding to $NV^0$ (beta 1) is shown with the weighted mean lifetime from the MLE fit and the corresponding phasor modulation lifetime. The peak at 580 nm of 605 nm emission beta 1 (green line) is caused by laser bleed through in the red bordered plot. ..... 180*

*Figure 82 – A power-corrected excitation-emission-lifetime matrix for a location containing $SiV^-$ and $NV^0$ in the CVD diamond. The black outline is a projection of the emission wavelength graphs, which produces a PLE spectrum, dominated by $SiV^-$ emission. Below excitation wavelengths of 600 nm, the weighted mean lifetime shows a more complex profile due to contributions from the $NV^0$ phonon side band, causing a variation in the weighted mean lifetime with emission wavelength. For excitation*

*wavelengths above 600 nm, there is insufficient energy to excite $NV^0$, reducing the decay to a monoexponential with the lifetime of $SiV^-$ at 1.1 ns. ..... 185*
*Figure 83 – The graph shows the PLE spectrum for emission dominated by $SiV^-$ collected at 738 nm (black line), the weighted mean lifetime (red line), and the population fraction of $SiV^-$ (beta 2, blue line). The energy level diagram shows the ground and excited state, where the 737 nm ZPL originates, with a higher energy level above the excited state. Below 637 nm, the electron is excited into the 2nd excited state, whilst above 637 nm, the electron is excited directly to the first excited state, where the ZPL originates. ..... 186*
*Figure 84 – This figure describes the polarisation orientations in relation to the sample position during the polarisation-resolved PLE measurements. For a {100} sample, as shown here, there are four orientations of the SiV defect, as shown by the four images below the image representing the diamond. The orientation of the vertical and horizontal illumination and detection polarisation states are constant in all cases, and the sample is rotated to a 'parallel' case, where the edges of the sample are parallel to the polarisation states, and 'diagonal' where they are 45° offset. The location excited on the sample is shown by the orange dot. ..... 188*
*Figure 85 – A polarisation-resolved PLE measurement of the $SiV^-$ taken at 738 nm emission in the 'parallel' case. The location excited on the sample is shown by the orange dot. All four polarisation measured spectra overlap irrespective of excitation wavelength, suggesting an equal contribution from all four orientation of the defect within the sample. ..... 189*
*Figure 86 - A polarisation-resolved PLE measurement of the $SiV^-$ taken at 738 nm emission in the 'diagonal' case. The location excited on the sample is shown by the orange dot. There are two pairs of spectra here for each. The two matched spectra are the opposite excitation cases, and this is explained in detail in the text. The crossover occurs at approximately 637 nm, and the large peak at 546 nm is a constant feature in all spectra. ..... 190*
*Figure 87 - A polarisation resolved PLE measurement of the $SiV^-$ defect taken at 738 nm emission in the 'diagonal' case. The location excited on the sample is shown by the orange dot. This sample has been rotated by 90° relative to the data in Figure 86, but the spectra are similar. This measurement continues to 400 nm in excitation. ..... 191*
*Figure 88 – The graph in a) shows a combination of the data from Figure 85 and Figure 86 using the notation of (P) for 'parallel' and (D) for 'diagonal'. Below 600 nm the 'parallel' spectra are approximately averaged positions of the 'diagonal' spectra. Graphs b) and c) show the 'diagonal' case contrasts described by Equation 28 and Equation 29 respectively. The zero-point crossover for contrast in b) and c) is shown to be 637 nm in both cases. In all graphs the green region represents the ZPL phonon side band maximum extension. ..... 192*

*Figure 89 – Theoretical models showing the projection of the expected contrast for the XY dipole in a) and Z dipole b) for a {100} plane. The orange and purple plots show the expected contrast for the two pairs of SiV orientations in the lattice. The vertical and horizontal polarisation states are 0°, 90°, 180°, and 270°, noting that that for 'diagonal' case data these positions are rotated by 45°. ..... 194*
*Figure 90 – Excitation below 650 nm has theoretical contrast shown (left), and represents a XY dipole, whilst the data (right) shows the theoretical contrast for the Z dipole, the colour scale bar denotes the contrast. Excitation and emission polarisation run from 0 to 90°. The exact contrasts are not achieved due to effects discussed in the text. The central graph shows the measured data from Figure 88, with an energy level diagram above showing the main transitions. ..... 195*
*Figure 91 – Data collected using the same parameters as Figure 85 for a 'parallel' case, on a high birefringent region (high strain). As shown in the data from Figure 85, this should be four identical spectra. This data shows variation in the PLE spectra below 560 nm. This splits into two pairs, with common emission polarisation. This could suggest strain splitting of energy levels, or wavelength dependant birefringence. ..... 196*
*Figure 92 – Images (left) show the colour white-light transmission and birefringence of the sample. The sample does exhibit some strain induced birefringence. In the image (right) the emission spot can be seen when the excitation source is blocked by filters. Images were taken with the side port colour CMOS camera, on the CVD diamond. ..... 197*
*Figure 93 - A polarisation resolved PLE measurement of the $SiV^-$ defect taken at 738 nm emission in the 'parallel' case. The location excited on the sample is shown by the orange dot. This is a CVD diamond with the same cut ({100}), and shows the same spectral features seen in Figure 85. ..... 198*
*Figure 94 - A polarisation resolved PLE measurement of the $SiV^-$ defect taken at 738 nm emission in the 'diagonal' case. The location excited on the sample is shown by the orange dot. This is a CVD diamond with the same cut ({100}), and shows the same spectral features seen in Figure 86. ..... 199*
*Figure 95 – The graph (left) shows the PLE lifetime data fitting of the SiV- defect with a monoexponential decay for eight different polarisation and sample orientation measurements. The graph (right) is an extracted PLE spectrum one of the decays. The red dotted lines at 546 nm indicate where the large feature in the PLE spectra is, whilst the blue dotted line shows a region of fluorescence lifetime anisotropy in the lifetime data. This blue line corresponds to a feature in the PLE spectra. Below 546 nm the lifetime slowly increases and is discussed in the text. The lack of $NV^0$ in this sample enabled this measurement to be more accurate. ..... 200*
*Figure 96 – Luminescence decays for SiV- defect. Graphs a) and b) show the example decays normalised to 100. The colour of each line indicates the emission wavelength from dark red (680 nm) to purple (450 nm). The variation in t0 with excitation wavelength due to path differences in the*

*prism based monochromator causes a 'rainbow' effect where the curves are increasingly shifted in time for increasing excitation wavelength. For fitting, t0 was included as a fitting parameter, and the results for all eight measurement as a function of excitation wavelength are shown in graph c). Note that in c) a negative value corresponds to the decay being shifted further in time (to the right). .... 201*

*Figure 97 – SiV- luminescence decay profile for an excitation wavelength of 546 nm and an emission wavelength of 738 nm. A monoexponential decay fit (blue dashed line) to the data (blue circles) is shown together with the IRF (red line). The plot on the right shows a zoom of the region near the rising edge. ..... 202*

*Figure 98 – A comparison between PLE data taken from Figure 83 at room temperature (red line) and absorption data from the University of Warwick (black line) at liquid nitrogen temperatures. Despite the large temperature difference most of the features are resolvable in the PLE measurement, and they align well, which strongly suggests this is a fundamental measurement of the $SiV^-$ defect. ..... 203*

*Figure 99 - a) Intensity-modulated false-colour mean wavelength hyperspectral image of a natural cut and polished diamond, taken under 355 nm excitation, using a 4X, 0.16 NA objective of a 170 nm spectral band from 400 nm, with spectral resolution of 1 nm. The red dotted box indicates the region imaged with FLIM. b) White-light colour image of the sample 0.25 carat cut natural diamond. c) Integrated intensity point-scanned image of the emission at 430/5 nm, acquired with a 40x 0.55 NA objective in a). d) 3x3 binned intensity weighted mean lifetime luminescence lifetime map (ps), fitted pixelwise with a triple exponential decay, showing spatial variations in intensity weighted mean lifetime. e) Luminescence emission spectrum of the sample integrated across the whole hyperspectral image. The ZPL at 415.2 nm indicates this is the emission from the N3 defect and its lifetime has been significantly quenched to an average of 23.6 ns. f) Spectrally resolved intensity weighted mean lifetimes of two regions on the sample that showed a variation in lifetime in the luminescence lifetime map d)..... 208*

*Figure 100 – A set of intensity-merged and not intensity-merged images showing the spatial variations of various parameters. $T_2$ and $\tau_3$ had fixed lifetimes and so the images are not shown here. The $\chi^2$ map shows no obvious structure, suggesting the model is a good fit for the data to within the noise level for all regions of the image. This data corresponds to the model from Figure 99 d). ..... 209*

*Figure 101 - Analysis of luminescence lifetime data from the natural diamond sample excited at 355 nm with a 430/5 nm detection band for pixelwise fitting: a) shows a 2D false-colour histogram of the intensity-weighted mean lifetime plotted against the total photon count (I), presenting a linear relationship between the total photon count and weighted mean lifetime; b) is an exemplar single pixel luminescence decay profile showing the fit to the triple exponential decay model. The table shows the fitted parameters. ..... 210*

*Figure 102 - a) Spectrum of a point on the natural cut sample under 355 nm excitation using a 4X, 0.16 NA objective, with a log scale indicating the presence of the 1st and 2nd order Raman shift at 372 and 392 nm respectively. b) Spectrally resolved decay profiles from same region with a decay plotted every 0.05 nm. c) Spectrally resolved intensity-weighted mean lifetimes globally fitted with three exponential decays, binned to 0.5 nm resolution. d) Spectrally resolved β and τ values of each decay component globally fitted, binned to 0.5 nm resolution. ..... 211*

*Figure 103 – Images taken by De Beers showing a blue transmission filter light transmission image (left), and a DiamondView™ image of the same sample (right) of a natural diamond plate. The emission colours indicate blue and green emitters, potentially indicating N3 and H3 defects. ..... 213*

*Figure 104 – Hyperspectral data from the natural diamond plate under 405 nm excitation using a 4x 0.16 NA objective. A white-light transmission image of the sample is shown in a) and does not reveal anything significant about the sample. Crossed polarisers were used in conjunction with white-light transmission to form the birefringence image of the sample in b). This reveals regions of strain in the lattice, which causes birefringence. The median wavelength from the hyperspectral data was calculated and a grey scale map is shown in c). The diamond is split into two distinct regions. One region to towards the top of the image is uniform with a median wavelength of 520 nm, whilst the bottom right of the sample shows a more structured and complex profile, with varying median wavelengths. Combining a summed intensity image (not shown) with the median wavelength (as colour), the image in d) reveals that the more complex region of the sample is the brightest. The scale bar is 500 µm. ..... 214*

*Figure 105 – The median wavelength (left) and intensity modulated median wavelength images (middle) are shown here with various regions of interest highlighted, under 405 nm excitation. The averaged spectra from these regions have been highlighted on the graph (right), which show the variation in spectral features. The vertical coloured lines in the graph indicate the emission bands used for the FLIM experiments discussed below. The scale bar is 500 µm. ..... 215*

*Figure 106 – An example decay from the natural diamond plate, measured at 600 nm emission using 405 nm excitation. The fluorescent component of this measurement decays to the noise floor inside the pulse period of the laser. The large offset observed here originates from long lived emission/phosphorescence, not from dark counts on the detector. This decay was fitted with a quadruple exponential model from a 3x3 binned pixel from FLIM data. ..... 216*

*Figure 107 – Five locations on the sample were measured using the single-point spectrally resolved lifetime technique, using 405 nm excitation. The median wavelength intensity modulated and median wavelength images are shown, with the five locations indicated. Each coloured ROI has a corresponding graph, and these are analysed in the text. Each graph contains a summed background*

*phosphorescence photon count line (phosphorescence, black), a total summed photon count line (including background phosphorescence, red), a background subtracted summed photon count line (after background phosphorescence subtraction, green), and a phase lifetime line (after background phosphorescence subtraction, blue). The scale bar is 500 µm. ..... 217*
*Figure 108 – The phase lifetime (phosphorescence background removed) and modulation lifetime (phosphorescence background included) for each of the five ROIs in Figure 107 under 405 nm excitation are shown in the two graphs. The complex profiles indicate multiple emitting species, of which, one attributed to N3 emission is quenched..... 219*
*Figure 109 – Summed intensity and background phosphorescence photon count images of a natural diamond plate at five emission wavelengths, under 405 nm excitation. The structure of the emission varies as a function of wavelength, whilst the background emission structure is mostly consistant, with the exception of 450 nm emission. The red arrows inidcate the locations of the three-finned structure discussed in the text. ..... 220*
*Figure 110 – Phase lifetime (with background photons subtracted) and modulation lifetime (without background photons subtracted) at five emission wavelengths under 405 nm excitation, extracted from phasor analysis. Corresponding phasor diagrams are shown in Figure 111. The phase lifetime images represent only the fluorescent components of the emission, whilst the modulation lifetime images show the total variation of lifetime of both the fluorescent and phosphorescent emission. These images are discussed in the text. ..... 223*
*Figure 111 – These phasor plots correspond to the images in Figure 110. The non-background-subtracted phasor plots were used to extract the modulation lifetimes, and the background-subtracted phasor plots were used to extract the phase lifetimes. The background has a significant impact on the distribution of the data points in the phasor plot, due to the contribution of the background to total photon count. The coloured data points represent the number of pixels in the image. ..... 224*
*Figure 112 – Two images from DiamondView™ taken by De Beers of a natural diamond plate showing emission from opposite sides of the sample. There is some structure present, but the sample primarily emits in the blue spectrum, attributed to N3 emission. ..... 226*
*Figure 113 – Concentration data for three nitrogen related defects taken by Dr Phil Diggle (De Beers) using spatially mapping IR absorption spectroscopy. There is variation in all three defects, and the A-centre and nitrogen spatial variation are similar. ..... 227*
*Figure 114 – FLIM of the natural diamond plate sample was taken using a 405 nm laser, 40x 0.6 NA objective and 5 MHz to collect the data shown above. The emission wavelength was 450/3 nm. The frequency divider setting was used to allow phasor analysis to be utilised. The phasor plot (left)*

*shows an arcing cluster, with many pixels centred at one end of the "comet" and the rest of the pixels spread along a "tail". The summed intensity and modulation lifetime images show a clear correlation between intensity and lifetime. This emission is dominated by N3 defects, and the modulation lifetime reveals the defect is quenched and shows significant variation. ..... 228*

*Figure 115 – A zoomed in region of the phasor plot is shown, with a region of interest centred at the "head" of the "comet". The extracted modulation lifetime image for this region reveals that it is the top part of the sample that has the lowest modulation lifetime. ..... 229*

*Figure 116 - A zoomed in region of the phasor plot is shown, with a region of interest centred at the "tail" of the "comet". This shows a much larger variation in modulation lifetime and contains significantly more structure in the resultant modulation lifetime image. ..... 229*

*Figure 117 – The graph above shows the relationship between photon counts and modulation lifetime across the entire image. This is a complex profile that requires additional data to be analysed accurately. Broadly, there is a relationship between photon count and modulation lifetime, where the lifetime variation is due to quenching. ..... 230*

*Figure 118 – A flow chart showing a possible strategy to analyse an unknown sample using the developed multidimensional luminescence microscope. Typical data acquisition times are given, although these are heavily dependent on the acquisition parameters, including dwell time, spectral ranges, and sampling. ..... 232*

*Figure 119 – An optical diagram showing the excitation and emission paths using a small, mirrored region on a glass substrate. The excitation light is reflected by this mirror onto the sample, whilst the emission passes through the glass into the detector. The mirrored region blocks the emission light creating a mask. This would be wavelength independent, unlike dichroic mirrors. The above design works for point scanning, such as employed for FLIM measurements. ..... 237*

# List of tables

*Table 1 – A summary of the different excitation mechanisms and their associated emission names. 35*

*Table 2 – Table showing some of the ZPLs and lifetimes for some of the key defects investigated in this work. ..... 83*

*Table 3 – A table giving the overview of the spectral properties for the imaging port of the spectrograph for the two detectors. ..... 104*

*Table 4 – A summary of the lifetime components under 500 nm excitation at 675 nm emission and their attributed defect..... 161*

*Table 5 - A summary of the lifetime components under 500 nm excitation at 737 nm emission and their attributed defect..... 170*

# Chapter 1 – Thesis overview

For this PhD thesis, a novel multidimensional luminescence microscope was developed, which combines hyperspectral imaging, FLIM, polarisation and spectroscopy. Experimental parameters such as excitation wavelength, emission wavelength and polarisation can be varied for luminescence measurements. These modalities can be combined to provide multimodal data for a wide range of applications. The instrument can also apply these modalities to imaging. The instrument was developed to study diamond luminescence and was used to map several different samples and defects spatially, spectrally, and temporally.

**Chapter 2** will discuss the photophysical mechanisms and properties of luminescence (also described as "fluorescence"), including energy, lifetime, wavelength, and outline how fluorescence can be useful to determine material or defect properties. Fluorescence can be useful to determine the emitters present in a sample, which can inform about the growth condition in diamond for example. Optical microscopy is then briefly reviewed, including the primary spectroscopy and imaging techniques exploited in this PhD project: hyperspectral and lifetime measurements and photoluminescence emission (PLE) measurements. A discussion of design considerations for instrumentation to study luminescence in both natural and synthetic diamond is also included.

In **chapter 3**, the crystal properties of diamond are discussed, covering basic structure, crystallinity, and its structural properties, which include its mechanical and thermal properties. A pure diamond's optical properties and Raman scattering process are also discussed, along with a discussion of band structure. The complex growth of natural and synthetic diamond is briefly reviewed, including an overview of the primary growth techniques for synthetic diamond - focusing on high pressure high temperature (HPHT), and chemical vapour deposition (CVD) synthesis. Lattice defects found in diamond are then discussed, with their properties and potential applications.

**Chapter 4** reports the development of the luminescence instrumentation. It includes the description and evaluation of a developed simple grism based hyperspectral line scanning luminescence microscope, which was used as the starting point for the final instrument developed. A previously-constructed time-resolved spectrofluorometer designed for bulk measurements was also used and adapted for application to diamond luminescence. The limitations of both systems were addressed in the finally-developed, novel multidimensional luminescence microscope, for which the constituent components are detailed, and their performance characterised in terms of spectral and spatial resolution. Several exemplar data sets are shown for hyperspectral imaging, FLIM, and excitation-emission-lifetime techniques applied to diamond luminescence.

The data analysis techniques are introduced. Luminescence data collected in this thesis is multidimensional and therefore is non-trivial to analyse or visualise. The discussion covers hyperspectral and lifetime data analysis. Lifetime analysis is divided into iterative exponential fitting, and phasor analysis. The merits of these techniques are discussed. For phasor analysis, the background theory is explored and a solution to utilise the incomplete decay profiles obtained from TCSPC measurements, as implemented in the developed instrument, is presented.

**Chapter 5** reports the application of the capabilities of the developed instrument to synthetic diamond sample. A single synthetic diamond, consisting of a HPHT substrate and grown CVD diamond, was studied using hyperspectral imaging, spectrally resolved FLIM, single point-spectrally resolved lifetime and excitation-emission-lifetime matrix measurements. Phasor analysis was used in conjunction with iterative lifetime fitting to reveal spatially dependant quenching of the negatively charged nitrogen vacancy ($NV^-$) defect in the HPHT substrate. This was revealed to be spectrally dependant on excitation wavelength through the excitation-emission-lifetime matrix analysis.

**Chapter 6** discusses measurements on two separate diamond samples, where the energy level structure of the negatively charged silicon vacancy ($SiV^-$) was probed using polarisation resolved PLE lifetime measurements. This data indicated that an $2^{nd}$ excited state exists with a different dipole orientation than the excited state. The fluorescence lifetime of the defect was also found to vary towards shorter excitation wavelengths (<550 nm).

**Chapter 7** reports the application of the capabilities of the developed instrument to several natural diamonds. Two natural diamonds were investigated using hyperspectral imaging, spectrally resolved FLIM, and point-spectrally resolved lifetime measurements. These measurements revealed several spatially-varying defects and quenching caused by A-centres. The second diamond presented quenching of N3 defect emission within a complex luminescence profile and so a third diamond presenting just emission from N3 defects was also studied. This sample was investigated using FLIM and analysed with phasor analysis, which indicated a possible correlation between photon count and modulation lifetime.

**Chapter 8** concludes the thesis, summarising progress to date and outlines several possible future research paths and potential upgrades to the instrument.

# Chapter 2 – Optical microscopy, spectroscopy, and lifetime

## Outline

This PhD thesis concerns the spectroscopy, lifetime analysis and imaging of luminescence from diamond, which can provide information about the sources of emission. In this chapter the underlying photo physics of luminescence, techniques for its measurement, and the required instrumentation is reviewed. Luminescence is first discussed, giving an outline of the important parameters, including quantum efficiency, emission/absorption spectra and lifetime. Optical techniques used in this thesis are then discussed, including an analysis of different lifetime measurement techniques. Finally, the instrumentation required for each of these techniques is discussed, along with their respective advantages and disadvantages. Photoluminescence techniques are widely used to probe structure and function of diverse materials. They are mostly non-destructive in solid-state media. Luminescence measurements are useful for diamond defect analysis because of the potential for unique spectroscopic fingerprints and applications for quantum optical devices.

## Luminescence

Luminescence can occur in a material following excitation (i.e. the absorption of energy), when electrons decay from higher energy excited states to a lower energy ground state, emitting a photon of light in a radiative process[1]. This photon energy will usually be equal in energy to the loss of the electron's energy, i.e., the difference in energy between the two energy states. A Jablonski energy level diagram is a common method to show these electronic transitions, as shown in Figure 1[1].

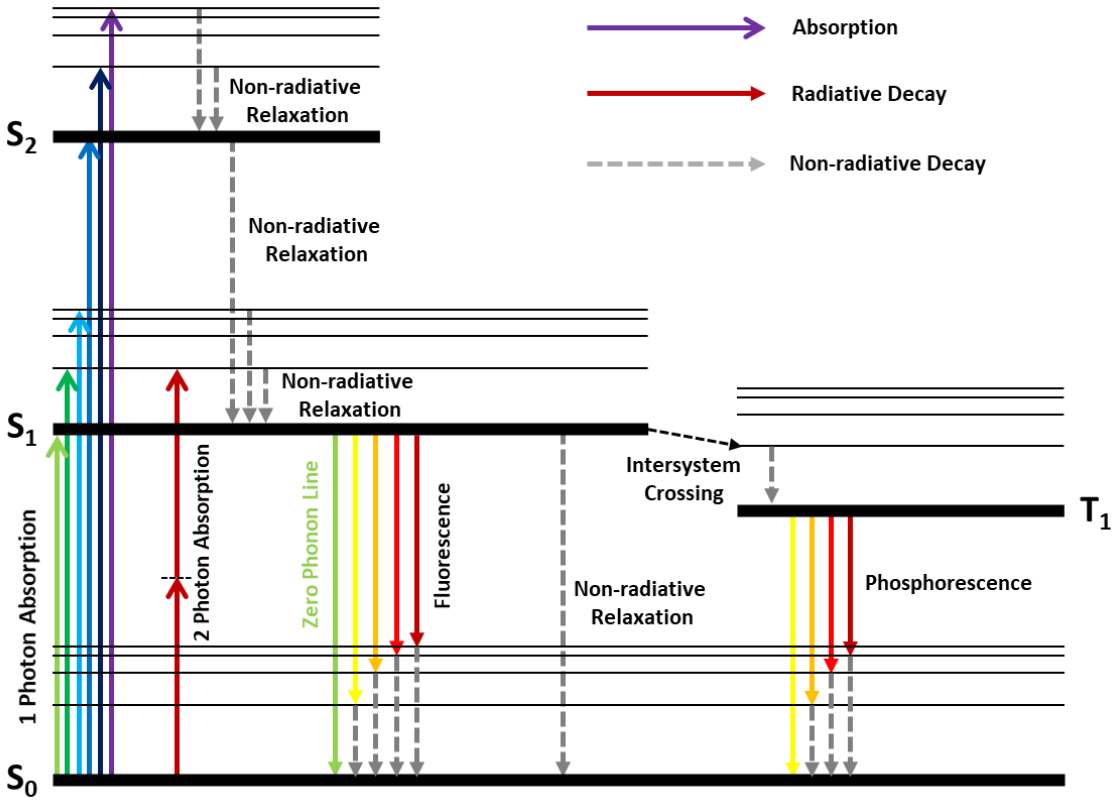



*Figure 1 – A Jablonski energy level diagram showing the common electronic transitions in a luminescent species. The exact energy level structure will depend on the emitter. Colour is used here to represent the approximate wavelengths of light (and therefore energy) in each process. Non-radiative relaxation does not involve the emission of light and therefore is coloured grey.*

There are several relaxation processes which can occur following excitation, as shown in a Jablonski energy level diagram. Luminescence can be classified as "fluorescence" or "phosphorescence", which can be distinguished by the relative timescales of each process[1]. Fluorescence typically occurs on ~$10^{-9}$ s time scales and occurs when an electron decays from a singlet (excited state $S_1$) to a singlet energy level (ground state $S_0$)[1]. Phosphorescence typically occurs on much longer time scales, up to minutes and beyond, and occurs when an electron makes a "spin-forbidden" transition, decaying from a triplet state ($T_1$) to a singlet energy level[1].

Immediately after excitation, the system typically relaxes to the ground vibrational and or rotational state of that excited electronic state through non-radiative processes (vibronic relaxation is an example process), which is usually a very fast process occurring on $10^{-13}$ s timescales[1]. From this state, the electron can relax through luminescence or non-radiative decay. Non-radiative relaxation can occur where energy is lost to the lattice as heat in a crystal[2], and occurs on similar time scales to luminescence for luminescent transitions. In vibrational relaxation, an electron will decay down through the vibrational energy levels but stay in the same singlet state. In internal conversion, an

electron will move from a low vibrational energy level of a singlet state and move to a high energy vibrational energy level of a lower energy singlet state, without a change of overall energy. At room temperatures, an electron will decay from the bottom of the excited state to the ground state. and this is called Kasha's rule[3].

## *Absorption, Emission, Stokes shift*

Absorption and subsequent excitation of an electron can occur in several forms, and emission caused by these forms of excitation is referred to differently; in this thesis, only photoluminescence is explored. These alternative excitation pathways are reviewed in Table 1.

*Table 1 – A summary of the different excitation mechanisms and their associated emission names.*

| Energy Source | Emission |
|---|---|
| Photons | Photoluminescence |
| Sound (Acoustic energy) | Sonoluminescence |
| Heat | Thermoluminescence |
| Electric field | Electroluminescence |
| Electrons | Cathodoluminescence |
| Friction or Pressure | Triboluminescence |
| Biological (Organic) | Bioluminescence |
| Chemical (Inorganic) | Chemiluminescence |

The absorption spectrum of a material will be governed by how the energy and vibronic levels overlap, causing some transitions to be stronger than others. The more vibrational or thermal energy in a system, the broader the spectrum, applying to both the absorption and emission.

The energy required from a photon to move an electron between the energy levels is given by[1]:

$$E = \frac{hc}{\lambda}$$

*Equation 1 - where h is Planck's constant, c is the speed of light, E is the difference in energy between the two levels, and λ is wavelength.*

This equation, which is also valid for photon emission, links energy to wavelength and indicates how different colours can be emitted from excited materials according to the energy gap between the

two states. Thus, photons can be used to probe the electronic transitions inside a material to provide a spectroscopic fingerprint for specific materials[4]. This is the basis of photoluminescence spectroscopy.

The emitted photons will usually have less energy than their excitation photons due to the losses associated with non-radiative relaxation (e.g. vibrational relaxation where energy can be lost to phonons within a crystal lattice). This red shift is called a 'Stokes shift'[1] and can vary, with temperature and material.

An excitation, or emission process of an electron that does not involve a phonon, or any vibronic energy level is referred to as a zero phonon line (ZPL). A ZPL spectral feature will overlap with the excitation (absorption) and emission spectra, with the vibrational structure mirrored around it. Phonon replicas of the ZPLs (which are inherently phonon free emissions) can exist for specific energy phonons. This manifests as further, red-shifted peaks at specific wavelengths/energy, where the replica distance from the ZPL indicates the energy of the interacting phonon[5]. An "anti-Stokes" shift can also occur when a photon absorbs the energy of a phonon and re-emits at a shorter wavelength (i.e. with higher photon energy). This process is much less common than the Stokes shift but becomes more prominent at higher temperatures.

The emission band of an excited material will, in general, mirror the excitation or absorption spectrum[1].

The ratio between the emitted and absorbed photons is referred to as the quantum efficiency or quantum yield and is shown in the equation[1]:

$$\eta = \frac{N_{\text{emission}}}{N_{\text{absorption}}}$$

*Equation 2 - where η is the quantum efficiency, $N_{\text{absorption}}$ is the number of absorbed photons, and $N_{\text{emission}}$ is the number of emitted photons.*

A higher concentration of the emitting species produces more emission photons, and therefore intensity measurements can be used to quantify their concentration, providing the excitation intensity and quantum efficiency is known. In practice, this is much more difficult than absorption spectroscopy, due to complications such as scattering, absorption and variations in quantum efficiency of detectors. Another complication due to the emission being emitted over a range of angles, is that not all the photons can physically be collected, unlike absorption measurements that can be configured to implement a collimated light path.

## *Absorption and PLE spectroscopy*

The absorption spectrum of a material can be determined using the following equation (Beer-Lambert law) by measuring the transmission as a function of wavelength[6]:

$$I(l) = I_0 e^{-\varepsilon_\lambda l C}$$

*Equation 3 - where $I_0$ is the initial intensity, $\varepsilon_\lambda$ is the absorptivity of the species at wavelength λ, l is the optical path length, and C is the concentration of the species.*

However, this technique requires two flat parallel faces to work effectively, as scattered, or refracted light would contribute to the observed signal attenuation, resulting in incorrect data. Depth information cannot be collected using a traditional parallel-faced absorption technique. In the example of diamond, which exhibits a large Fresnel reflection, multiple passes of the sample can occur from reflections off each face of the sample, modifying the measured spectra.

If the sample of interest contains an emitting species, then it is possible to tune the excitation wavelength[7] and measure the emitted photons in a technique called photoluminescence emission (PLE) spectroscopy. This is a more sensitive method and could be applied to 3D imaging. This method requires a tuneable excitation source of sufficient intensity.

PLE can be combined with emission spectroscopy to generate excitation-emission matrices of a sample[8, 9]. These can be used to distinguish specific emitters, to identify the most effective excitation wavelength for a measurement, or to preferentially excite specific emitters of interest while minimising excitation of other species. Examples of such experiments are presented later in this thesis.

## *Luminescence Lifetime*

The time an electron will remain in the excited state is referred to as the upper/excited state lifetime, and in the case of fluorescence, the fluorescence lifetime, τ. The unperturbed lifetime is called the natural lifetime ($\tau_{natural}$) and occurs when all excitation events result in emission[1]. Lifetime is related to the decay rate by the equation:

$$k = \frac{1}{\tau}$$

*Equation 4 – where τ is the fluorescence lifetime, and k is the decay rate.*

Practically and experimentally, non-radiative emission occurs, and the resulting lifetime is usually referred to as the fluorescence lifetime or experimental lifetime ($\tau_{experimental}$)[10]. This can be expressed as the inverse of the rates of decay of radiative and non-radiative processes shown in the equation:

$$\tau_{experimental} = \frac{1}{k_{\text{radiative}} + k_{\text{non-radiative}}}$$

*Equation 5 - where $\tau_{experimental}$ is the measured experimental lifetime, $k_{radiative}$ is the radiative decay rate, and $k_{non-radiative}$ is the non-radiative decay rate.*

The radiative and non-radiative decay rate are also related to the quantum efficiency and lifetime by the equation:

$$\eta = \frac{k_{\text{radiative}}}{k_{\text{radiative}} + k_{\text{non-radiative}}} = \frac{\tau_{\text{experimental}}}{\tau_{\text{natural}}}$$

*Equation 6*

The fluorescence intensity can be written as an exponential decay of the form[1]:

$$I(t) = I_0 e^{-\frac{t}{\tau}}$$

*Equation 7 - where I(t) is the intensity at time t, and $I_0$ is the initial intensity*

This is only valid for single population of emitters or simple emitters, and often there are multiple emitting species resulting in more complex decay profiles, which can sometimes be modelled as a sum of multiple exponential decay profiles[1]:

$$I(t) = \sum_{i=1}^{i=n_\tau} A_i \, e^{-\frac{t}{\tau_i}}$$

*Equation 8 - where, $A_i$ is the initial amplitude of component i, and n is the number of components.*

The population fractions (beta, β) of the separate components are expressed as:

$$\beta_i = \frac{A_i}{\sum_{i=1}^{n_\tau} A_i}$$

*Equation 9 – where $\beta_i$ is the population fraction of component i[11].*

Where:

$$\sum_{i=1}^{i=n_\tau} \beta_i = 1$$

*Equation 10*

The initial intensity can then be shown as a sum of the component amplitudes[11]:

$$I_0 = \sum_{i=1}^{i=n_\tau} A_i$$

*Equation 11*

The lifetime of an emitter is defined as the time it takes for the emission to decay to 1/e, i.e. 36.7%, of the original value. It is common to use the intensity weighted mean lifetime when displaying average lifetime data of multiple emitters, which is described by the equation[19]:

$$\tau_{IW} = \frac{\sum_{i=1}^{i=n_\tau} A_i \tau_i^2}{\sum_{i=1}^{i=n_\tau} A_i \tau_i}$$

*Equation 12 - where $\tau_{IW}$ is the intensity weighted mean lifetime.*

## *Polarisation*

Photon absorption and emission of a species involves electronic dipoles within the material. This can result in polarisation dependent absorption and polarised emission, which can affect measurements in some optical systems due to the polarisation response of the instrument itself[1]. The difference in emission resolved with respect to polarisation axes is called luminescence anisotropy, r, and can be calculated using the equation[1]:

$$r = \frac{I_\parallel - I_\perp}{I_\parallel + 2I_\perp}$$

*Equation 13 - where $I_\parallel$ is the intensity of emission parallel to the excitation source, and $I_\perp$ is the intensity of the emission perpendicular to the excitation source.*

Polarisation discrimination can also be applied to luminescence lifetime measurements, where it can be used to study the rotation of molecules[12].

In a crystal, only specific dipoles can exist due to the symmetry of the defect that allow specific optical transitions[13, 14]. This can result in the emission being polarised with respect to certain orientations in the lattice. Polarisation can therefore be used to help determine the orientation and symmetry of defects in a lattice with sufficient prior knowledge of the lattice structure[15]. For example in diamond, this requires information about the lattice orientation, and knowledge about the potential orientations of the investigated defect. Polarisation resolved PLE spectroscopy of the $SiV^-$ defect in diamond is explored later in the thesis.

Instrumentational effects will affect the perceived intensity of different polarisation states, due to different efficiencies of diffraction gratings for example. Therefore it is important to characterise the response of an instrument to different polarisation states. This is characterised by the G-factor of an instrument, described by the following equation, and is wavelength dependant[16]:

$$G = \frac{I_{HV}}{I_{HH}}$$

*Equation 14 – where G is the G-Factor, I is the intensity, H is horizontally polarised light and V is vertically polarised light.*

## *Sources of emission*

Many materials are luminescent, and this has a variety of applications such as molecular fingerprinting, light emitting devices and labelling specific biological structure, e.g. for microscopy of cell biology. Emitters can be organic dyes, which can emit over broad wavelength ranges, and can lend themselves to being a good lasing medium[17], as well as fluorescent labels that can be functionalised to attach to specific components of a cell, such as tubulin or actin[18]. This then allows specific excitation to image only those features labelled with the emitters. Multiple labels can be applied, and using different excitation and emission wavelengths, separate colour images can be collected and overlaid.

This thesis is primarily concerned with solid-state material (diamond) exhibiting optical emitters in a crystal lattice. The emission can cover a wide range of wavelengths, and diamond can present emission from 225 to >1000 nm, due to the wide bandgap and the large number of potential defects[19]. Unlike organic fluorophores, these defects do not suffer from photobleaching, an effect which reduces the number of emitting molecules after a certain number of excitation-emission processes[20], because usually no physical change occurs in diamond with photoluminescence. However, it is possible that a defect can be ionised by the excitation radiation, which can turn it into

a different optical species that may be inactive or change its emission/excitation band[21]. Unlike photo-induced changes to organic fluorophores however, these ionisation processes are usually reversible.

## Optical Microscopy

### *Wide-field Transmission*

The traditional optical microscope employs wide-field illumination, an objective lens, a tube lens, and a detector (this can be a camera or a human eye) to form a magnified image of a small sample. Most objective lenses are manufactured to be infinity corrected, which allows flat optical elements to be introduced into the 'infinity' space, without adversely affecting the image quality. The sample can be illuminated through transmission, reflection, or fluorescence modalities. In the case of transmission microscopy, the light source is placed on one side of the sample, and the collection optics at the other, as shown in Figure 2. Polarisers can be introduced before and after the sample, with their fast axis at 90° to each other, to visualise birefringence in a sample, in a method called crossed-polarisation transmission microscopy[22].

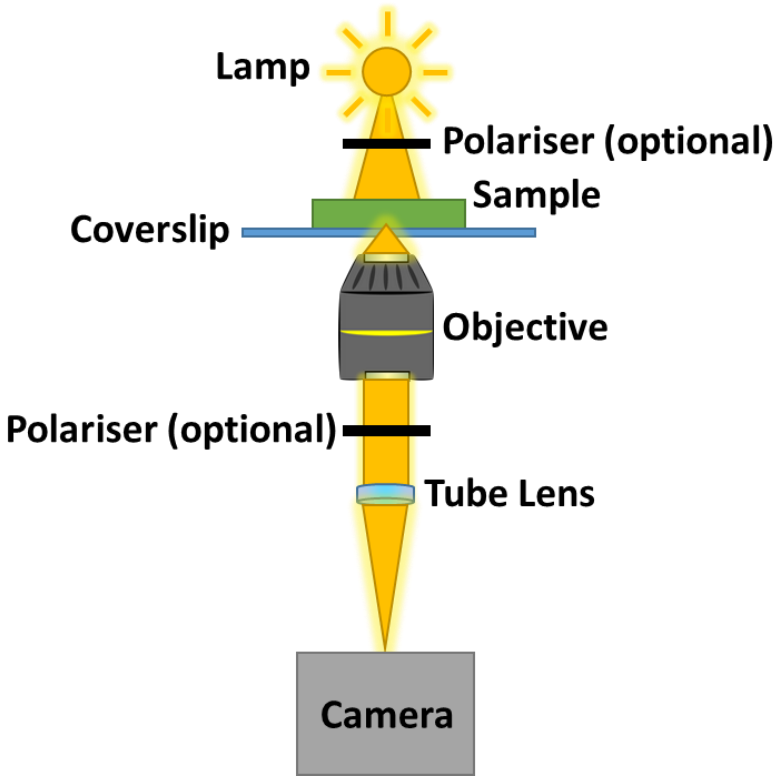



*Figure 2 – A schematic of a conventional wide-field microscope with optional polarisers using white-light transmission illumination.*

## *Fluorescence Microscopy*

A wide-field microscope can be configured for fluorescence imaging using an epi-configuration where both the excitation and emission radiation propagate through the objective lens. The excitation light is directed to the sample via the objective lens, and then the emitted light is collected by the objective lens and directed to the detector. This requires an optical element to separate these two light paths. In fluorescence microscopes, this is usually a dichroic beamsplitter, which is specifically coated to reflect/transmit shorter wavelengths, and transmit/reflect longer wavelengths, based on microscope configuration. A diagram of an exemplar system is shown in Figure 3. The epi-configuration can also be used for brightfield microscopy where a 50/50 beamsplitter can be used to separate incident and reflected/back-scattered light. This is also applicable to fluorescence microscopy when broadband excitation and emission sources are used. However, this results in only 25% of the desired light being collected by the detector due to the double pass of the beamsplitter. It should be noted that wide-field microscopy does not provide any optical sectioning of a sample and so it is most successfully used to image thin samples.

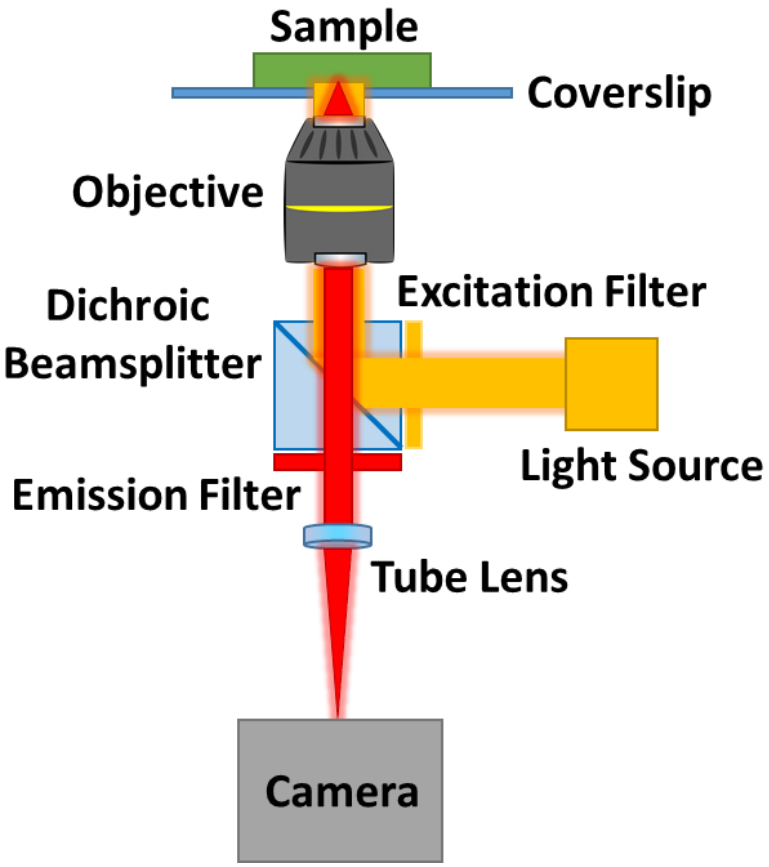



*Figure 3 – A conventional epi-fluorescence microscope for wide-field excitation. The dichroic beam splitter ensures that the red-shifted emission (red) reaches the detector, whilst the emission filter blocks the reflected excitation light (yellow). Dependant on excitation source, an excitation filter may not be required.*

## *Laser Scanning Confocal Microscopy*

While a wide-field microscope provides the entire field of view for rapid imaging using a camera it will collect out-of-focus light. Images of the in-focus plane of an extended (3D) sample will have a strong background due to out-of-focus light from other planes due to the lack of optical sectioning. It is possible to block the out-of-focus light by focussing the incident light to a single point on the sample and by placing a 'small' pin hole near the detector, which rejects the light from outside of the focal volume in the sample[23]. To acquire an image, the illumination spot must be scanned over the sample, which can be achieved through stage or beam scanning using fast electronic mirrors. This is called laser scanning confocal microscopy and can be implemented with brightfield or fluorescence microscopy. An example system diagram is shown in Figure 4.

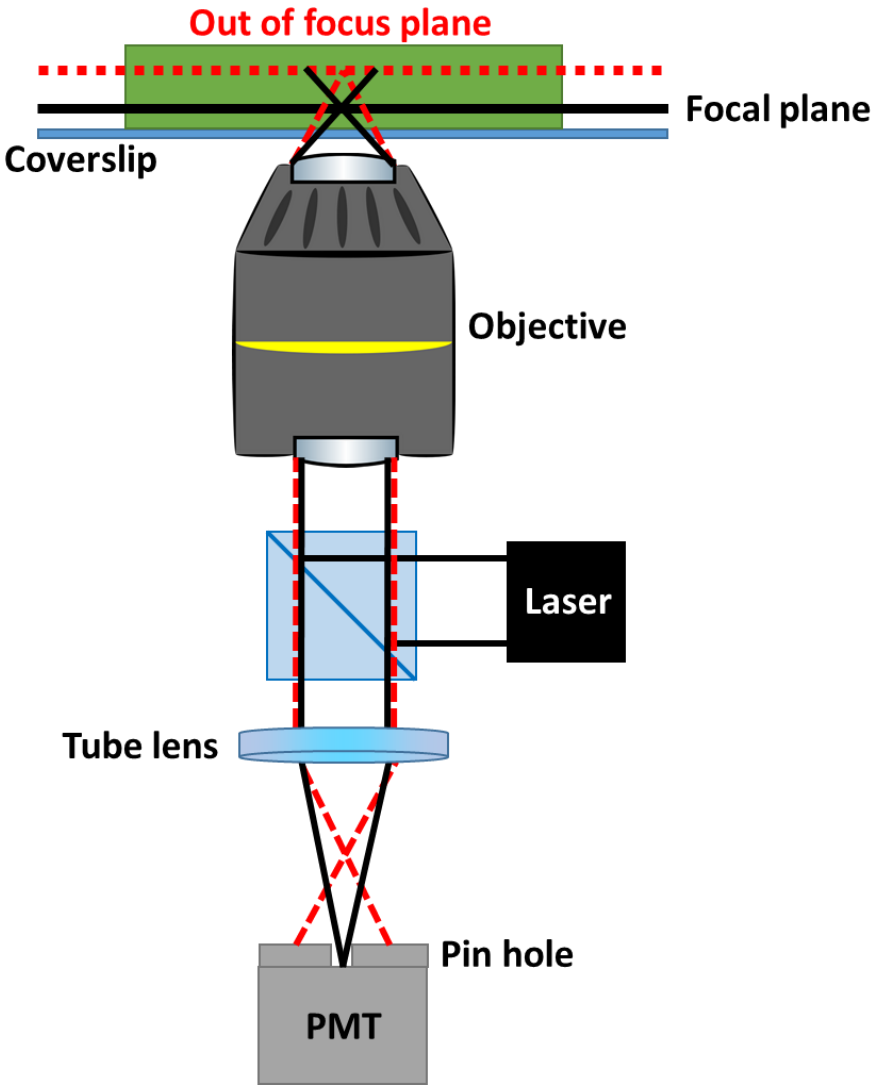



*Figure 4 – An optical diagram of confocal microscopy, which shows how optical sectioning is achieved by blocking the out of focus light from other focal planes. The black lines represent the emission light from the correct focal plane, whilst the red dashed lines are out of focus emission.*

An extension of laser scanning confocal microscopy is to use line illumination with a slit in front of the detector. This parallelised confocal microscopy technique offers faster imaging with slightly inferior rejection of out-of-focus light. Parallel to the slit, the optical system is a wide-field microscope but perpendicular to the slit axis, the system acts as a confocal microscope where the slit acts as a line of pinholes. This can be referred to as semi-confocal slit scanning, assuming the slit is small enough to provide a useful sectioning effect. Line illumination is usually implemented using a cylindrical lens, but a Powell lens, fast scanning galvanometric mirror, or polygon mirrors can also be used to create a line of illumination. A cylindrical lens will create a non-uniform (Gaussian) intensity profile along the line and so it is usual to over-expand the beam at the pupil of the objective lens to create a more uniform illumination line over the field of view of the system. This results in a loss of excitation power at the sample. Additionally, the excitation power density on the sample is lower for line illumination than for the same source in point illumination (at the same average power). This results in a lower photon count per pixel, which results in longer dwell times than for point illumination.

## *Spectral Imaging*

When performing standard fluorescence microscopy, whether that be through confocal, widefield, or another variant, the detection channel typically includes a large fraction of the emission spectrum to maximise the detected signal. However, if there are two or more emitters presenting overlapping emission spectra, signals from different emitters can be difficult or impossible to separate. One approach is to measure multiple signals in different narrower spectral channels, e.g. using band-pass filters. The need for multiple spectrally-resolved measurements reduces photon detection efficiency (assuming spectrally close emitters) and increases the acquisition time and the light dose at the sample. Light dose can be an important parameter for biological samples. Where the emission spectra overlap more than one spectral detection channel, it can be possible to computationally unmix the signals[24].

## *Hyperspectral Imaging*

A more powerful approach to spectrally-resolved imaging data is hyperspectral imaging[25], which entails acquiring a 3D data stack for which a measurement of the emission spectrum is recorded for each pixel of the image. In effect, an XY image in the stack of data exists for each wavelength channel. Hyperspectral imaging can be employed as a reflective technique[26], or for luminescence.

This thesis involves only luminescence hyperspectral imaging, where the analysis and visualisation of this data are discussed in a later chapter.

The range of detection wavelengths, spectral resolution, and spectral sampling parameters required for a specific application need to be considered when designing a hyperspectral imaging system. Whilst smaller pixels provide more sampling and higher potential spatial/spectral resolution, the emission from the sample will be spread out over these pixels and the background noise from the camera will be more significant. Also, increased sampling will result in larger data volumes and increased data processing times.

A hyperspectral 3D (X-Y-$\lambda$) "data cube" can be recorded using a large number of sequentially-acquired narrow-band spectrally-resolved full-field images. This approach is called "framing" and can be achieved by using a filter wheel containing many narrow band-pass filters, a liquid-crystal tuneable filter (LCTF)[27], acousto-optic tuneable filter (AOTF)[28], or linear/circularly varying filter[29]. If only a narrow wavelength range or coarse spectral resolution is required, then a filter wheel is a practical option, but this can become slow or cumbersome if high spectral resolution is required. For example, a wavelength range from 400 to 700 nm with 5 nm spectral resolution would require 60 sequential images with different narrowband filters. This is impractical to implement with mechanical filter wheels. Instead LCTF or AOTF filters can provide rapidly tuneable narrowband filter functionality that is much faster than using filter wheels, but they offer inferior out-of-band suppression. Particularly in the case of LCTFs, the transmission can be low, resulting in longer acquisition times, partly negating the benefit of faster wavelength switching times. Rapid tuning of narrow band detection can also be implemented by translating linear/circularly variable dielectric filters, although the continuous variation of the peak transmission wavelength along the filter results in spectral blurring across the images. The spectral bands are also usually quite broad, >5-10 nm, which is unsuitable for high spectral resolution hyperspectral imaging.

Higher resolution and more photon-efficient hyperspectral imaging can be implemented by combining scanning point or line illumination with a spectrally dispersive element[30]. One of the most common methods is "whisk-broom" or point scanning[31]. This approach scans the point illumination across a sample and directs the collected radiation to a spectrograph that is capable of acquiring a spectrum at each point. The collected point emission is spectrally dispersed onto a 1D or narrow 2D detector, which typically operates with a very high speed and efficiency, relative to larger 2D detectors. This is a slow approach to hyperspectral imaging, for which the image acquisition time directly scales with the number of image pixels. Imaging speeds can be increased by using fast stage scanning or scanning mirrors, but these increase the cost and complexity of an instrument.

A faster, parallelised variation on whisk-broom imaging is “push-broom” scanning, which is the technique employed for the instrument discussed in this thesis. For push-broom hyperspectral imaging, line illumination is employed, and the emission is imaged to the entrance slit of an imaging spectrograph[32]. This 2D line emission is spectrally dispersed perpendicular to the line, to create a 2D X-λ image, which is collected using a full 2D detector (camera). The sample is then scanned through the missing (Y) axis and X-λ “images” are collected at each Y co-ordinate. The (X-λ-Y) data cube is referred to as a hypercube, and can be resliced to produce XY images at each λ. Thus, push-broom hyperspectral imaging can provide similar spectral resolution and range as the whisk-broom approach but with significantly faster acquisition. The intensity profile of the line illumination suffers from the same issues as for line-scanning confocal microscopy and shares the issue of cross-talk along the line due to e.g. scattering. Field-dependent aberrations in the optical system can also lead to effects such as ‘smile’ and ‘keystone’, depending on the type of aberration[33]. There are methods using optical elements or computational methods to mitigate these aberrations[34,35].

Spectral dispersion can be achieved using a grating, a prism, or a grism which is a combination of a grating and a pair of prisms.

A summary of these different hyperspectral techniques is shown in Figure 5.

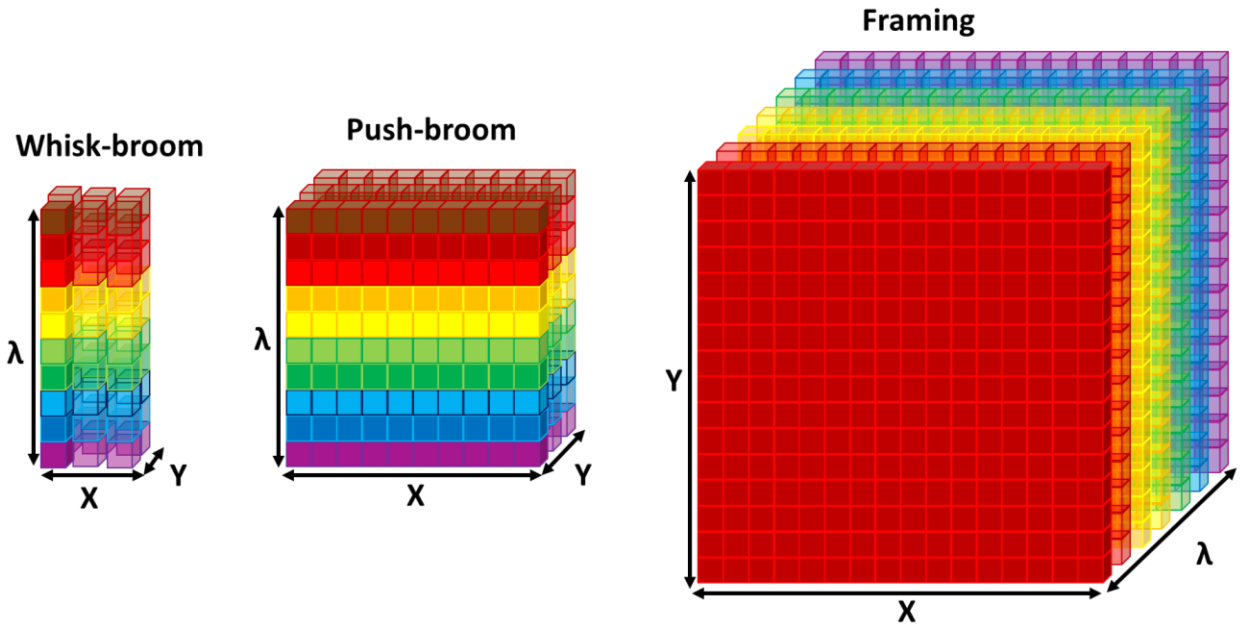



*Figure 5 – Three techniques for achieving hyperspectral data sets are shown. The transparent blocks indicate data that is taken in the next step/s, whilst solid-coloured blocks represent the current acquisition. The number of colours (representing wavelengths) gives an indication of the expected spectral resolution of each technique.*

Hyperspectral imaging has previously been applied to diamond using cathodoluminescence on carbonado[36] and photoluminescence[37]. However, the spectral resolution of this photoluminescence system was relatively low (10 nm) and operated with low transmission efficiency.

## *Luminescence Lifetime Microscopy*

Luminescence lifetime measurements can be implemented on timescales from ps to seconds+ and can be used as a contrast mechanism for spectrally overlapping emitters. It can also be used to probe the effect of different local environments on the lifetime of specific emitters. The measurement of fluorescence lifetime in each pixel of an image is called fluorescence lifetime imaging (FLIM). Lifetime measurements can be combined with spectral resolution, which can be useful to disentangle signals from multiple emitters or indicate quenching.

### ***Fluorescence lifetime measurements and FLIM***

A common approach to measure fluorescence lifetimes involves exciting a sample with a pulsed source and resolving the emission detected over a wide spectral detection channel with respect to time. This is most commonly implemented using point excitation and detection[38] with spatial scanning to realise FLIM, but wide-field FLIM methods have also been developed using temporally-modulated image intensifiers, e.g. [39]. These full-field approaches are typically faster than scanning techniques. The impact of time-of-flight of photons originating over a large sample volume may need to be considered and spatial variations of the time-gating function in image intensifiers[40] – known as 'irising' – may need to be addressed. For all lifetime measurements, it is important to take account of the temporal instrument response function (IRF) [41] that represents the system response to a delta function input. The measured luminescence decay profile will be a convolution of the optical signal with the IRF, which itself is the convolution of the excitation pulse with the response function of the detector, optical path elements and the detection electronics.

***Frequency Domain lifetime measurements***

Fluorescence lifetimes can be measured using a modulated excitation source (usually a sinusoidal modulation) and synchronous detection of the modulated emission from the sample[42]. The modulated emission from the sample will present a reduction in modulation depth and a phase offset with respect to the excitation signal. These parameters can be used to calculate two different lifetimes: the modulation and phase lifetimes. An example of a frequency domain measurement is shown in Figure 6. These equations are[1]:

$$\frac{A_{\text{emission}}B_{\text{excitation}}}{A_{\text{excitation}}B_{\text{emission}}} = \frac{1}{\sqrt{1+\omega^2\tau^2_{\text{modulation}}}}$$

*Equation 15*

$$\tan\varphi_\omega = \omega\tau_{\text{phase}}$$

*Equation 16*

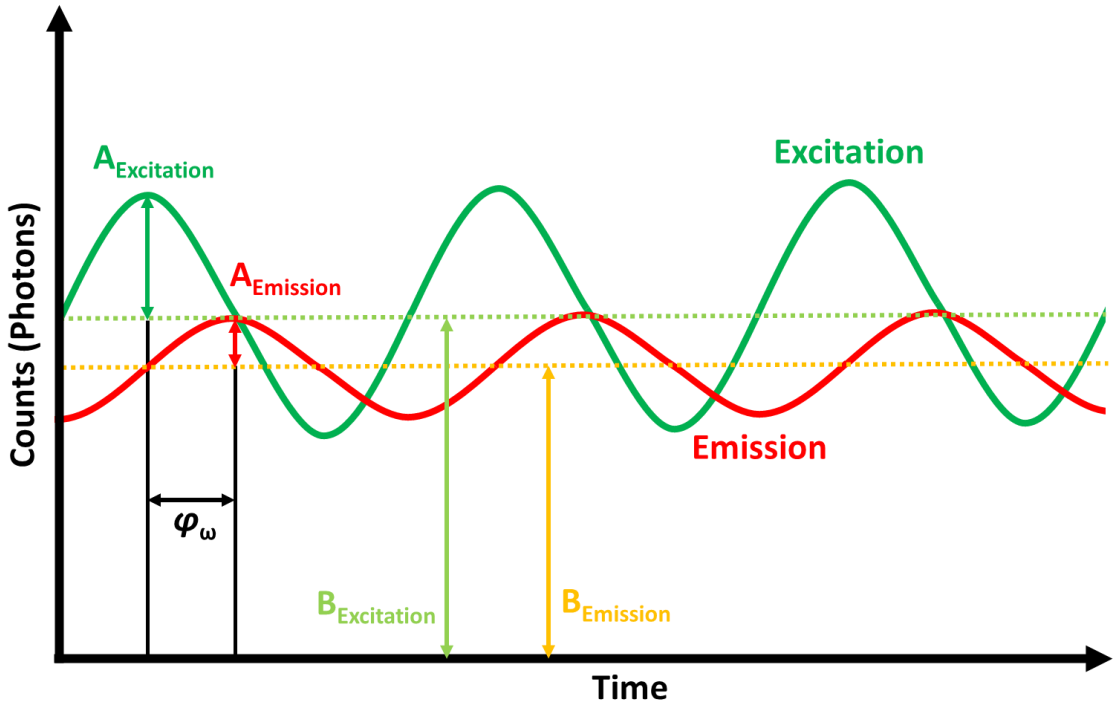



*Figure 6 – An example of a frequency domain measurement, showing the excitation modulation (green) and emission modulation (red). The amplitude is given by A and the average intensity B for excitation and emission. The phase difference between the two signals is given by* $\varphi_\omega$.

In the case of a monoexponential decay, these two lifetime values are the same, but they differ if the decay is more complex. These extracted lifetimes for a more complex decay can be thought of as 'average' lifetime parameters characterising the emission. For more complex decays, measurements at different excitation modulation frequencies can be used to separate different lifetime components. This frequency-domain (FD) technique can be applied to point measurements, point scanning FLIM, or wide field FLIM, depending on the detector used[42]. In general, FD lifetime measurements are cheaper than time-domain measurements since they do not require ultrashort pulsed excitation. However, they acquire less information than time-domain measurements, unless measurements are made at many modulation frequencies.

***Time Domain lifetime measurements – time-gated imaging***

Fluorescence decay profiles from repetitively excited samples can be measured in the time domain using time-gated detection to sample the fluorescence signals at a range of delays after excitation. For wide-field time-gated FLIM, a gated optical intensifier (GOI) acts like an ultrafast shutter that transmits an image resulting from photons arriving at the detector in a precise (electronically controlled) time window[39]. If a series of time-gated (TG) fluorescence images is acquired at known delays, then the decay data for each image pixel can be used to calculate a lifetime, either using an analytic approach or iterative fitting to a model.

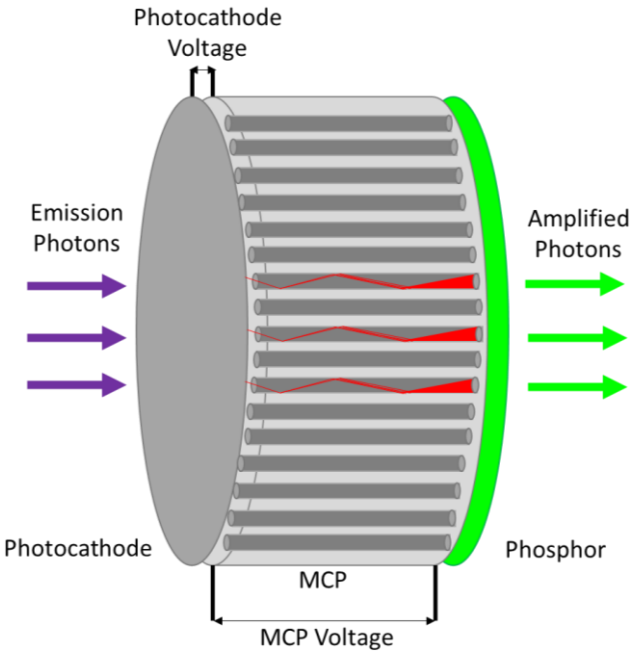



*Figure 7 – A diagram of a GOI, showing the emission photons, the detection photocathode, MCP, and phosphor. The photocathode voltage is rapidly switched to block or accelerate the photoelectrons from the photocathode to the MCP to implement the time-gated imaging.*

As illustrated in Figure 7, a GOI comprises a photocathode, a multichannel plate (MCP) and a phosphor. Incident fluorescence photons at the photocathode excite photoelectrons. This photoelectron "image" is amplified by the multichannel plate when a high voltage is applied across it to produce an intensified photoelectron image that impacts the phosphor, which outputs the corresponding optical image, which is recorded by a camera. The ultrafast shutter function of the GOI is controlled by rapidly varying the voltage from the photocathode to the MCP to switch the GOI from an "off" (zero gain) to an "on" (positive gain) for a duration called the "gate width".

The spatial resolution of the system is determined by the channel size of the MCP and the lateral spread of photoelectrons between the photocathode and the MCP. The latter can be reduced using a magnetic field and the most recent designs offer a spatial frequency cut-off of ~30 line pairs/mm[43]. Because it takes a finite time for the rapidly-switched photocathode voltage to reach all of the photocathode, the IRF of the system varies spatially, and this should be accounted for when using a GOI[40]. The primary advantage of wide-field time-gated FLIM is the ability to acquire FLIM data more rapidly than laser scanning FLIM techniques. This is achieved with wide-field illumination, and therefore the peak intensity at the sample is lower compared to confocal FLIM imaging, and therefore can reduce phototoxicity for biological FLIM experiments. In diamond, light dose is not a significant concern, and the parallelization of wide-field time-gated FLIM makes fast image collection possible. However, the quantum efficiency of these systems is limited, the signal to noise ratio can be low, and the FOV is lower than diffraction-limited confocal point scanning.

### ***Time Domain lifetime measurements - TCSPC***

An alternative time-domain method to measure luminescence decay profiles is time-correlated single-photon counting (TCSPC). In this technique, a repetitively pulsed laser source is used to excite an emitter with sufficiently low fluence such that, on average, only a single photon is detected per excitation pulse. Using ultrafast single photon counting electronics, a histogram of photon arrival times is constructed, which gives the fluorescence decay profile (convolved with the IRF). The primary detection components are a single-photon counting detector (e.g. a photomultiplier tube (PMT) or an avalanche photodiode) and TCSPC electronics, which can be implemented on a "card" in a computer. TCSPC cards typically have two signal inputs: a sync signal from the repetitively pulsed excitation source, and the signal from the detector. The sync signal from the excitation source can be provided from an internal photodetector (in the case of a supercontinuum laser source), an external pulse generator for a laser diode, or a fast photo detector in the beam path.

An implementation of TCSPC is depicted in Figure 8 (which was used for the work in this thesis). These signals enter a constant fraction discriminator (CFD) that produces a robust electrical signal (mitigating the impact of varying pulse amplitudes) for subsequent processing by the time-to-amplitude converter (TAC). The adjustment of the CFD and PMT voltages must be carefully optimised to ensure the maximum number of viable counts are detected[44]. The signal that the TAC receives from the CFD starts charging a capacitor, which is stopped when the next excitation laser pulse signal arrives. The capacitor charge is amplified and converted to a digital signal using an analogue to digital converter (ADC) for the histogram of photon arrival times. This methodology is referred to as "reverse stop-start" and is useful when exciting with a high repetition rate laser (over ~2 MHz), as this reduces the impact of dead time on the TCSPC measurement. The photon arrival time histogram will have a maximum number of time bins equal to the ADC bit depth - typically 4096- or 1024-time bins for 12 and 10 bit depth respectively. Multiple time bins can be combined to provide higher signal levels/bin at the cost of reduced temporal sampling.

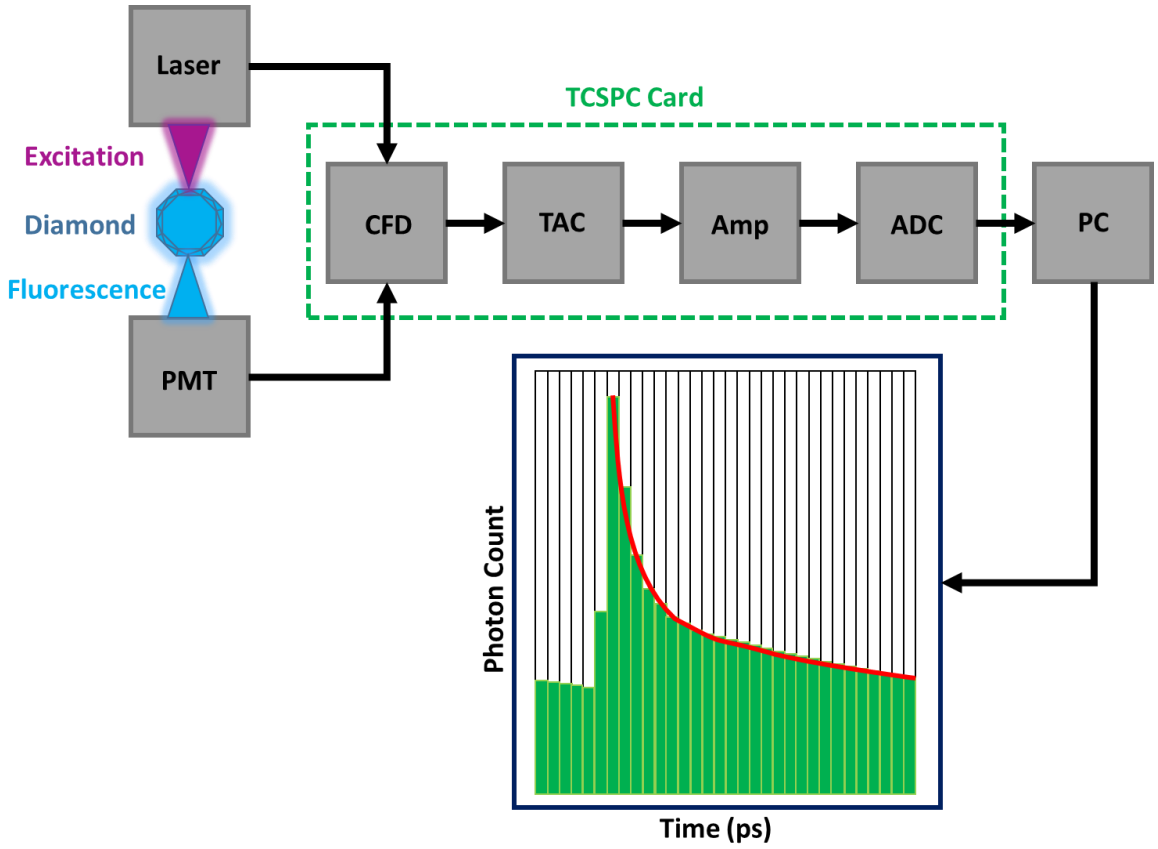



*Figure 8 – An implementation of TCSPC, using a pulsed excitation source with an output signal (laser), and the detected signal (PMT). The TCSPC card contains the CFD, TAC and ADC and outputs the shown decay to the PC. An example fit of the decay is shown in red, with the green bar representing counts in the histogram.*

Detection using a TCSPC system is shot noise limited (Poisson), and therefore the signal to noise ratio increases with $\sqrt{N}$ photons[44]. The maximum count rate is limited due to 'pulse pile-up'[45], where more than one photon is incident at the detector within the illumination pulse period. This can cause artefacts in lifetime measurements because earlier-arriving photons would be preferentially detected, which would skew the resulting decay measurement towards shorter lifetimes. A rule of thumb is that the maximum photon detection count rate should be less than 5% of the excitation pulse repetition rate[46]. This can be mitigated by splitting the incident optical signal between multiple detection channels, but this adds significant cost and complexity to an instrument.

A further issue with some implementations of TCSPC (such as that employed in this work) is that the measured temporal windows is less than the excitation pulse period as there is a 'roll-on' and 'roll-off' of the time window that is partly determined by the settings of the TAC. This can result in the beginning and end of long decays to not be measured, which leads to problems in the lifetime data analysis[44]. This is addressed later in this thesis. More modern TCSPC electronics, using time-to-digital converters do not have this limitation.

***Instrument response function***

For any luminescence lifetime analysis, it is necessary to determine the IRF to analyse the lifetime data[10]. This is usually accomplished by measuring a back-scattered/reflected excitation pulse, by measuring an emitter with a fluorescence decay much shorter than the expected IRF width, or an emitter with a known fluorescence decay profile.

The simplest system involves placing a mirror or diffuse scatterer at the sample plane and measuring a heavily attenuated reflection of the excitation pulse. It is important that the mirror or scatterer is in the sample plane, as changes in the light path relative to the emission to be measured will cause a temporal shift in the IRF relative to the fluorescence decay. The photon wavelength incident on the detector may also affect the IRF due to changes in light path, group velocity dispersion or the response of the detector[47]. Ideally, the IRF should be measured at the emission wavelength, but this is not always practical or possible.

A second method is to use an emitter with known lifetime, such as fluorescein. Here the reference lifetime must be included in the lifetime data analysis. However, the lifetime of the "known" emitter can be affected by excitation source, concentration, or quenching[48, 49] and so this method should be used with caution.

For the work in this thesis, the IRF was determined by measuring a reflected excitation signal. In some cases this was performed as a function of excitation wavelength in the case of PLE lifetime spectroscopy.

***PLE lifetime spectroscopy***

With a pulsed tuneable excitation source, it is possible to measure the lifetime of an emitter as a function of excitation wavelength. This can be useful to probe the response of an emitter's higher excited states, and potentially measure thermal decay processes. Lifetime can also be used as an effective contrast mechanism with multiple emitting species and close excitation spectra. As explained above, PLE lifetime spectroscopy can be combined with emission to produce excitation-emission-lifetime matrices[50, 51]. This is a powerful technique for unknown samples and is explored later in the thesis.

## Instrumentation

### *Excitation sources*

The choice of excitation source for fluorescence microscopy can be a spatially incoherent source such as a lamp, an LED, or it can be a laser. Lamps were widely used for wide-field fluorescence microscopy - due to their spectrally broad emission and high brightness in the ultraviolet - but are increasingly being replaced by LED sources or lasers, which are more efficient, more economic to run and can provide more uniform illumination. Laser sources can provide diffraction-limited focusing, e.g. for confocal microscopy, and ultrafast pulsed lasers are convenient for luminescence lifetime measurements and for nonlinear microscopy.

Lasers are also the most common excitation source used for photoluminescence microscopy. Historically, lasers used in microscopy were fixed wavelengths, with the 488 nm, 515 nm and 647 nm lines from argon ion and krypton ion gas lasers dominating laser scanning confocal microscopy. A range of fixed wavelength lasers can now be obtained from semiconductor diode laser-based sources and it is possible to obtain continuously tuneable laser radiation from frequency-doubled Ti:Sapphire lasers, optical parametric oscillators/amplifiers and supercontinuum laser sources, although these are significantly more expensive than monochromatic sources.

For the work reported in this thesis, the main excitation source was based on a fibre-laser-pumped supercontinuum, which emits spatially coherent light from a single-mode optical fibre over a wide

wavelength range from 400 nm to 2350 nm. This is achieved by using an ultrafast mode-locked optical fibre laser that delivers high peak power picosecond pulses at 40 MHz to a single-mode micro-structured optical fibre, in which nonlinear optical processes including self-phase modulation and Raman scattering spread the energy over a broad spectral range[52]. The output light retains the spatial coherence of a single mode laser but has a polarisation state that varies as a function of wavelength. The total average power of this supercontinuum is 2 W, with 380 mW over the visible spectral range from 400-780 nm. The supercontinuum laser output retains the periodic pulsed character of the ultrafast pump laser. The pulse duration is usually <50 ps, which makes it useful for fluorescence lifetime measurements and FLIM.

## *Detectors*

The choice of detector is important as it will impact the sensitivity of the instrument as a function of wavelength range, the spatial properties of any imaging capability and the temporal resolution. Most photodiodes in the visible are based on silicon devices, which can be sensitive from 200-1100 nm, but this range is sometimes limited by the specific detector implementation. In the near infrared (NIR) photodiodes can be based on Germanium (800 - 1800 nm) or InGaAs (900 - 1700 nm). Multialkali PMTs do not operate at more than 900 nm. Many PMTs are available with sensitivity in a similar range to silicon detectors. There are some NIR photocathodes but NIR photomultipliers tend to be significantly more expensive and present more thermal noise (detected as dark counts), even when cooled with liquid nitrogen.

### ***Cameras***

The main current camera technologies are charged coupled devices (CCD) and complementary metal oxide semiconductor (CMOS)[53]. Scientific cameras are cooled to reduce dark noise and, historically, CCDs offered higher signal to noise than CMOS cameras, but slower image acquisition. For higher speed or single photon sensitivity, electron multiplying CCD (EMCCD) that amplify the detected signal in each pixel can be used. EMCCDs allow very weak signals to be detected, although the amplification adds excess noise. Recently, a development of scientific complementary metal oxide semiconductor (sCMOS) cameras[54] has occurred, which are implementations of cooled CMOS sensors with onboard signal processing to improve image quality. This has driven a shift to sCMOS cameras for microscopy, providing both imaging speed and excellent signal to noise (with typically less than one electron readout noise) performance. sCMOS cameras are available with a wide range

of sensor and pixel sizes, with different dark current and read-out noise characteristics, and typically have quantum efficiencies of 60-90%. In this thesis, a larger sCMOS sensor with small pixels is exploited, and an EMCCD is used for lower-light-level measurements.

### ***Photomultipliers***

Photomultiplier tubes (PMTs) are very sensitive detectors that amplify the detected photoelectric signals to reach single photon sensitivity. For the work reported in this PhD thesis, they have primarily been used for single photon counting in the TCSPC system. PMTs typically have lower quantum efficiencies than photodiodes or cameras that reduce away from the spectral region of peak sensitivity. PMTs are often Peltier-cooled to reduce their dark counts, which are then typically ~<200 cps. The dark count is important for single photon counting applications, where signal levels corresponding to a few photons per second can be swamped by the background noise. The PMT used in this thesis operates from 310-830 nm, with a quantum efficiency that peaked at ~20%.

### ***Single photon counting avalanche photodiodes (SPADs)***

Single photon counting avalanche diodes (SPADs) are a newer technology than PMTs and operate in a 'Geiger mode' where an uncontrolled avalanche of electrons occurs after a photon absorption[55]. This allows the weak signals from single photons to be detected, which is not possible with standard avalanche photodiodes (APDs). The quantum efficiency of these silicon based SPADs is usually higher (up to 70%) than a typical PMT for visible and NIR detection. PMTs can provide higher quantum efficiency in the UV/blue spectral regions than SPADs, which have much higher quantum efficiencies in the redder regions. The IRF is also wavelength dependant, becoming broader <500 nm, making them unsuitable for blue measurements. Unlike PMTs, SPADs suffer from large dead times (up to 1 µs), which is more than the timescales in some TCSPC circuitry (~80 ns). The dead time increases with size of the SPAD active area, as does the dark count rate and the temporal IRF. This IRF can also change dependant on the illuminated area of the SPAD. Therefore, the minimum useful count rate for a practical application may be lower than for a PMT. Their small size (25-100 microns) is much less than the (8 mm) collection area that is available from a PMT.

### *Filters*

Optical filters are critical components for luminescence microscopy and spectroscopy since they enable weak (single photon) signals to be detected, while blocking the much more intense excitation signals. In a standard luminescence microscope, the excitation light is separated from the emission using a dichroic filter, which is usually a dielectric coating on a glass substrate. While this provides some blocking of the excitation radiation, an emission filter is usually required to provide additional attenuation of the excitation signal. Excitation filters are used to limit the spectral width of the excitation radiation to ensure that only the desired excitation wavelengths are incident on the sample, and that the excitation radiation is blocked by the emission filter. Emission filters are usually either band pass or long pass filters. For diamond luminescence measurements, long pass filters are convenient to permit wide spectral detection windows. Spectral filters sometimes utilise doped glasses that absorb unwanted radiation, but it is now more common to use dielectric interference filters that provide spectral selection through reflection or transmission. This can provide sharper spectral edges than doped glass filters, with a higher blocking factor.

## Conclusion

This chapter has outlined the photo-physics of luminescence and the techniques and tools used for imaging and spectroscopy. Photoluminescence measurements of solid-state samples can provide non-destructive capabilities to study photophysical properties and map spectroscopic and spatial characteristics of the emission. These may be used for diverse applications with respect to diamond luminescence, including “fingerprints” of specific gemstones, non-optically active defects through quenching, and non-destructive evaluation of (quantum) optical devices.

# Chapter 3 – Diamond defects and properties: photo-physics, characterisation, and applications

## Outline

The key aim of this PhD project was to construct a multidimensional luminescence microscope for application to diamond imaging and spectroscopy. A single instrument integrating multidimensional imaging and spectroscopy with tuneable excitation and co-registered hyperspectral/lifetime/polarisation imaging capabilities has not previously been applied to study diamond luminescence, which possesses a uniquely broad range of emitting defect species. This chapter reviews the underlying luminescent defects, the properties and structural composition of diamond. Examples of current and potential applications are given to describe the motivation for this research. The structure of pure diamond is first explored, together with the properties this confers on the bulk material. Growth of natural and synthetic diamond is then described. Defects that can be incorporated into the diamond lattice are then outlined, several of which have been studied in this thesis.

## Structure

Pure diamond is a metastable allotrope of carbon, which exhibits strong covalent bonds in an $SP^3$ configuration[56], and is tetrahedrally connected[57]. This is different to other allotropes of carbon, such as graphite and graphene which possess $SP^2$ bonding[58]. The unit cell for diamond is a face centred cubic crystal Bravais lattice. This is similar to other group 4 elements, such as silicon and germanium. The diamond lattice is two face centred cubic (FCC) unit cells, translated by ¼ of a unit cell in all three dimensions, and the length of the unit cell is 0.357 nm in all axes. A diagram of the diamond unit cell is shown in Figure 9.

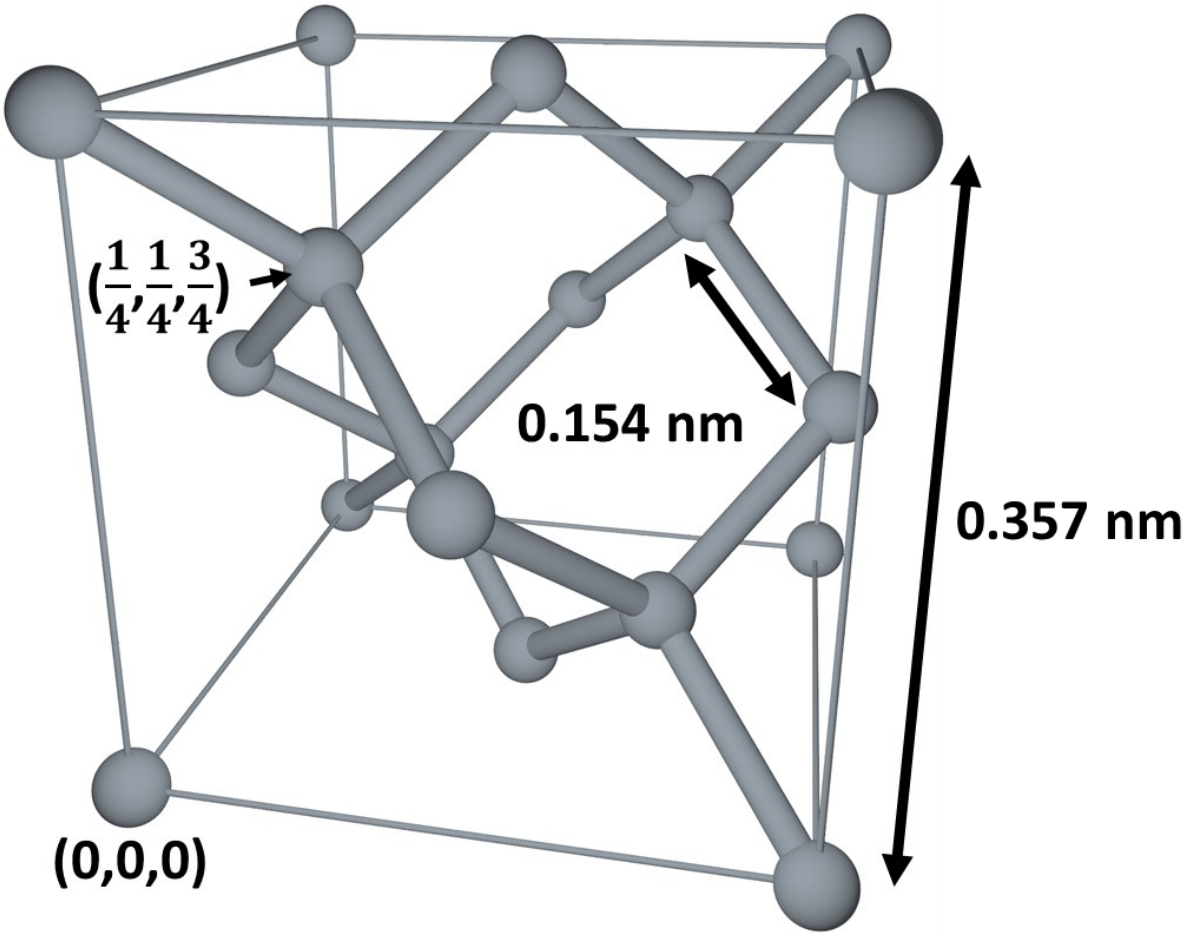



*Figure 9 – Structure of the diamond unit cell showing the two-atom basis. The tetrahedral symmetry is shown, along with other important parameters. All grey atoms are carbon-12 atoms.*

The length of each carbon-carbon bond is 0.154 nm[59], and this helps to create a very strong covalent bond of 347 $kJmol^{-1}$ [60], which results in many of its extreme physical properties. This also makes diamond very resistant to ionising radiation damage, enabling diamond devices/components to be applied in high ionising radiation environments. This diamond lattice repeats indefinitely, creating the large crystalline structure present in bulk diamond. The repeating lattice may be terminated in several ways, including oxygen and hydrogen termination, to form the finite bulk material. The surface properties of diamond are related to its termination surface, which can be important for specific applications. The form of termination can be modified through various methods in order to add other functional groups to a diamond surface[61]. Diamond has poor chemical/biological reactivity, other than with ferrous materials, which makes it suitable as a targeted drug delivery host in the form of nano diamonds[62]. The fluorescence inherent in some defect-containing nanodiamonds could then enable tracking of drug containing particles inside cells.

## *Crystallinity*

Diamond exists in two forms of crystallinity, which are monocrystalline (single crystal), or polycrystalline[63]. These two crystallinities of diamond have different properties. Monocrystalline diamond is the more familiar and common form, whilst polycrystalline diamond is typically synthetic. At any point in a crystal lattice, the orientation of the unit cell will be the same. This applies to the bulk scale, and not to localised regions where strain, defects, or extended defects have distorted the lattice.

Polycrystalline diamond consists of many smaller regions of monocrystalline diamond, called grains, bounded together in a larger bulk structure. These grains are separated by grain boundaries, which are usually rich in non-diamond carbon such as $SP^2$-bonded carbon[64]. The grains themselves can have uniform properties and are analogous to monocrystalline diamond. Each grain can vary in size, and this may be altered during CVD growth[65, 66]. The orientation of each grain may be different to that of neighbouring grains, which can lead to different mechanical properties. It is possible to adjust the growth parameters to preferentially grow grains with specific orientations[67]. Natural diamond only exists rarely in this form, as carbonado or 'black diamond'[68]. Polycrystalline diamond is more usually encountered as a product of heteroepitaxial CVD growth (PCCVD) and can be described as micro, nano, and ultra-nano crystalline, based on grain size[69], or polycrystalline diamond (PCD) sintered in HPHT presses[70]. For HPHT sintering, metal is a significant component of the resultant product, unlike PCCVD diamond. An example of monocrystalline and polycrystalline diamond is shown in Figure 10.

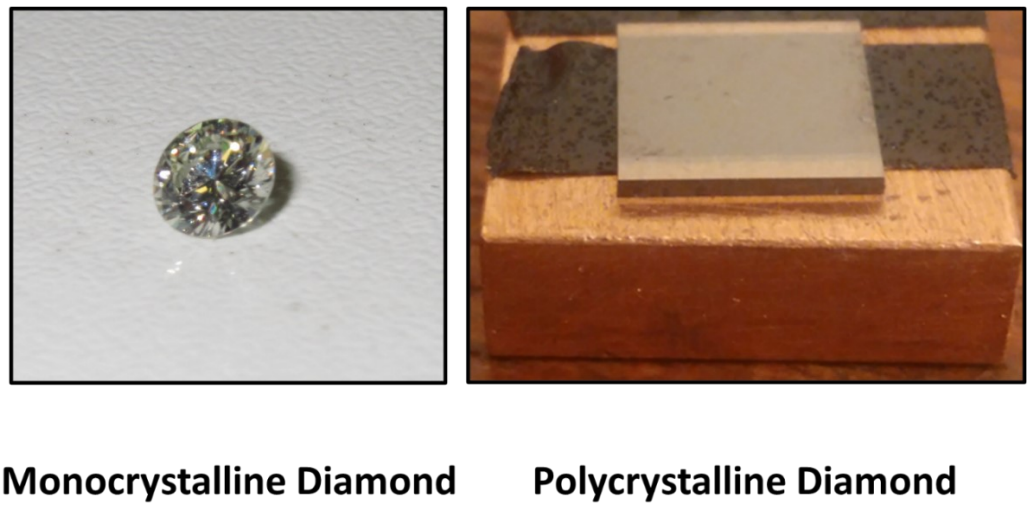



*Figure* 10 *– An example of a monocrystalline faceted natural diamond (left), and a polycrystalline CVD synthetic diamond mounted to a copper block with carbon tape (right). Here the grains in the PCCVD diamond are only visible under a microscope, but regions of black graphitic/non-$SP^3$ carbon are visible to the naked eye.*

### *Nanodiamond*

A diamond can be classified based on the number of atoms which are bonded in an $SP^3$ configuration in its internal structure. As additional carbon atoms are added to the structure, there is a transition from a 'diamondoid'[71] to nanodiamond. In an example of a few hundred carbon atoms, only the centre of the structure will be 'diamond' ($SP^3$ bonded), and the surface atoms constitute a much higher percentage of the carbon atoms than the inner 'bulk' atoms. As the number of carbon atoms increases, this percentage of internal bulk $SP^3$ configured carbon atoms increases, and the surface non-$SP^3$ carbon atoms decreases. The higher the percentage of $SP^3$ bonded carbon atoms, the closer the properties will be to bulk diamond.

Nanodiamonds, are nm-scaled diamonds that exhibit some of the bulk properties of diamond. They can be synthesised in several ways, and natural nanodiamonds can be acquired from petroleum[71]. Nanodiamonds can contain defects such as H3 and NV centres and, due to the lack of unperturbed diamond and surface effects, the charge states and properties of these defects can vary from their bulk diamond counterparts[72]. Due to their small size and ability to be functionalised, nanodiamonds have been considered for targeted drug delivery[62], and as fluorescent markers for biological imaging, due to their potential brightness and lack of bleaching[73].

## Properties of diamond

Diamond possesses many properties, some of which are unrivalled in the material world. This makes it an attractive material for a wide variety of applications, from mechanical to quantum optical.

### *Mechanical Properties*

As a consequence of the strong carbon-carbon covalent bond and its crystal lattice, diamond has some of the highest known mechanical properties of any natural material. Diamond is the hardest known material, with variation in its hardness being based on crystallographic orientation[74]. Material hardness is a measure of its resistance to plastic deformation. Diamond has a value of 10 on the Mohr's scale of hardness[75], which runs from 1 to 10 where 10 represents the highest material hardness. Diamond's mechanical properties are heavily influenced by larger defects in the lattice[76]. Diamond possesses a low toughness, which is a measure of how resistant the material is to fracture. Crystals are often hard and resist plastic deformation, but they fracture easily. Because the

mechanical properties are a function of crystal orientation, this information is important for cutting diamond, which is generally performed along a cleavage plane[77].

These properties mean diamond is a suitable material for a wide variety of mechanical applications. However, the lack of toughness means that diamond needs to be treated for many mechanical applications. This can involve sintering with metals to create PCD, which is used in drill bits. For this application, diamond's poor toughness would be less desirable, but the polycrystalline diamond metal matrix increases the toughness, whilst retaining much of the inherent hardness[78]. Diamond will form a carbide with ferrous materials, and this significantly reduces the mechanical properties. Therefore, the materials in contact with diamond for these mechanical applications must be considered. Diamond turning is an industry standard for creating accurate surfaces for optical components, including free-form optics. This entails using a sharp diamond single crystal tip to machine a material, such as silicon or germanium with low surface roughness. Diamond will usually be many times harder than the machined material, and so the tip of the diamond tooling remains sharp.

## *Thermal Properties*

In many materials, electrons carry the majority of the thermal energy around a solid. Diamond possesses the highest thermal conductivity of any material, at 3320 $Wm^{-1}K^{-1}$ in some isotopically enriched diamonds[79]. For typical single-crystal diamond the conductivity is around 2000-2500 $Wm^{-1}K^{-1}$, making it 5-6 times more efficient than copper, a common heat spreader[80]. Whereas with copper or other materials, electrons provide the bulk of the thermal energy conduction, phonons in diamond allow a much higher thermal conductivity.

Diamond is a crystal, which entails quantized vibrations called phonons, moving through the lattice. Phonons efficiently transfer thermal energy across the diamond lattice, enabling a high thermal conductivity. Phonon scattering causes a loss in thermal conductivity, and this can be caused by defects, grain boundaries, and other phonons[81]. Minimising these defects is therefore key to creating high thermal conductivity diamond.

## *Optical Properties*

Pure diamond is transparent from its bandgap at ~225 nm, to microwaves and beyond[80]. An exception to this is a region of two and three phonon absorption[82] between 2.6 and 6.2 µm in the

infrared (IR). This multi-phonon absorption occurs when multiple phonons are excited in the lattice by infrared photons[83]. In unperturbed diamond, there is no single phonon absorption, due to the symmetry of the lattice. Any breaking of this symmetry will allow single phonon absorption, which manifests at 7.5 µm[82]. The lack of optical absorption in the visible wavelength range of pure diamond means that it is colourless. Defects can introduce energy levels into the diamond bandgap, generating absorption bands, which can give diamond colour.

The physical property which gives diamond its 'fire' and attraction as a gemstone is its dispersion (defined as the difference in refractive index between 430.8 and 686.7 nm[84]) with a value of 0.044[85]. Its refractive index is high for a solid, e.g. 2.421 at 550 nm[86]. This high refractive index causes significant Fresnel reflection at diamond-air surfaces (16.8% per surface at 1.2 µm), which results in a need for anti-reflection coatings in high efficiency diamond-based optical devices.

The refractive index mismatch between air and diamond also leads to a high degree of spherical aberration when imaging inside diamond[87]. Immersion oil has a higher refractive index than air and this can be used to reduce such aberrations, but not eliminate them. One approach to minimising aberrations is to use adaptive optics to modify the wavefront before it enters the diamond, and this can be achieved using a deformable mirror[87], or a spatial light modulator (SLM)[88]. An alternative method would be to use a precisely formed lens after the objective lens, but before the diamond, to focus the light to a specific focal plane inside the diamond by introducing a counter aberration to nullify the induced refractive index mismatch aberration. This would only be a solution for a specific depth and wavelength.

## *Birefringence*

Diamond is naturally a non-birefringent crystal due to the symmetry of its lattice[89]. However, distortion to the lattice, typically through larger extended defects, breaks the lattice symmetry. This then allows birefringence to be observed[82]. As a distortion in the lattice is related to strain and stress, regions of birefringence can be used to identify strained regions using a simple optical set-up. White-light transmission through two crossed polarisers before and after the sample can reveal strained areas of a diamond. Linear polarised light incident on the sample will be resolved into components along the axes of the birefringence, and the analyser polariser can be set to reject one component, e.g. the unperturbed light, and transmit the other polarisation component. Regions where the birefringence is higher will appear brighter on the detector, and therefore can indicate regions of higher strain. In a natural diamond, the 'tatami' pattern of birefringence is apparent, whereas synthetic diamond does not often exhibit this pattern[90].

## *Raman scattering*

Raman spectroscopy, which entails measuring the Raman shift of scattered photons, can be used to identify diamonds. The red (Raman) shift is caused by inelastic scattering of photons with phonons, where a phonon absorbs some energy from the photon[82] and is excited to a higher virtual energy state. This effect can be exploited in Raman lasers[91].

The 1st order Raman shift in diamond, peaking at 1332 $cm^{-1}$ (165 meV), can be used as a spectral fingerprint. This has a narrow linewidth (1.5 $cm^{-1}$)[19] and measurements of the linewidth, peak position and splitting can be used to measure stress in the lattice[92, 93]. An example Raman spectrum, showing the 1st order Raman shift, from a single crystal diamond is shown in Figure 11.

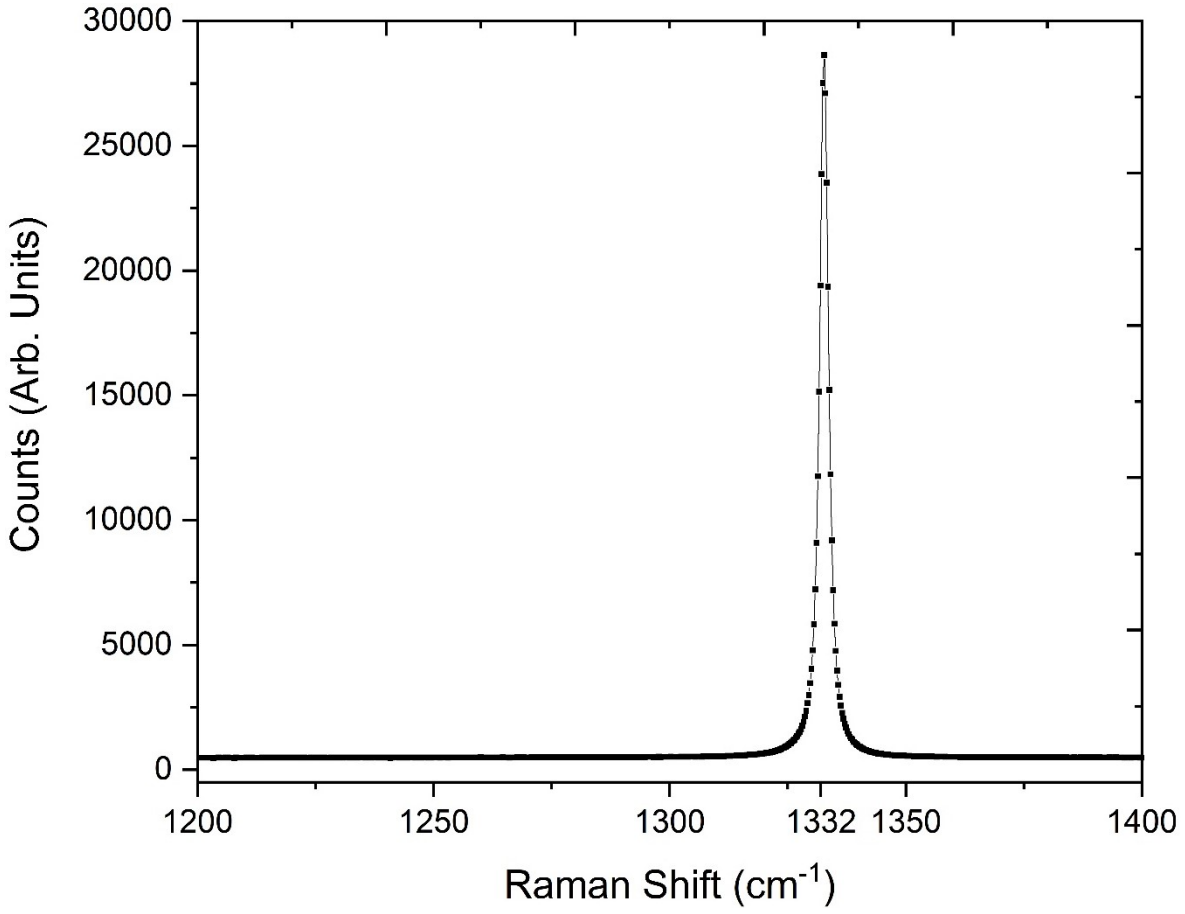



*Figure 11 – An example of the first order Raman shift at 1332 $cm^{-1}$ from a single crystal natural diamond. The laser source was a 633 nm HeNe laser. This data was acquired by the author on a previous project at Aberystwyth university using a Horiba spectrometer.*

Spontaneous Raman scattering is a weak process[94], and practical measurements require a high incident laser power and/or efficient detection and long integration times. Measuring the absolute

linewidth is usually limited by the spectral resolution of the spectrometer or linewidth of the laser source. The scattering efficiency obeys a $\lambda^4$ power law, meaning that shorter wavelengths are more strongly scattered[94]. However, the Raman shift is often small relative to the laser wavelength, and the laser blocking filter employed must have sufficiently sharp edges. A notch filter is often employed to block the laser line for Raman measurements. Visible detection is practically straightforward, due to the availability of high-resolution diffraction gratings and low-cost silicon-based detectors. A 532 nm laser source, e.g. a frequency doubled Nd:YAG 1064 nm laser, can be used due to the high QE of silicon based detectors at this wavelength. However, the 1$^{st}$ order Raman peak in diamond from incident 532 nm radiation is at 574 nm, which is very close to the ZPL of $NV^0$ (575 nm), making it a poor choice for most synthetic diamond, which often contain $NV^0$.

## *Band structure*

Diamond is a wide bandgap semiconductor, in between an insulator and a standard semiconductor. It exhibits an indirect bandgap of ~5.5 eV, which is in the UVC wavelength band at ~225 nm[19, 82]. The large gap and the resulting spectral window of transparency allows emission from many energy states caused by defects inside the bandgap to be detected. This enables diamond to emit from 235 nm from exitonic emission (recombination), to >1000 nm[19]. Diamond is an indirect bandgap, which means it is unsuitable for efficient LED devices, as an emission process requires conservation of momentum, requiring phonon involvement[95]. Diamond can be effectively doped with boron to generate p-type material, but cannot be sufficiently doped to generate good n-type material. This causes difficulty in creating efficient electronic devices with diamond using traditional semiconductor techniques[96].

## Growth

The growth of diamond has been explored for hundreds of years, partly driven by the goals to manufacture synthetic diamonds and to understand the deep geological properties of the Earth. As diamond is simply carbon, an abundant element on the Earth, diamond could be common. However, the processes to generate diamond require extreme thermodynamically favourable conditions, in the form of heat and pressure. Under "normal" conditions, diamond is only metastable, and graphite is the preferred allotrope under these conditions[56]. Diamond does not decay into graphite, however, due to the large activation energy barrier.

The morphology of a diamond will vary significantly based on its growth parameters, and the slowest growing faces will be left after growth has been terminated[97]. Single crystal diamonds are typically of the octahedral or cubic habit (shape), but mixtures of the two do exist, called a cuboctahedron. A carbon phase diagram, showing the important regions related to diamond growth, is shown in Figure 12.

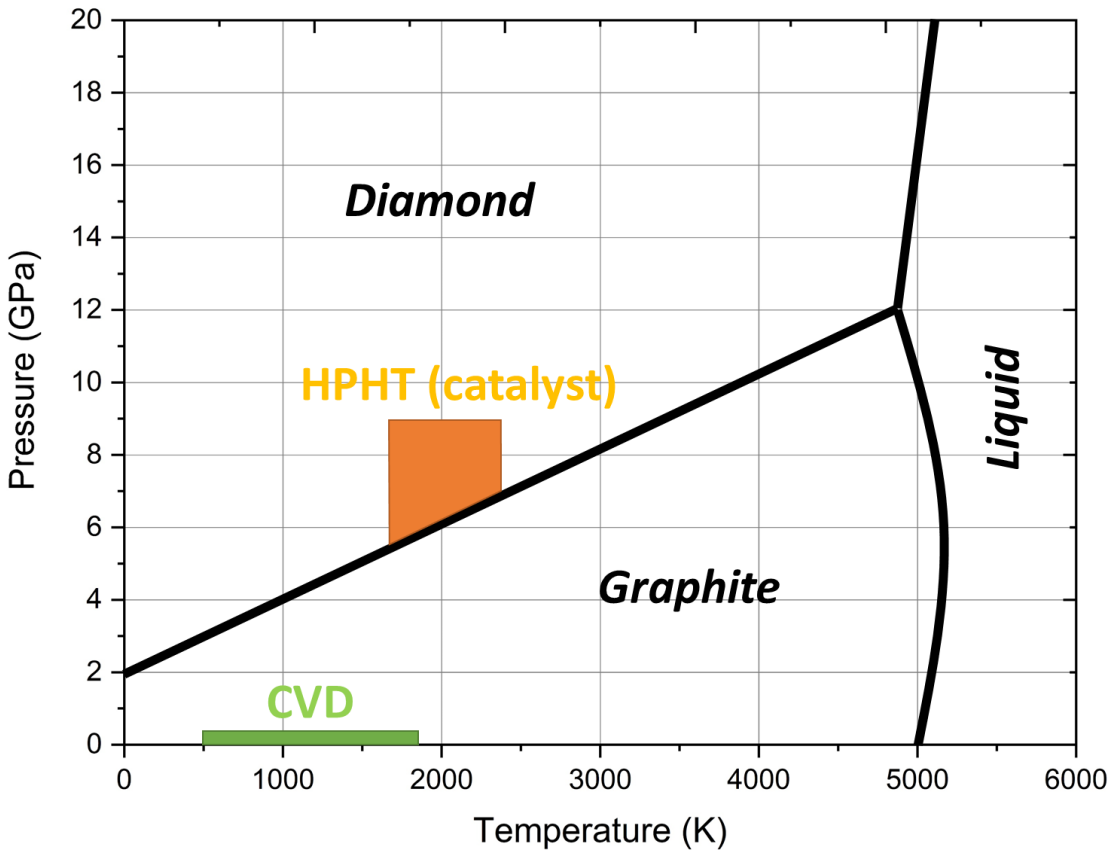



*Figure 12 – A carbon phase diagram for diamond showing the stable regions for graphite, diamond, and liquid carbon. The line separating the graphite and diamond stable regions is called the Berman-Simon line. HPHT (with catalyst) and CVD synthesis conditions are shown, with an exaggerated pressure scale for CVD growth. Figure redrawn from[76, 98].*

## *Natural growth*

The term 'natural' is applied here to describe geological processes that caused the diamond to form in the Earth over many millions to billions of years, under high temperature, high pressure. The conditions to grow diamond are only found inside the Earth's mantle, and diamond is deposited on or near the surface through volcanic processes[99]. Kimberlite is heavily associated with diamond deposits and exists as large vertical columns called kimberlite pipes[99].

The growth of natural diamond over very large timescales potentially results in variations in growth conditions and environments. This means that natural diamond can have far more irregular structures than synthetic diamond[99]. The differences are usually apparent when using above bandgap excitation and imaging of diamond luminescence[100].

Diamonds are one of the few materials which can survive the journey from the mantle to the surface and so are interesting from a geological standpoint. Garnets, and other minerals can be found encased inside diamond, and this can offer indications to the composition of the mantle[101].

## *Synthetic growth*

The synthetic growth of diamond is very different to natural growth. There are three primary methods to grow synthetic diamond: chemical vapour deposition, high pressure high temperature, and detonation. Detonation is only used to manufacture nanodiamonds and is less common. The main methods are highly energy intensive, mostly due to the temperatures required or the need to generate a plasma. The ability to synthetically grow diamond opened the possibility to generate specific features in a diamond, either in bulk or on smaller scales. The unreliability of natural diamond properties can then be avoided, as the desired properties may be specifically engineered.

Since graphite is the stable allotrope under normal conditions, there is a transition region where diamond will become this more stable form of carbon. The line in the phase diagram at which this transition occurs is called the 'Berman-Simon Line', where above the line, diamond is more stable than graphite[102]. The phase diagram of carbon in Figure 12 shows the line between graphite and diamond and the regimes in which different growth techniques operate.

## *High Pressure High Temperature (HPHT)*

HPHT was the first method used to grow bulk synthetic diamond. There have been many attempts historically to grow diamond, but General Electric is considered to be one of the first successful groups to manufacture synthetic diamond by HPHT in 1954[103]. HPHT growth operates in the thermodynamically stable regime shown in Figure 12. This is analogous to the growth method inside the Earth where natural diamonds are grown. A carbon source for the diamond is either provided by a seed diamond, or by graphite.

HPHT synthesis can be made more efficient using catalysts such as nickel, cobalt, and iron, which reduce the energy required to crystallise carbon into diamond. This allows diamond to be grown at temperatures of 1200-1500 °C, and pressures of 5-6 GPa[104]. Inclusions made from these 'solvent-catalysts' can exist inside a grown HPHT diamond[105]. Nitrogen can also be used to increase the speed of growth, but high nitrogen concentrations can result in black $SP^2$ rich diamond[106]. Due to the nitrogen concentration in the air, and other sources, nitrogen is very commonly incorporated into the lattice of HPHT diamonds. Nitrogen-getters can be used inside the pressure vessel, which absorb some of this nitrogen, instead of letting it incorporate into the diamond. Examples of nitrogen-getters are aluminium or titanium[107]. Again, this can be unintentionally incorporated into the grown diamond, similar to the solvent-catalysts.

HPHT is the best method to manufacture larger monocrystalline diamonds, due to the comparatively rapid growth rate versus CVD growth. It can be easy to identify HPHT diamonds using above bandgap excitation, as this can reveal luminescent structures which are not consistent with natural growth. These result from the quick growth process, which cannot replicate the significantly slower growth of natural diamond and the variations in conditions that natural diamond would experience[100].

## *Chemical Vapour Deposition (CVD)*

CVD diamond growth is the most recent primary method to synthesise diamond and was further developed in the 1980s[108]. Whilst HPHT synthesis is used to provide diamond for more physical applications, or for seed crystals, CVD diamond is primarily used for specifically engineered samples. CVD growth operates in a regime (kinetic) where diamond is not the most stable phase of carbon, using lower pressures, and temperatures than for HPHT synthesis. Above a substrate, a gas, usually containing methane, and a high proportion of hydrogen, is turned into a plasma. This creates radicals, which deposit themselves onto a diamond lattice site on the substrate/seed. The diamond

is grown atom by atom, which is a very slow process. Atomic hydrogen selectively etches graphitic carbon at a much higher rate than diamond, which greatly increases the quality of the grown material[109]. Nitrogen has been shown to also increase the growth rate of CVD diamond, which is inherently low due to the kinetic atomic process[110].

In principle, CVD can be applied to grow large wafers of diamond, but there are significant challenges. The plasma must be uniform over the substrate, including the temperature, gas mix and pressure, otherwise different regions will exhibit variations in growth rate, and defect production. This is especially challenging for single crystal growth, where variation in conditions would lead to highly strained samples. The dimensions of growth are therefore practically limited. If the substrate lies on an XY plane, then the grown diamond is in the Z axis of growth. The XY plane can be comparatively large relative to the Z growth dimension. The 'taller' it grows, the more extended defects and graphitic carbon may be created. If a small defect is generated near the substrate, this can cascade up through the diamond, and in extreme cases, appear as 'rivers' of graphitic carbon[111]. Practically, this results in CVD diamond presenting much larger XY dimensions than the Z dimension.

Heteroepitaxial growth is a method of CVD synthesis, where a diamond-like substrate, such as silicon, is seeded with small diamond particles in a process called nucleation[112]. These seed crystals then grow in the reactor, before encountering a neighbouring seed. These seeds grow out and upwards, away from the substrate, until there is no more room for growth. There is a competition of growth, and eventually seeds are "outgrown" by their neighbours and their growth is terminated. These seeds become the grains in the final polycrystalline diamond, which can be referred to as PCCVD diamond. Homoepitaxial growth of CVD diamond can use HPHT substrates or natural diamond and usually produces monocrystalline CVD diamond.

There have been recent developments of monocrystalline heteroepitaxial CVD diamond growth, using a layering of materials onto a silicon substrate, using an iridium layer[113]. This initially produces polycrystalline diamond; however, as the growth is continued, the seeds can fuse together to form a structure much closer to monocrystalline than polycrystalline diamond. There are, however, a significant number of extended defects or dislocations generated by this approach. This method shows promise to produce much larger surface area "wafers" of diamond, which is beneficial for electronic applications of diamond[111].

The plasma in CVD diamond synthesis can be formed by microwave generators, although techniques such as hot filament and arc jets have been explored[112]. A problem with hot filament techniques is that the filament material itself is etched away by the plasma, causing impurities in the diamond. The delicate conditions, and large numbers of parameters required for diamond growth by CVD

mean that the gas feed must be closely monitored, and the microwave modes that generate the plasma must stay constant. The careful control enables highly pure diamond to be grown using CVD, by using pure feed gasses and clean reaction chambers.

### *Detonation nanodiamonds (DNDs)*

Creation of nanodiamonds via detonation (DNDs) is a relatively unusual method for manufacture of diamond and requires explosives. The lack of oxygen in the reaction vessel means there is no burning of the carbon, after the explosion. For a short period of time during the explosion, diamond is the preferred allotrope of carbon and rapidly forms nanodiamonds. The vessel which contains the explosives is rapidly cooled, and a powder is created that is made from ~5 nm sized nanodiamonds[114]. These nanodiamonds are often aggregated together in clumps and are rich in graphitic carbon, which needs to be removed in post processing[115]. This is an effective method to make smaller nanodiamonds, which would otherwise require processing using a centrifuge and milling beads of larger diamond.

## Defects

Pure materials seldom exist in nature. Due to the chaotic microscale world, defects can grow or are formed into solids. These defects can affect their properties, or in some cases provide specific qualities which are highly desirable.

### *In crystals*

Defects in crystals originate in many forms. They are broadly divided up into point defects, which apply to highly localised regions, or extended defects, which can involve large regions of the crystal lattice. These defects can be unintentional, when they are commonly referred to as impurities, or intentionally incorporated, such as a dopant. One of the primary reasons diamond is researched is not because of pure diamond, but because of properties caused by defects inside the lattice. These defects disrupt the lattice, change, or create energy levels, and generate stress and strain. These defects in impure diamond can have properties which make it suitable for a specific application, such as high performance magnetic sensing with a $NV^-$ defect[116].

Point defects are usually single to few atom variations in the standard lattice. The simplest examples are vacancies and interstitial defects. If one considers the repeating diamond crystal lattice, there are specific locations where a carbon atom should reside. A vacancy is a lack of an atom where there should be one, creating a gap in the lattice. An interstitial defect is an atom in a location where it should not be, such as in a gap near a bond between several other lattice sites. In diamond these defects can be produced by radiation damage, or by growth in the case of vacancies in CVD synthesis. Isotopic variation can be considered as a form of defect, and in diamond this could be a carbon-13 atom.

Impurity or dopant-related point defects are more complex, as they are non-native elements to the lattice. These defects can either be substitutional, meaning they replace a native elemental atom in the lattice, or interstitial. These other elements can be similar in size to the original element, differing by only a few atomic numbers, or can differ significantly. The lattice will distort around these defects, and this distortion increases with their size. This means that some elements are easier to incorporate into a lattice than others. The defects can also have their own energy states within the diamond bandgap, which can allow them to be electronically or optically active. Examples of these defects are shown in Figure 13.

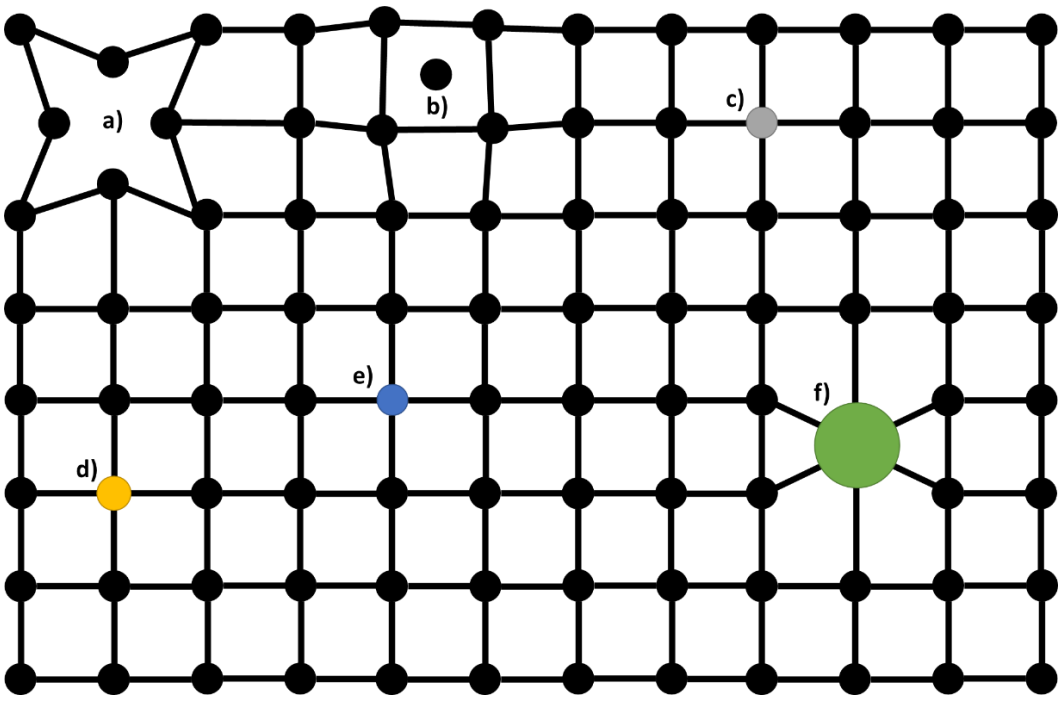



*Figure 13 – This diagram shows a simplified homo-elemental 2D lattice with a selection of defects. a) shows a vacancy, with an exaggerated distortion to the lattice. b) shows a native elemental interstitial atom, slightly distorting the lattice. c) is a substitution of an isotope of the native element. d) represents a larger substitutional atom, and e) a small substitutional atom. Defect f) represents a larger lattice distortion from a much larger element occupying a bond centred site, between two vacancy sites.*

## *Diamond defects*

Defects in diamond can cause colour in its appearance and can provide specific quantum electronic properties. Whilst larger extended defects do exist, this section will focus on point defects.

### ***Nitrogen in diamond***

The most common impurity in diamond is nitrogen, due to its similar atomic size and abundance on/in the Earth. In extreme cases, nitrogen can constitute 1% of the total number of atoms in a diamond lattice[117]. Nitrogen in diamond is only optically active in absorption and must combine with other defects such as vacancies to emit optical radiation[118]. Nitrogen atoms tend to aggregate when heated[118]. NV, H3, N3 and B centres form a chain of nitrogen aggregation from a single nitrogen atom adjacent a vacancy (NV), to four nitrogen atoms surrounding a vacancy (B centres).

Nitrogen is present in the Earth and so is common in natural diamonds. The amount of aggregation is indicative of growth temperatures and the pressures to which the diamond was exposed, and there can be significant spatial variation in defect distributions[119]. HPHT diamonds are also rich in nitrogen, from the atmosphere and raw materials[120], but CVD diamonds can have low amounts of nitrogen[121]. This is important for quantum electronic applications, where it is beneficial for defects to be engineered into specific locations and to limit any perturbations caused by other local defects. In HPHT and natural diamond, a few ppm of nitrogen is common, whereas CVD diamond can reach as low as a few hundred ppt of nitrogen[122].

### ***Diamond classification***

Diamonds are graded based on their concentration of nitrogen, as it is the most common defect. They are classified by using IR absorption data, as first proposed in 1933[123] into type I and type II. A type II diamond contains less than 1 ppm of nitrogen, whilst a type I diamonds contain more than 1 ppm of nitrogen. These values were established by what was previously classed as ‘detectable’ using IR absorption spectroscopy.

Type II diamonds are divided into type IIa and type IIb. Type IIa diamonds contain no or little impurities, meaning they are typically colourless and are close to pure diamond. These make up less than 2% of all natural diamonds[118]. Plastic deformation and other extended defects can still occur, which can impart colour onto these traditionally colourless diamonds. Type IIb diamonds which represent ~0.1% of all natural diamonds[118], contain boron in sufficient quantities to turn diamond

blue. Due to their rarity and attractive colour, these are some of the most expensive natural diamonds.

Type I diamonds constitute ~98% of all natural diamonds and contain nitrogen in detectable quantities[118]. They are divided into type Ia and type Ib diamonds. Type Ia is further divided into type IaA and type IaB. Type IaA diamonds contain A-centres that do not cause a change in colour, whilst type IaB diamonds contain B centres. There are also diamonds containing a mixture of the two defects called type IaAB, although they are less common. Type 1b diamonds contain primarily C centres and are also rare.

### ***C and A-centres***

Single substitutional nitrogen gives rise to C-centres or using the notation $N_s^0$ [19]. C-centres exist in the neutral charge state but can be ionised to produce $N_s^+$ defects which are called C+ centres[124]. The extra electron from nitrogen makes the diamond n-type, but $N_s^0$ has a donor level 1.7 eV below the conduction band, making it a deep level impurity, which makes it unviable for semiconductor devices[21]. The structure of the C-centre defect is shown in Figure 14[125].

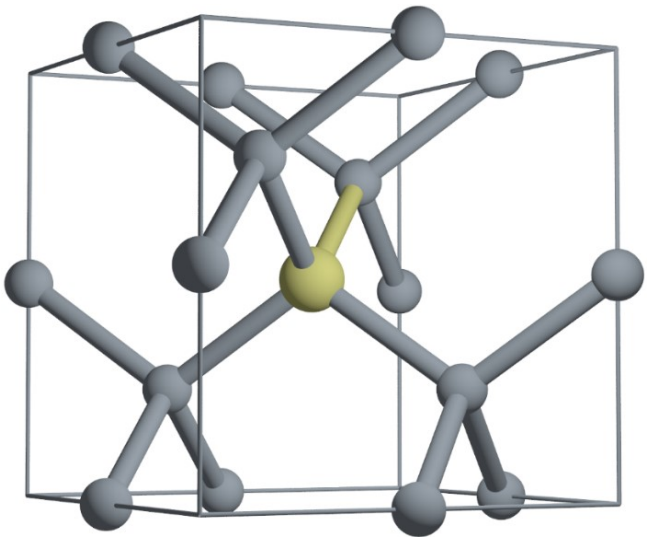


*Figure 14 – A structural diagram of the C-centre in diamond a lattice of carbon atoms (grey) surrounding a single substitutional nitrogen atom (yellow).*

A-centres comprise two substitutional nitrogen atoms next to each other in the lattice and are common in natural diamond[126]. The defect's structure is shown in Figure 15[126]. A-centres in a neutral charge state are known to interact with other emissive defects such as H3 and N3 through energy transfer mechanisms[127, 128]. This causes quenching of the emission from these defects, which is

manifested as a reduction in emission lifetime and total photon count. The energy transfer mechanism is thought to be dipole-quadrupole, but the decay associated with this model has not been accurately fitted[129]. C- and A-centres present IR absorption signatures and A-centres also absorb in the UV at ~300 nm[118].

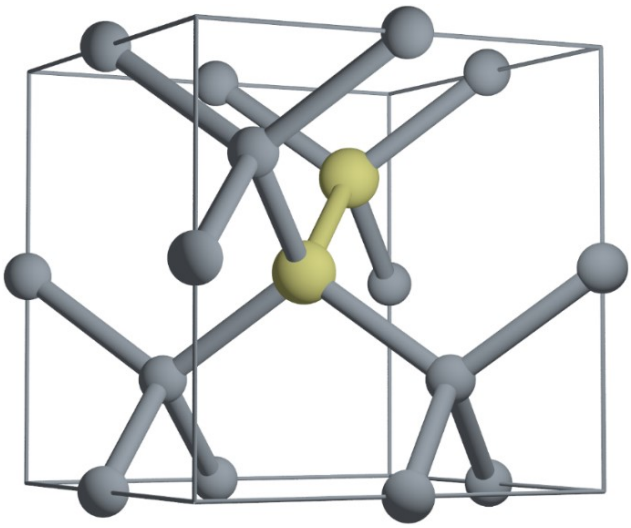


*Figure 15 - A structural diagram of the A-centre in diamond: a lattice of carbon atoms (grey) surrounding a pair of substitutional nitrogen atoms (yellow) next to each other.*

### ***NV centres***

The nitrogen-vacancy (NV) is one of the most researched emissive defects in diamond, due to its optical properties, which enable a variety of quantum mechanical applications and magnetic field sensing[116, 130]. Its structure consists of a vacancy adjacent to a substitutional nitrogen atom, as shown in Figure 16[131]. The defect exists in two known emissive charge states; $NV^-$ and $NV^0$. A third charge, $NV^+$ is currently anticipated by theory[132], but has not been identified experimentally. The negatively charged $NV^-$ centre attracts most interest because its energy level structure enables complex quantum and magnetic sensing applications, due to spin orbit coupling and optical readout methods[130]. Optically, $NV^-$ has a ZPL at 637 nm, whilst $NV^0$ has a ZPL at 575 nm[19]. Both charge states exhibit strong phonon coupling, leading to a very large phonon side band, which extends >150 nm from the ZPL[133]. $NV^0$ has a reported lifetime of 19 ± 2 ns[134], whilst $NV^-$ has a $m_s = 0$ lifetime of 13.7 ± 0.1 ns, and an $m_s = \pm 1$ lifetime of 7.3 ± 0.1 ns[135].

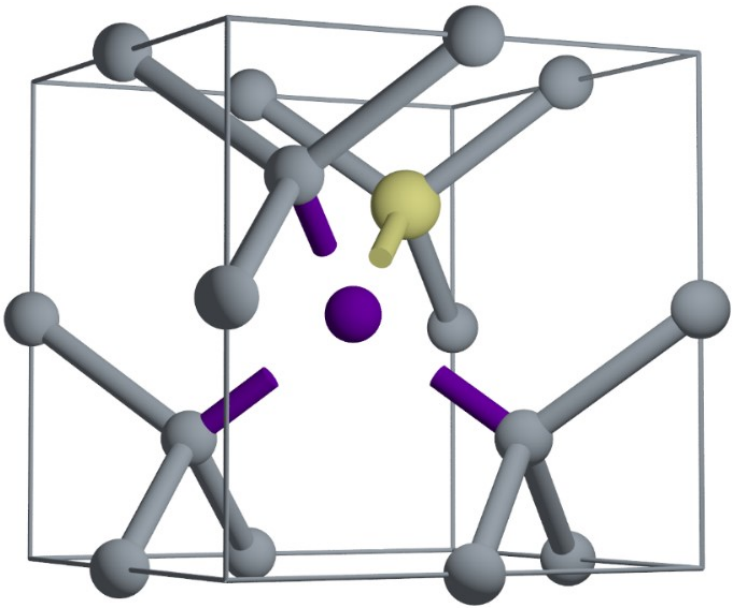


*Figure 16 - A structural diagram of the NV centre in diamond: a lattice of carbon atoms (grey) surrounding a single substitutional nitrogen atom (yellow) next to a lattice vacancy (purple).*

$NV^0$ has primarily been studied to help understand the nature of the $NV^-$ defect, and how to engineer NV production to increase the yield of $NV^-$. In this work, NV centres have been primarily investigated with respect to their variation in emission lifetimes, which can be relevant to quantum electronic applications. The structure of the NV defect is shown in Figure 16; it possesses trigonal symmetry along the [111] axis. However, its suitability for optical applications can be compromised by its low Debye-Waller factor, which means that the majority of the photons are emitted in the phonon band and not the ZPL[130]. There are techniques currently in development using cavities that preferentially generate ZPL emission, increasing the efficiency of the defect[136].

## Manufacture of NV centres

NV centres in diamond are typically found in CVD diamond as an 'in grown' state, meaning they are an inherent product of the synthesis technique. The charge state of the defect will depend on the local environment and the dopants introduced into the diamond during growth.

Ion implantation is a common method for generating vacancies and subsequent heating (annealing) is then used to form NV centres[137]. This is a comparatively destructive method and can reduce the quality of the produced centres[138]. Any strain introduced will impact the quantum electronic properties of $NV^-$, such as the emission lifetime. Ion implantation does allow for spatially targeted vacancy generation, including axially, by varying the implantation energy.

A new technique has recently been shown to generate NV defects in diamond using laser writing with varying single and then multiple-shot short pulses[139]. These defects can be localised accurately in the diamond, including axially, allowing for potentially high densities of defects to be written. The initial pulse causes damage in the diamond and the subsequent multiple-shots form the NV centre.

## Energy level structure of $NV^-$

A diagram representing the $NV^-$ energy level structure is shown in Figure 17[130,140]. Significant research has been conducted on the energy level structure of $NV^-$, because many of the applications use optical techniques to read out the state of the defect, e.g. for quantum computing or magnetic sensing applications. Both the ground state and the excited state are triplets, with a 2.88 GHz separation for the ground spin state. A second set of singlet energy states exist with a ZPL of 1042 nm[130]. The electrons can decay from the $m_s = \pm 1$ state of the excited triplet state into the $^1A_1$ excited singlet state, which provides an alternative relaxation path through which the electron will then decay to the $^1E$ state, emitting a 1042 nm photon, and then decay non-radiatively to the $m_s = 0$ triplet ground state level. This allows for optical preparation of the spin states of $NV^-$. The separation between the spin states of the ground state can be increased with a magnetic field, and the reduction in emission caused by resulting changes in the decay rates enables optically detected magnetic resonance (ODMR)[141, 142].

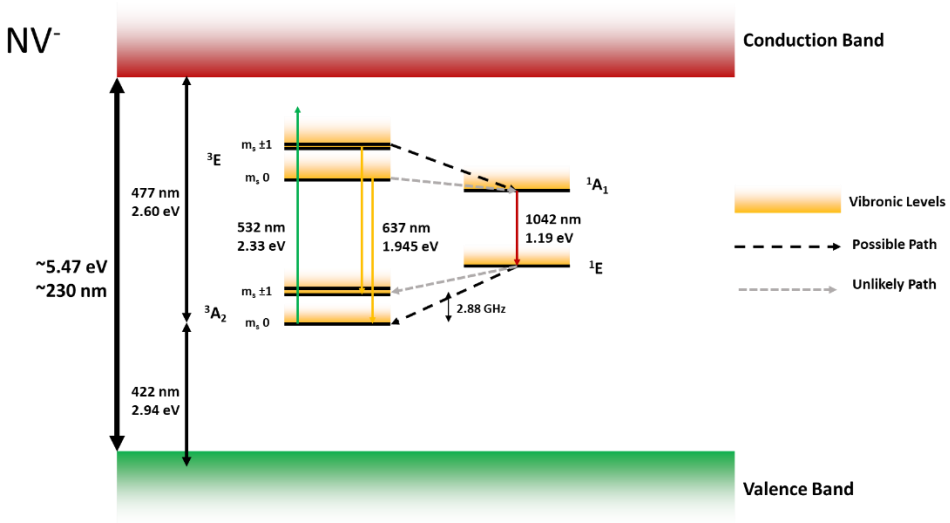



*Figure 17 – This is the currently understood energy level structure of the $NV^-$ defect in diamond. The current location within the band gap has been inferred from excitation wavelength measurements[140]. The defect consists of two primary energy levels, the $^3A_2$ ground state and $^3E$ excited state, which are spin degenerate. A second pair of energy levels are also shown. The black and grey dotted arrows show the likely transitions, and the second decay path allows the $m_s \pm 1$ excited state to decay into the $m_s \pm 0$ ground state.*

### Charge transfer (Photochromism)

The ability to ionise defects and change their charge state is an important consideration for defect stability, which is desirable for quantum electronic applications. Recent studies have shown that the ionisation energy for $NV^-$ is 2.60 eV, and recombination energy is 2.94 eV[140]. This has been measured using several techniques, including using single-shot measurements to ensure the correct processes were probed. Single-shot measurements are important to remove nonlinear effects. It is important to determine the optimum excitation wavelengths and powers for applications utilising such defects, and probe where the defect energy levels are in the bandgap of diamond. The ability to switch between two charge states, in a reversible process, can be exploited to enable super-resolution microscopy such as stochastic optical reconstruction microscopy (STORM)[143] and reversable saturable optical fluorescence transitions (RESOLFT) microscopy to be applied[144].

## ***H3 defect***

The H3 defect in its neutral charge state consists of a vacancy surrounded by two nitrogen atoms. Its structure is shown in Figure 18[127]. Its negative charge state is thought to be the H2 defect[19]. H3 is optically active in emission with a ZPL of 503.2 nm[19], which is close to another similarly named defect called 3H at 503.4 nm[19]. These defects can both be present in the same sample[145], highlighting the importance of high-resolution spectroscopy to study diamond photo-physics. The H3 defect has a large phonon side band and a natural lifetime of 16.7 ± 0.5 ns[19, 145]. This lifetime is readily quenched by interactions with A-centres, which also reduces the quantum yield[127]. The defect is found in nitrogen-containing diamonds and can be found along with N3 defects in the same sample.

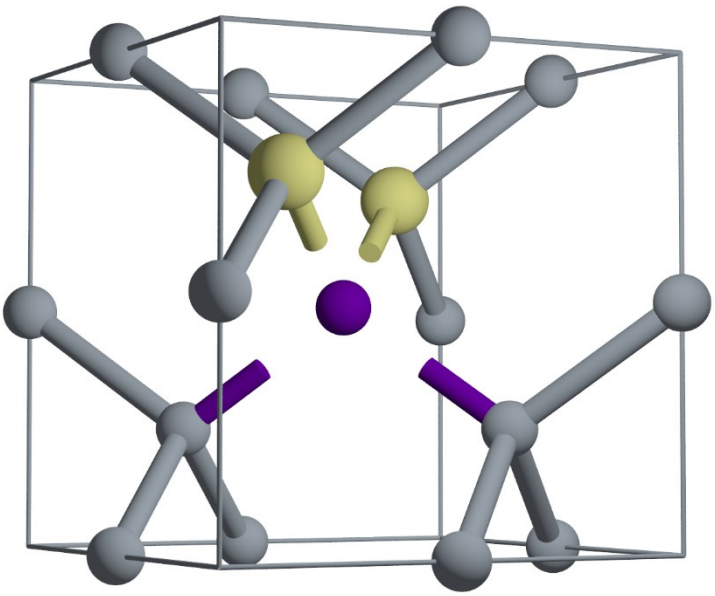


*Figure 18 - A structural diagram of the H3 centre in diamond: a lattice of carbon atoms (grey) with a pair of substitutional nitrogen atoms (yellow) surrounding a lattice vacancy (purple).*

### ***N3 defects***

The N3 defect represents the next level of aggregation after H3, and consists of three nitrogen atoms surrounding a vacancy, as shown in Figure 19[146]. It is common in natural diamonds and usually exists alongside A- and B- centres. N3 is also found along with H3 defects[118, 145]. It has a ZPL at 415.2 nm and is readily excited with 405 nm and 355 nm excitation[19]. The N3 defect has been extensively studied, due to its presence in natural diamond. It has a natural lifetime of 41 ± 1 ns, but similar to H3, can be quenched by local A-centres[128]. This is studied later in the thesis.

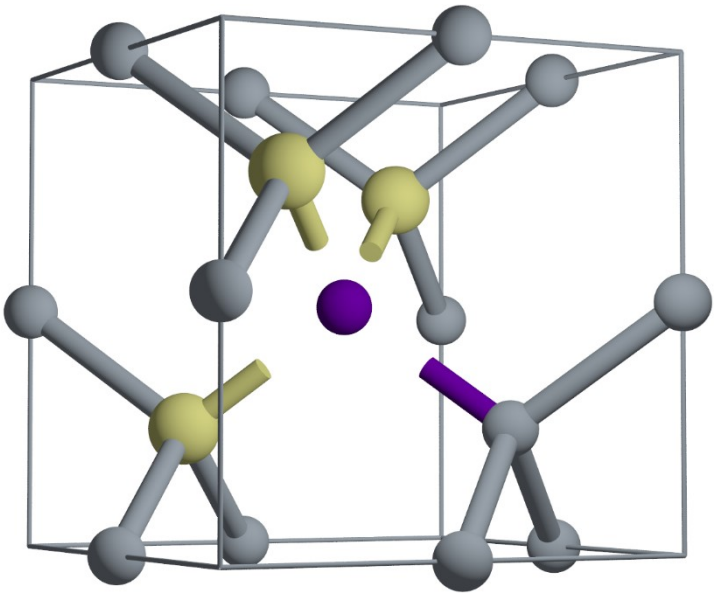


*Figure 19 - A structural diagram of the N3 centre in diamond: a lattice of carbon atoms (grey) with three substitutional nitrogen atoms (yellow) surrounding a lattice vacancy (purple).*

## *Group 4 vacancy defects*

Group 4 elements of the periodic table can be incorporated into diamond, either naturally during growth, e.g., silicon during CVD diamond synthesis, or by other methods. All three known defects exist on bond-centred sites and require two vacancies in the lattice to accommodate the much larger atom[147]. In the case of the heavier elements such as tin, the lattice is distorted significantly more than with silicon, causing more strain and variations in optical properties[148].

### ***Silicon vacancy***

Non-optimal optical properties of the NV centre for some quantum electronic applications have stimulated exploration of other defects within diamond. SiV exists in two confirmed charge states: $SiV^-$ and $SiV^0$ [149], and one inferred charge state, $SiV^{2-}$ [150]. $SiV^-$ has a ZPL at 737 nm[19], with a phonon side band peaking at 760 nm[19], whilst $SiV^0$ has a ZPL at 946 nm[151], and a phonon side band peaking at 976 nm[15]. Both defects have high Debye-Waller factors, and this makes them suitable for quantum applications since most of the photons emit in the ZPL. The defect's structure is shown in Figure 20 and has $D_{3d}$ symmetry along [111][15].

The lifetime of the $SiV^-$ defect has been established to be 1.28 ns ± 0.06[152]. The lifetime of $SiV^0$ defect has been less well studied but is thought to have a 1.8 ns lifetime[153]. The SiV defect has potential

applications in quantum devices, specifically for communications, but less research has been conducted on these defects compared to $NV^-$ defects.

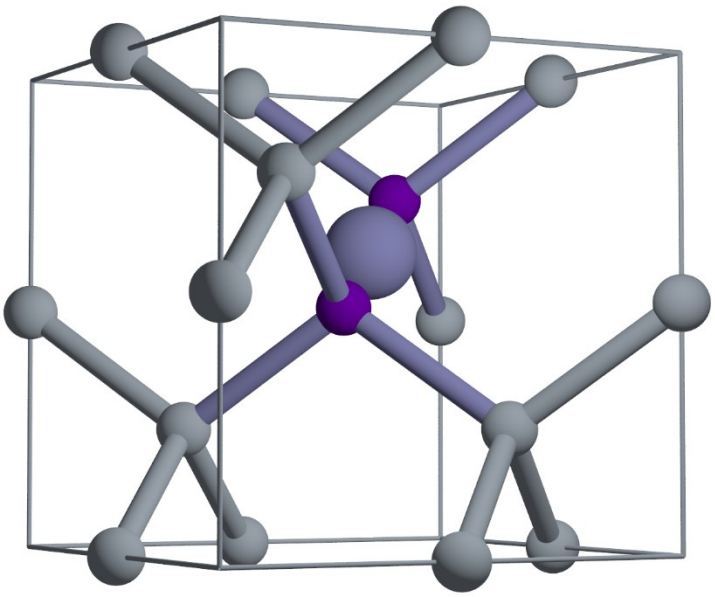


*Figure 20 - A structural diagram of the SiV centre in diamond: a lattice of carbon atoms (grey) with a large silicon atom (light purple) at a bond centred site between two vacancies (purple).*

## Energy level structure

The energy level diagram for $SiV^-$ is represented in Figure 21[15], which indicates four split emission lines, resulting from doublets in both the excited and ground states[154]. These transitions differ in their emission polarisation and their relative strength[154]. Their emission lines are only experimentally resolvable near liquid helium temperatures. Previous PLE spectroscopy[155] and polarisation PLE spectroscopy resolved studies[154,156] have suggested a further excited state above the excited state. This is explored later in the thesis.

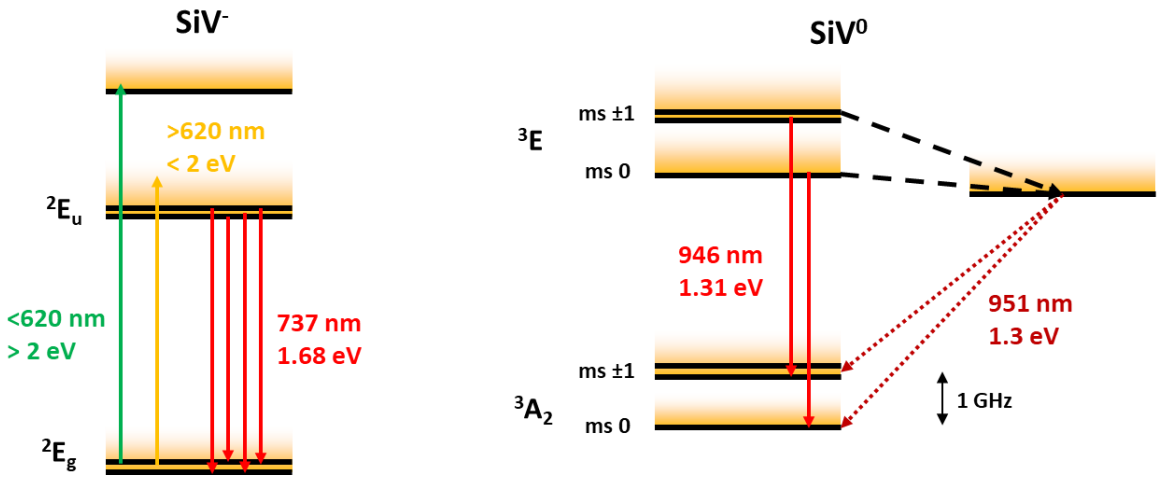



*Figure 21 – The diagram on the left depicts the energy level structure of the SiV$^-$ defect in its negative charge state, as currently understood[154]. Recent research on the SiV$^0$ has produced the energy level structure (right), where the side energy level at 1.3 eV is currently not well understood[15].*

Recent stress measurements of the SiV$^0$ defect have revealed a new energy level (previously hinted at in previous measurements[149]), with an emission line at 951 nm[15]. This transition is normally a forbidden transition and is only optically active when the symmetry of the system is broken, such as during uniaxial stress measurements. Currently, no ODMR has been detected in SiV$^0$ and the splitting of the excited spin states is not known. The strain-induced transition at 951 nm, is potentially useful as an optical read-out of local lattice strain. Further investigations of the energy level structure of this defect are ongoing.

## Charge transfer (photochromism)

Charge transfer between SiV$^-$ and SiV$^0$ defects has been documented. It has been shown that above bandgap UV excitation and heating in the dark can switch the defects between the two charge states[149] (SiV$^-$ can also be charge transferred with excitation energy above 1.9 eV, although the resultant charge state is unknown[157]). This can be useful to maximise emission from specific charge states. The wavelengths of the transitions have not been precisely determined, due to the complexity of these measurements. If the switching is a stochastic or controllable process, then SiV could be a viable target for super resolution microscopy.

***Germanium and Tin vacancy***

Whilst the optical properties of the SiV defects may be more suitable for some applications than the $NV^-$ defect, the quantum mechanical properties are not as useful. This is partially due to the small energy gap of the ground state, which leads to phonon related decoherence[158]. For the heavier elements down the periodic table, the separation between the ground state energy levels increases, reducing the thermal phonon decoherence effect. Such defects include the germanium vacancy (GeV) and tin vacancy (SnV), whose optical properties were theorised to be similar to the silicon related defects.

## *Boron defects*

Boron is similar to nitrogen in that it can be easily incorporated into the diamond lattice, partially due to its similar size to carbon. The defect takes on a substitutional site, as depicted in Figure 22[90]. Boron makes a diamond blue, with a striking example of this being the 'hope diamond'. Boron acts as an acceptor with an energy level 0.37-0.39 eV above the valance band[159]. Boron doping is the most common way to generate p-type diamond and it is more effective than n-type doping of diamond with phosphorus[160]. Achievable boron concentrations in diamond are at least an order of magnitude higher than with phosphorus doping. Boron-doped diamond will transition from an insulator at low concentrations, to metallic conduction at higher concentrations (typically $>10^{20}$ $cm^3$ of boron atoms)[161].

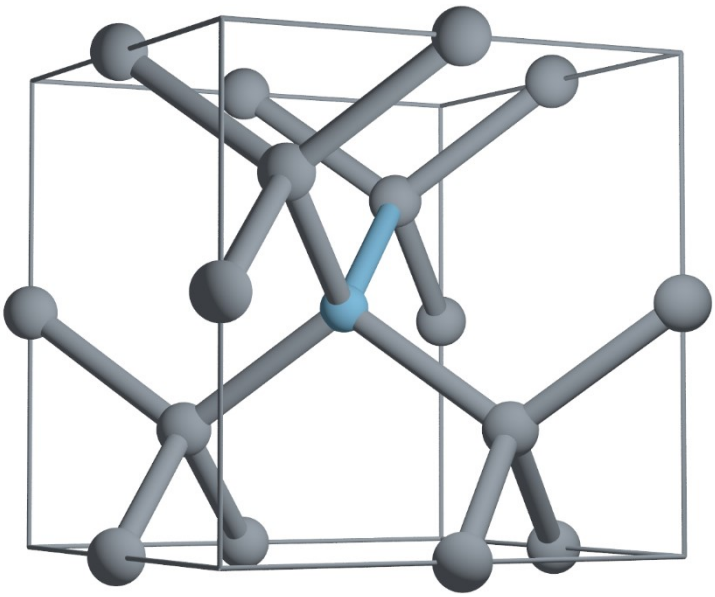


*Figure 22 - A structural diagram of a Boron centre in diamond: a lattice of carbon atoms (grey) surrounding a substitutional boron atom (blue).*

When boron-doped diamond is heavily doped and cooled to 4 K, the diamond becomes superconductive[162]. This is an interesting phenomenon, as diamond is naturally an insulator, and it illustrates how the material can be applied to a wide variety of applications. Superconductivity in diamond could be used for superconducting quantum interference devices (SQUIDs)[163] or Josephson junctions for a variety of applications[164]. Boron can be doped into diamond through CVD or HPHT synthesis.

## *Hydrogen defects*

Hydrogen defects in diamond are currently poorly understood. In CVD growth especially, atomic hydrogen makes up most of the gas phase, and so it has been expected that hydrogen related defects would exist within diamond. Hydrogen has been found to 'decorate' other defects, examples of which are NVH[118] and $N_3VH$[165].

## *Defect incorporation*

Defects in diamond can have a preferential uptake into specific growth planes, based on many factors. One of the most well studied variations is that of nitrogen[67], which can lead to different growth planes having different optical, electrical and quantum properties, due to the difference in defect concentration. Synthetic diamonds are often studied by looking at the different growth planes using above bandgap excitation, with which the different growth planes can be easy to identify. In natural diamond, this is significantly more difficult since the structure is more irregular, due to the different time scales of growth and variations in environment.

## Conclusion and outlook

This chapter has reviewed the properties of diamond, including the effect that lattice defects have on its luminescence properties, which can impact various applications. The following chapters will discuss the analysis techniques used with a multidimensional instrument developed to study diamond luminescence. Natural and synthetic diamonds have been investigated using this instrument and several of the optically active defects described in this chapter will be explored. Below is a summary of the defects which have been investigated in this work (Table 2):

*Table 2 – Table showing some of the ZPLs and lifetimes for some of the key defects investigated in this work.*

| **Defect** | **Zero Phonon Line** | **Lifetime (ns)** |
|---|---|---|
| $NV^0$ | 575 nm[19] | 19 ns ± 2[134] |
| $NV^-$ | 637 nm[19] | $m_s$ = 0 - 13.7 ns ± 0.1[135]<br>$m_s$ = ±1 - 7.3 ns ± 0.1[135] |
| $SiV^-$ | 737 nm[19] | 1.28 ns ± 0.06[152] |
| N3 | 415.2 nm[19] | 41 ns ± 1[128] |

# Chapter 4 - Development and characterisation of instrumentation for multidimensional luminescence microscopy and spectroscopy

## Outline

This chapter discusses the use of a time-resolved spectrofluorometer, and the design, characterisation and application of a line scanning hyperspectral luminescence microscope. Abilities of these two instruments were then combined into a multidimensional luminescence microscope that integrates hyperspectral and lifetime imaging, spectroscopy techniques with white-light transmission and polarisation-resolved imaging. The application of a hyperspectral microscope to diamond luminescence will first be discussed, followed by the application of a previously developed excitation-emission-lifetime-polarisation resolved fluorometer[166].

The rest of the chapter will describe the development of a novel, multidimensional luminescence microscope, capable of hyperspectral imaging, spectrally resolved lifetime, and excitation-resolved luminescence measurements. This instrument is discussed in terms of its optical components, excitation sources and techniques for the emission analysis modalities. The performance of the components will be characterised, and some exemplar measurements of complex diamond luminescence will then be presented.

## Design of a grism-based line scanning hyperspectral microscope

Hyperspectral imaging is a powerful tool to image materials with varying spatial and spectral properties. The aim of the work reported in this section was to develop a line scanning hyperspectral instrument able to distinguish spatially varying spectral features on diamond samples. This would be tested by measuring several unknown diamonds using the available excitation source. The instrument would also be designed to measure birefringence and white-light transmission images to co-register them with the hyperspectral data. The instrument was controlled by a custom-written *LabVIEW* program.

An inverted commercial microscope frame (IX71, Olympus) with a motorised *x*-*y* translation stage (Märzhäuser Wetzlar) provided the basis for the instrument. To construct *x*-*y*-*λ* images, line illumination generated using a cylindrical lens was implemented through the illumination port of the microscope frame, and the sample is scanned in one axis (*y* axis), orthogonal to the line illumination on the sample. This line is imaged onto the entrance slit of a grism-based spectrograph, to disperse the excited emission along one axis. The dispersed emission is then relayed onto a 2D EMCCD (iXon

887, Andor), which acquires an *x*-*λ* intensity image, with the spatial *x* dimension along one axis and the dispersed wavelength along the other axis. An image is taken at each step, corresponding to each *y* axis position, and a resultant hyperspectral *x*-*y*-*λ* data cube is acquired. This is described as "push-broom" hyperspectral imaging. A system diagram of the constructed instrument is shown in Figure 23.

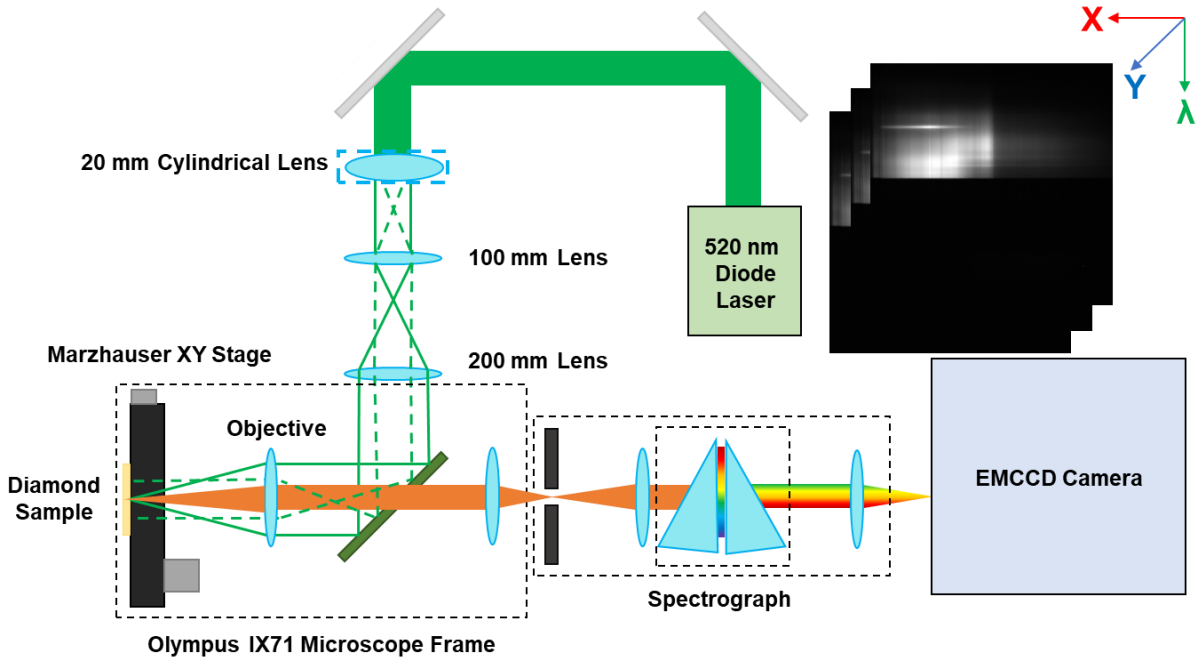



*Figure 23 – System diagram of the push-broom hyperspectral imaging microscope. This diagram shows the excitation and emission paths, with exemplar camera images. In the excitation beam path, a beam expander and cylindrical lens are used to achieve an overfilled line on the back focal plane of the objective. This is then imaged to the entrance slit of the 'spectrograph' grism system, and onto the camera.*

## *Illumination and optical elements*

Excitation was provided by a multimode diode laser emitting at 520 nm (LDM-520-1000-A, Lasertack) with a total power output of 1 W. This laser diode is driven by a diode controller (LDC2000, Thorlabs), whilst cooling is provided by a Peltier cooler, with power and control provided by a TED (TED200C, Thorlabs). Two dielectric mirrors (EO2, Thorlabs) are used to steer the beam into the optical assembly, which is mounted at the input of the microscope frame. Line illumination is formed by an optical relay consisting of a 20 mm cylindrical lens, a 100 mm achromatic doublet, and a 200 mm achromatic doublet, mounted to a cage system (Thorlabs), where the doublets are 1" in diameter. In one axis, the optical beam is not affected by the cylindrical lens, and so it is magnified by 2X to form a focus on the sample, shown as the solid green lines in Figure 23. The other axis is focused by the curved surface of the cylindrical lens, at a distance of 120 mm from the first lens and

is magnified by a factor of 5X and then focused to the back focal plane of the objective lens, which forms a collimated beam at the sample, for which the beam path is indicated by the green dotted lines in Figure 23. The result of these two beam-shaping optical paths is an illumination line on the sample with a Gaussian intensity profile along both axes. The beam is expanded to overfill the back aperture of the objective lens to mitigate the non-uniform illumination formed by the cylindrical lens along the line. This gives more uniform illumination at the cost of reduced laser power at the sample. The diode laser possesses an oval shaped beam, and this is set so the long axis of the laser output is aligned to the long axis of the line at the sample plane, to minimise the impact of its multiple transverse spatial modes.

The microscope frame also has an incandescent lamp for transmission measurements, which is also used as an aid when positioning the sample. Polaroid film can be added after the transmission lamp, and a crossed Polaroid film can be added to the detection side to enable crossed polarisation imaging. Due to diamond's inherent lack of birefringence in an unstrained state, crossed polarisers can be used to identify strained regions in the sample.

### *Emission collection and spectral resolution*

A fluorescence cube containing an excitation (525/50 BP), dichroic (565), and emission filter (594 LP) is used to separate the excitation from the emission. The spectral range of the spectrograph (V8E, Specim) is 380-800 nm. The tube lens from the microscope (180 mm, Olympus), focuses the emission onto a slit contained within the spectrograph housing, which has a fixed width of 80 microns. Inside the spectrograph, a lens collimates the light from the slit and it is spectrally dispersed by the prism-grating-prism (grism) optical element. Each wavelength component is focussed to the image plane, which is recorded by the electron-multiplying charge coupled device (EMCCD) camera, and collects a 2D $x$-$\lambda$ image. The EMCCD is Peltier cooled (typically to -20 to -30°C) to reduce the dark noise on the camera. EM gain can be applied on the camera, which can amplify weak signals above the readout noise, but the EM gain will also amplify dark noise on the camera, so it is important to minimise this noise by cooling the sensor.

The acquisition process for imaging a sample consists of initially using the eyepieces of the microscope with lamp illumination to get the sample into focus and then selecting the region of interest. The $x$ axis of the system (the long illumination line axis) is fixed by the field of view (FOV) of the objective lens, but the scanning axis $y$ is limited only by the stage scanning range. A typical procedure involves selecting either a 4X 0.16 NA (Olympus, UPlanApo) or 10X 0.3 NA (Olympus,

UPlanFLN) objective lens, depending on FOV and spatial resolution required, and then setting the start and end position. The developed *LabVIEW* program then uses a fixed step size, based on the size of a pixel on the camera and objective magnification, to divide the distance up into many steps. The step size must equal the pixel dimensions for isotropic pixel size, to avoid stretching of the images. If other step sizes were to be chosen, for example to speed up acquisitions, then interpolation or binning could be used to achieve the correct aspect ratio. The optimum camera integration time per step can be determined through a test acquisition at small integration times, or by testing a single slice of the sample. The aim is to avoid saturation of the camera and maximise the dynamic range. An example data set is shown in Figure 24

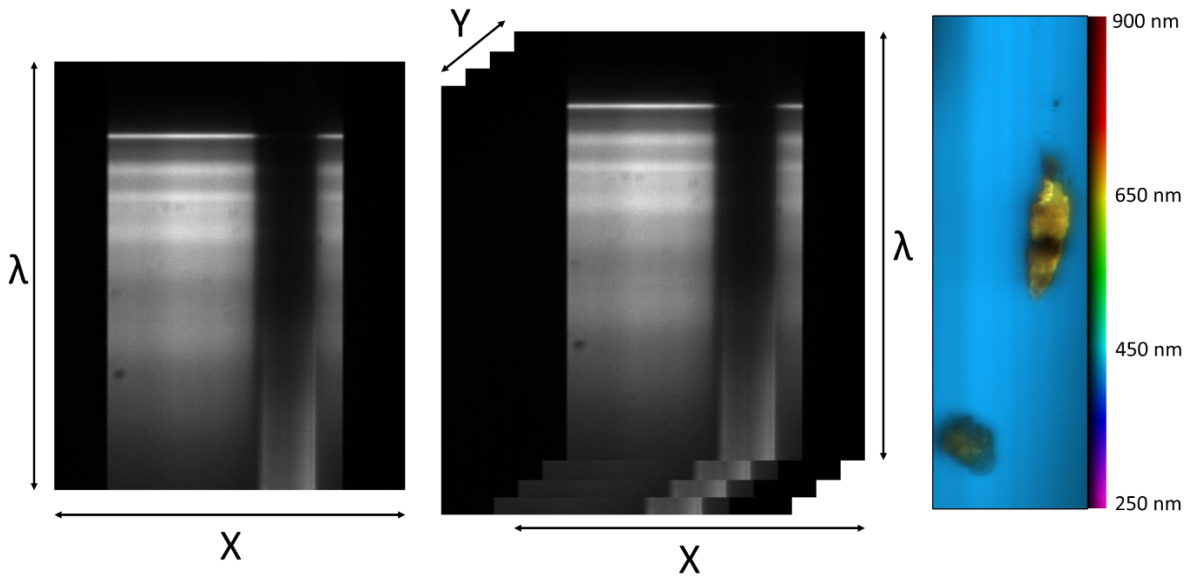



*Figure 24 – Left: an example slice from a single hyperspectral data set showing the spatial x-axis and wavelength axis. Centre: a stack of three images showing the spatial y-axis. Right: an example hyperspectral image of diamond and dust (yellow-coloured region), where average wavelength has been converted to colour and modulated by intensity.*

The spectral resolution of the spectrograph is determined by the entrance slit width, the spectral dispersion, and the sampling at the image plane. A mercury emission line was measured, and the resultant full width half maximum (FWHM) of a fitted Gaussian function was found to be 5 nm, which is the spectral resolution of the system. The spectral dispersion of the grism results in 1.2 nm for each pixel on the detector, and so the light is sampled above the Nyquist criterion. The spatial resolution in one axis is limited by the spectrograph entrance slit width of 80 microns, with the spatial resolution in the sample being determined by the lateral magnification of the microscope used.

## *Sample mounting*

It is standard practice in microscopy to mount samples onto a thin glass slide or "coverslip", and some objective lenses contain an adjustment ring to compensate for the spherical aberration contributed by this coverslip. Diamond has a relatively high refractive index of 2.421 (at 550 nm)[86], meaning that the Fresnel reflection for a diamond-glass and diamond-air interfaces are significant. This can result in an interference effect between the sample and slide, as can be seen in Figure 25. A pragmatic solution to this was to create a metal plate with different sized holes, on which a sample could be mounted above, supported by overlap of the sample with the plate. This has the advantage that only air is in between the objective and sample, but the disadvantages of a reduced collection NA towards the periphery of the hole, and a loss of the region obscured by the metal. This mounting method was used in all subsequent experiments.

An alternative method of sample mounting was explored, involving the use of an upside-down vacuum suction pad, which was generated by a simple vacuum pump. The loss of transmission illumination modes and vibrations caused by the pump made this method of limited utility and so it was not used any further.

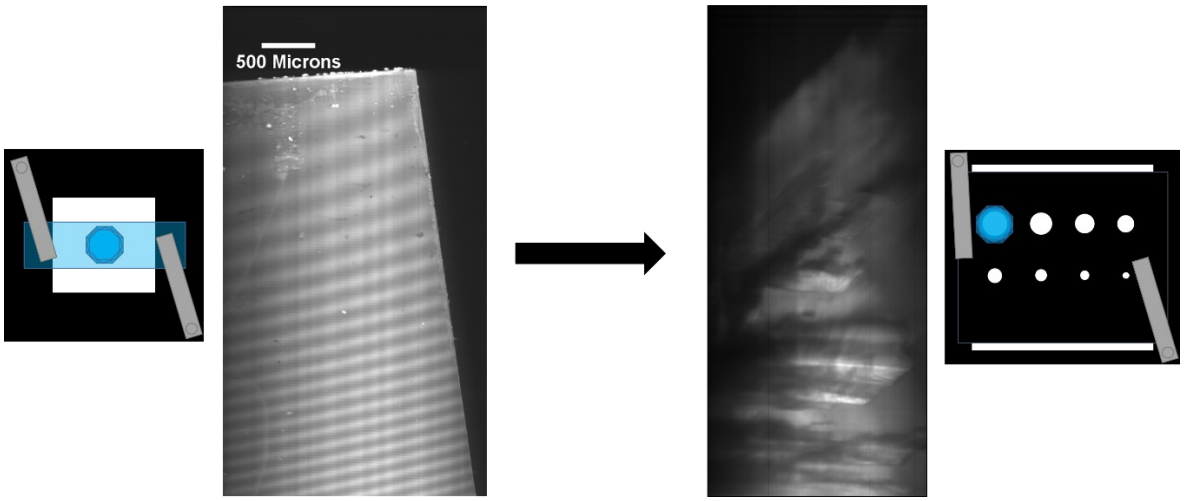



*Figure 25 – (left) The original mounting apparatus, using a glass slide and corresponding summed intensity hyperspectral fluorescence image showing the observed interference pattern resulting from light reflected between a diamond sample and glass slide. (right) A summed intensity hyperspectral fluorescence image with the new mounting method, showing no interference effects.*

## *Application of hyperspectral luminescence microscope to synthetic diamond*

The system was applied to image a synthetic diamond, which consisted of a CVD region grown on a HPHT substrate. This CVD diamond was not specifically grown to have particular properties and so only emission from NV and SiV defects was expected to be imaged. With the excitation wavelength of 520 nm, both charge states of NV (if present) should be excited along with $SiV^-$.

The hyperspectral image data were acquired in 2,714 separate 1.6-micron steps, with an integration time of 1 s per step. The total acquisition time was 2,985 s, including 271 s for reading of the image and the translation of the stage. This was acquired with a 10X 0.3 NA objective lens (Olympus, UPlanFLN) and the results are shown in Figure 26.

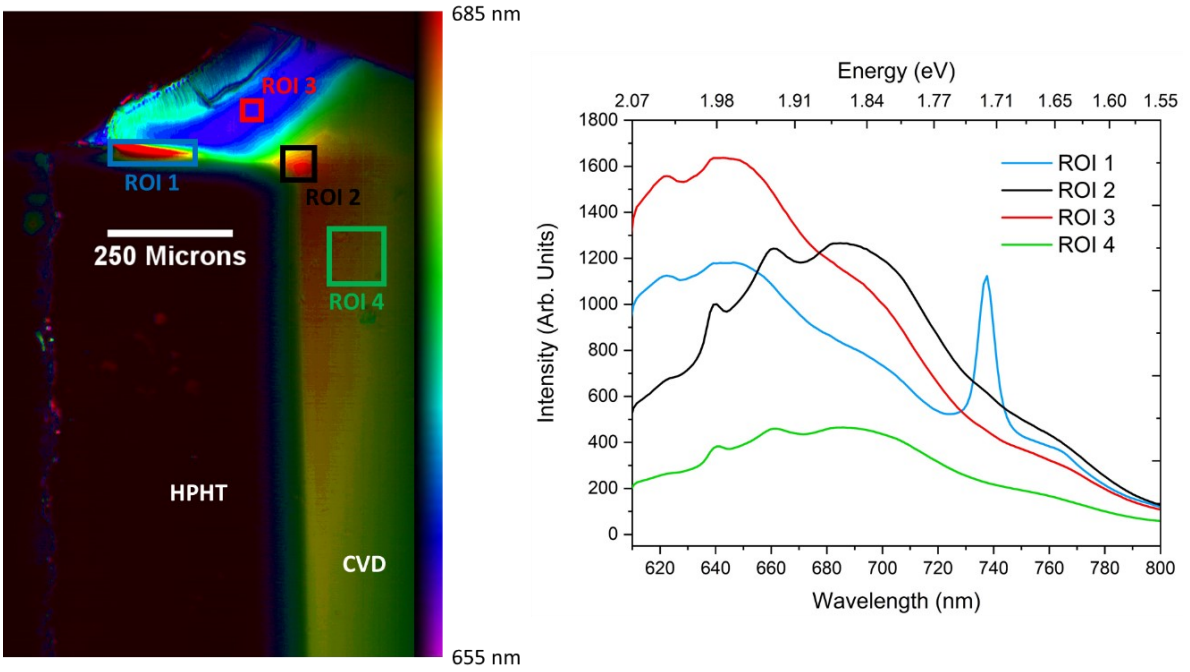



*Figure 26 – (left) An intensity modulated median wavelength image of a CVD diamond with HPHT substrate. 520 nm excitation was used. (right) Extracted spectra from four ROIs on the image. Spectral features from $NV^-$ (637 nm ZPL) and $SiV^-$ (737 nm ZPL) are present.*

The emission filter blocks radiation for wavelengths lower than 600 nm. Defects in diamond are most readily identified through their ZPLs, and so the ZPL at 575 nm for $NV^0$ is not visible[19]. However, its phonon side band stretches well beyond 600 nm and this is apparent. The image in Figure 26 shows the intensity-merged median-wavelength image.

The image shows spatial variations in the median wavelength and can be used in conjunction with a Z-stack (spectral axis) ROI tool to determine regions with different spectral properties. The

significant advantage hyperspectral imaging has over conventional spectral imaging is that at each pixel a spectrum can be extracted, which can be used to elucidate multiple emitting species. Emission spectra from several ROIs are shown in the graph in Figure 26.

ROI 1 shows a feature, which is not present in any of the other ROIs, and is attributed to $SiV^-$, due to the location of the peak at 737 nm, corresponding to its ZPL[149]. In addition to this peak position, a small secondary peak is noted at 760 nm, which corresponds to the weak phonon side band of the defect. The origin of this emission is concentrated at the interface between the HPHT substrate and CVD diamond. The presence of silicon in the gas phase during growth is unlikely to have been intentional due to the lack of $SiV^-$ in the other regions. This defect could have been incorporated unintentionally through etching of a silicon substrate or quartz window in the CVD reactor[167].

ROI 2 and 4 show a peak at 637 nm which originates from $NV^-$, as the ZPL is 637 nm. The concentration of $NV^-$ is higher in ROI 2, due to the higher count, and this could correspond to emission from a different growth plane to that for ROI 4 – with the growth plane in ROI 2 having incorporated more nitrogen than ROI 4. In ROI 3, no obvious ZPL is apparent but, as seen in ROI 1, a large band from below 600 nm is present, which extends to >800 nm. This band likely originates from $NV^0$, given the presence of $NV^-$ in this sample, although no ZPL is visible. The HPHT substrate does not appear to emit at this excitation wavelength, suggesting that this sample has not been annealed and irradiated to produce vacancies and related centres. N3 and H3 defects could have been present but are not excited by this laser source and wavelength.

Comparing the crossed polariser imaging with the white-light transmission and hyperspectral imaging allows correlation of strain with spectral features. An example of this is shown in Figure 27, and presents a different region from the same sample. The white-light transmission image of this CVD diamond shows black “rivers” of probable $SP^2$ and non-diamond carbon, which can occur during CVD growth[111]. As expected, the birefringence image shows that this is a region of strain in the sample, which is attributed to lattice mismatch.

The summed fluorescence intensity image shows fluorescence from the sample and banding in the region above the “rivers” of carbon. These could be striations from step growth. The combined median wavelength and intensity image shows a variation from 670 nm to 700 nm across the image, and spectral analysis from the spectral image reveals that this is likely arising from $NV^0$ to $NV^-$ concentration changes across the sample. The co-registered parameters in these images demonstrate the potential for correlative measurements to aid understanding of consequences of growth conditions and interventions.

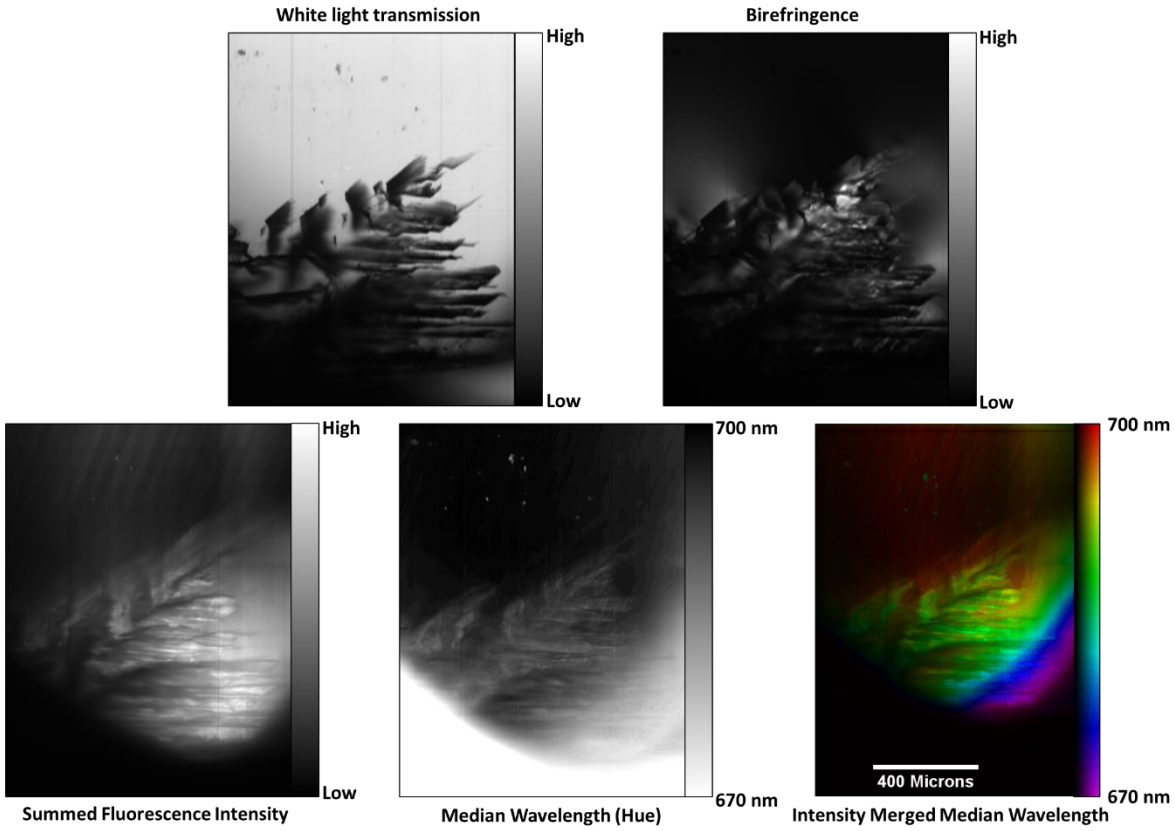



*Figure 27 – A set of five images taken using white-light transmission, crossed polarisers, and hyperspectral fluorescence emission at 520 nm excitation. The hyperspectral data is broken into summed fluorescence intensity, median wavelength and intensity modulated median wavelength images. This shows how different features can be related between the different modalities.*

## *Summary*

A line-scanning hyperspectral imaging microscope was presented, using a high-power diode laser at 520 nm, based on a commercial microscope frame and grism-based imaging spectrograph. Hyperspectral imaging has also been combined with white-light transmission and crossed polarisers to provide three different imaging modalities, all co-registered on the same instrument. Cross correlation between different phenomena can therefore be performed, as illustrated in Figure 26 and Figure 27. Several emitting defect species were identified, with emission from different growth planes being observed.

The system had several limitations, primarily due to the imaging spectrograph (grism). The spectral resolution was fixed at 5 nm, which would be insufficient for separation of H3 and 3H ZPLs for example[145], or the fine structure of $SiV^-$ if liquid helium cooling was used. The limited spectral resolution also reduces the ability to distinguish components of different median wavelengths when

these differences are small. Raman spectroscopy would also be significantly limited using this spectrograph, as variations in FWHM or spectral position of typical features would not be resolvable. The spectral range from 380 to 800 nm is sufficient for most experiments, however, $SiV^0$ has a ZPL at 946 nm, which is outside of the range[15]. A fixed wavelength source can be useful for some measurements; however, a tuneable source would offer significantly more flexibility to study a broad range of emitting defects such as are present in diamond.

## Single-point time-resolved spectrofluorometer

### *Introduction*

Fluorescence lifetime measurements on diamond are occasionally conducted using HBT (Hanbury-Brown and Twiss) instruments[168], which usually measure the emission from one or a few specific defects. TCSPC has previously been performed on diamond samples, both synthetic and natural, and has been used to measure quenching caused by energy transfer to neighbouring defects[129, 134]. At room temperature, some defects in diamond such as N3, $NV^-$ and $NV^0$ have strong vibronic interactions, which cause wide phonon sidebands[19]. This spectral overlap can obscure weak emission signals. Fluorescence lifetime contrast can help identify these weak emissive signals. Defects in diamond can exhibit fluorescence lifetimes varying from less than 1 ns to 40+ ns.

A previously developed single-point time-resolved spectrofluorometer (TRS)[16, 166]was applied to bulk measurements of luminescent lifetime of diamond samples. This TRS instrument had been developed to provide a broad range of excitation and emission wavelengths in a compact frame[166]. A schematic of this instrument is shown in Figure 28. Two excitation sources are available: a 375 nm pulsed diode laser (LDH-P-C375B, PicoQuant), and a pulsed supercontinuum laser source (SC400-2, Fianium). The 375 nm laser operates at 80 MHz, but this can be reduced to 40, 20, 10, or 5 MHz, and has a peak average output of 3.2 mW at 80 MHz. The supercontinuum laser source was not used for any experiments, but a variation of the prism-based spectral selection setup is used in the multidimensional instrument described later[169].

A neutral density (ND) filter wheel (NSR1 and nsFW1, Newport) containing seven ND filters of varying densities provided adjustable attenuation of the excitation beam, shown in Figure 28. For measurements of diamond luminescence, the detected emission was very low and so the excitation source was not attenuated. Polarisation of the excitation laser is adjusted by a Glan Taylor polariser cube in a manual rotation mount. A 50 mm quartz lens then focuses the excitation source to the sample holder, which is located at the focal length from the lens. For liquid samples, a cuvette

holder is used, but this was swapped for a purpose-designed vacuum holder for solid samples such as diamond. This holds the diamond in place and prevents vibrations from displacing the diamond. A small catchment area was machined into the side of the holder to prevent samples from falling into the holes of the optical breadboard.

In the emission path, two quartz lenses of 50 mm and 100 mm form a 4-f relay into an electronically controlled grating-based monochromator (CM110, CVI Laser), with manual slotted copper slits, shown in Figure 28. For the lifetime measurements, the system uses a PCI TCSPC card (SPC-730, Becker and Hickl) and the system is controlled using a previously programmed custom *LabVIEW* interface. Detection is provided by a photomultiplier (PMC-100-1, Becker and Hickl). Before light enters the monochromator, a rotation stage (NSR1, Newport) mounted polaroid film allows the polarisation of the emission to be analysed. Coupled with the excitation polariser, this allows fluorescence anisotropy to be characterised. A long-pass blocking filter is used to block any scattered excitation light from the sample, but this is removed during IRF measurements.

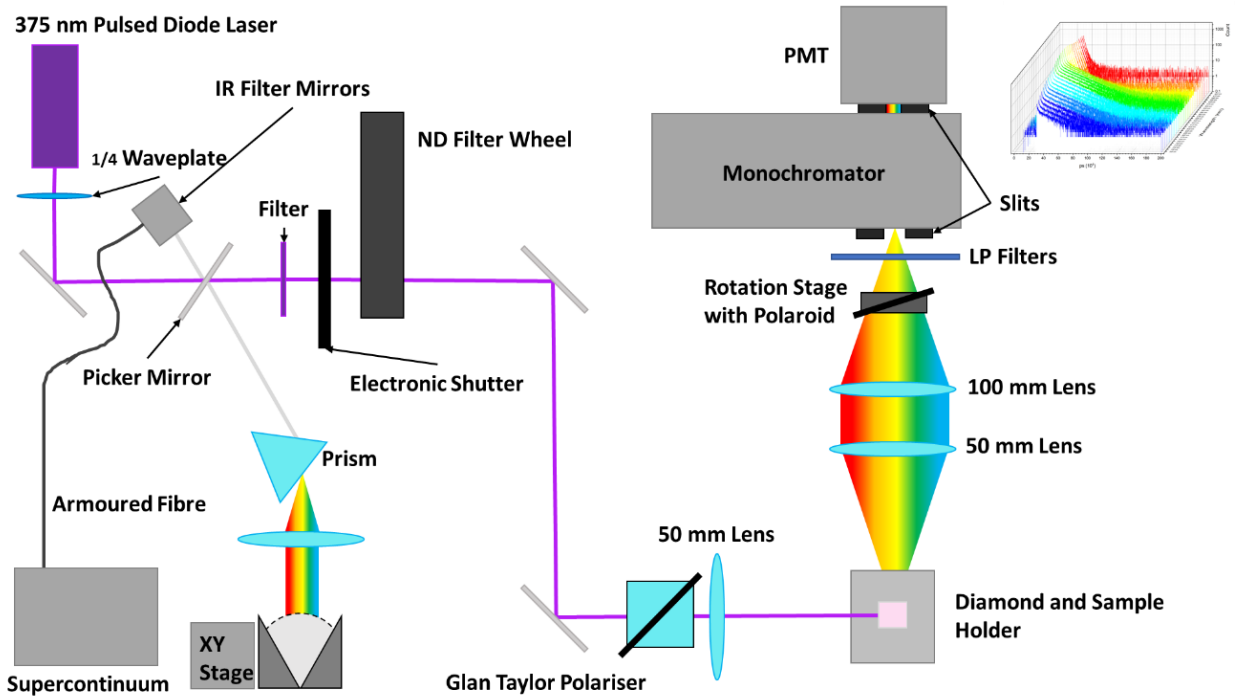



*Figure 28 – A schematic of the spectrofluorometer showing the excitation and emission paths with their optical elements. The tuneable excitation supercontinuum was not used from this system. The excitation polarisation state is adjusted using the Glan Taylor polariser. Vertical is defined as parallel to the entrance slit and a pair of quartz lenses image the sample onto the entrance slit of the monochromator.*

## *Application of time-resolved spectrofluorometer to synthetic CVD diamond*

A large (1 carat) CVD grown diamond was used to test the application of this instrument to the study of diamond luminescence lifetimes and was not measured in any other sections. This sample was thought to contain nitrogen, but nothing else was known about the sample. For excitation, the 375 nm laser was used with a repetition rate of 5 MHz. The emission was measured through horizontally and vertically polarised light, for vertical excitation polarisation. Here vertical is defined as parallel to the entrance slit. Decay curves were acquired every 5 nm, from 460 to 710 nm and '*FLIMfit*' was used for the lifetime data analysis. The spectrally varying G-factor of the system was accounted for using data from the PhD thesis of Hugh Manning[16]. IRF measurements were acquired using scattered light from a colloidal solution of silica beads (Ludox), diluted in a cuvette of 'Milli-Q' distilled water.

Decay curves for the horizontal and vertical polarised emission is shown as contour plots in Figure 29, as a function of wavelength. There is an increase in the longer-lived component of the decay above 575 nm, which also corresponds to a peak in the emission, and this is shown in the spectra on the graph. This emission is attributed to the ZPL of $NV^0$ at 575 nm and its large phonon side band. A triple exponential decay model was required to fit the data with a low $\chi^2$ and residual, yielding lifetime components of 19.6 ns, 3 ns and 800 ps. The normalised decay component population fractions ($\beta$s) are plotted in the lower right panel of Figure 29. This indicates that the 19.6 ns component (beta 1), has a peak at 575 nm and slowly increases towards the red end of the spectrum. This lifetime and spectral profile are consistent with $NV^0$, to which we attribute this 19.6 ns component (beta 1)[134].

It is harder to determine the origin of the other two lifetime components. In the vertical spectra shown in black in Figure 29, a large peak can be seen at 510 nm, which is not identifiable in the horizontal case. This suggests that some of the emission from this sample is highly polarised relative to the emission from $NV^0$, which is isotropic. The beta parameter profile shows that the 3 ns (beta 2) lifetime dominates the emission at <530 nm. The origin of this emission is unknown, but its polarization state is interesting. The fastest decay of 800 ps (beta 3) appears to rise at 525 nm, peaking at 560 nm, and then slowly reduces as the phonon side band of $NV^0$ increases. The defect's decay is fast and does not exhibit any obvious spectral features. This is unlikely to be related to $NV^0$ due to the slight decrease of its beta at 575 nm, as this would remain constant if they were related.

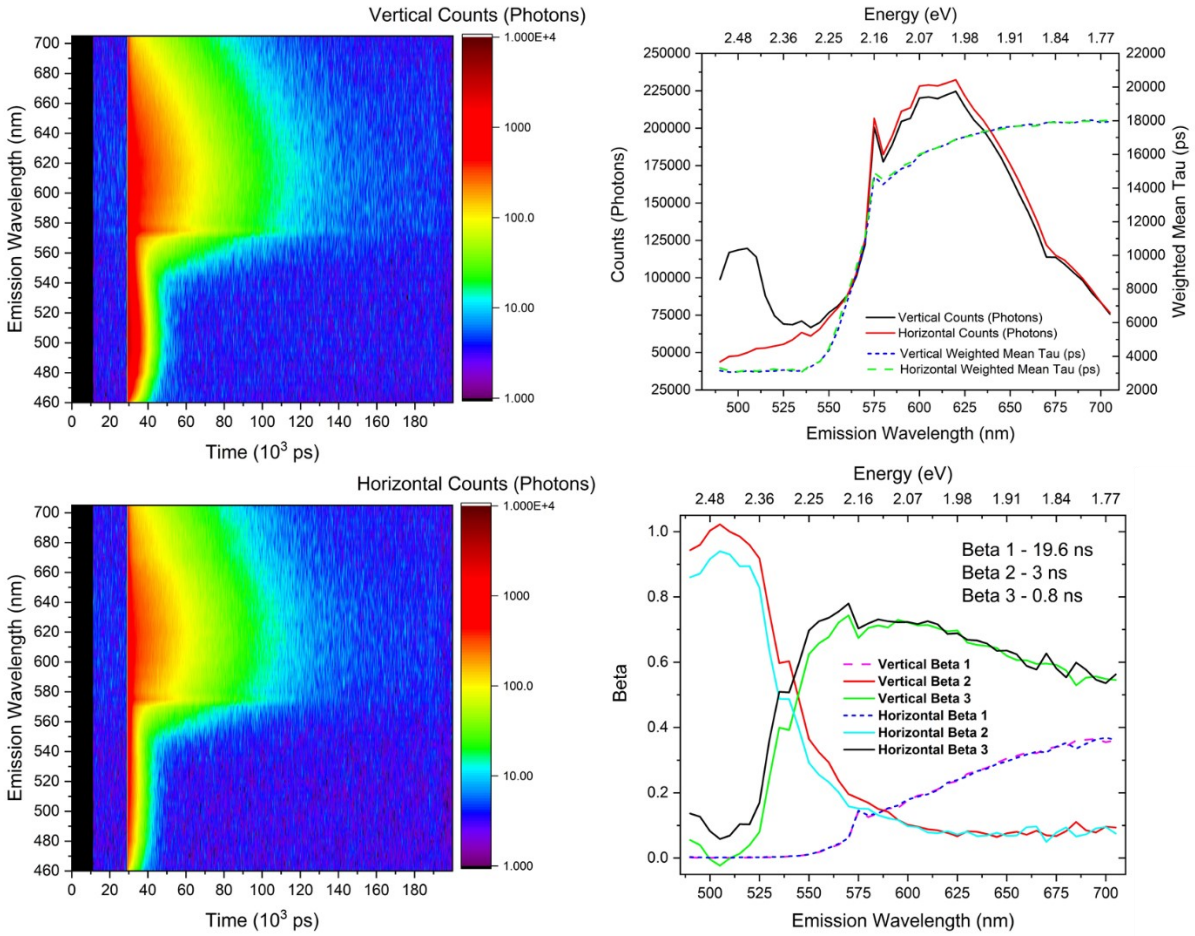



*Figure 29 – Two colour contour plots show the decay information for the horizontal and vertical emission for vertically polarised excitation (375 nm) of a synthetic CVD diamond. Lifetime analysis shows the emission spectra and intensity weighted mean lifetime (tau) as a function of wavelength. A breakdown of the different beta (population fraction) parameters is also shown as a function of wavelength for both polarisation states. This reveals emission from $NV^0$ (Beta 1) with a lifetime of 19.6 ns, and two other unknown components.*

## *Summary*

In this section, a spectrally and polarisation resolved spectrophotometer was used to measure the lifetime of diamond at several emission wavelengths as a function of emission polarisation. This acquisition took in excess of 14 hours to complete, due to the extremely low count rates, resulting in 12-minute integration times per wavelength. This study was important to explore how the technology could be applicable to diamond emission, and if there were any interesting phenomena to be observed. Polarisation of emission can indicate the orientation of the dipoles that cause the absorption and emission processes. These measurements can be used to narrow the potential shapes and orientations of the defects inside the lattice. The methods used in this instrument are applied later using the multidimensional luminescence microscope.

## Multidimensional luminescence microscope

### *Introduction*

Combining the capabilities of the hyperspectral microscope and the time-resolved spectrofluorometer in a single flexible single instrument would be attractive to the diamond and material science communities, due to the capabilities to characterise spatial variations in spectroscopic properties without requiring the movement of the sample between different instruments[170]. This could be useful to identify characteristic signatures of specific diamonds, to evaluate properties of quantum electronic devices based on diamond, to determine the effect of growth condition on defect incorporation, and for basic research. Ideally, such a microscope would offer high (<1 nm) spectral resolution hyperspectral imaging co-registered with (spectrally resolved) lifetime mapping and white-light and birefringence transmission imaging. Excitation should be electronically tuneable, with adjustable excitation and emission polarisation states, and the instrument should be able to switch between line and point illumination. A PMT and monochromator can provide spectrally resolved TCSPC measurements, and FLIM can be realised with stage-scanning.

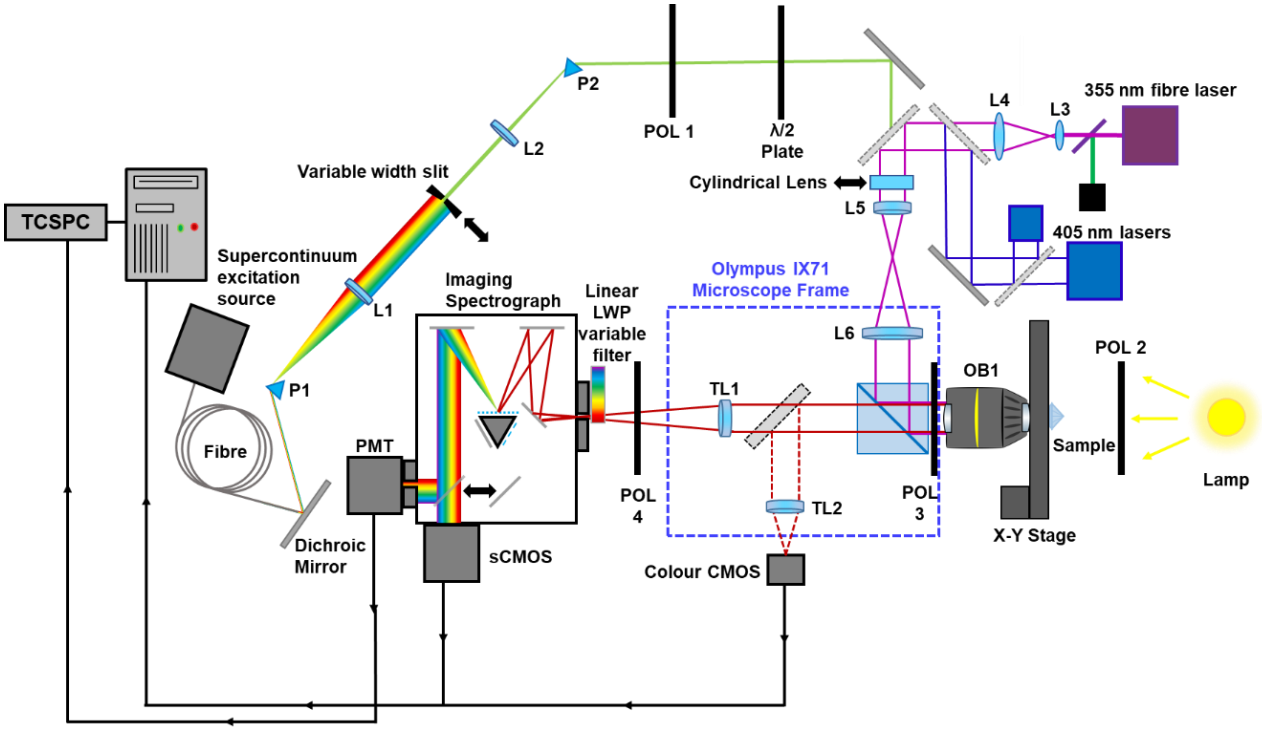



*Figure 30 – A schematic of the multidimensional luminescence microscope, showing the various excitation sources, emission paths, and optical elements. Manual flipper mirrors are used to switch between the different excitation sources. A manual mirror/prism inside the microscope frame (blue dashed box) allows the output to be switched from a colour CMOS camera on the side port of the microscope frame to the imaging spectrograph mounted on its left-hand port. An internal mirror switches the output of the spectrograph between the PMT and imaging ports.*

A system diagram of the developed instrument is shown in Figure 30. Ultrashort pulsed excitation can be provided by a fibre-laser-pumped supercontinuum laser, a pulsed frequency tripled Yb:glass fibre laser providing picosecond pulses at 355 nm emission, or a gain-switched diode laser operating at 405 nm. A CW diode laser at 405 nm is also available. Excitation can be switched from line to point illumination, depending on the experiment, and several objective lenses are available. Emission from the sample can be directed to either a colour CMOS camera or to an imaging spectrograph that can enable hyperspectral imaging or spectrally resolved lifetime measurements. All electronic equipment is connected to a custom-built PC and is controlled through a custom *LabVIEW* program.

The capabilities of the instrument include: -

- White-light transmission imaging – monochromatic or colour
- Imaging through crossed polarisers to map birefringence – monochromatic or colour
- Hyperspectral imaging – high spectral resolution
- Point measurements of emission spectra – including polarisation discrimination and emission lifetime measurements
- Measuring PLE spectra – including polarisation discrimination and lifetime measurements
- Excitation-emission-lifetime matrices
- Spectrally resolved lifetime mapping - FLIM

All of these modalities are co-registered to the same sample stage, allowing imaging and measurement with different modalities and at different magnifications. This provides a powerful tool to characterise unknown samples or devices.

## *Supercontinuum excitation laser source and characterisation*

A key requirement for the instrument was a tuneable ultrashort pulsed excitation source that would enable excitation-resolved luminescence measurements, including excitation-emission-lifetime matrices, to be acquired. Excitation-resolved and lifetime-resolved measurements of diamond luminescence are useful to identify and distinguish a wide variety of emissive defects that each have different absorption bands and luminescence lifetimes. The experiments conducted with this instrument were undertaken at room temperature, which results in large phonon side bands for many defects[19]. This can make the identification of weak, overlapping spectral features challenging. The variation of excitation wavelength can distinguish some of these defects through their PLE spectra. Luminescence lifetime provides a further, sensitive, contrast mechanism.

In this instrument, tuneable ultrashort pulsed excitation is provided by a commercial supercontinuum laser source (SC-400-4, Fianium), which provides picosecond pulsed radiation continuous from ~400 nm to 2350 nm with a total output power of 2 W, operating with a repetition rate of 40 MHz. This supercontinuum laser source uses a pulsed Yb:glass fibre laser from which the output at 1064 nm is focused into a micro-structured fibre to produce strong spectral broadening through a cascade of non-linear optical effects. This radiation is collimated at its optical fibre output using a proprietary optical element. The 3.5 mm diameter output beam is then either directed into a series of four cold mirrors, to remove the IR radiation above 750 nm, or when this light is required, a long-pass (LP) mirror with a cut-off at 1000 nm (DMLP1000, Thorlabs).

After these mirror(s) that remove unwanted infrared components, the collimated beam is directed onto a dispersive Brewster prism (SF10, P1, Edmund Optics). A 400-1000 nm coated achromatic doublet lens, with a 150 mm focal length (50 mm diameter, L1, Edmund Optics) is placed at its focal length from the prism. This causes the ray bundle at a particular wavelength to be focused to the focal plane of the lens and causes the central rays of all ray bundles to become parallel. At the focal plane of this lens, a manual variable-width slit (VA100C/M, Thorlabs) is mounted on a motorised translation stage. The motorised translation stage (TRA25PPD, Newport) has 25 mm of travel, is controlled using a motion control box (ESP300, Newport) and interfaced to the PC using COM port commands, with a positional accuracy of 2.5 µm. After spectral selection by this adjustable slit, the beam continues to another identical lens (L2) and prism (P2) set to reverse the effect of the first two optical elements. The output from this prism-based monochromator is a collimated spectrally-selected beam. Figure 31 shows exemplar spectra of this beam as its centre wavelength is tuned by translating the slit, measured using photon counting detection after the high-resolution grating of the microscope monochromator (SP300i, Acton). The OD blocking for this system is ~OD4 and this measurement is limited by the noise floor of the detector. A prism-based monochromator was chosen over a grating-based system due to the lower loss.

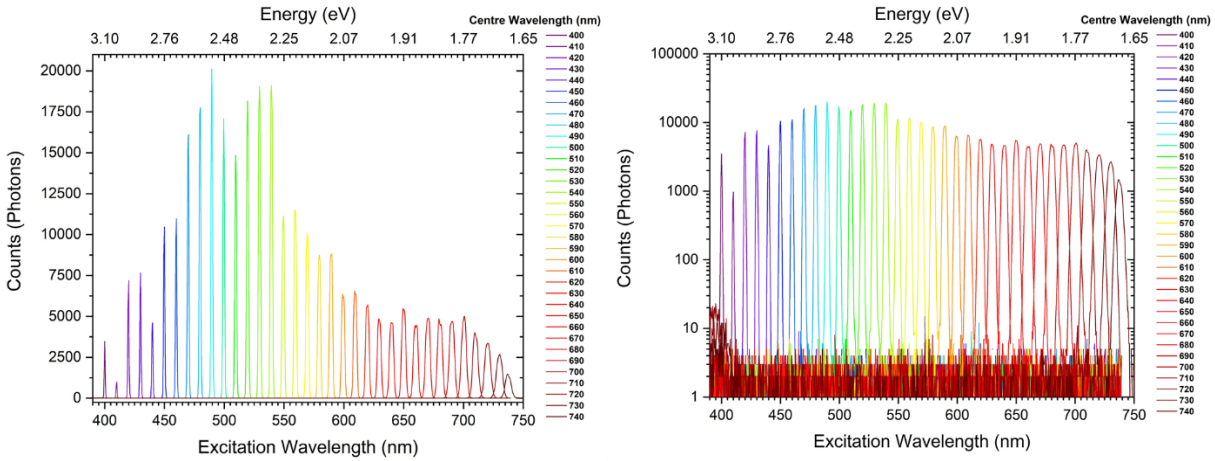



*Figure 31 – Measured excitation source wavelengths from the spectrally selected monochromator. This was measured using the spectrograph's monochromator port with 10-micron entrance and exit slits. (right) is the same graph on a log scale.*

This prism-based monochromator was calibrated using a commercial spectrometer with an optical fibre input (USB2000+, Ocean Optics). A circular, variable ND filter wheel (NDC-50C-4M, Thorlabs) was used to reduce the beam intensity below the saturation level of the detector. The spectral peak is then fitted and the FWHM and peak position determined. The results of this fitting process are shown in Figure 32. With the given accuracy of the translation stage, the centre of the

monochromator's bandpass will deviate by less than the resolution of the detecting spectrometer. A double exponential model was fitted to the data to switch between spatial position on the linear state and central wavelength position.

The spectral resolution of the tuneable super continuum source was measured during calibration by fitting the emission to a Gaussian function. The spectral resolution varies with wavelength as the dispersion of the prism is not constant as a function of wavelength, resulting in a narrower linewidth at the blue end of the tuning range. In addition, the focused spot size at the slit is theoretically smaller in the blue than red, which would reduce the spectral discrimination in the red, but this is partly offset by chromatic aberration of the lenses. The change in spectral width of this excitation source with wavelength is shown in Figure 32. The spectral power density (SPD) of the laser is also not constant with wavelength, noting that typical supercontinuum sources provide more power at the red end of the spectrum compared to the blue end. It is possible to measure the SPD at the output of the monochromator by measuring the output power for a given wavelength (i.e. fixed slit width and stage position) and dividing by the spectral FWHM. The average optical power was measured using a calibrated optical photodiode power meter (S170C, Thorlabs), and the variation of SPD with wavelength is shown in Figure 32.

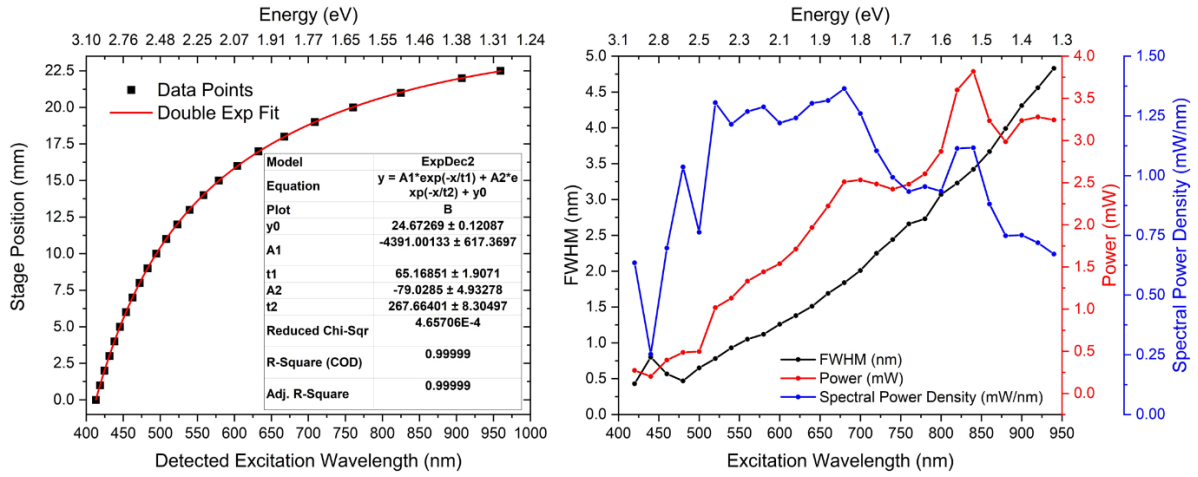



*Figure 32 – (left) The double exponential fit relating excitation wavelength to stage position. (right) Measured FWHM of a fitted Gaussian function to each spectrally selected output. The power and spectral power density are also shown. This data was collected using a USB2000+ spectrometer (Ocean Optics) and a photodiode power meter (S170C, Thorlabs).*

For polarisation related measurements, the polarisation state of the excitation beam needs to be controlled. Supercontinuum sources typically provide beams of arbitrary polarisation state, which can be linear, circular or elliptical at any given wavelength. The losses at the prisms in the

monochromator are also polarisation sensitive, so a broadband linear wire grid polariser (WP25M-VIS, Thorlabs) was used to select linearly polarised light from the monochromator output. A broadband halfwave plate (AQWP05M-600, Thorlabs) mounted in a motorised rotation stage (NSR1, Newport) was used to rotate the linear polarisation state of the output beam.

## *Other excitation laser sources*

Natural diamond is frequently investigated using excitation <400 nm, with the commercial DiamondView™ instrument exciting samples <225 nm (DiamondView™, De Beers)[100]. One reason for this is because many of the common defects in natural diamond emit at wavelengths below 550 nm, and so must be excited at shorter wavelengths. Optical sectioning is also an important aspect of imaging emission, and with DiamondView™ this is achieved by strong absorption (above bandgap) at the surface, ensuring only surface emission.

A frequency-tripled mode-locked Yb:glass fibre laser system, in which 1064 nm laser radiation is frequency doubled to 532 nm, and then mixed with the fundamental radiation to generate laser radiation at 355 nm, provides picosecond pulses at 40 MHz. The fundamental radiation is blocked internally and laser outputs at 532 nm and 355 nm are available. For the work reported here, the 355 nm line is separated from the combined output beam using a 440 nm SP filter (FF01-440/SP-25, Semrock) and the reflected 532 nm light is directed into a beam dump. The average power of the 355 nm radiation can reach 200 mW, but the system is not stable at this power level for which temperature variations of the frequency-conversion-crystal oven can result in significant variations in output power. Typically, the output power was set to 50-100 mW, which was sufficient for the experiments and resulted in lower variation in power. A small optical relay magnifies the beam by 7X, as shown in Figure 30 with L3 (20 mm singlet, Linos) and L4 (150 mm singlet, Linos). Manual flipping mirrors can be used to switch between the laser sources.

Picosecond pulsed laser radiation at 405 nm can be provided from a gain-switched laser diode (LDH-D-C-405M, PicoQuant) for excitation controlled by a versatile driver (PDL-800-B, PicoQuant) that can provide pulses at repetition rates from 2.5 MHz to 40 MHz. The ability to excite diamond samples at repetition rates below 40 MHz is important to facilitate measurements of lifetimes of defects such as N3 (41 ns), which are greater than the 25 ns inter-pulse period of the supercontinuum source or fibre laser. The gain-switched diode laser pulse duration can vary with repetition rate and output power, but is typically adjusted to be <300 ps. As the pulse rate is decreased, the pulse energy stays approximately constant and so the average power decreases proportionately.

For measurements of long (phosphorescence) lifetimes, a modulated CW laser providing up to 100 mW average power at 405 nm (MLD 405, Cobolt) can be used.

## *Illumination optics and steering mirrors*

Similar to the previously described hyperspectral microscope, line illumination is used for push-broom hyperspectral imaging. The previously described optical relay was modified to incorporate best form N-BK7 uncoated singlet lenses, L5 (LBF254-100, Thorlabs), and L6 (LBF254-200, Thorlabs), when the 355 nm excitation laser was used. This was to avoid generating fluorescence in the optical cement typically found in achromatic doublets. For lifetime measurements using TCSPC, the illumination could be switched to point illumination by removing the cylindrical lens, which was mounted on a manual translation stage. As indicated in Figure 30, manual magnetic flipping mirror mounts (Flipper Optic Mount 9891-M, Newport) were used to rapidly switch the excitation beam between the supercontinuum source and the fixed wavelength lasers, with minimal realignment.

## *Emission optics and imaging spectrograph*

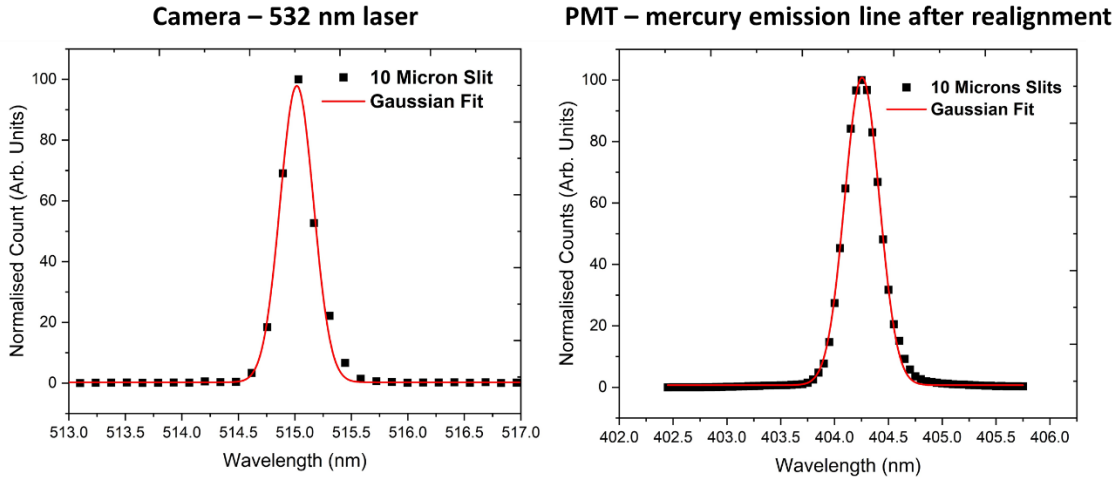
A polarisation analyser is required for fluorescence anisotropy measurements of the emission of diamond defects and other samples. This was an ultra-broadband wire grid polariser (WP25M-UB, Thorlabs) mounted into a removable filter holder (CFH2-F, Thorlabs) that itself was mounted in a rotation mount (NSR1, Newport) after the output port of the microscope frame. A custom-made metal enclosure was designed to block stray light from this emission path and to enable this polarisation analyser assembly to be easily removed when polarisation measurements were not required, such that it could be replaced with high reproducibility of position.

Spectral dispersion in this instrument was provided by a dual imaging spectrograph/monochromator (SP-300i, Acton). This has an entrance slit, with a minimum width of 10 μm and maximum of 3 mm, controlled by a manual micrometre. The optical path in this instrument is incident onto a tri-turret containing two diffraction gratings and a mirror. The two diffraction gratings are a 150 lines/mm low resolution grating, and a 600 lines/mm high resolution grating, both blazed for 500 nm radiation. An electronic flipping mirror located inside the housing can switch the dispersed radiation between the monochromator or imaging port. This allows the sample emission to be used for hyperspectral imaging using the spectrograph functionality, or lifetime-based measurements using a photon-counting PMT at the monochromator output.

***Monochromator port***

The monochromator port has an exit slit, identical to the entrance slit, with a mounting plate to a large-area photon-counting photomultiplier (PMC-100-1, Becker and Hickl) of 8 mm diameter. This detector is responsive from 310 to 830 nm, but the quantum efficiency reduces after 750 nm, and it presents less than 160 dark counts per second (manufacturer specification) when cooled with the integrated Peltier cooler. It is powered by a PCI card (DCC-100, Becker and Hickl), and has an overload protection system for when the incident light rises above a value expected to damage the detector. The IRF of the PMT is <180 ps (manufacturer specification), which is much greater than the pulse duration of the mode-locked fibre laser or supercontinuum source.

The spectrometer system was calibrated using a 532 nm diode laser (CPS532-C2, Thorlabs) and a fluorescent lamp with mercury emission lines. After realignment to ensure the focal plane of the internal mirror was at the exit slit, a spectral resolution of 0.38 nm was measured for the 150 lines/mm grating with the 10 μm slit width, which was close to the expected resolution of 0.4 nm. Typical measurements are shown in Figure 33.




| Model | Gaussian |
|---|---|
| Equation | y = y0 + A/(w*sqrt(pi/(4*ln(2)))) * exp(-4*ln(2)*(x-xc)^2/w^2) |
| Plot | 10 |
| y0 | 0.27306 ± 0.16241 |
| xc | 515.01746 ± 0.00208 |
| A | 36.32666 ± 0.45782 |
| w | 0.34968 ± 0.00495 |
| Reduced Chi-Sqr | 1.77474 |
| R-Square (COD) | 0.99294 |
| Adj. R-Squar | 0.99263 |

| Model | Gaussian |
|---|---|
| Equation | y = y0 + A/(w*sqrt(pi/(4*ln(2)))) * exp(-4*ln(2)*(x-xc)^2/w^2) |
| Plot | Normalized1 |
| y0 | 0.71061 ± 0.16623 |
| xc | 404.25482 ± 0.00112 |
| A | 40.48878 ± 0.28182 |
| w | 0.37997 ± 0.00278 |
| Reduced Chi-Sqr | 1.37721 |
| R-Square (COD) | 0.99818 |
| Adj. R-Square | 0.99809 |

*Figure 33- Two different Gaussian fits showing the monochromator spectral resolution (right), and for comparison, the attainable resolution using the imaging port and an sCMOS camera is shown (left).*

The photon-counting photomultiplier is connected to a TCSPC card (SPC-830, Becker and Hickl) mounted to a PCI slot inside the main computer. An electronic sync signal from the excitation laser in use, derived from an internal detector or signal generator, is attenuated, and amplified to reach the correct voltage for the TCSPC card input. The relative timing between the excitation pulses and the sync signal was adjusted using different cable lengths.

***Spectrometer imaging port***

Two cameras are used on the imaging port of the spectrograph, dependant on the experimental requirements. These are the EMCCD previously described, and a sCMOS camera (Zyla 5.5, Andor). The sCMOS camera has a higher intrinsic (no EM gain) quantum efficiency, smaller pixels (6.5 vs 16 µm), more pixels, (2560 X 2160 vs 512 X 512), and a larger sensor (22 vs 11.6 mm in diameter). The sCMOS camera provides higher spectral resolution due to its smaller pixel size and larger spectral range - for the 150 lines/mm grating, it covers the entire visible spectrum from 400 to 755 nm.

Parameters describing the performance of these cameras for hyperspectral imaging are given in Table 3. Figure 34 shows an exemplar measurement of the spectral resolution for the sCMOS camera acquired using a mercury emission line with the 150 lines/mm grating.

*Table 3 – A table giving the overview of the spectral properties for the imaging port of the spectrograph for the two detectors.*

| Imaging Port<br>Spectral Range (nm) | Andor iXon 887 EMCCD | Andor Zyla 5.5 sCMOS |
|---|---|---|
| 150 lines/mm | 170 | 355 |
| 600 lines/mm | 44 | 85.5 |
| Sampling (nm/pixel) | | |
| 150 lines/mm | 0.344 | 0.139 |
| 600 lines/mm | 0.086 | 0.033 |
| Spectral Resolution (nm) | (10-micron entrance slit) | (10-micron entrance slit) |
| 150 lines/mm | 1 | 0.28 |
| 600 lines/mm | 0.25 | 0.08 |

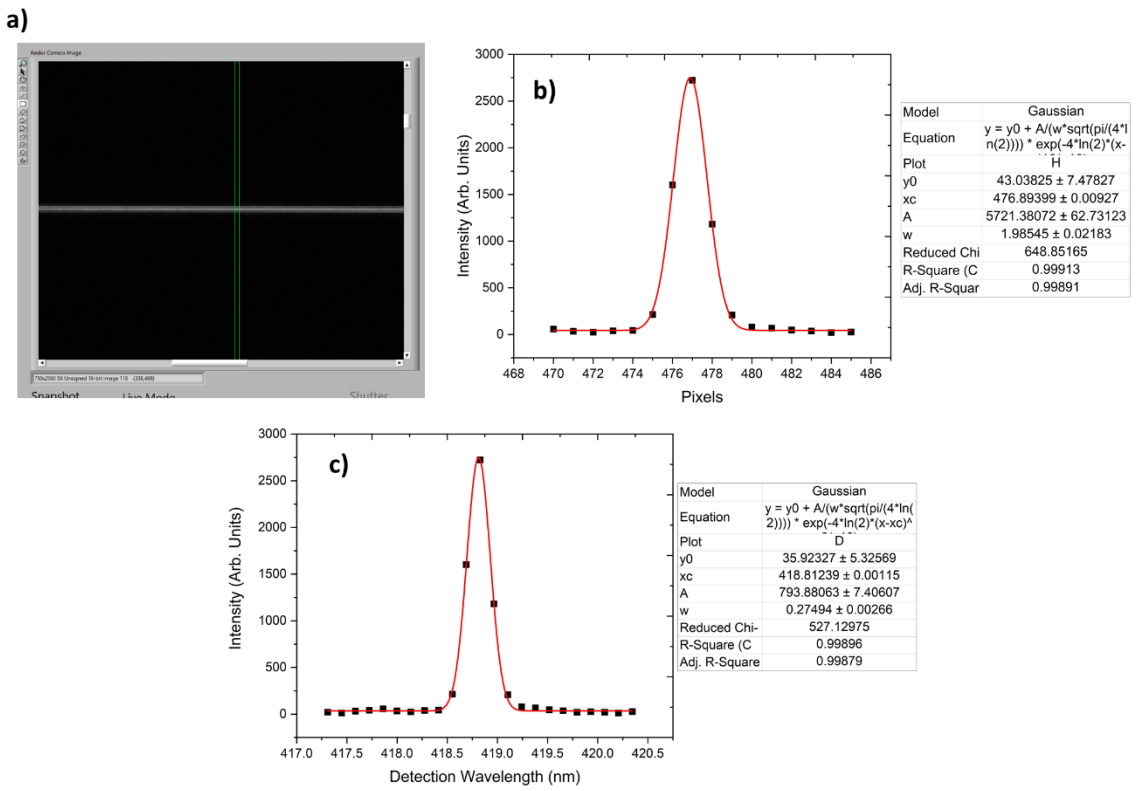



*Figure 34 – a) The camera view of the spectrally dispersed mercury emission line. b) A comparison between the pixel based and c) converted wavelength emission line.*

The spatial-spectral calibration at the imaging port was undertaken by measuring the separation of two narrow mercury emission lines to obtain the dispersion (pixels per nm) from their spatial separation. In addition, a mercury emission line was scanned across the sensor using the internal motor and wavelength readout of the spectrograph. These two measurements were averaged to provide the values shown in Table 3.

This imaging port can be used for push-broom hyperspectral imaging as described previously, where a 2D image of *x*-λ is acquired and the stage is stepped to form a 3D data cube of *x*-*y*-λ.

## Spatial Resolution

The spatial resolution of the imaging port, using the sCMOS camera, was measured using 100 nm TetraSpeck™ beads, which emit over four different wavelength ranges in the visible. These beads were applied to a glass slide with a cover slip and used to measure the spatial resolution of the line illumination for the hyperspectral system. For the spatial resolution, the entrance slit was set to 1 mm. Two line profiles were measured from the image of an isolated bead, one in the *x* and one in

the y direction *y* (parallel and perpendicular to the slit) using FIJI and are shown in Figure 35. An Olympus 100x 0.95 NA objective was used with 500 nm excitation.

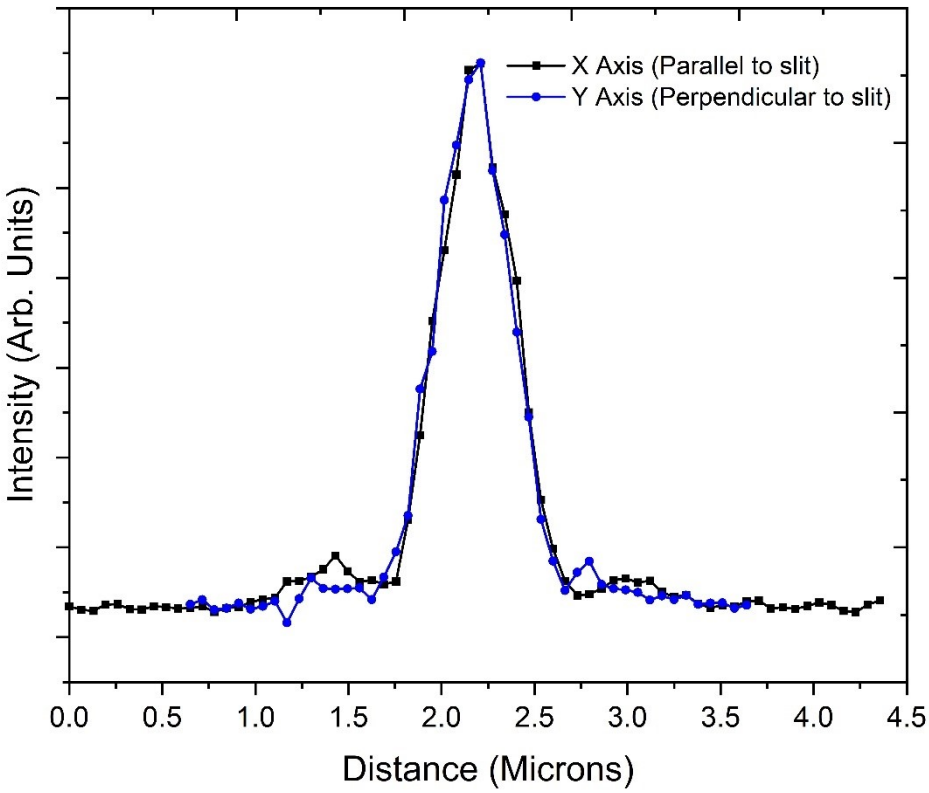



*Figure 35 – A graph showing the line profiles through the image of a single TetraSpeck™ bead under 500 nm excitation using a 100x 0.95 NA objective, detected using the sCMOS camera on the imaging port of the spectrograph. The entrance slit was set to 1 mm.*

A Gaussian function was fitted to each profile, and the *y* axis had a FWHM of 0.459 ± 0.008 µm, whilst the *x* axis had a FWHM of 0.463 ± 0.009 µm. There is some astigmatism present in the system, and the focal point of the bead was chosen so that the object appeared circular, as the 'circle of least confusion'. This means that dependant on the focal position, the resolution in one axis will be greater than in the other. These values compare well against the theoretical limit, which using the Abbe equation is 401 nm. This is calculated from using the emission light wavelength peak of 747 nm. It would be expected that the spatial resolution would be higher perpendicular to the slit when the slit is narrow due to the confocal improvement.

## *Linear variable filter*

To utilise the broad excitation wavelength range, from 355 to 1000 nm, and corresponding emission wavelength range, from 375 to 1000 nm, requires multiple excitation/emission filter cubes. It is also desirable to have a beam splitter that can appropriately direct excitation and emission radiation over a wide wavelength range. One approach is to use a UV fused silica 50/50 power-splitting beamsplitter (BSW26R, Thorlabs) instead of a dichroic beamsplitter, which was adopted for some of the work presented here. This has the disadvantage that only up to 25% of the emission radiation can reach the detector and there is no blocking of the excitation light that would usually be provided by a dichroic beamsplitter – typically up to OD2. Any reflected or scattered excitation light must therefore be blocked by the emission filter and this needs to be matched to the excitation wavelength as the supercontinuum is tuned.

In this instrument a linear variable long wave pass filter (3G LVLWP, Delta Optical Thin Film) was incorporated in the emission path that provided a means to block the tuneable excitation radiation. An image of this LNLWP filter is shown in Figure 36 a). It has an out of band suppression of >OD3 and is tuneable from 310 to 850 nm, covering much of the excitation spectral range. The filter was mounted inside a machined metal arm, which slotted inside a plate mounted in front of the entrance slit to the spectrograph. Mounting the filter close to the focal plane of the tube lens is important to minimise the spatial extent of the beam since the spectral transmission of the filter varies along its length. A 100 mm travel translation stage (UTS100PP, Newport) is used to move the filter in and out of the spectrograph mount.

Calibration of the filter was performed by measuring the fluorescence from several plastic slides (Chroma), every 1 mm along the linear filter. The cut-on wavelength was determined as the wavelength at which the fluorescence from the plastic slide is transmitted through the filter as shown in Figure 36 b). A linear relationship between the stage position and cut-on wavelength was then obtained shown in Figure 36 c). The application of this tuneable excitation/emission capability is illustrated in Figure 36 d) for the fluorescent plastic slides. A minimum wavelength interval of 20 nm between excitation and emission cut-on wavelength is required to block the excitation light - and this must be increased when highly sensitive TCSPC measurements are undertaken, noting that the blocking of >OD3 plus OD0.3 (from the 50/50 beamsplitter) is less than the typical OD6 plus OD2 blocking that would usually be realised with a dichroic beamsplitter and emission filter. It is important to consider the blocking of the spectrometer which also factors into measurements.

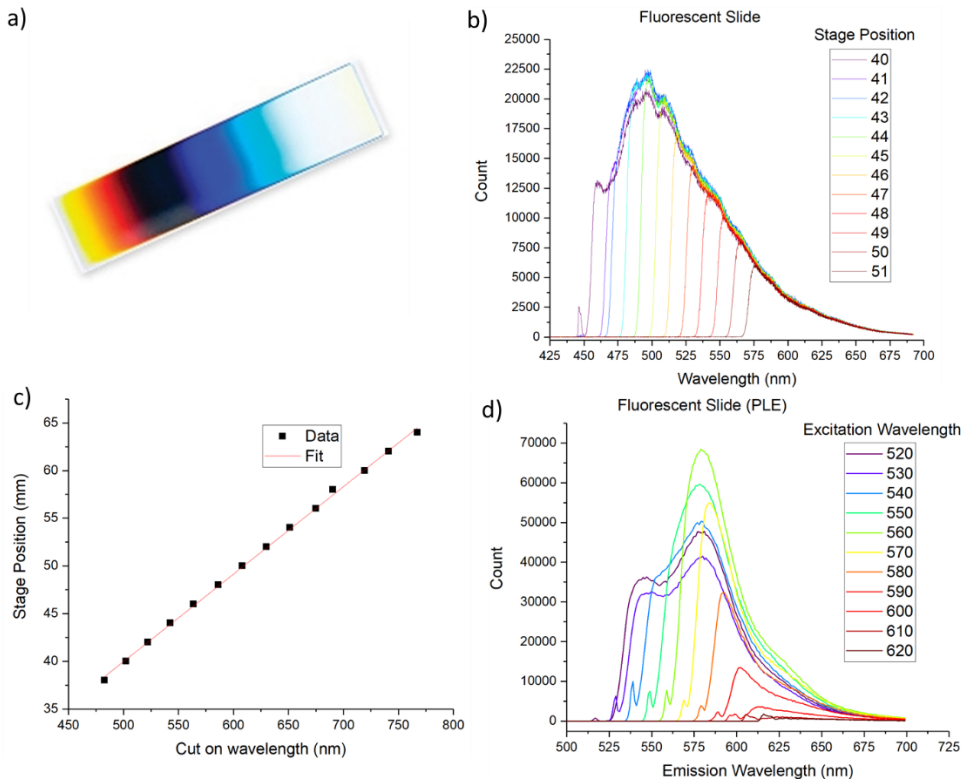



*Figure 36 – a) is an image showing the linear variable filter[171]. Emission from a fluorescent slide at various cut-on wavelengths is shown in b), with given stage positions in mm. Graph c) shows the linear fit between cut on wavelength and stage position for the linear variable filter. Graph d) is an example set of emission spectra at different excitation wavelengths for the same fluorescent slide.*

## *Side port colour camera*

A colour camera for ROI finding, calibration, and focusing was used on a secondary port of the microscope frame. This CMOS (Chameleon 3 Colour, Point Grey) camera can provide full FOV images and can be used for the white-light transmission and crossed polariser imaging, of which examples are shown in Figure 37. This is the same sample previously shown in Figure 26 and Figure 27.

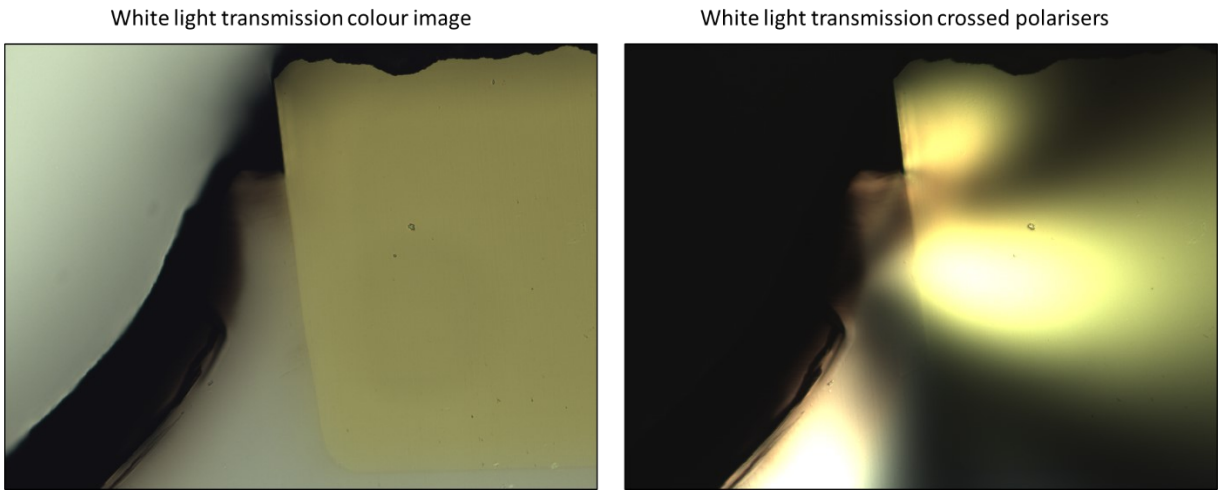



*Figure 37 – Two colour images showing white-light transmission (left) and birefringence (right - obtained using crossed polarisers) of a monocrystalline diamond sample. In these images, the HPHT diamond is the yellow substrate, and the CVD diamond is the region grown around it. A dark region to the left of the sample shows non-$SP^3$ carbon.*

## *LabVIEW interface and experimental methods*

A *LabVIEW* program was written to provide a single interface to control the different imaging modalities and enable acquisition of correlated images of the same FOV. *LabVIEW* was chosen due to the availability of drivers and software development kits (SDKs) for many of the instrument components and its potential for expanding the instrument capabilities. This allowed, for example, TCSPC measurements to be easily implemented in the *LabVIEW* program. The main interface screen is shown in Figure 38.

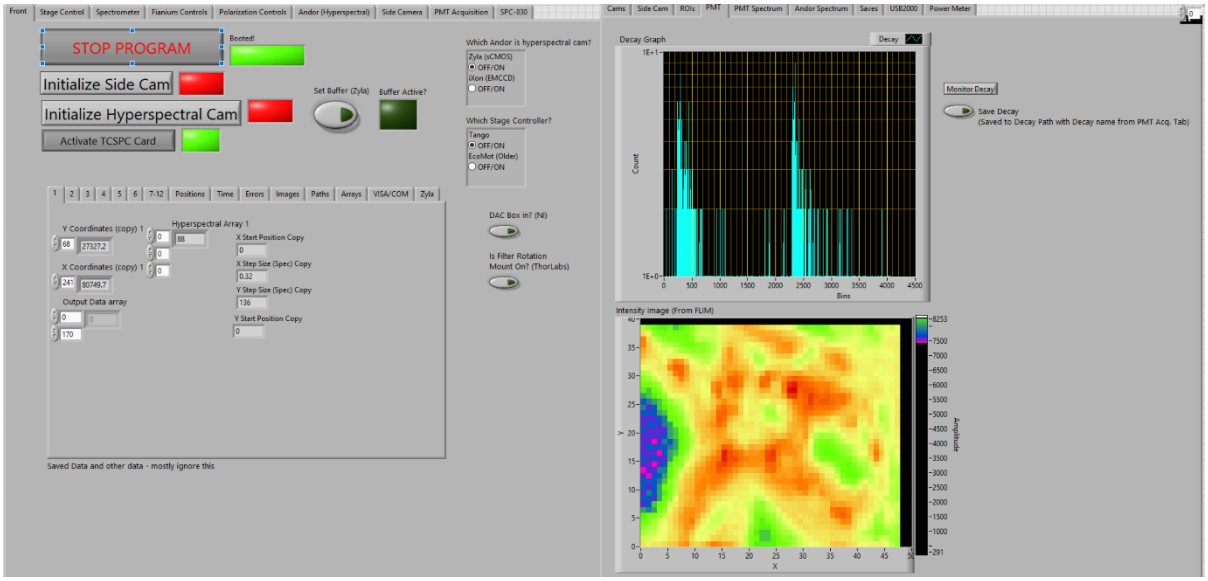



*Figure 38 – The main LabVIEW interface screen, showing the split sections and multiple tabs. The tabs on the right are used to view acquired data, and the tabs on the left are used to modify settings and start acquisitions.*

The program is designed so that the tabs on the left can be used to edit settings for the imaging port camera, PMT, side camera, spectrograph and TCSPC card, including options such as integration time, wavelength range and file saving locations. The spectrograph panel, which allows the spectrograph and linear variable filter to be controlled is shown in Figure 39.

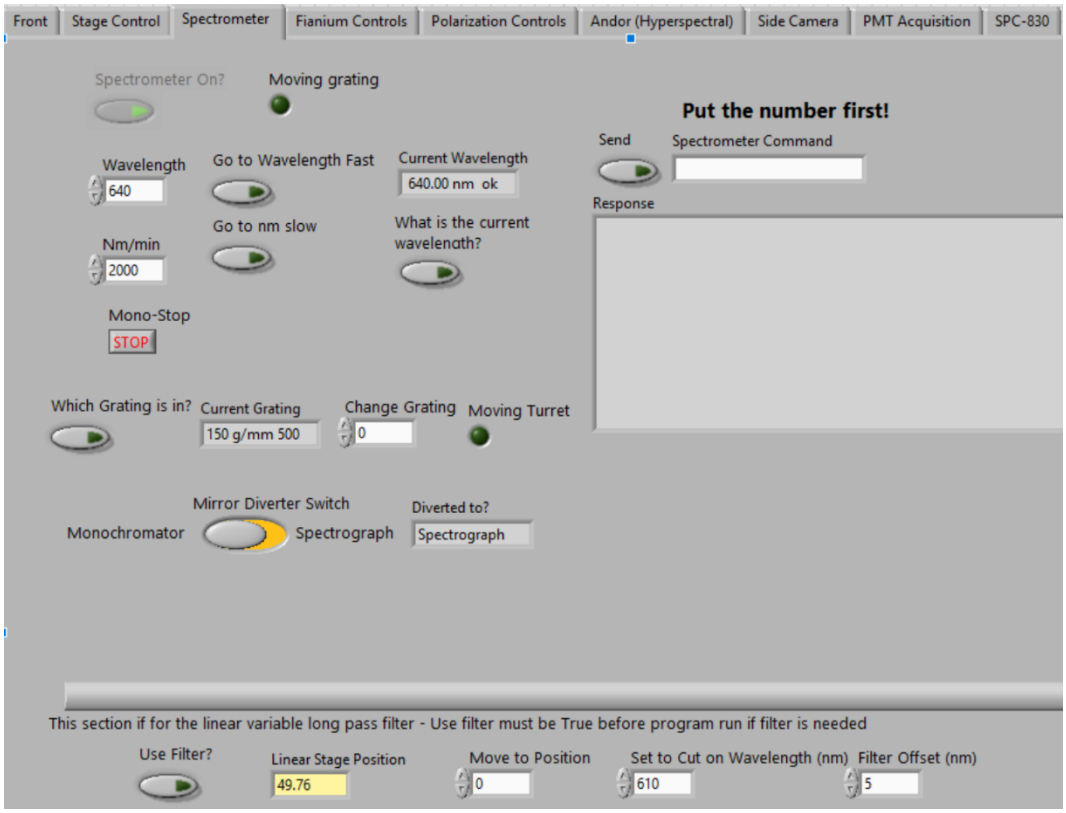



*Figure 39 – This shows the interface for controlling the spectrometer and the linear variable filter. Wavelengths can be set for the monochromator, which corresponds to the central wavelength on the imaging port.*

Single point luminescence decay profiles can be recorded inside the *LabVIEW* program and saved to text files with the relevant timing information. This is typically performed for testing purposes or IRF measurements. Single point spectral measurements can also be recorded using the monochromator. The imaging port of the spectrograph can also be used to acquire spectra from line/point excitation that can be scanned to acquire push-broom hyperspectral image data. An example of which is shown in Figure 40. Due to the significant RAM required to store a hyperspectral image data cube in *LabVIEW*, pixel spectra cannot currently be extracted whilst the program is running. This analysis is instead performed post-acquisition using 'FIJI'.

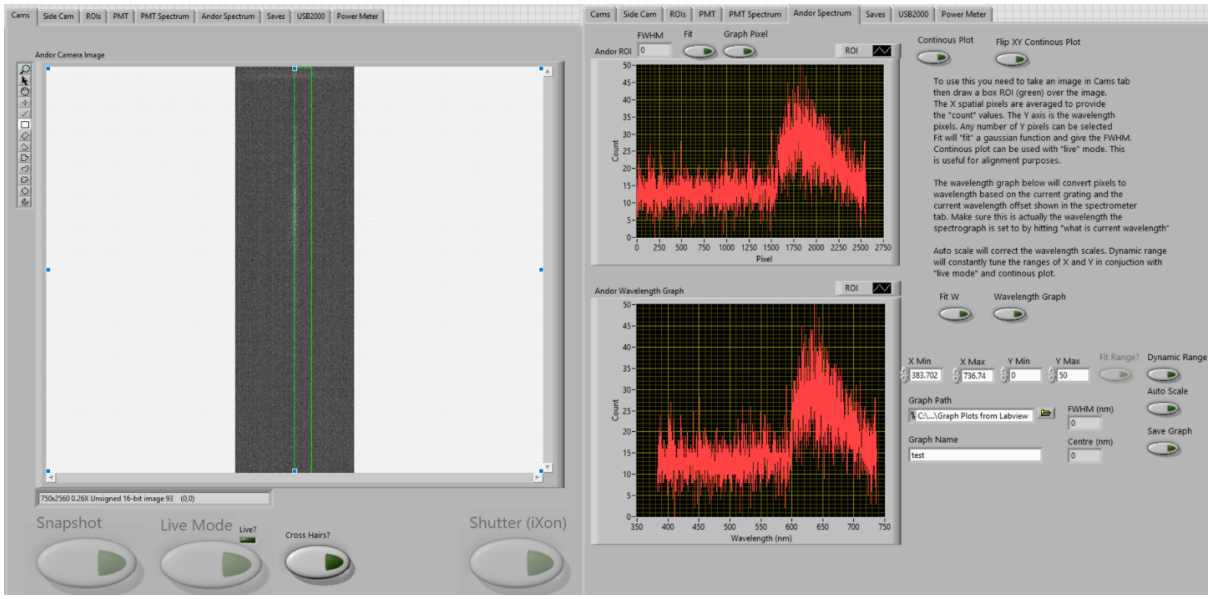



*Figure 40 – Images from the imaging port can have ROIs selected through them, and the spectrum can be extracted, as shown on the red plots (right). This allows spectral features to be identified for targeted spectral analysis by hyperspectral imaging or spectrally resolved FLIM.*

A typical experiment could start by identifying the ROI on a sample using the white-light transmission image acquired by the colour CMOS camera and then acquiring the corresponding hyperspectral image data. A rapid scan can be initially undertaken to determine the optimum integration time to use the dynamic range of the camera, or a test measurement can be taken instead, of a single line. Typically, the samples do not vary in brightness significantly across a FOV and so the latter method is often used, as it is faster. Testing the brightness of the sample over an FOV can be performed rapidly using the side mounted colour CMOS camera. The step size is automatically adjusted, based on the selected objective lens, to provide spatial resolution, but this can be manually modified. The stage setup screen is shown in Figure 41.




*Figure 41 – User interface for the stage controls. This includes step size variations for use in hyperspectral imaging and FLIM, start and end positions for all imaging, and the ability to save and recover spatial positions. The step size for hyperspectral imaging is linked to the magnification and is set by changing the current objective.*

Different objective lenses will image an FOV with different centre positions, resulting in images which are not co-registered. This has been calibrated for three different objective lenses, so the spatial axes on the stage are adjusted by an appropriate amount for experiments at different magnifications.

Camera settings can be modified in the tab shown in Figure 42. Where options are not available (such as '*EM gain*' on the sCMOS camera) they are greyed out. When the correct settings have been chosen, the number of steps should be calculated, and the results displayed with an estimated time to complete the image data acquisition. When the '*Proceed?*' light is green, the '*Acquire*' button becomes available, and this will start the acquisition. The progress bar 'Saved' will report progress of the image acquisition until it is complete.




*Figure 42 – Control interface for the imaging port of the spectrograph, allowing starting wavelength, hyperspectral re-slicing, and hyperspectral imaging acquisitions to be started. Some options are not used, based on the camera currently in use, which is set on the front panel. Another set of tabs provides information for specific cameras.*

If the '*Do Hyperspectral Reslicing*' command is true, then the data is re-sliced to provide a stack of images, which is available to view in the ROI tab shown in Figure 43. Hyperspectral binning is used to spectrally bin the data. A spectrally binned version of the images can be viewed by scrolling through '*Hyperspectral Slice*', and the current wavelength of the image is also available in the ROI tab shown in Figure 43. A summed intensity image is also calculated and displayed.

After this data is acquired, an ROI can be drawn (currently only as a square/rectangle), and the pixel positions are mapped to stage positions. These values can then be used for further hyperspectral measurements, or FLIM.

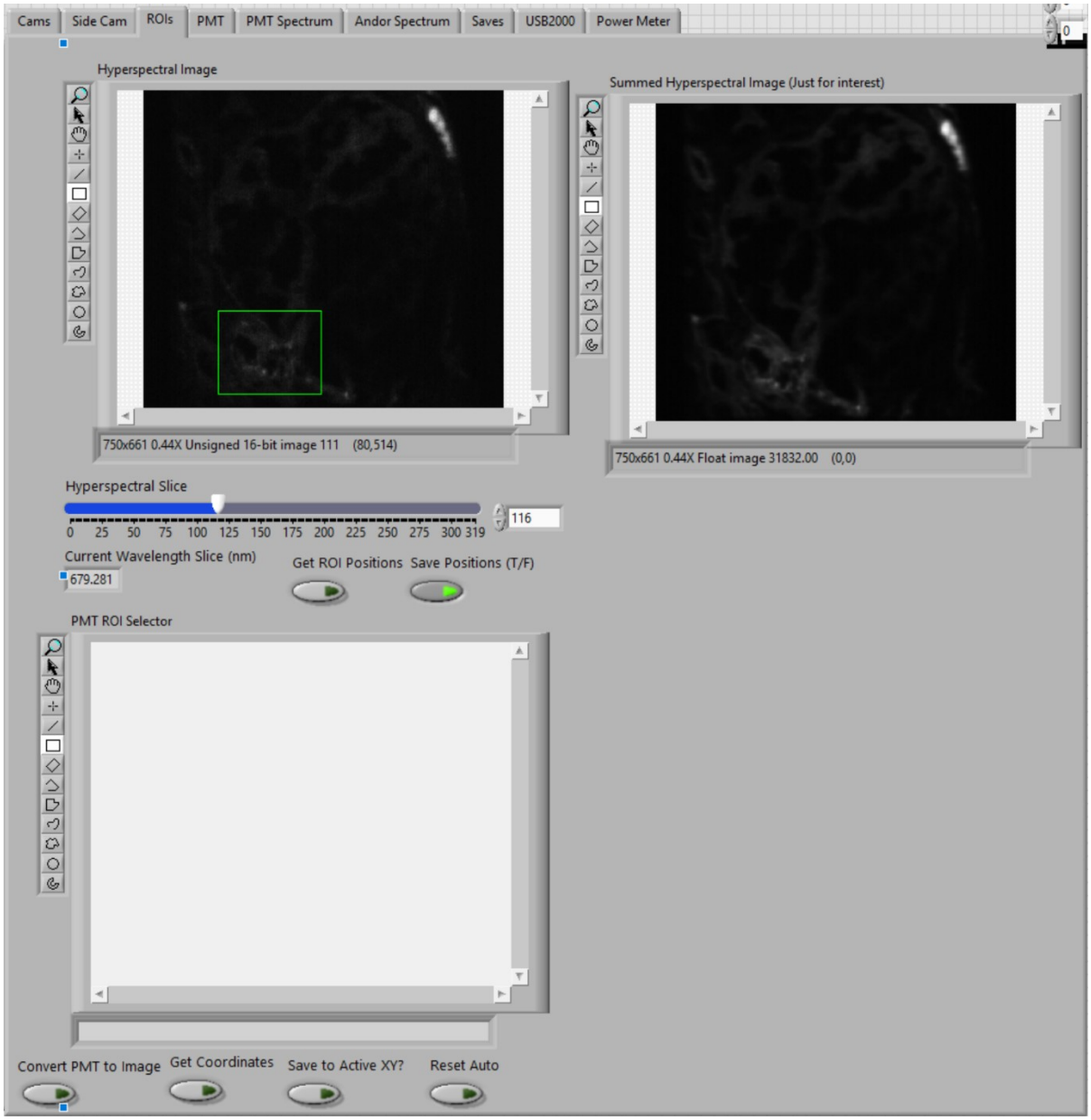



*Figure 43 – This panel controls the ROI view from the hyperspectral imaging and PMT images. The hyperspectral slice bar can be used to switch between the different binned spectral channel images.*

The user interface controlling the PMT on the monochromator port is more complicated, as shown in Figure 44. Some key parameters such as the sync rate of the TCSPC card, wavelength options for the monochromator, and saving locations can be modified/viewed on this tab.

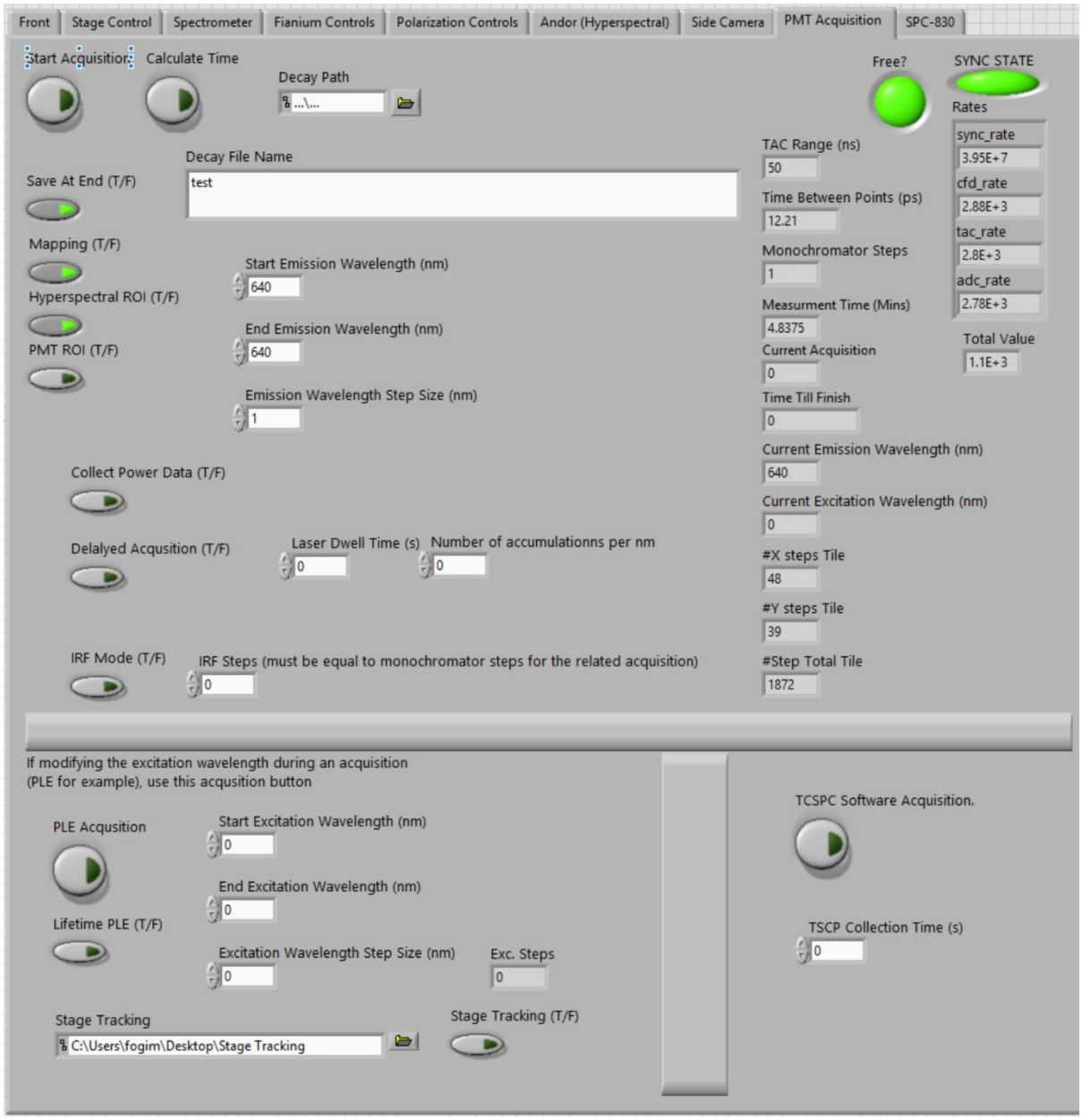



*Figure 44 – The PMT control tab allows the start wavelength, end wavelength and 'resolution' (practically this is the wavelength step size) to be set, and acquisitions started. There are many experiments, which can be performed using the PMT, and they are broadly split into static and variable excitation wavelength acquisitions. If 'Mapping?' is true, then the acquisition will use the spatial information in the 'Stage Control' tab to acquire an image. If this is not selected, point-spectrally resolved decays are acquired instead. Measurements which involve the variation of excitation wavelength require the 'PLE Acquisition' button in the bottom left section of the interface.*

In the current example, an ROI for hyperspectral FLIM has been selected for which the starting and ending wavelength of the FLIM map can be adjusted (currently in fixed wavelength steps). The total measurement time is estimated when the 'Calculate Time' button is pressed. This is based on the

number of steps for the FLIM, the single pixel integration time and the estimated time for stage translation. The integration time for a single TCSPC measurement is adjusted in the tab shown on Figure 45. Similar to the hyperspectral imaging, FLIM images can be used to select an ROI and the stage positions recovered so that different experiments can be conducted on that ROI on the sample. This is the 'PMT ROI Selector' box in Figure 43. The PMT can also be used to acquire simple point scanning intensity measurements, yielding higher spatial sampling but longer image acquisition times than using the camera.




*Figure* 45 *– This tab controls all the parameters the LabVIEW program can modify for the TCSPC card. The most important options are the TAC range, Collection Time (s), and CFD settings. The SYNC frequency divider setting can be changed from 1 or 2, to switch between measuring one or two periods.*

A lifetime mapping acquisition (FLIM) entails sequentially collecting photons with TCSPC for a defined pixel integration time at a series of locations using the scanning stage. The results of the scan in progress are displayed on the '*PMT'* tab along with the last measured decay profile, as shown in Figure 46.

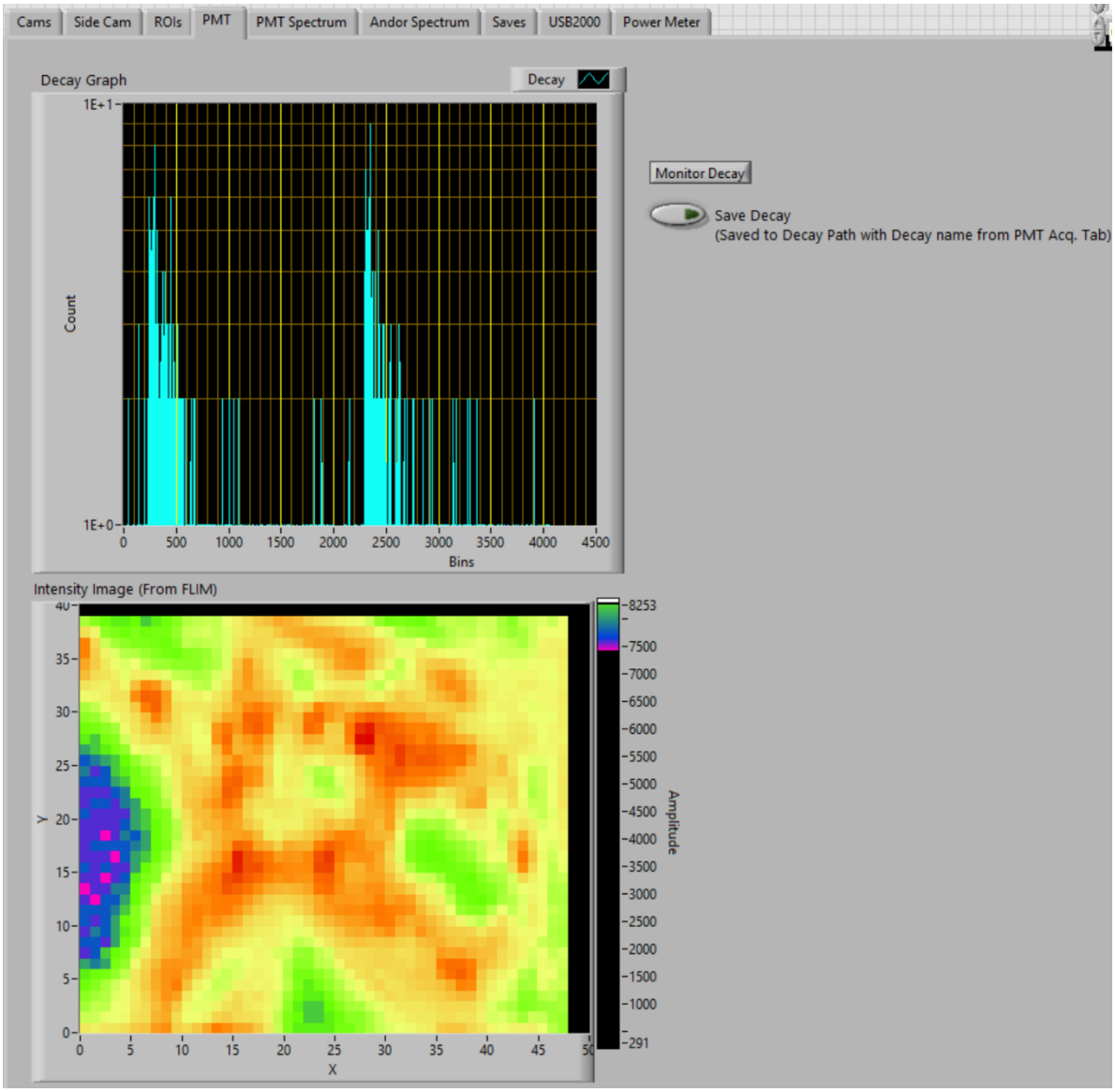



*Figure 46 – Fluorescence decays from the TCSPC card are shown on the top graph, along with the current mapped total intensity from the PMT tiling acquisition. Monitoring the current decay information (using 'monitor decay') is used to measure the IRF for single excitation wavelength applications.*

After this measurement is completed, a new ROI can be chosen, or a spectrum at a specific location can be acquired, according to the specific goals of the experiment.

The *LabVIEW* interface can also control the polarization stages, a USB2000+ spectrometer and a power meter. The power meter control is important for acquiring the excitation spectral power density (SPD) at the sample plane for calibration.

## *Long-lived luminescence measurements*

The TCSPC card used in the system can use macro timing for long-lived decays, which have a lifetime >1 µs. This capability can be expanded to measurement on timescales of seconds, enabling measurements of phosphorescence and other long-lived luminescence processes.

These macro time measurements are made by generating a square signal (from a signal generator) and modulating a CW laser (405 nm, Cobolt) with this signal. The same signal is also input into the TCSPC card and this is used in the FIFO mode, which records the arrival time of a photon in addition to its timing from the square pulse specific events[44]. The TCSPC card CFD must still be synced to a fast repetition source; in this case the sync from a 40 MHz 405 nm laser (PicoQuant) and driver was used. A flow diagram is shown in Figure 47.

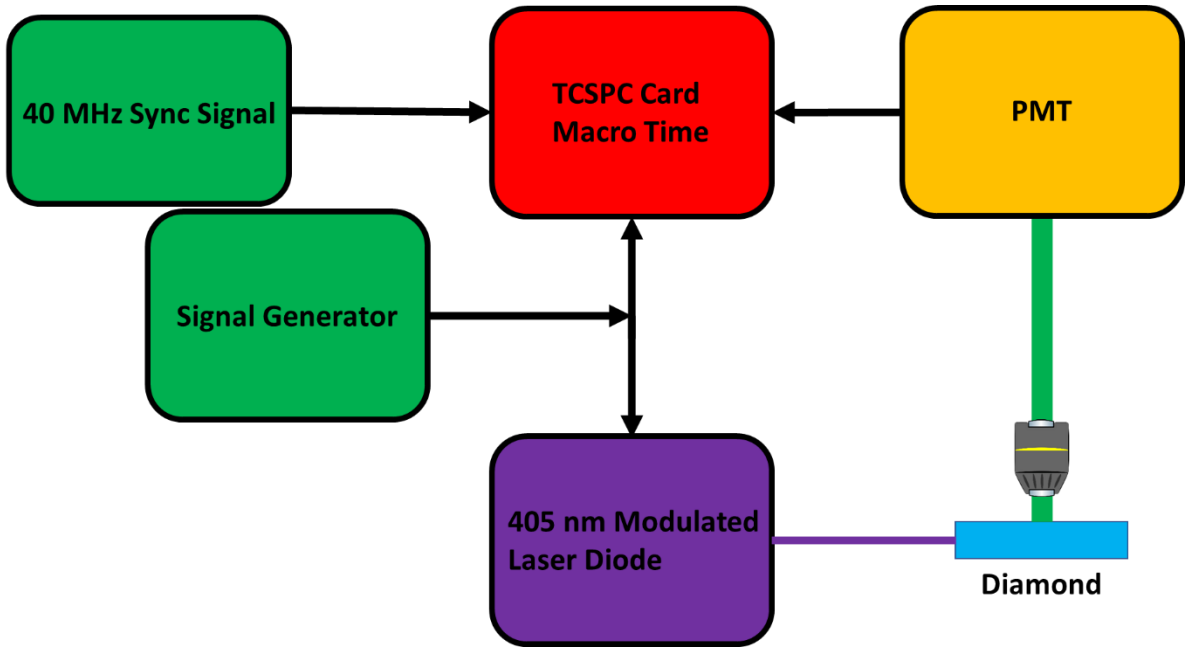
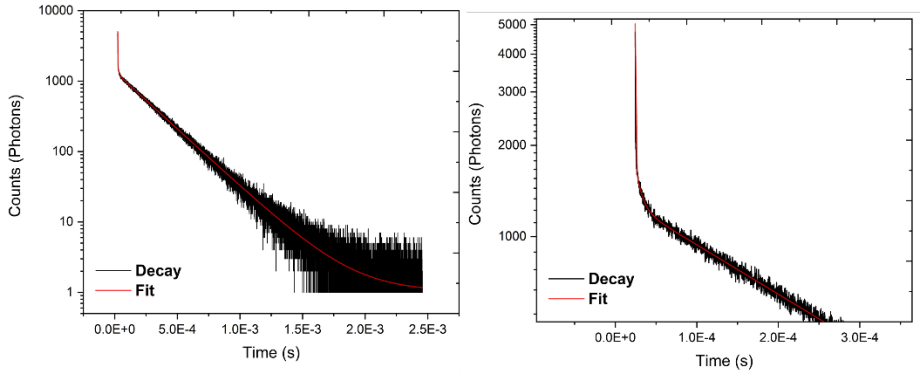



*Figure 47 – Flow diagram showing the components and signal paths used for long lifetime luminescence measurements.*

A natural diamond suspected to contain nickel was studied using this capability of the instrument. The monochromator was set to an emission wavelength of 520 nm, and the CW 405 nm laser (Cobolt) was modulated at a repetition rate of 179 Hz with a 3 ms pulse duration. A 50 s integration

time was set, and the resultant emission decay profile was fitted to a triple exponential decay model, for which the results are shown in Figure 48. The rising part of the data has been removed from these plots.




| Model | ExpDecay3 |
|---|---|
| Equation | y = y0 + A1*exp(-(x-x0)/t1) + A2*exp(-(x-x0)/t2) + A3*exp(-(x-x0)/t3) |
| Plot | B |
| y0 | 1.03544 ± 0.13801 |
| x0 | 1.63944E-5 ± -- |
| A1 | 2.8179E11 ± -- |
| t1 | 4.32786E-7 ± 3.15636E-9 |
| A2 | 1284.76103 ± -- |
| t2 | 2.66374E-4 ± 2.48491E-7 |
| A3 | 1440.99557 ± -- |
| t3 | 7.43097E-6 ± 1.10294E-7 |
| Reduced Chi-Sqr | 170.02572 |
| R-Square (COD) | 0.9977 |
| Adj. R-Square | 0.9977 |

*Figure 48 – An example long-lived luminescence decay from a natural diamond at 520 nm emission and 405 nm excitation with a fitted triple exponential decay model. The rising part of the data has been removed from these decays.*

There are three components to this luminescence decay: a 432 ns component ($\tau_1$), a 266 µs component ($\tau_2$), and a 7.43 µs component ($\tau_3$). The IRF should be measured and convolved with the model to fully account for its effect. The 432 ns component is thought to originate from the IRF of the system, as the IRF was not included in the fitted model used here. The lifetime of 266 µs is close to the reported lifetime of the NE3 defect, which would be expected to emit in this spectral band[19]. The 7.43 µs component could be emission from another defect in the sample with a long luminescence lifetime or could be due to phosphorescence from an optical element. Analysis of the rising edge of the data (not shown) indicated that the 7.43 µs component does not originate from the IRF. The exact origin of this component would require more analysis, such as emission wavelength variation, which was not carried out on this sample.

This long-lived luminescence decay measurement approach can be expanded to lifetime mapping, which allows the data to be fitted in the same way as for FLIM. This requires information about the stage position to be synced to the TCSPC card, and this presented several problems, which were not

solved within this thesis. Furthermore, the pixel dwell times would be significant, resulting in very long image acquisition times for high spatial resolution.

It would be possible to combine ps/ns lifetime measurements with this long-lived luminescence lifetime measurement, to simultaneously study emission on both time scales. This would require a MHz picosecond laser that could also be modulated on slower timescales, either through direct drive current modulation or using an external modulator such as an acoustic-optic modulator.

## Hyperspectral data analysis

Hyperspectral image data entails image data sets for which an emission spectrum is acquired for each image pixel. The analysis and visualisation of such hyperspectral image data is challenging because of its multidimensional nature. While it is sometimes possible to display 3D or even 4D data using three graphical axes and contours or colour scales, this is only easily applicable for sparse data sets, such as 3D surfaces (*x*-*y*-*z*), e.g. the contour plot of a mountain. In hyperspectral imaging, the 3D data volume (sometimes described as the *x*-*y*-*λ* "data cube or hypercube") is more challenging to visualise on a static 2D display. Attempts have been made to show a cube of hyperspectral data, where one face shows the 2D *x*-*y* image, and the axial faces show the spectral variation[172]. However, this only provides spectral information about the periphery of the 2D *x*-*y* images. Hyperspectral data lends itself better to dynamic data analysis/visualisation, such as a "fly-through" animation, or active data manipulation.

One method, which was used in this thesis, is to represent the spectral profile with a single number such as the mean wavelength, the median wavelength or the spectral width. However, this clearly does not present all the information present in hyperspectral image data[173]. A colour scale can be used to represent the average wavelength, allowing a 2D image to be plotted. The relative intensity of the signals in the image pixels can be encoded in the 2D plot of hyperspectral image data, e.g., by encoding the integrated pixel intensity in the image brightness. This has been applied in this thesis by summing/integrating the intensity across all wavelengths and modulating the image brightness of the colour by intensity. Full spectral profiles associated with specific regions of interest on such images can be recovered from the full hyperspectral image data set, although this may not be required for many applications. For this thesis, hyperspectral imaging was primarily used to identify specific emission bands of interest for lifetime and spectrally resolved lifetime measurements.

'FIJI' (ImageJ) can be used to display and interrogate 3D image data stacks where the *z*-axis can be used to encode the spectral profiles in each pixel. These data can be viewed, resliced/re-ordered to

form *x-y* images at every λ, or the data can be viewed as a colour plot and then the ROI function can be used to extract spectral profiles corresponding to specific averaged areas (ROIs). This is useful to identify or characterise specific luminescence features in diamond, e.g. to compare ZPLs and emission bands with known emitting species in the sample.

## *Median wavelength plots and images*

In this thesis, the method used to display hyperspectral image data was to plot the median wavelength of each pixel, either directly or encoded in the hue channel, for a hue-saturation-brightness (HSB) colour image. In the latter case, the median wavelength encoded by hue can be complemented by encoding the spectrally-integrated image intensity, i.e. summing the data cube along the wavelength dimension, with the brightness channel. The saturation channel is set to the maximum value for all pixels. This will be referred to as an intensity-modulated plot of median wavelength.

The median wavelength image was determined by first calculating the summed intensity value at each x-y location and then dividing this value by two. The cumulative sum in the wavelength dimension of each x-y pixel's spectrum was then calculated and the location in pixels in the wavelength dimension at which this reached the value calculated in the first step was returned. This resulted in a pixel coordinate which can be converted to actual wavelength by Equation 17, giving the median wavelength:

$$\lambda = \lambda_{\text{offset}} + (\Delta\lambda \times \text{pixel})$$

*Equation 17 - where λ is the wavelength, $\lambda_{\text{offset}}$ is the starting wavelength, Δλ is the wavelength per pixel (nm/pixel), and pixel is the pixel number acquired from the above process.*

This median wavelength image can be plotted, e.g., to highlight specific regions of interest that may not be discernible in the dimmer regions of intensity-modulated plots. The median wavelength values were encoded to hue by rescaling the median wavelength range to fit on the hue scale. The hue scale is a 360° colour wheel, and this means that the two ends at 0 and 255 (for the 8-bit scale conversion) are red. In this thesis, only hue values in the range from 0 to 210, starting in red and ending in purple, were used to ensure no repeating colours. For some plots, the start and end wavelength positions were adjusted for display purposes to enhance contrast in specific regions, with the resulting range then being rescaled over the hue value range (0 to 210). This is useful where it is desirable to display small changes in median wavelength.

The image data analysis was performed using FIJI using its HSB stack, image mathematics, and maths functionality. An average background value was subtracted from the raw x-*λ* images. The

background was determined by averaging over a large dark region of a single *x*-*λ* image. The dark regions on the hyperspectral images result from a fixed internal rectangular aperture in the spectrograph imaging port, which is used to block off-axis light, and their brightness values are similar to those for a completely dark sample. Calculations of median wavelengths and hue values were performed in a custom written *LabVIEW* program.

## Luminescence decay analysis

There are several methods for luminescence decay analysis, of which a common implemented method uses iterative nonlinear least square fitting of lifetime data collected from a time-resolved measurement to a model of discrete exponential decay profiles[44]. Phasor analysis was also investigated as a viable, fast, fit-free method to analyse the complex emission decays observed with diamond samples, particularly natural diamonds. These two techniques can be used together synergistically, e.g., the outputs of phasor analysis can inform the initial guesses of nonlinear iterative fitting.

### *Nonlinear iterative fitting to discrete exponential decay models using FLIMfit*

Iterative fitting of luminescence decay data can provide various parameters to represent a decay profile and is used by many commercial instruments for luminescence lifetime measurements, such as those from Becker and Hickl[44], Horiba, and PicoQuant. In this thesis, an in-house developed software package called *FLIMfit*[174] was used to iteratively fit spatially varying luminescence data to models with up to five discrete exponential decay components. The software was developed by *Sean Warren*[11], and uses maximum likelihood estimation (MLE) to iteratively fit exponential decay models to the experimental data. *FLIMfit* can analyse either single decay profiles, or lifetime image data. This program implements a convolution of the IRF with the chosen decay model to account for the IRF in the measured decay. Spatially varying IRF data can also be used, which is primarily intended for wide-field time gated imaging techniques using gated image intensifiers. The spatially-varying IRF functionality was used in this work for the excitation-emission-lifetime measurements. *FLIMfit* can also take account of the impact of luminescence decay profiles extending beyond the excitation pulse period, allowing for decay components with lifetimes on the order of, or longer than, the excitation pulse period to be fitted. For more detailed information of this program please see[11, 174].

Parameters that can be extracted from fitting luminescence decay data to discrete exponential decay models include initial intensity ($I_0$), lifetime ($\tau$), population fraction (also described as beta ($\beta$)), mean lifetime and intensity-weighted mean lifetime, and the fitting error parameter, $\chi^2$. The $\chi^2$ parameter is usually normalised such that an average value of 1 corresponds to the data agreeing with the fit model to within the noise on the measurement. Further information about the validity of the fit model can be obtained by calculating the normalised residuals (normalised difference between the experimental data and the model) and ideally should be randomly distributed about zero. In general, as the decay model becomes more complex it is necessary to have experimental data with higher signal to noise (i.e. more detected photons) in order to achieve reasonable estimates of the fit parameters. Due to the complex decay profiles observed in diamond, 10,000 collected photons were generally the minimum goal for data collection, and in practice, the photon counts often exceeded 100,000. This resulted in long experimental acquisition times, especially for mapping spatial variations in lifetime, but this does not adversely affect diamond as it would a biological sample for which photobleaching and phototoxicity would present challenges.

Any iterative fitting software requires initial "guesses" to start the process. *FLIMfit* can generate its own reasonable initial guesses through a quick (iterative with a fixed number of iterations) analysis of the decay data, although a starting value is always needed, which is set to a default value of 2 ns. For relatively simple decay profiles from common (biological) fluorophores with only a few exponential decay components, this approach is usually adequate. However, more complex decay profiles, or profiles with similar lifetime components, can be incorrectly fitted if the initial guesses are not sufficiently accurate. As described below, phasor analysis of the luminescence decay data can be used to acquire reasonable values for this purpose.

During the work reported in this thesis, hyperspectral imaging was frequently performed to identify the emissive defects in the sample, and then literature values for their lifetime components could be used to provide the initial guesses where they are known. While this was useful for most defects, the emission of several of those defects studied here can be quenched, sometimes resulting in significant reductions in lifetime compared to their natural (unquenched) values. It is then necessary to find the best values for the parameters of the fitting model through trial and error, testing additional lifetime components if they can be justified, or modifying lifetime values. In this process it can be useful to fix lifetime values, where known, and allow others to vary to attain more accurate fitting for a given signal to noise ratio. Alternatively, phasor analysis can be used to provide the initial guesses.

## *Phasor analysis*

Phasor analysis was originally applied to analyse frequency domain lifetime measurements[175,176] and was subsequently applied to TCSPC lifetime data[177]. The key advantage of phasor analysis is that it is model-free, relying on a transformation of periodically sampled experimental decay data. This means that no 'a priori' information or assumptions are required about the sample[178]. The complexity of some of the decay profiles presented by diamond luminescence challenged the conventional iterative fitting approach to lifetime analysis, and so phasor analysis was used to inform the fitting procedure. All phasor analysis was conducted using a custom-written MATLAB script.

### ***Theory***

Phasor analysis requires a periodically sampled data of complete lifetime decay profiles, which can be provided by TCSPC measurements or frequency domain lifetime measurements. Equation 18 and Equation 19 are used to calculate real and imaginary coordinates (G and S respectively) for a phasor plot. This has been described by G. Weber[179] and D Jameson et al[180]. In this thesis, only experimental TCSPC data has been collected, and so phasor analysis will be described from that basis. The exponential decay from TCSPC is converted to real and imaginary components by the following equations[175, 179]:

$$G = \frac{\int_0^\infty I(t)\cos(\omega t)\,dt}{\int_0^\infty I(t)dt}$$

*Equation 18*

$$S = \frac{\int_0^\infty I(t)\sin(\omega t)\,dt}{\int_0^\infty I(t)dt}$$

*Equation 19*

The angular frequency (ω) is related to the laser frequency (or repetition rate) by Equation 20[181]:

$$\omega = h2\pi f = \frac{h2\pi}{T}$$

*Equation* 20 - *where h is the harmonic (typically only the 1st harmonic is used), f is the pulse repetition frequency of the laser, and T is the time between laser pulses (pulse period):*

This can be adapted for lifetime image data (x, y) using the equations:

$$G(x,y) = \frac{\sum I_{(x,y)}(t)\cos(\omega t)}{\sum I_{(x,y)}(t)}$$

*Equation 21*

$$S(x,y) = \frac{\sum I_{(x,y)}(t)\sin(\omega t)}{\sum I_{(x,y)}(t)}$$

*Equation 22*

Phasor analysis can also be used to help separate different spectrally emitting species to enhance contrast between different emitters[182]. In the work reported in this thesis, the technique was applied to excitation-emission-lifetime matrices for the first time, to the best of our knowledge.

For a monoexponential decay with lifetime τ, the G and S coordinates can be described by the following equations, obtained by analytically solving Equation 18 and Equation 19[181]:

$$G = \frac{1}{1+(\omega\tau)^2}$$

*Equation 23*

$$S = \frac{\omega\tau}{1+(\omega\tau)^2}$$

*Equation 24*

There are two lifetime parameters that are generated by phasor analysis: the modulation lifetime and the phase lifetime. They can be calculated using the equations[183, 184]:

$$\tau_{modulation} = \frac{1}{\omega}\sqrt{\frac{1}{(G^2 + S^2)} - 1}$$

*Equation 25*

$$\tau_{phase} = \frac{1}{\omega}\frac{S}{G}$$

*Equation 26*

For a monoexponential decay, the modulation and phase lifetimes are equal. For a more complex decay, the modulation and phase lifetimes will be different, and these lifetime values can be considered as 'average' lifetime parameters when representing the emission of complex decay profiles.

The IRF of the system must also be accounted for in phasor analysis. The specific IRF decay profile for the instrument can be mapped to co-ordinates on a phasor plot using the same equations as for the emission lifetime data. To account for the IRF, the emission lifetime points on the phasor plot are rotated and scaled using the equation[185]:

$$G_{\text{corrected}} - iS_{\text{corrected}} = \frac{(G - iS)}{(G_{IRF} - iS_{IRF})}$$

*Equation 27 - where $G_{IRF}$ and $S_{IRF}$ are the converted IRF coordinates.*

## Universal circle

One of the primary advantages of phasor analysis is the graphical representation of the lifetime data using the G (real) and S (imaginary) coordinates displayed on a phasor plot. This can enable direct visualisation of lifetime contrast, e.g. from different regions from the sample, with no assumptions or fitting of the decay data. All monoexponential lifetimes exist on a semicircle, from ∞ lifetime at (0,0), to 0 lifetime at (1,0). This is known as the "universal circle" and can be appreciated by comparing Equation 23 and Equation 24 to the equation for the circumference of a semicircle[186]. An example phasor plot showing three monoexponential lifetimes is shown in Figure 49. The

monoexponential lifetimes are not uniformly distributed around the universal circle, with longer lifetimes becoming more closely spaced as you move along the universal circle towards the origin.

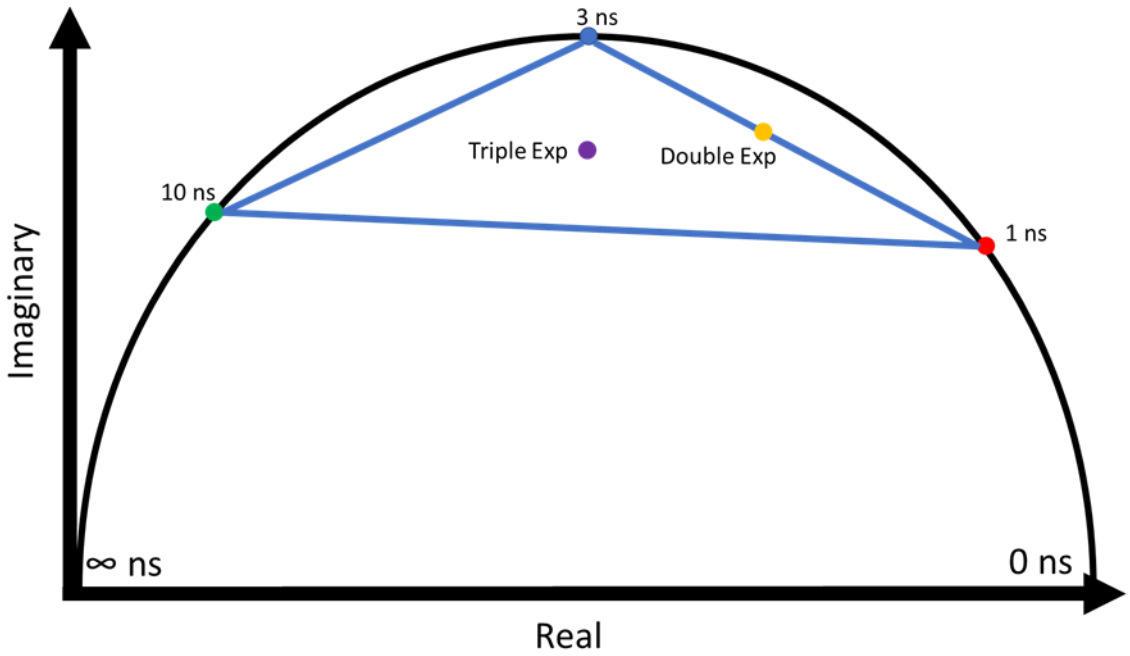



*Figure 49 – Phasor plot of the real and imaginary components from the converted decay. The semicircle represents a continuum of monoexponential lifetimes from 0 (1,0) to ∞ lifetime (0,0). Several data points are shown, with 1 ns (red), 3 ns (blue) and 10 ns (green) monoexponential decay lifetimes (assuming a 80 MHz laser repetition rate). The yellow point presents an emission decay profile with a mixture between the 1 and 3 ns lifetime components and so should sit along a chord between the two lifetime components on the universal circle. A purple data point representing a mixture of all three lifetime components should sit in a triangle between the 3 component lifetimes on the universal circle.*

More complex decays should appear inside the universal circle. A complex decay from two emitting species, presenting two lifetime components, would result in points plotted on a chord between the two component lifetimes on the universal circle according to the relative proportion of each lifetime component in the emission[187]. This is illustrated in Figure 49, where the yellow dot represents a combination of the 1 ns and 3 ns lifetime components. Plotting experimental (double exponential decay data) data from multiple pixels that present a range of different mixtures of the same lifetime components would result in a line (or linear cluster) on the phasor plot that could be extrapolated to its intersection with the universal circle to determine the component lifetime values. A decay with three components would exist inside a triangle formed between the three component lifetimes on the universal circle, as illustrated by the purple dot representing a mixture of lifetime components (10 ns, 3 ns, and 1 ns) in Figure 49. More complex decays would be represented by higher polygons,

from which it becomes increasingly difficult to estimate the native lifetime components from a point cloud of multiple measurements[188].

If the experimental data results in a cluster of data points in the phasor plot with no clear shape, it is difficult to determine the component lifetimes, as the points could result from a large (potentially infinite) number of possible component lifetimes. In this case, measurements at higher harmonic excitation frequencies may be useful to help unmix the lifetime components. Alternatively, it may be possible to vary the spectral emission and excitation wavelengths to provide additional contrast and more points on the phasor plot. This latter method has been utilised in the work reported in this thesis.

Since each point on the phasor plot corresponds to a specific pixel (i.e. location on an image) or to a spectral component, selecting regions of interest on the phasor plot can be used to spatially segment the image data by plotting the corresponding image coordinates. In biological applications this can be useful for identifying specific labelled features, or other sources of contrast. For analysis of diamond luminescence, it can be used to separate different concentrations of defects and indicate regions of quenched luminescence. This approach has also been used to separate CVD and HPHT diamond luminescence based on the lifetime of the emitting defects.

***Background contributions to the measured signals***

Any background signal will appear as a long-lived lifetime component – both in phasor analysis, and when using iterative fitting methods. For phasor analysis the background 'pulls' the data points towards ∞ lifetime (0,0). Background counts from the PMT were no more than 160 cps, and the signal was considerably larger by several orders of magnitude for most of the decay data presented in this thesis. Therefore, this did not need to be taken into account. However, for some experiments there was a significant background contribution to the signal due to a long-lived (much greater than the inter-pulse period T) fluorescence/phosphorescent component. This was removed by averaging the first 50-200 bins of the measured decay profile, just before the onset of the excitation pulse, and subtracting that value from the signal in each temporal bin[189]. This background could vary spatially or spectrally, and so this was calculated on a per pixel or per spectral bin basis.

The disadvantage of this subtraction method is that for longer-lived luminescence components, that would normally not decay fully in the excitation pulse period time window, the part of their decay profile overlapping the next excitation period would also be subtracted. This reduces the apparent

lifetime of that long component. In such cases it would be desirable to use an independent measurement to determine the background value.

Phase lifetime is less impacted by background photons than modulation lifetime. This is because the angle (or phase) of the phasor data points does not change with a constant background signal. However, the modulus, or length of the line from (0,0) to the data point does decrease with increasing 'background' photon counts. This can affect the measured modulation lifetime. Therefore, if the background due to dark counts is significant, or there is a long-lived lifetime component, phase lifetime is more indicative of the actual luminescence lifetime. However, the phase lifetime offers a lower accuracy than the modulation lifetime for longer components.

***Incomplete decays***

The Fourier transform of the decay requires all the data points to be collected in the frequency range, with equally spaced periodic sampling. If this is not the case, then it manifests as a distortion to the universal circle. Practically, the infinite lifetime point of the universal circle moves from the origin (0,0) to a location above, and the whole universal circle is distorted, with an example of this shown in Figure 50. The change in ∞ lifetime position is indicated by the black arrow. In TCSPC, a full decay is not always measured due to limitations with the electronics, and so ~5% of the total period is lost, and this is usually distributed to the beginning and end of the decay period[44].

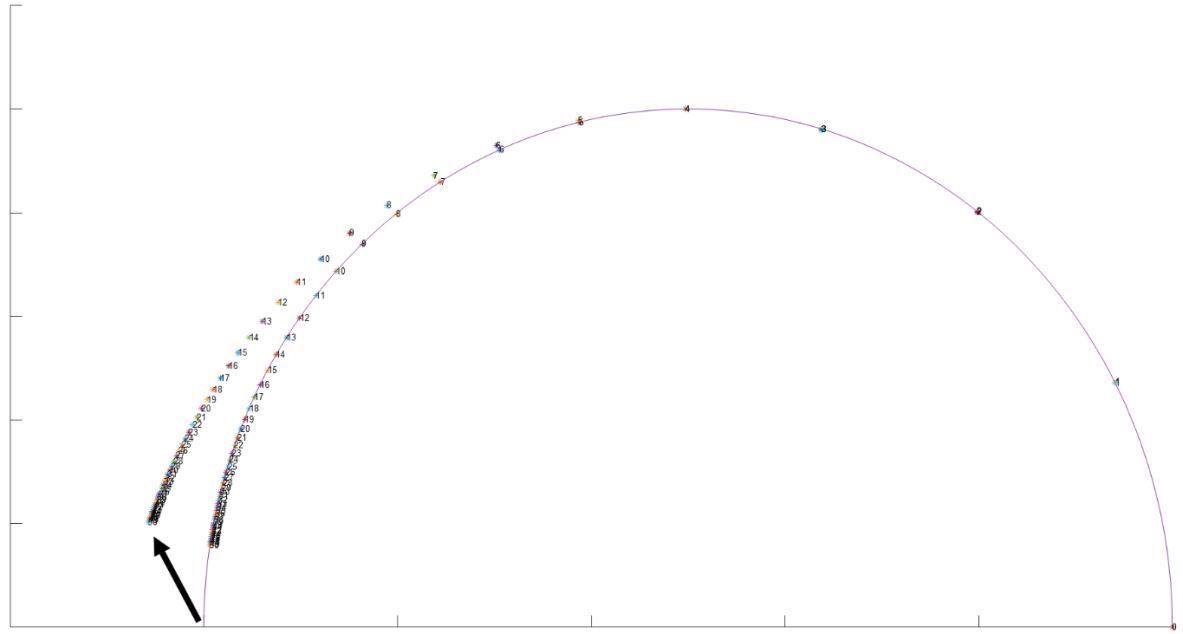


*Figure 50 – The above figure shows a standard universal circle, and the distorted universal circle which originated from missing decay data in the time period T. The black arrow represents the moving of the ∞ lifetime origin point.*

One solution to the problem is to extrapolate the missing data from the recorded decay data, thereby generating a complete decay profile. This requires modelling the decay profile and filling in the missing values from the model – which compromises the advantage of phasor analysis being model-free. For lifetimes longer than ~25% of the excitation pulse period, the decay profile will be detectable in the following excitation period, making the problem more complex[181].

A second approach to this challenge involves changing the angular frequency equation to account for a new period. This would modify the equation to be[181]:

$$\omega_{\text{modified}} = \frac{2\pi}{T_2 - T_1}$$

*Equation 28 - where $T_1$ is the starting time of the decay, and $T_2$ is the end time of the decay.*

This approximation can reduce the impact of the missing data, as described in the thesis of *Romain Laine*[181], but does not address the problems arising from longer lifetime components.

For the work reported here, our approach was to try to experimentally obtain a fully sampled decay profile and not compromise the phasor analysis. This was achieved setting the frequency divider on

the TCSPC card to acquire luminescence decay data over two consecutive excitation pulse periods for each TCSPC histogram (of length 2T). Within this 2T sampling period, two incomplete decay profiles are measured, missing the beginning of one decay and the end of the second decay. From this data, one complete decay with no missing data over the full period T can be measured. Previously this approach has been implemented[44] by shifting the TSCPC data collection window so that one complete decay is measured in the centre of the two excitation laser periods, which results in a loss of approximately half of the detected photons.

Since most of the full decay profile is measured, we wanted to use the majority of the photons. As shown in Figure 51 a) the time window for the TAC was shifted so most of the lost data was at the end of the 2T period.

The time difference between the peaks of the two decays was measured and the starting bin of the second decay is identified at a time equal to the measured excitation pulse period after the first useful time bin of the first decay. The second decay profile is then overlaid onto the first decay profile, as shown in Figure 51 b). After the missing data has been identified, the first decay is treated as the 'master' full decay as it contains all the decay information in the laser pulse period T. The last correct bin on the second decay is identified manually and the corresponding data from the first decay is substituted to replace the missing data at the end of the second decay, as shown in Figure 51 c). These two decays are then summed to yield one complete decay over the full laser period with no missing data, as shown in Figure 51 d).

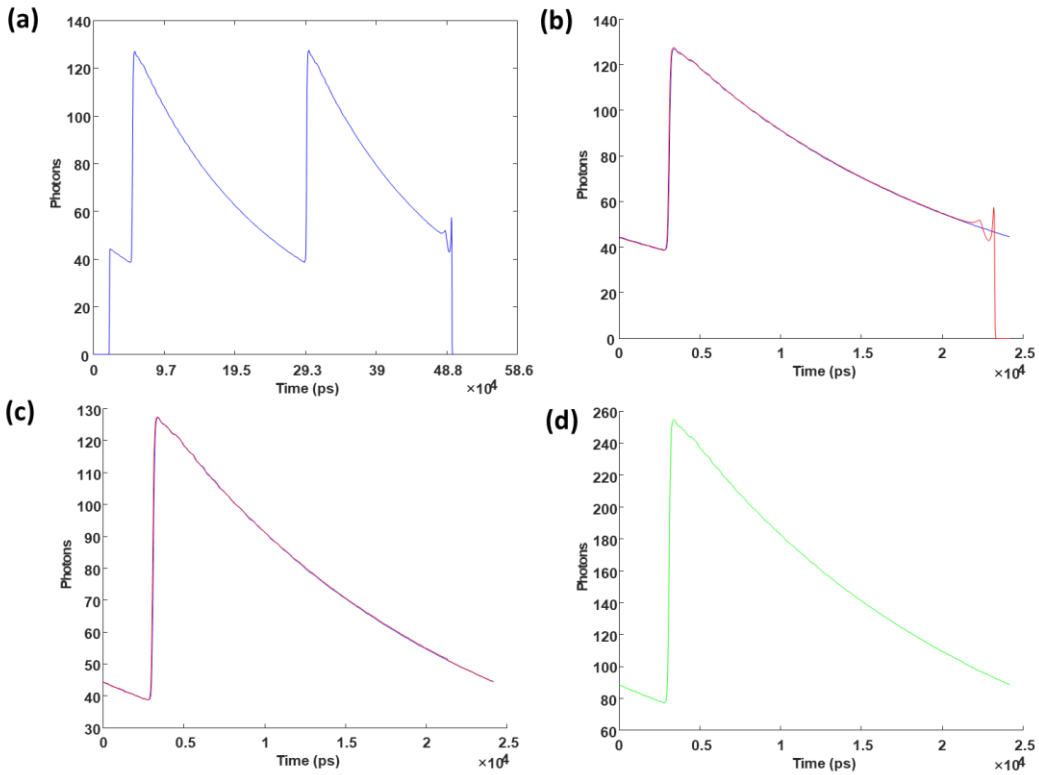



*Figure 51 -A set of four graphs showing the progression of the solution to the missing data. Graph a) shows the two decays, each with a 25 ns period, over the collection time. Note the missing data at the start and near 50 ns due to the limitations of TCSPC electronics. In b) the two decays have been moved to overlap each other over an individual pulse period of 25 ns. The incorrect and missing data is shown at the end of the red decay. In graph c) this missing/incorrect data has been removed and replace with a duplicate from the first blue decay. The decays are summed in d) to produce the green profile.*

There are several disadvantages to this method. Since the missing data only exists in one of the measured decay profiles, the associated errors/noise is multiplied by two, along with the signal. However, this part of the decay profile is less important than the region near the IRF and make a small contribution due to the reduced photon count. A further disadvantage is that the timing precision (bin width) is half the maximum precision of the instrument, as this is directly related to the period measured. However, the temporal resolution is usually limited by the IRF rather than the temporal binning precision. The advantages of regaining nearly a full decay of useful photons, outweighs the disadvantages and allows phasor analysis to be applicable to TCSPC data, including for samples presenting long lifetimes.

The following example shows data which was collected without accounting for the missing decay data, and also illustrates the impact of background subtraction. In Figure 52, point-emission spectrally-resolved data is shown from a natural diamond sample excited at 405 nm and at a

2.5 MHz repetition rate. For the top row figures, the colour scale denotes the emission wavelength for the phasor plots. The universal circle has been significantly distorted and the circle shown is that of the new modified circle caused by the missing decay data[181]. This modified universal circle was generated by modelling monoexponential decays and cropping the data to the same period as the measured data. In the bottom row figures, the photon decay graphs show the complex decay profiles – note that the colour of these decay profiles does not correspond to wavelength and is used here to distinguish each decay.

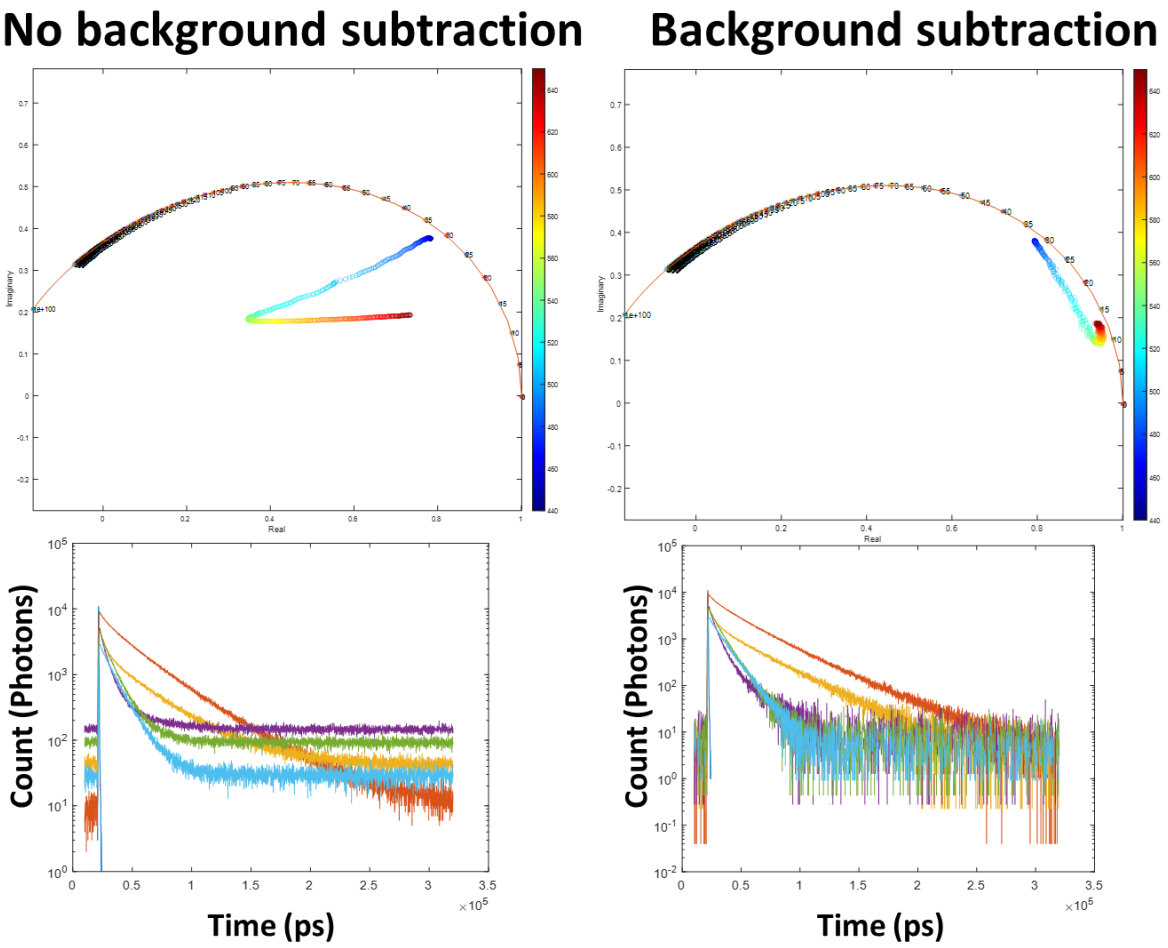



*Figure 52 – Figure showing luminescence decay data before and after background subtraction on the left and right respectively from a point spectrally-resolved decay data set. Top: phasor plots. Bottom: exemplar fluorescence decay profiles at selected emission wavelengths. In both top panels the colour of the data points indicates the emission wavelength, as shown by the scale bar which is in nm. The bottom panels curve colours do not correspond to wavelength. This data was collected using a 400 ns laser pulse period. The phasor plot points are distorted due to the missing data. The universal circle has been distorted in accordance with the missing data.*

The luminescence decays where no background subtraction has been applied show a large offset, which varies with emission wavelength. In the phasor plot, this manifests as a shifting of data points towards ∞ lifetime, peaking at 540 nm in emission. If background subtraction is used, then the data points follow a new path in the phasor plot, allowing more accurate extraction of the component fluorescent lifetimes. The corresponding decay profiles show the consequences of removing the background. This background subtraction is valid in this case because the longest lifetime component (red decay profile) has fully decayed before the next excitation pulse.

Other than providing rapid qualitative contrast and indications of the components' lifetimes as inputs for iterative fitting, phasor plots have limited use when there are distortions caused by the incompletely sampled measurement period and when the decays are not complete before the next excitation pulse.

## Exemplar luminescence data from a synthetic CVD diamond

### *White-light transmission, birefringence, and hyperspectral luminescence imaging*

A CVD diamond with attached HPHT substrate that exhibited strong, spatially varying and spectrally diverse defects was chosen to illustrate the capabilities of this instrument. This sample is different to that shown in Figure 26 and Figure 27. The following data were taken using the imaging spectrograph with a 10-micron entrance slit, using the 150 lines/mm grating, and were acquired using the EMCCD camera. A 10x 0.3 NA objective (Olympus, UPlanFLN) was used. A region of the sample with a small section corresponding to the HPHT substrate, and a larger section corresponding to the CVD diamond was first imaged in transmission with white-light. Crossed polarisers were then added to the system to enable the birefringence to be visualised. For the hyperspectral luminescence imaging, the supercontinuum laser source was tuned to 475 nm, and the spectral detection band was set to encompass the emission from both NV charge states and $SiV^-$ defects. The integration time for a frame was set to be 1 s, resulting in a total acquisition time of ~17 minutes. Hyperspectral image analysis as previously described was used to generate intensity-modulated median wavelength luminescence images. Several ROIs were then selected on the resultant hyperspectral data, and the spectra resulting from binning the data over each ROI were plotted. Figure 53 shows the results of these three measurements[190].

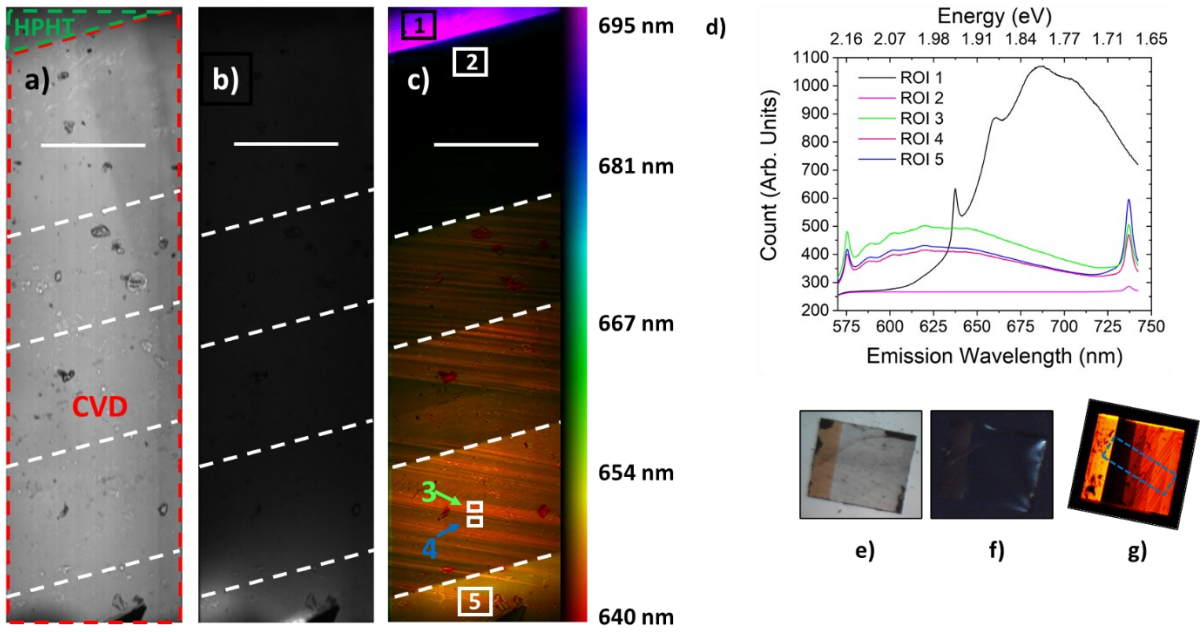



*Figure 53[190] – Image a) shows a white-light transmission image of the sample, with white dotted lines indicating locations of the new growth layers. Image b) is a crossed polariser view of the same region. An intensity modulated median wavelength luminescence image excited at 475 nm is shown in c) of the same region. Extracted spectra from ROIs in c) are shown in d). Image e) is a larger-scale white-light transmission image. Image f) is a large-scale crossed-polariser image of the same region as e). A fluorescence image from DiamondView™ is shown in g). Scale bar is 250 microns.*

In the white-light transmission image, the HPHT region is distinguishable by its reduced intensity, which is caused by the absorption corresponding to its yellow/orange colouration. The crossed-polariser birefringence image presents little contrast, although there is a region of strain apparent towards the bottom of the image, which is furthest away from the substrate. Since this corresponds to a region near the edge of the sample, higher strain is not unexpected. No significant strain was observed at the HPHT substrate CVD diamond interface.

Excitation at a wavelength of 475 nm excites both NV charge states and $SiV^-$, and this sample has been irradiated and annealed to increase the concentration of these defects. The intensity-modulated median-wavelength luminescence image indicates that the HPHT substrate and CVD diamond have different emitting defects, and this is apparent in the extracted spectra from the ROI. ROI 1 in the HPHT substrate shows a pronounced $NV^-$ ZPL at 637 nm and phonon side band, with no other obvious features. This emission is the strongest of the entire imaged region. This strong emission from $NV^-$ in the HPHT substrate confirms that this sample has been irradiated and annealed, because NV defects are not typically found in HPHT diamond without such processing.

The CVD diamond was grown in stages, with varying amounts of nitrogen added to the gas phases at intervals during growth. Throughout the growth phase, silicon was constantly doped into the gas phase by a fixed amount. “Older” CVD diamond, with lower nitrogen, is indicated closer to the HPHT substrate at the top of the image. Newer diamond was grown onto this, with increasing distance from the substrate, towards the bottom of the image. Well-defined bands in the emission from the defects are visible in the median-wavelength luminescence image, presenting spectral and intensity contrast. In the white-light transmission and birefringence images, these bands are not visible.

ROI 2 on the CVD diamond, near the interface with the HPHT substrate, indicated a weak emission from $SiV^-$, with a ZPL at 737 nm, but no other emission was observed. The wavelength range of the hyperspectral scan did not include the weak phonon side band of $SiV^-$ at 760 nm. The CVD diamond furthest from the HPHT substrate in ROI 5 shows a strong emission from $SiV^-$ and $NV^0$, with a ZPL at 575 nm, and a large phonon side band. $SiV^-$ intensity increases with distance from the substrate, and therefore nitrogen concentration, which is consistent with nitrogen acting as an electron donor for SiV, generating the negative charge state. This is explored further in later chapters.

In addition to the band caused by variation in nitrogen incorporation during growth, striations running at 30° to the bands are also visible by their stronger emission intensity. ROI 3 and ROI 4 show the spectra on and off these striations and indicate there is a stronger emission from $NV^0$ on the brighter striations. It is known that nitrogen will incorporate more readily into specific growth planes than others[119], and this may explain this variation in emission. The striations are also visible in the DiamondView™ fluorescence image, but this system does not offer much spectrally resolved information. The key advantage of hyperspectral imaging, is that spectral fingerprints of defects can be definitively identified, as shown here.

This can be seen more clearly in Figure 54, using the same objective lens, excitation wavelength (475 nm), grating and slit width (10 microns) as Figure 53, but acquired with the sCMOS camera. The sCMOS acquisition time was 2 s per slice which resulted in a longer total image acquisition time of ~78 minutes, compared to ~17 minutes for the EMCCD camera for similar spatial dimensions. However, the increased spectral range enabled the full extent of both NV charge states and $SiV^-$ phonon side bands to be recorded.

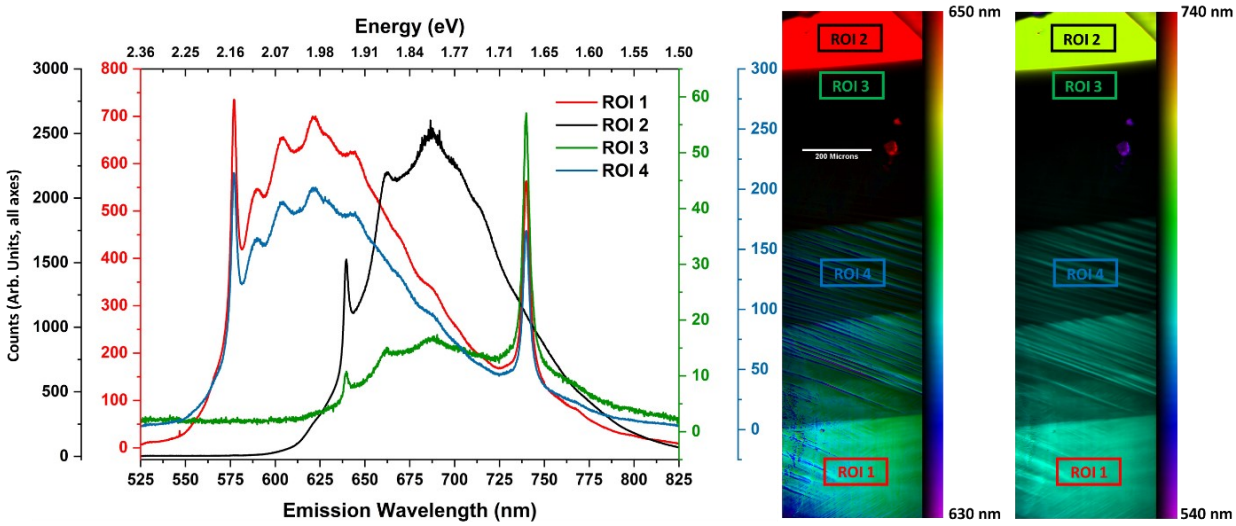



*Figure 54 – Extracted spectra from the four ROIs shown in the intensity-modulated median-wavelength images (right). Note the different scale bars on the graph per spectra, where the colour matches the coloured axis. The spectral resolution, spectral range, and spatial resolution are all higher using the sCMOS camera compared to the EMCCD in Figure 53. Data was collected using a 10x 0.3 NA objective and 475 nm excitation. The two intensity-modulated median-wavelength images have different colour scales to enhance contrast.*

Two different spectral ranges have been used to display the median wavelength images; one to better highlight the different median luminescence wavelengths in the striations, and the other to display the full range of values observed in the image.

ROI analysis of these hyperspectral luminescence images provides information that was not apparent from the previous measurements shown in Figure 53. For example, in the spectral profile corresponding to ROI 3, near to the HPHT substrate CVD diamond interface. $SiV^-$ is still present but $NV^-$ is now visible in the CVD diamond. This is the only region where the $NV^-$ charge state has been found in the CVD diamond. When CVD samples are grown, a region of higher purity material is first grown in order to reduce extended defects propagating through the remaining CVD diamond. Nitrogen or other dopants may/may not have been added during this initial growth phase, to facilitate this purer growth. Silicon and nitrogen related defects are still present in this region but may have been an unintentional contamination at this stage of growth. The unusual charge state of NV could be attributed to this.

## *Spectrally resolved FLIM*

Spectrally resolved FLIM using TCSPC was applied to a large section of the same region of the sample for which images are shown in Figure 53. As designed, this instrument can provide co-registered image data from FLIM and hyperspectral imaging. Three FLIM images were acquired for three distinct spectral detection bands using 475 nm excitation. These spectral detection bands encompassed the ZPLs of the three emitting defects, which are $SiV^-$ and both charge states of NV. Exemplar FLIM maps are shown in Figure 55. The images were 68 x 282 pixels with 5 micron pixel size. The fixed repetition rate of 40 MHz of the supercontinuum laser leads to a TAC window of 25 ns. A pixel dwell time of 100 ms was used, which is long in comparison to typical FLIM measurements performed on biological samples. However, diamond does not bleach, unlike organic fluorophores, and high detected photon numbers are required to accurately analyse the complex (e.g. triple exponential) luminescence decay profiles observed for this sample. To acquire a single lifetime image required ~40 minutes, of which ~8 minutes were used for stage translation. This stage translation time could potentially be reduced by using polygon scanners to sweep the excitation beam instead of stage scanning. The luminescence decay data was fitted pixelwise with 3 x 3 binning using *FLIMfit*. An IRF measurement was acquired by placing a mirror at the sample plane and detecting a strongly attenuated reflection from the laser at the excitation wavelength.

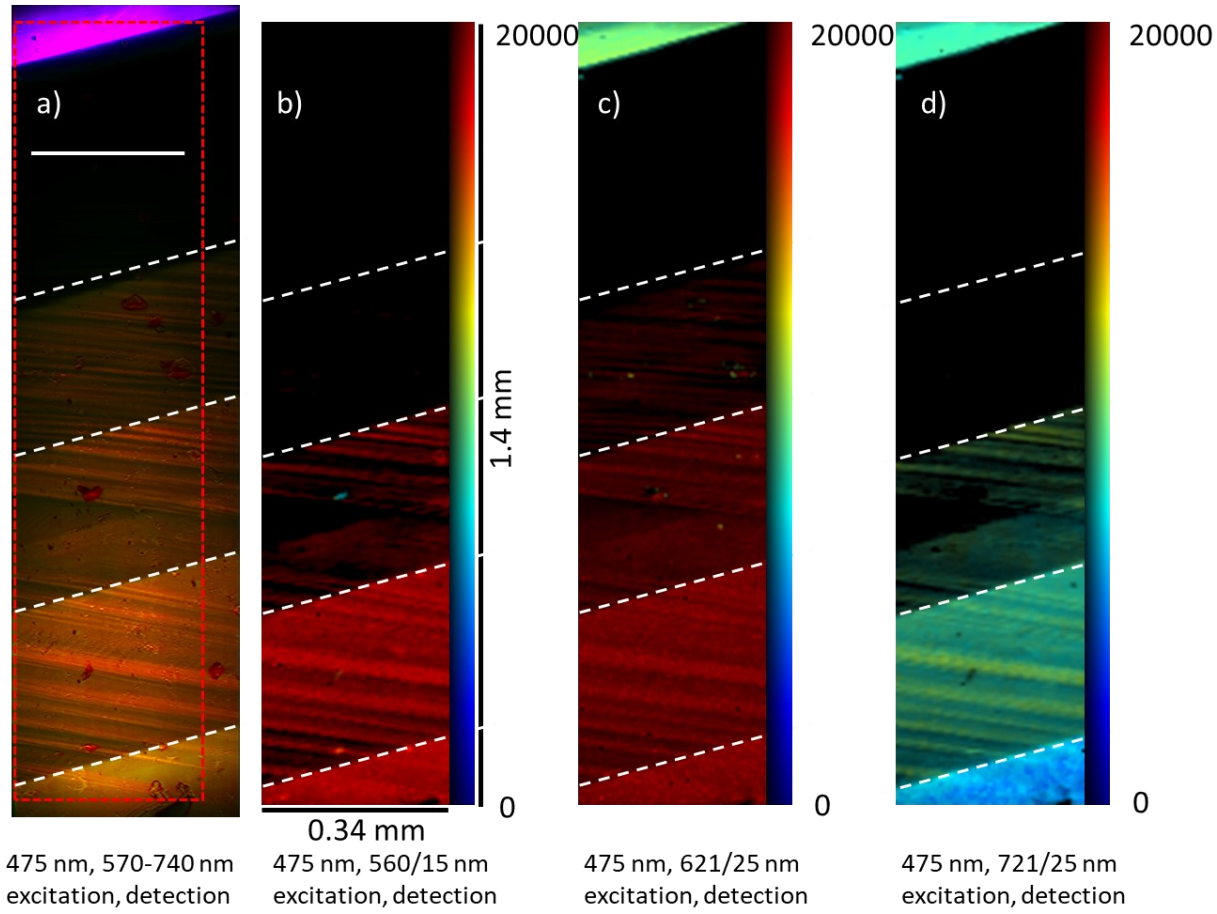



*Figure 55[190] – a) is the intensity-modulated median-wavelength luminescence image (from Figure 53) excited at 475 nm, where the colour represents median wavelength in nm (colour scale bar shown in Figure 53). Images b), c) and d) are three intensity-modulated weighted-mean-lifetime FLIM maps acquired for three different emission bands of the red bounded ROI in a), where the colour scale bar represent lifetime in ps. The scale bar is 250 microns[190].*

The intensity-modulated luminescence lifetime image for the first detection band (560/15 nm) is shown in Figure 55 b). This emission should only originate from $NV^0$, and the lifetime should be 19 ns, from literature[134]. As shown in Figure 56 c), a simple monoexponential decay was fitted with a lifetime of 19.3 ns, resulting in a $\chi^2$ of 1 and noise in the residual. This emission only originates from the CVD diamond, which concurs with the hyperspectral extracted spectra. The striations are also clearly resolved in Figure 56 a) which shows an intensity modulated median wavelength image from Figure 53. This supports the hypothesis that variations in the concentration of nitrogen-related defects are the cause for variations in intensity on the striations.

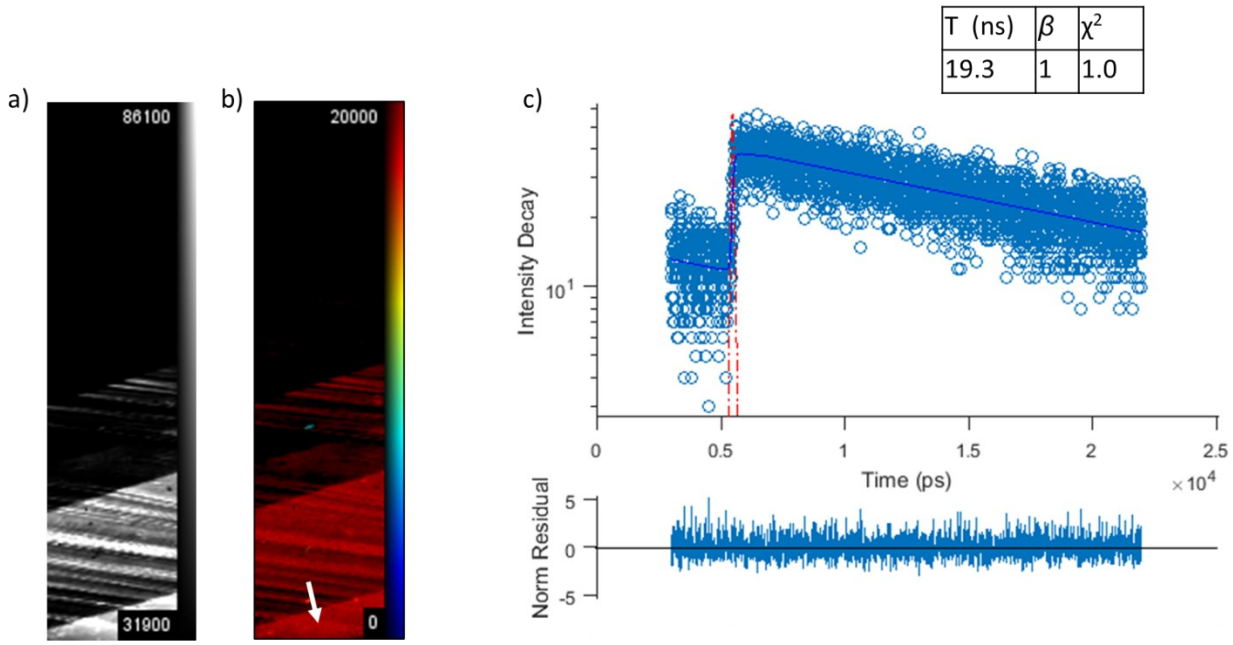



*Figure 56[190] – Image a) is a summed intensity map of the FLIM map of Figure 55 b), which is reproduced in b). The colour scale bar in b) represents lifetime in ps. An exemplar decay profile and fitting model with residuals corresponding to the point indicated by the white arrow in b) is shown in c).*

The second detection band (621/25 nm) is closer to the emission of the $NV^-$ ZPL. Its intensity-modulated weighted-mean-lifetime image is shown in Figure 55 c). The phonon side band of $NV^0$ extends out to this detection range and so should be included in the fitting model. The lifetime of $NV^-$ is 12 ns from literature[129], but this has been reported to vary as a function of local environment[191]. Examples of corresponding fitted decay profiles are shown in Figure 57.

The CVD diamond luminescence decay profiles were best fitted to a triple exponential decay model, for which the spatially averaged component lifetimes were 20.4 ns, attributed to $NV^0$, and a 3 ns component, for which the origin is unknown. A 530 ps component was also observed in some regions of the sample, but this constituted less than 1% of the decay. The 20.4 ns lifetime is slightly high for the $NV^0$ defect and requires further investigation. The fitting parameters were found by averaging over a region of the CVD diamond and fitting that to the minimum number of components. A value of 19.3 ns from the previous data for $NV^0$ was used as the initial guess in the fitting.

The HPHT substrate also presented complex decay profiles that were best fitted to a triple exponential decay model. The spatially averaged lifetime components were 13 ns, 4 ns and 600 ps. The 13 ns lifetime is close to the expected lifetime for $NV^-$, but the others have no known origin and

did not appear as spectral features in Figure 53. However, as discussed later in this thesis, we hypothesise that $NV^-$ is quenched in the HPHT substrate and this may explain the short lifetime components observed. The beta and lifetime (τ) maps are shown for these lifetime components in Figure 57.

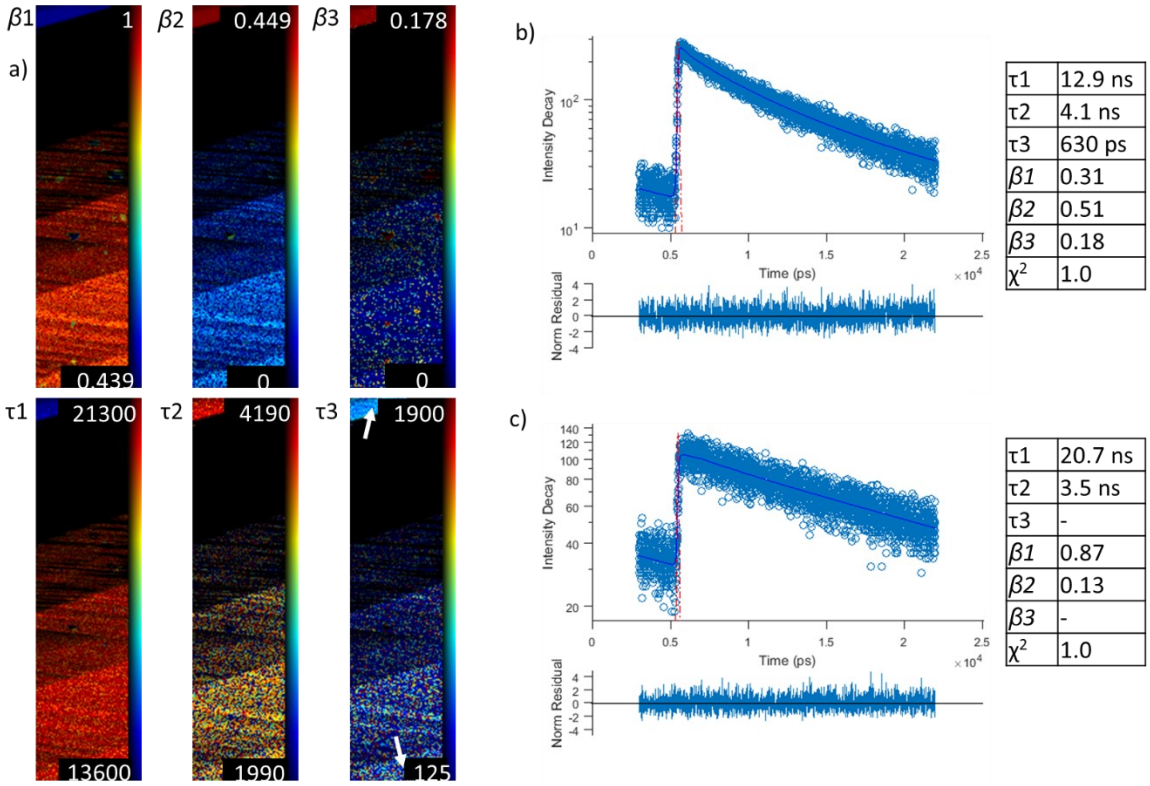



*Figure 57[190] – The images in a) show the variation of the three beta (β) parameters and lifetime (tau, τ) for the 621/25 nm emission band. Lifetimes are measured in ps in all three τ images. Graphs b) and c) show example fits and residuals at the two arrows for the HPHT substrate b), and CVD diamond c). The fitting parameters for those particular decays are also given.*

The third detection band (721/25 nm) should encompass the emission from $SiV^-$. The calculated intensity-modulated weighted-mean-lifetime image is shown in Figure 55 d). The emission from $SiV^-$ is expected to be present in the CVD diamond and the lifetime of 1.1 ns is in accordance with the expected lifetime for the $SiV^-$ defect[152], but variation has also been reported depending on local environment[192]. In Figure 58, exemplar luminescence decays and fitted models are shown for the HPHT substrate and the CVD diamond. The HPHT substrate presents a complex decay, which will be further discussed in chapter 6. The CVD diamond emission is dominated by a 1.1 ns lifetime component, which is attributed to $SiV^-$. Two other weaker components were an 18.7 ns lifetime, which has been attributed to $NV^0$, and a 100 ps component, which has an unknown origin. This 100 ps decay component could be related to a previous measured component associated with $SiV^-$

[193]. The intensity-weighted mean lifetime image shown in Figure 55 d) is especially interesting, because it shows a variation in the lifetime of the striations. Considering the beta (β) maps in Figure 58, this may be caused by variations in $NV^0$ and $SiV^-$ concentrations.

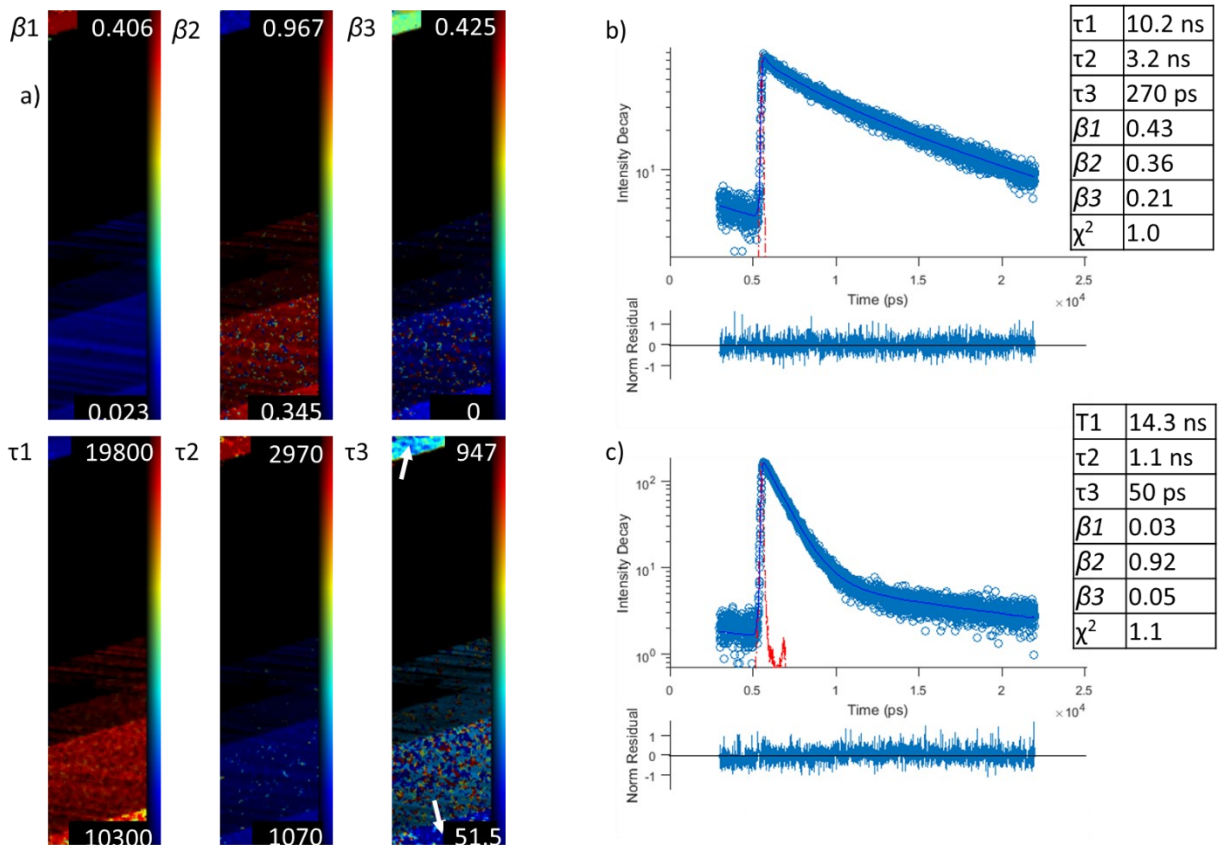



*Figure 58[190] - The images in a) show the variation of the three beta (β) parameters and lifetime (tau, τ) for the 721/25 nm emission band. Lifetimes are measured in ps in all three τ images. Graphs b) and c) show example fits and residuals at the two arrows for the HPHT substrate b), and CVD diamond c). The fitting parameters for those particular decays are also given.*

## *Excitation-emission-lifetime matrix*

A powerful capability of this instrument is the ability to resolve luminescence with respect to excitation, emission and lifetime. Instruments have previously been developed that can collect such excitation-emission-lifetime matrices (EELM) data[166], but typically they make bulk measurements, e.g. of homogeneous liquid samples. Here I report the first acquisition of such EELM data for diamond luminescence. The higher detection NA and tuneable supercontinuum laser excitation source of this microscope-based instrument make it more sensitive than a previous spectrofluorometer implementation[155].

For this experiment, the prism-based monochromator is tuned to provide a specific excitation wavelength, and a luminescence decay profile is acquired at each detection wavelength of the scanning monochromator. The supercontinuum prism-based monochromator is then tuned to the next excitation wavelength and the acquisition process is repeated. Eventually, a full EELM of time-resolved and excitation-resolved emission data is recorded. Each 2D slice of the excitation-emission matrix is saved with a different (photon-arrival) time stamp in the TIFF format. This spectral "spatial" image set can be analysed in the same way as FLIM data, with the *x*-*y* coordinates relating to spectral instead of spatial coordinates.

Exemplar data was acquired at a location on the same CVD diamond, chosen to be far from the HPHT substrate, and the excitation wavelength was scanned from 450 to 680 nm with a 2 nm step size, and the emission monochromator was stepped from 550 to 770 nm with a 1 nm step size. A pixel dwell time of 0.75 s was used, which resulted in a 7-hour total data acquisition time. The linear variable filter was set to automatically tune the transmission peak to be 20 nm longer than the excitation wavelength. A single IRF measurement was recorded using an attenuated reflection from a mirror placed at the focal plane. A 3D contour plot of the fitted EELM data is shown in Figure 59, where colour represents the intensity-weighted mean lifetime.

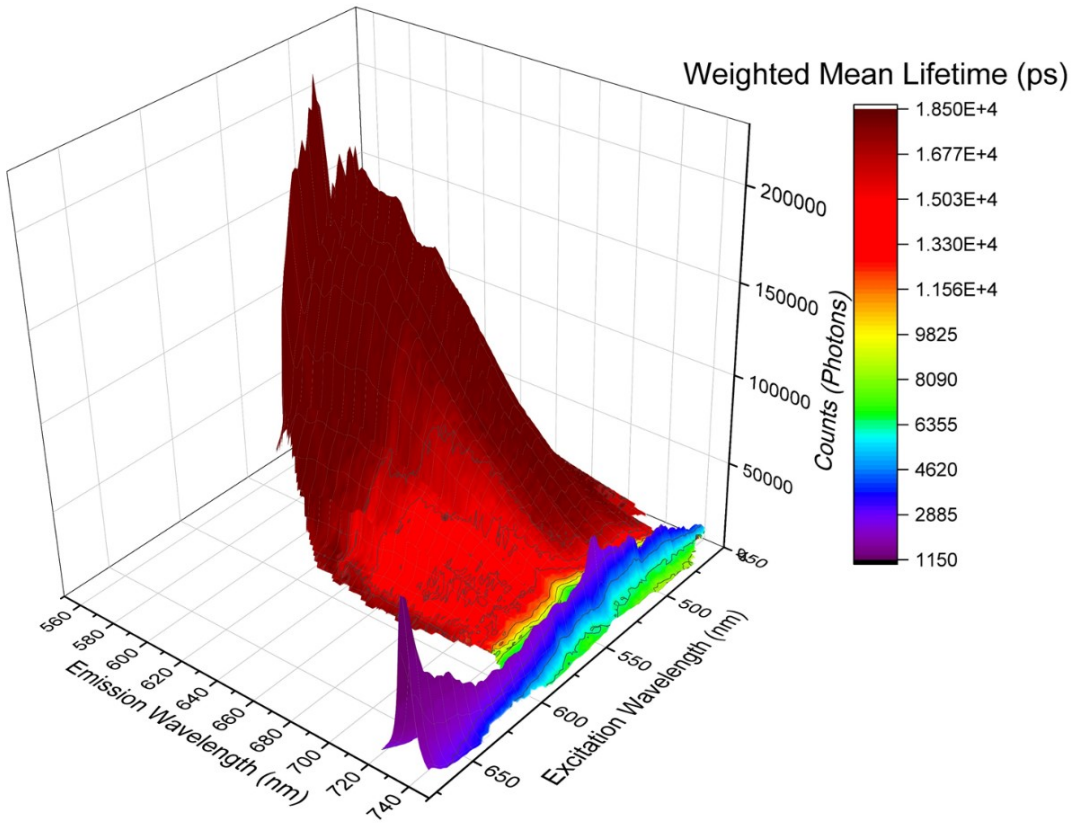



*Figure 59 – A 3D colour contour map of the excitation-emission-lifetime matrix from a region on the CVD diamond. This is explained in the text.*

Visualising 4D data is challenging, and several methods have been explored. The 4D data set represented in Figure 59 can be presented interactively on a computer monitor, such that the entire data surface can be explored. For printed figures, one can use contour plots, as shown in Figure 60. It is also possible to print intensity-modulated contour plots, although low-intensity regions can then be lost for data with high dynamic range.

This EELM data was analysed by finding regions of the EE (excitation-emission) spectral map that presented monoexponential decays. The data were then averaged over larger regions of approximately the same lifetime and globally fitted. The resulting lifetime components were found to be 18.5 ns ($\beta_1$, attributed to $NV^0$), 14 ns ($\beta_2$, attributed to $NV^-$), and 1000 ps ($\beta_3$, attributed to $SiV^-$). The weighted-mean-lifetime plot shown in Figure 60 presents three distinct regions on the EEM (excitation-emission-matrix). A dark red region is present over most of the plot that is attributed to the emission of $NV^0$, with high values of $\beta_1$. A second region extends in all bands of excitation from 450 to 680 nm at an emission wavelength of 737 nm, and this is attributed to the emission from $SiV^-$. The corresponding $\beta_3$ presents high values around 737 nm. $NV^-$ emission is apparent but only for excitation from 520 to 590 nm. These defects could have been generated by charge transfer from $NV^0$. Shown in the corresponding $\beta_2$ plot that the 475 nm excitation radiation used in work discussed above would not excite $NV^-$, and this is consistent with the results of the FLIM data from the CVD diamond in Figure 55, for this location.

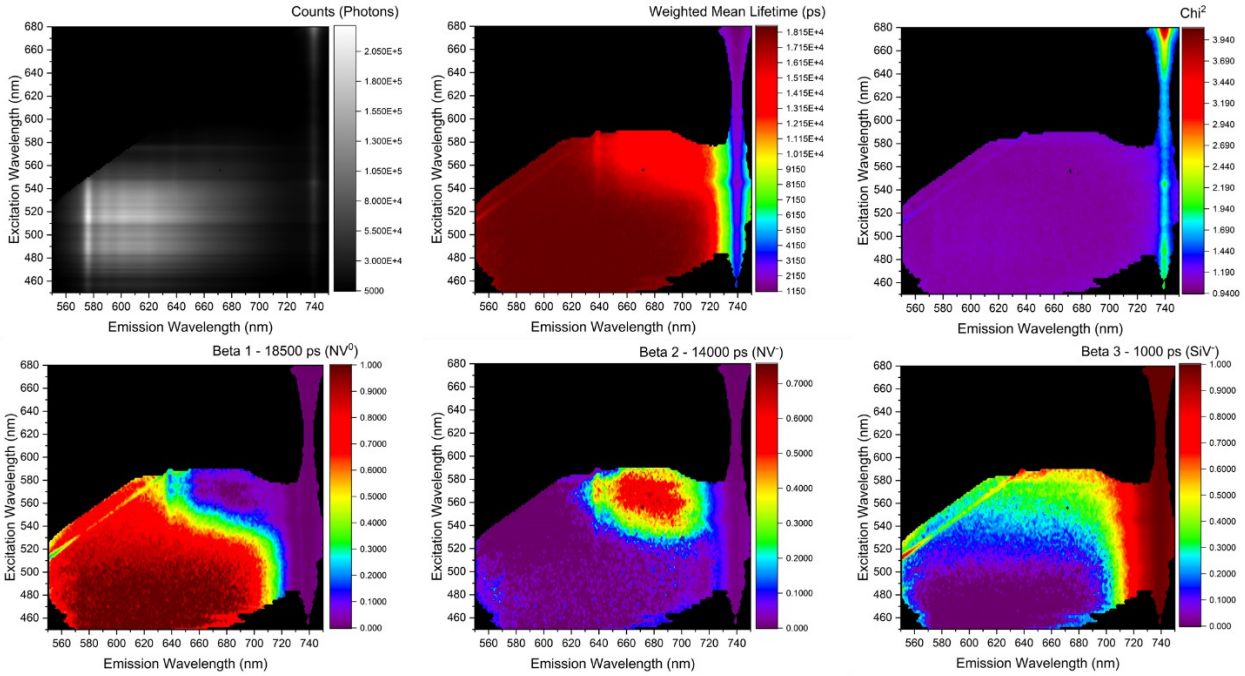



*Figure 60 – A set of six contour maps of the excitation-emission-lifetime matrix, showing the various extracted parameters from the lifetime fitting, including total count (photons), weighted mean lifetime (ps), Chi², and all three beta parameters.*

After this experiment had been conducted, it was noted that a single IRF measurement was insufficient to fit the data, and an IRF varying as a function of excitation wavelength should be used instead. Spectrally varying IRFs were not used in this exemplar study, and so the fit and the $\chi^2$ is worse than for later experiments. This is illustrated by the relatively large $\chi^2$ in Figure 60 around 737 nm emission. The intensity (total photon counts) image is not corrected for the variation of excitation laser power as a function of wavelength and so this data cannot be directly used for quantitative PLE spectroscopy analysis. Thus, this exemplar study can illustrate qualitative trends but should not be used for quantitative analysis. Future measurements presented later in this thesis do take account of spectrally varying IRFs and excitation power.

Despite these caveats, excitation-emission-lifetime data was measured using this system and agreed well with the previous FLIM maps. Emission from $NV^-$ was unexpected and the lifetime measurements allowed the contrast to be easily visualised using the beta plots.

### *Power variation experiment*

The power density at the sample plane varied with excitation wavelength, and this was corrected by measuring the power at the sample plane as a function of excitation wavelength and dividing the detected signal by this data, in future experiments. This was conducted for an early measurement of the $SiV^-$ PLE data, discussed in chapter 6. To test this compensation of variations in excitation intensity with wavelength, a standard PLE spectroscopy measurement was conducted where the excitation power was measured after the polarisation optics, and then the collected PLE spectra was divided by this result. Then a PLE spectrum was acquired using a half-wave plate in conjunction with two polarisers to maintain the excitation power at a constant value as the excitation wavelength was tuned. Figure 61 presents the results of these two measurements together with an uncorrected PLE measurement. The (red) PLE spectrum measured at constant power and the (blue) normalised PLE spectrum are similar but are different from the (yellow) uncorrected PLE spectrum. This confirms that the normalization process reproduces the data correctly.

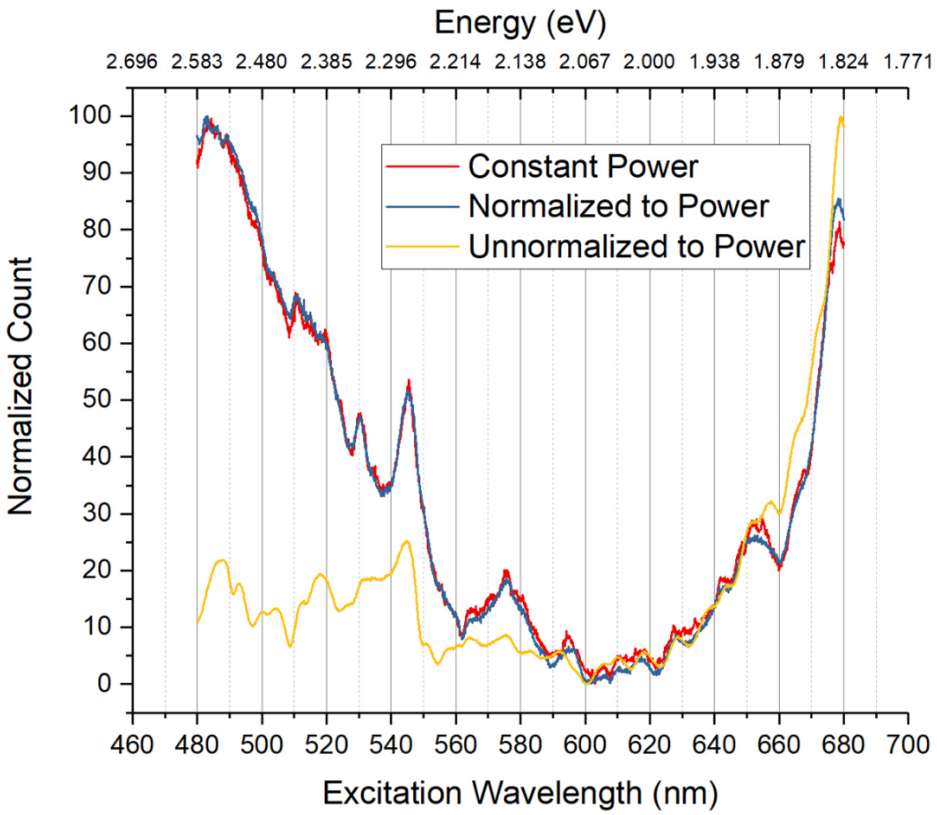



*Figure 61 – Two measurements to investigate the validity of laser SPD post experiment normalisation. A detailed account of the setup is discussed in the text. Both constant power (fixed to a minimum power and varied using a polarisation-based setup) and post experiment normalisation data are similar. Power measurement was not taken at the sample plane, which is incorrect for the blue end of the excitation spectrum, but this does not affect the experimental results.*

## Conclusion and outlook

This chapter has presented the application of three multidimensional luminescence instruments to diamond luminescence: a hyperspectral line scanning microscope, a time-resolved spectrofluorometer and a novel multidimensional luminescence microscope capable of resolving emission with respect to three spatial dimensions, excitation and emission wavelength, lifetime and polarisation – with all modalities co-registered to image/probe the same locations on the sample.

This new instrumentation enables many different parameters to be utilised to contrast and map different sources of luminescence. The spectral resolution of the spectrograph (down to 0.08 nm) is superior to many hyperspectral imaging instruments such as grism-based imaging spectrometers previously used in our laboratory. The combination of hyperspectral imaging and lifetime analysis of diamond luminescence has been illustrated through application to a CVD diamond on an HPHT substrate. This showed how this instrument can be used to study changes in growth conditions and the effect that this has on the emissive defects inside the diamond lattice. In particular,

luminescence lifetime imaging revealed differences between intentional variations in growth conditions and can help elucidate the origin of variations in emission from the observed striations.

Further experiments using this novel instrument are technically possible, including hyperspectral PLE imaging, where each spatial pixel contains an excitation-emission matrix. This could be extended to lifetime and polarisation to allow up to 6D imaging, although this would require long (hours) acquisition times if performed at high resolution.

# Chapter 5 – Application of multidimensional imaging and spectroscopy to synthetic diamond

## Outline

This chapter explores the application of the novel multidimensional luminescence microscope described in chapter 4 to synthetic diamond. Measurements include acquisitions of hyperspectral luminescence data, spectrally resolved luminescence lifetime maps, lifetime-resolved luminescence spectra, and excitation-emission-lifetime luminescence matrices from a specific synthetic diamond, consisting of a HPHT substrate and grown CVD layer. This is the same sample explored in Figure 53 to Figure 61.

The chapter illustrates the main capabilities of the developed instrument, including the acquisition of information that is not available from traditional white-light transmission imaging. In general, studies of luminescence of defects such as SiV, can lead to new applications, including for quantum optical information processing. The lifetime of the defect is an important parameter for quantum optical applications and understanding the interactions a luminescent defect has with other defects found in diamond can be important for future device fabrication. This chapter is based on previously published work[194].

## Introduction

The luminescence analysis that this instrument provides can reveal significant information about synthetic diamonds, which are important for practical applications (e.g. quantum sensing, computing, etc.) due to the ability to reproducibly engineer specific quantum electronic parameters. In contrast, natural diamonds have experienced a wide range of environmental conditions such as temperature and pressure variations, and are impacted by variations in local elemental composition, are each unique in terms of their luminescence properties. Together with their limited availability, this variation in properties means that natural diamond is ill-suited for industrial applications.

Ironically, one of the driving forces for research into growth of synthetic diamond was to manufacture diamond gemstones cheaper than their natural counterparts. However, the initial synthetic diamonds grown by HPHT were small. HPHT synthesis was eventually used to grow larger single crystal diamonds, and these have subsequently been used as the substrates for CVD diamond synthesis[195]. In CVD growth, it is significantly easier to modify the conditions the diamond grows under, due to the inherent nature of the technique. Feed gasses are externally controlled, and

correct ratios of hydrogen and carbon source (usually methane) are required. The control of the fundamental building blocks of the synthesized CVD diamond means that dopants can be incorporated at varying stages of growth[196].

An example of how this control affects the growth of diamond is apparent in the CVD diamond with attached HPHT substrate briefly studied in chapter 4. Intentional variations during growth are an effective method to study the interaction between multiple defects. The initial studies on this sample, described in chapter 4, showed several interesting features. We decided to investigate these using the full range of capabilities of this multidimensional luminescence instrument.

As shown in Figure 62, a colour white-light transmission image, acquired with a 1.25x 0.04 NA objective (Olympus, PlanAPO N), shows a yellow/orange HPHT substrate, with a larger section of CVD diamond. The diamond was grown and cut to show {100} faces. CVD diamonds grown in this way can be prone to corners or the edges of the samples being chipped. This contributes to "edge birefringence", as shown in the two smaller images of Figure 62, where a small chip is shown to be a source of strain (red arrow). This sample has been electron irradiated and then annealed to produce vacancy related defects such as NV and SiV.

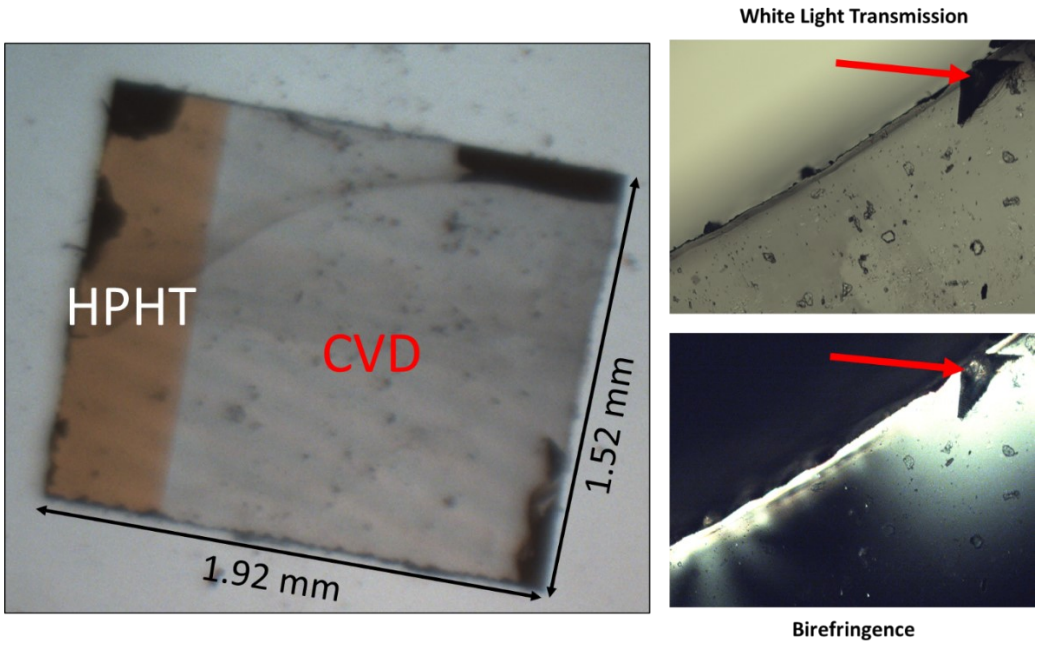



*Figure 62 – Colour image (left) shows a full view of the CVD diamond with HPHT substrate (yellow/orange) using white-light transmission and a 1.25x 0.04 NA objective. The two images (right) show a magnified region using a 10x 0.3 NA objective and show white-light transmission and crossed polariser FOVs. The birefringence indicated that there is strain (brighter regions) around the edge of the sample, particularly around the crack/chip (red arrow).*

## Hyperspectral Imaging of a CVD diamond with HPHT substrate

Unlike most commercial and laboratory-built systems, that typically incorporate only one or a few excitation lasers offering a limited choice of excitation wavelengths, this system provides tuneable (pulsed) excitation wavelengths from 400 nm to the NIR detection edge of the detector. This is provided by the supercontinuum source and is complemented by an additional UV laser source at 355 nm. The flexibility in excitation wavelength is important because it determines which defects will be excited. Whilst 355 nm will excite most defects in diamond, it will do so very inefficiently for red defects such as SiV[19]. In the situation where nothing is known about a sample, exciting at 355 nm excitation and measuring an emission spectrum extending to red wavelengths (i.e. above 700 nm) can provide initial information about the composition of the sample – with hyperspectral imaging providing spatially-resolved information. If this reveals no emission features, then an excitation emission matrix could be measured from a single point on the sample. The disadvantage of this is that if defects are spatially varying, then some defects maybe missed[190].

For this study, it was decided to excite defects at 500 nm using a filter cube comprising a 514 nm long-pass (LP) emission filter (Semrock), and a 525 nm edge dichroic mirror. Hyperspectral imaging was implemented using the sCMOS camera, which can cover the entire visible spectrum in a single acquisition with high spectral resolution (using the 150 lines/mm grating). Hyperspectral imaging can provide an image that may be useful to correlate with other measurement techniques, such as FLIM that may be undertaken with a more limited spectral range. The hyperspectral image data also allows specific regions and their main emission wavelengths to be identified. This can then be used to select the key emission wavelengths for luminescence lifetime acquisitions. This is especially important when considering multiple spectrally overlapping defects.

The 500 nm excitation wavelength (1.25 nm FWHM) was spectrally selected from the supercontinuum using the prism-based monochromator, and line illumination (0.4 mW total power) was implemented through the 4X 0.16 NA objective lens (Olympus, UPlanApo). Hyperspectral image data was acquired with a 1 s integration time per step, detecting emission wavelengths from 510 nm to 865 nm (using the 150 lines/mm grating), although the dichroic filter did not allow maximum transmission until 520 nm. The sCMOS camera was used because its sensor is large enough to collect the spectrum up to 865 nm with this grating, compared to 680 nm for the EMCCD, which would miss the $SiV^-$ emission.

The hyperspectral image data was processed using the technique previously described in chapter 4, to generate the intensity-modulated median wavelength images, as shown in Figure 63. In this image with a false colour scale, the HPHT substrate appears in green, and the CVD diamond appears

mostly in purple, with varying brightness. The image has been saturated to reveal more detail in the CVD diamond, as the HPHT substrate had stronger emission. The banding caused by the increase of nitrogen incorporation is prevalent in the CVD diamond, along with many clear striations. As the distance from the substrate increases, the emission increases in bands, caused by the stepped increase of defect concentration.

In all the emission spectra, a small signal from the 1$^{st}$ order Raman shift of the excitation wavelength is observed, although this is relatively weak compared to the luminescence features.

The emission spectrum shown in Figure 63, ROI 1, which is from the HPHT substrate, shows a dominant emission profile caused by $NV^-$, with a ZPL at 637 nm. There is no other strong emission in the HPHT substrate, noting that H3 emission might have been expected. It is probable the electron bombardment and subsequent annealing has primarily generated NV centres and the excess nitrogen present has made $NV^-$ the dominant charge state.

The CVD diamond shows several spectral features. ROI 2 is located furthest from the HPHT substrate, and therefore corresponds to the highest concentration of nitrogen due to the intentional increasing feed gas concentrations. There are two spectral features of note: the ZPL of $NV^0$ at 575 nm, and the ZPL of $SiV^-$ at 737 nm. ROI 3 is near the mid-point of the sample, and a comparison of this region with ROI 2 reveals that the $NV^0$ emission is approximately half that in ROI 2. Another point of note is that $SiV^-$ emission at ROI 3 is only 1/3$^{rd}$ the intensity of that from ROI 2.

The origin of the increased $NV^0$ emission with distance from substrate is related to the increase of nitrogen incorporation. However, the $SiV^-$ increase is more difficult to explain. Nitrogen could act as a donor to SiV, which would convert some $SiV^0$ to $SiV^-$ [119]. $SiV^0$ emission was not observed and is difficult to detect at room temperature because it emits at 946 nm (ZPL), which is in a low QE detection wavelength region of the Si based camera response and is usually quite weak[153], which can result in other emissive bands obscuring the signal. One hypothesis is that, because silicon feed gas concentrations were kept constant during growth, assuming it was incorporated at a constant rate during growth, and that vacancies are randomly distributed evenly, then regions where $SiV^-$ is high would correspond to low emission from $SiV^0$ and vice versa. This is complicated by theoretical modelling and recent inferred measurements of $SiV^{2-}$, which is a third possible species and is not optically active[150]. A spatial hyperspectral map of the two charge states, assuming constant silicon doping, could provide information about the existence of $SiV^{2-}$. Elemental silicon concentrations could be determine using a variety of mass-spectrometry techniques.

Most of the CVD diamond is similar to the representative data shown in ROI 2 and 3, but the region near the HPHT substrate/CVD diamond interface in ROI 4 reveals a different optical signature. The emission is relatively weak for this excitation wavelength, with most emission originating from $SiV^-$. In contrast to the rest of the CVD diamond, the emission from NV is only from the negative charge state. As this material was grown directly onto the HPHT substrate, the growth conditions are not always the same as later growth. This could explain the unusual charge state of NV at the interface.

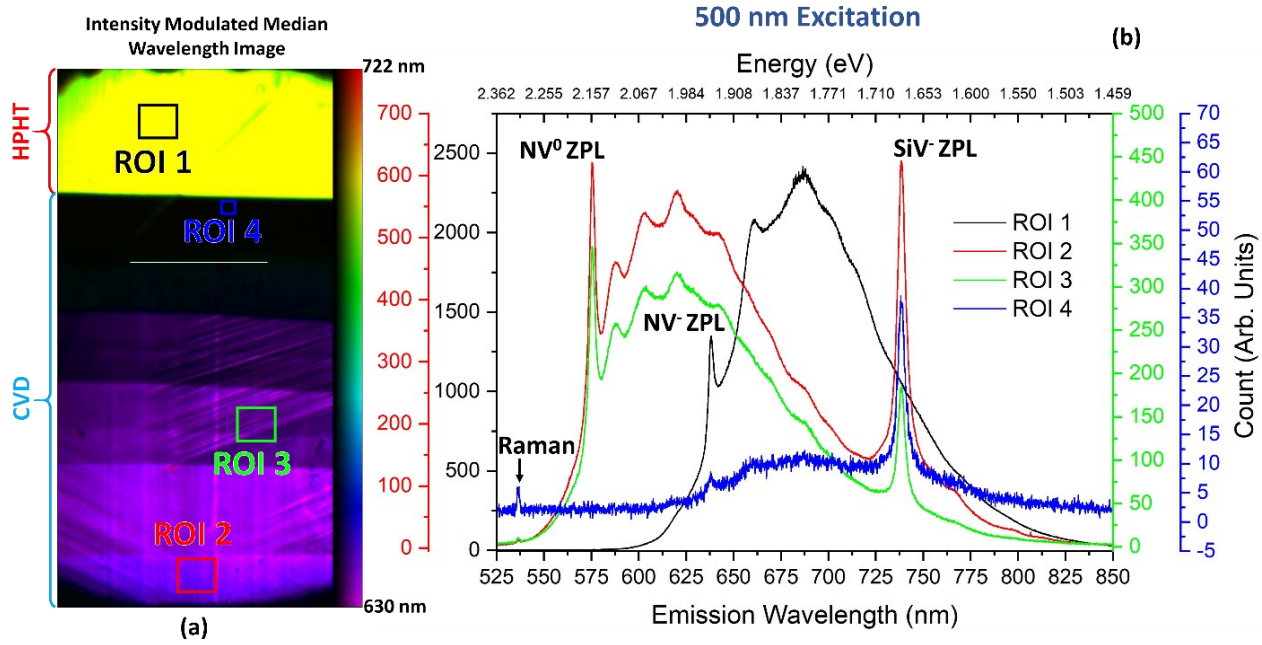



*Figure 63*[194] *- Hyperspectral luminescence intensity image data was collected using a 4x 0.16 NA objective, with luminescence excitation at 500 nm (1.25 nm FWHM), using line illumination and a line acquisition time of 1 s. (a) shows an intensity modulated median wavelength image. The scale bar is 0.5 mm. The intensity contrast has been adjusted to enhance the visibility of signal from the CVD diamond region. The maximum diamond CVD emission was 3x lower than that of the HPHT substrate, across all wavelengths. The spectra in (b) are taken from the four ROIs shown in (a) and show that the CVD diamond and HPHT substrate have different emission spectra, originating from different defects/charge states. The emission spectrum from each ROI is shown using a separate vertical axis that is coloured to match the line colour for that ROI.*

Combined, the hyperspectral luminescence spectra for 500 nm excitation indicates that only three emitting defects are present in the sample: $NV^0$, $NV^-$ and $SiV^-$. However, spectral variations in the striations are not clear due to the small variation in the median wavelength. To further explore these luminescence features, high spatial resolution FLIM with a 2-micron pixel size was then conducted over a 0.4 x 1.6 mm region that encompassed both the HPHT substrate and CVD diamond at two

emission wavelengths using the same excitation wavelength of 500 nm. The two emission wavelengths were chosen to be 675 nm and 737 nm.

## *Spectrally resolved FLIM on a synthetic CVD diamond with HPHT substrate – 675 nm emission*

The spectrally-resolved FLIM experiments were undertaken using the same fluorescence filter cube as for the hyperspectral imaging and detecting the fluorescence at the monochromator output of the imaging spectrograph, set to act as a 2 nm bandpass filter. Excitation at 500 nm (1.25 nm FWHM) was focused to a near diffraction-limited spot on the sample by a 40x 0.6 NA objective lens (Olympus, LUCPlanFL N) and the sample was point-scanned laterally using a motorised translation stage with a step size of 2 µm. The pixel dwell time was 0.275 s, which provided sufficient photons per pixel to enable the diamond luminescence to be fitted to complex decay models. The frequency divider on the TCSPC card was set to record luminescence over two excitation periods to fully sample a single decay profile, to enable accurate phasor analysis, as discussed in chapter 4. Phasor analysis proved instrumental in understanding the complex behaviour of this sample.

The emission band was centred at 675 nm (2 nm bandpass) to detect emission from $NV^-$ in the HPHT substrate, and $NV^0$ in the CVD diamond. This emission band should block any emission from $SiV^-$ since it is spectrally far away from the $SiV^-$ ZPL – as shown in the emission spectra of Figure 63. The resulting FLIM data is shown in Figure 64. The summed photon count (intensity) image in Figure 64 a) has been saturated in the HPHT substrate to reveal contrast in the CVD diamond. The detailed spatial phasor lifetime analysis is represented in Figure 64 b), with an inset showing the full phasor plot. In these spatial phasor plots, the colour bar indicates the number of FLIM image pixels with the same co-ordinates on the 2D phasor histogram plot. Three clusters are shown in the spatial phasor plot: a large cluster on the universal circle corresponding to a component lifetime of ~19 ns, and two clusters inside the universal circle. Figures 65 c, d) respectively show the spatial lifetime maps of the modulation lifetime and the intensity-weighted mean lifetime from a four-component MLE fit using FLIMfit. The banding seen previously in the intensity modulated median wavelength image in Figure 63 is apparent here, with the striations presenting high contrast.

The ~19 ns lifetime component on the universal circle corresponds to emission from $NV^0$ and agrees well with the expected lifetime for this defect[134]. The placement of the other two regions inside the universal circle suggests multiple lifetime components caused by a more complex decay. At this emission wavelength only two species should be present from the data acquired in Figure 63, and

one of those, $NV^0$, has already been attributed to the CVD diamond. This is explored further, later in the chapter.

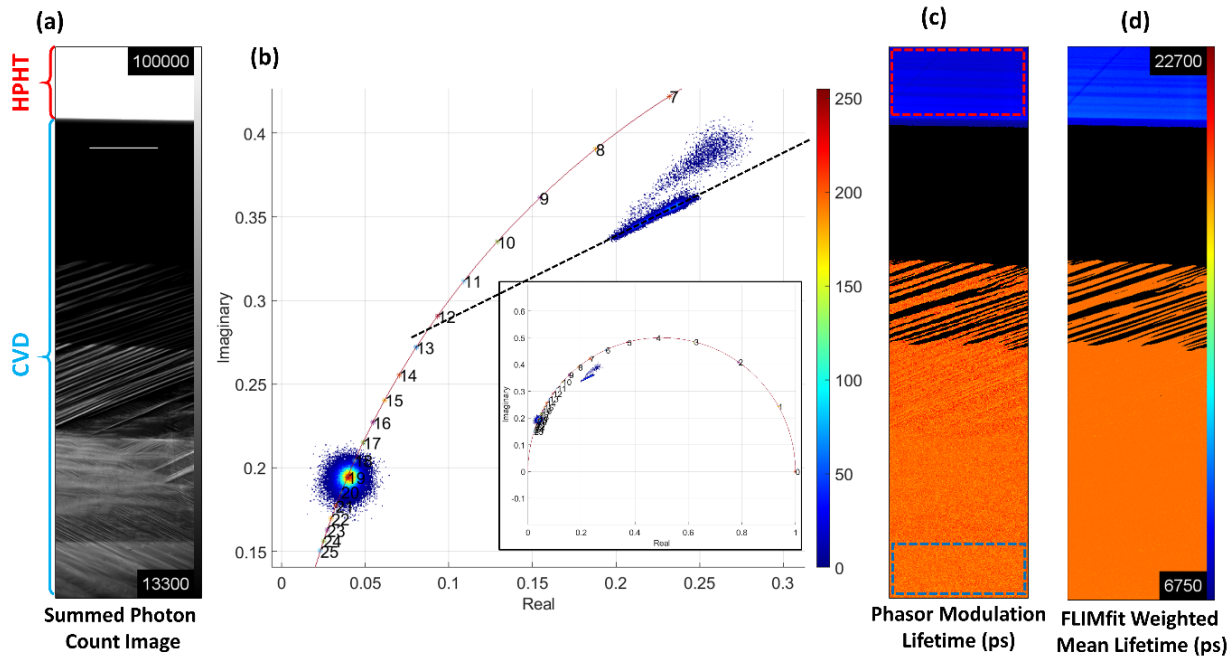



*Figure 64*[194] *- FLIM data set analysed using spatial phasor analysis and MLE decay fitting. Data collected using a 40x 0.6 NA objective under point illumination at an excitation wavelength of 500 nm (1.25 nm FWHM) and 675/2 nm emission, with a pixel dwell time of 0.275 s. The summed photon count image is shown in (a) showing bright emission from the HPHT substrate (top), and less emission from the CVD diamond (bottom). The scale bar is 0.2 mm. The contrast in this image has been adjusted to enhance visibility of the CVD diamond region. The corresponding spatial phasor plot is shown in (b), which shows three clusters of phasor coordinates. The numbers along the outside of the universal circle are the lifetime scale in ns. The inset to (b) shows the full range of the spatial phasor plot. The colour scale indicates the number of FLIM image pixels that map onto each location on the spatial phasor plot. A modulation lifetime map from the spatial phasor plot is shown in (c), which shows different modulation lifetimes in the CVD and HPHT substrate diamond regions. The intensity-weighted mean lifetime from a four-component MLE fit is shown in d) and shows a similar spatial variation in lifetime as (c). The lifetime maps use the same colour scale, which is in ps.*

The modulation lifetime can be extracted from the phasor plot, on a per pixel basis and is plotted in Figure 64 c) where the threshold for photon count was set to 10,000. There are two regions of different lifetimes on the image, corresponding to the HPHT substrate and CVD diamond. Averaging over an ROI corresponding to the entire HPHT substrate (red dashed box) and a second ROI at the bottom band of the CVD diamond (blue dashed box) leads to mean modulation lifetime components

of 8,418 ±258 ps and 19,000 ±393 ps, respectively. The tolerance values were calculated as the standard deviation of all the pixel lifetimes in the selected ROI.

The luminescence decays were iteratively fitted using *FLIMfit* using initial values derived from the phasor plot. The CVD diamond FLIM data were fitted to a mono-exponential decay with a fixed lifetime of $\tau_1$=19,000 ps. The HPHT substrate displayed a more complex decay and was best fitted (minimum $\chi^2$ and no structure in residuals) to a triple-exponential decay with lifetime components fixed to $\tau_2$=11,400 ps, $\tau_3$=4,400 ps, and $\tau_4$=615 ps. Then the FLIM data from the whole sample was fitted to a quadruple decay using the $\tau_{1\text{-}4}$ fixed lifetime components, to produce the intensity-weighted mean lifetime image shown in Figure 64 d). The phasor modulation and iteratively fitted intensity-weighted mean lifetime maps present similar features and values.

The mean and standard deviations of these fixed lifetime components of $\tau_1$=19,000 ± 401 ps, $\tau_2$=11,400 ± 188 ps, $\tau_3$=4,400 ± 125 ps, and $\tau_4$=615 ± 5.62 ps were determined by averaging decay profiles from ten regions of the HPHT substrate and CVD diamond and fitting either a triple or mono-exponential decay, respectively, without fixing the components. The initial parameters for this iterative fitting were 19,000 ps for the CVD diamond, taken from the cluster on the universal circle, and 12,500 ps with a shorter 3,750 ps component for the HPHT substrate. The two components for the HPHT substrate were estimated by drawing a line through the cluster on the phasor plot and calculating the two lifetime values at its intersections with the universal circle. These three lifetime components (one for CVD diamond and two for the HPHT substrate) were not sufficient for a good fit and the presence of the additional 615 ps component in the HPHT substrate was indicated in the residual analysis. The residual showed a clear feature of a fast decaying component, and so this additional component was added. The initial condition for this extra component was arbitrarily chosen as 1 ns. The phasor plot did not directly provide these three lifetime components because three or more components can be difficult to extract if there are no locations where only two components are present. The $NV^-$ decay and lifetime components will be discussed further in this chapter, where it was discovered to be a complex quenched decay, which is only approximately modelled by a three component exponential fit. Three exemplar decay profiles and their fitting models are shown in Figure 65.

Other fitting models with additional components and initial conditions were explored but did not significantly decrease $\chi^2$. In the beta 2-4 maps, shown in Figure 66, the HPHT substrate presents a banded spatial variation in the three lifetime components, which is explored further in this chapter.

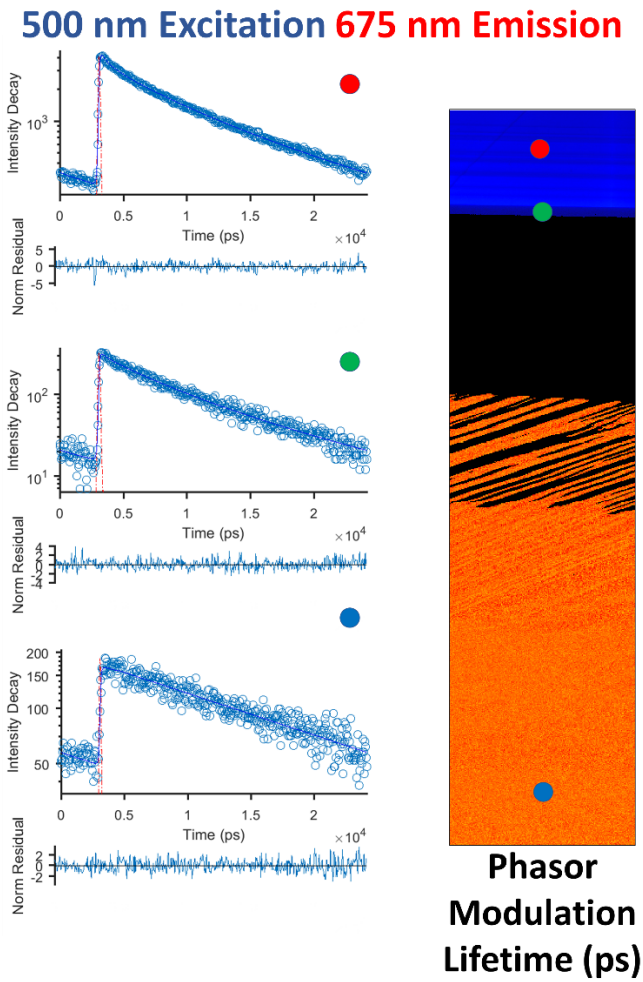



*Figure 65*[194] *- Exemplar decays and MLE quadruple-exponential fits from the FLIM data for an excitation wavelength of 500 nm and detection wavelength of 675 nm. Top graph for each panel: round points, raw data; solid blue line, fit; red line, IRF. Bottom graph of each panel: normalised fit residuals. The modulation lifetime image shows the locations where the decay originated.*

Iterative fitting of the decays profiles can provide the beta (β) values or population fraction of each of the lifetime components. The four beta and $\chi^2$ maps from this iterative fitting are shown in Figure 66. Beta 1 with a lifetime of 19,000 ns is non-zero only in the CVD diamond, whilst the other three components are found in the HPHT substrate. This is consistent with iterative fitting of luminescence from ROIs. The average $\chi^2$ is close to one in the CVD diamond, indicating that the fitting model describes the experimental decay to within the noise on the data, but presents a higher value (>1) across the HPHT substrate. Thus the fitted model does not fully describe the measured luminescence decay in the HPHT substrate. An explanation for this is explored later in the chapter.

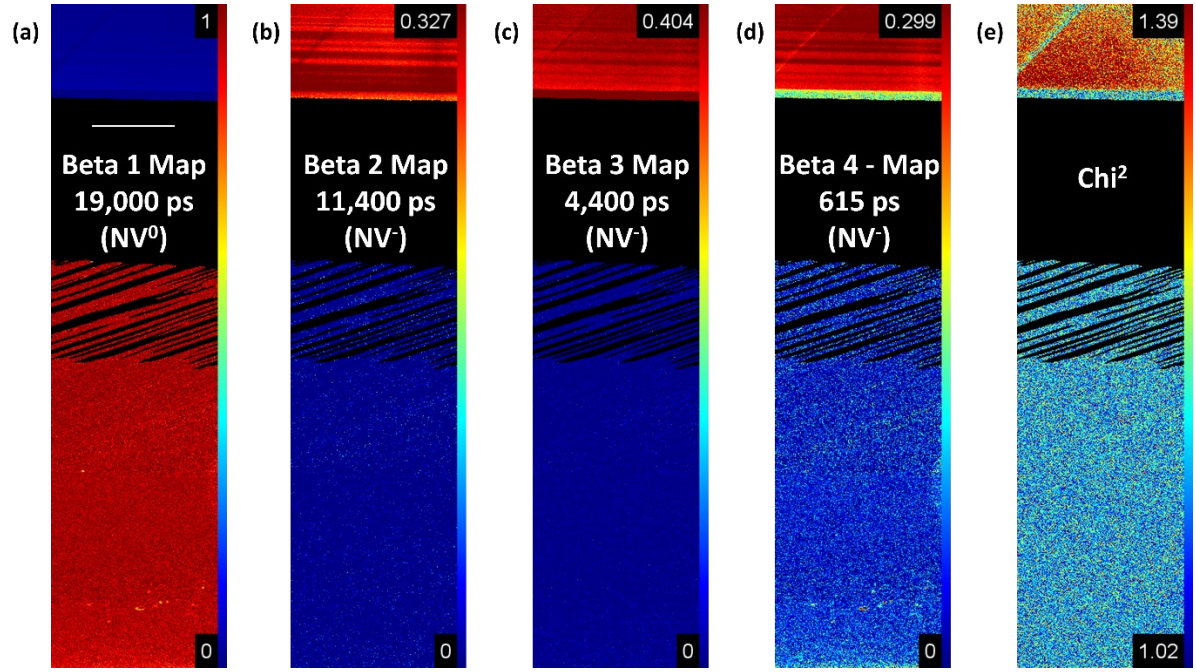



*Figure 66[194] - Population fraction ($\beta$) maps of Figure 64(d), showing the spatial distribution of the four fitted lifetime components. The scale bar is 0.2 mm. In (e) the $\chi^2$ shows that the fit is poorer in the HPHT substrate, and close to 1 in the rest of the diamond.*

Spatial phasor lifetime analysis can also be used to quickly segment images by lifetime contrast: selecting regions on the phasor plot indicates the corresponding pixels on the lifetime image, as illustrated in Figure 67. The red-bounded region on the spatial phasor plot in Figure 67 a) corresponds to the mapped modulation lifetime pixels in image b). This confirms the emission at 19,000 ps is originating from $NV^0$ emission in the CVD diamond, and there is no significant variation in the lifetime. The mean modulation lifetime of this region is 19,008 ±580 ps, and this agrees well with previous measurements and fitting.

The two other regions are more complex. The largest, by number of pixels, appears to be a linear cluster and, if this were a double exponential decay, the intersections of that line with the universal circle would provide the lifetimes of the two components. This approach can also be applied to a region – rather than a line – inside the universal circle. This is supported by the results of the iterative fitting; the three fitted lifetime components can be mapped to a cluster bounded by a triangle of those three points on the universal circle (shown in the phasor plot inset in Figure 67 a)). This adds evidence to the validity of the parameters because, if any points were outside that triangle, then the two analysis approaches would be inconsistent. The image in Figure 67 c) shows the modulation lifetime map corresponding to the orange-bounded region, which corresponds to the HPHT substrate region of the diamond and contains $NV^-$. Banding of the modulation lifetime is

shown, which is similar to that in the beta maps obtained from iterative fitting, and to the intensity-weighted mean lifetime map.

The region on the spatial phasor plot outlined in green appears to join with the orange-bounded linear cluster but 'flares' out towards the universal circle. This corresponds to the modulation lifetime map of Figure 67 d), which corresponds to the interface of the CVD diamond and the HPHT substrate. This region can also be found in the beta maps of Figure 66. The hyperspectral imaging revealed that this region showed emission from $NV^-$, but this indicates it has a different modulation lifetime to the HPHT substrate, where $NV^-$ is also present.

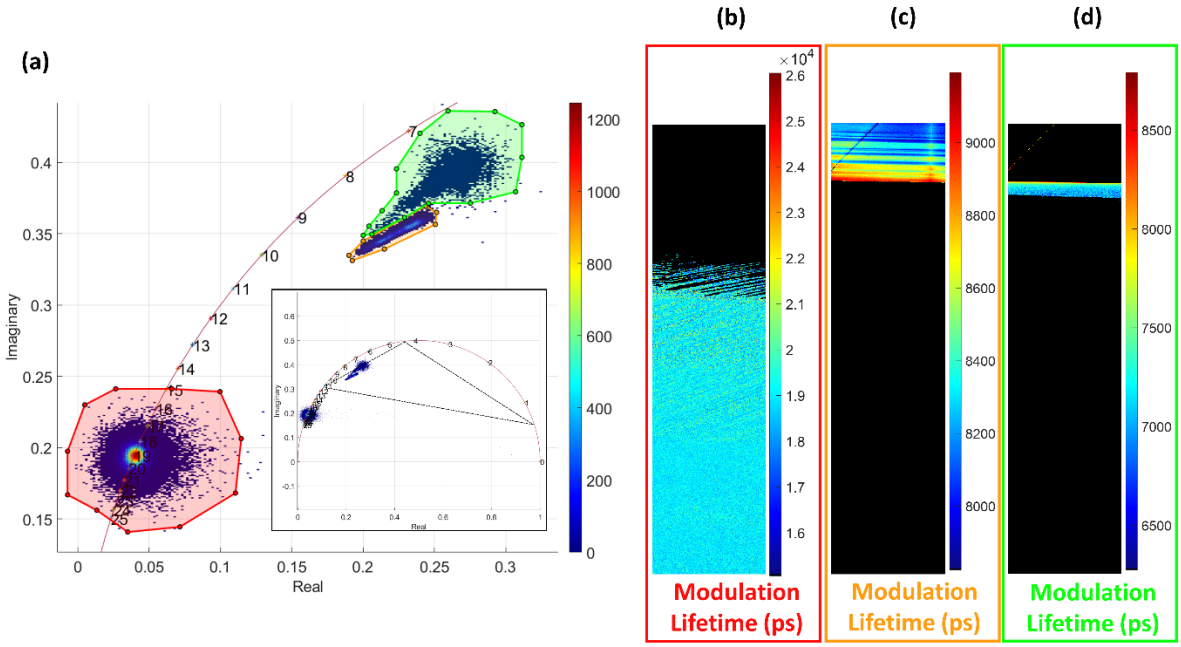



*Figure 67*[194] *- FLIM maps for extracted ROIs using phasor segmentation. (a) closer analysis of the spatial phasor plot in Figure 64, with inset showing the triangle of chords formed by the three lifetime components identified by iterative fitting from ROIs in the HPHT substrate. The numbers along the outside of the universal circle are lifetime scale in ns. Three ROIs (red, orange, green), each with different bounds on the false-colour lifetime scale, are shown along with their corresponding calculated modulation lifetime images (b, c, d). Here the colour of the ROI boxes (b, c, d) corresponds to the phasor plot ROIs.*

The banded lifetime features in the HPHT substrate were studied closely to reduce the possibility that this was a TCSPC artefact. The results of the analysis are shown in Figure 68, which shows that the banding is also apparent in the summed photon count (intensity) image, suggesting this effect could be due to quenching. If an emitter is quenched through a non-radiative decay pathway, then the intensity will be reduced, as will the lifetime[1]. If the emitters and quenchers were uniformly distributed, there would be a uniform decrease in intensity with a corresponding decrease in

lifetime. The existence of the banding suggests a potential spatially varying relationship between the quenching defect and emitter ($NV^-$). It is known that small variation in temperature can affect the incorporation of nitrogen into HPHT diamond, and this variation could appear as banding depending on growth direction[198, 199]. Regions with more incorporated nitrogen would likely create more NV centres after annealing and irradiation, which would create variations in intensity but not lifetime. The correspondence of variations in intensity and lifetime suggests that nitrogen related defects are involved in the quenching of $NV^-$ in this sample. However, the origin of this quenching is not yet fully understood.

The black-bounded (Figure 68 e) and f)) line plots correlating photon counts and modulation lifetime correspond to the vertical black line running perpendicular to the bands in the intensity and lifetime maps of Figure 68. There is a correlation between emission photon counts and the modulation lifetime. Conversely, the orange-bounded plots (Figure 68 c) and d)) of photon counts and modulation lifetime corresponding to the horizontal orange line running parallel to the bands do not show a strong correlation between the photon counts and lifetime. This indicates that the bands do not result simply from an intensity-dependent lifetime (artefact).

The two spin states of the $NV^-$ could have been related to this change in modulation lifetime. However, the two lifetimes are an intrinsic property of the defect, and so no spatial variation should be found. In addition, attempts to fit the two lifetime components corresponding to the two spin states resulted in a poor fit (structure in the residual and $\chi^2 > 1$). The result of this analysis suggests that the $NV^-$ defect could be quenched in the HPHT substrate and CVD diamond near the interface. A summary of the lifetime components and the defect they are attributed to is shown in Table 4.

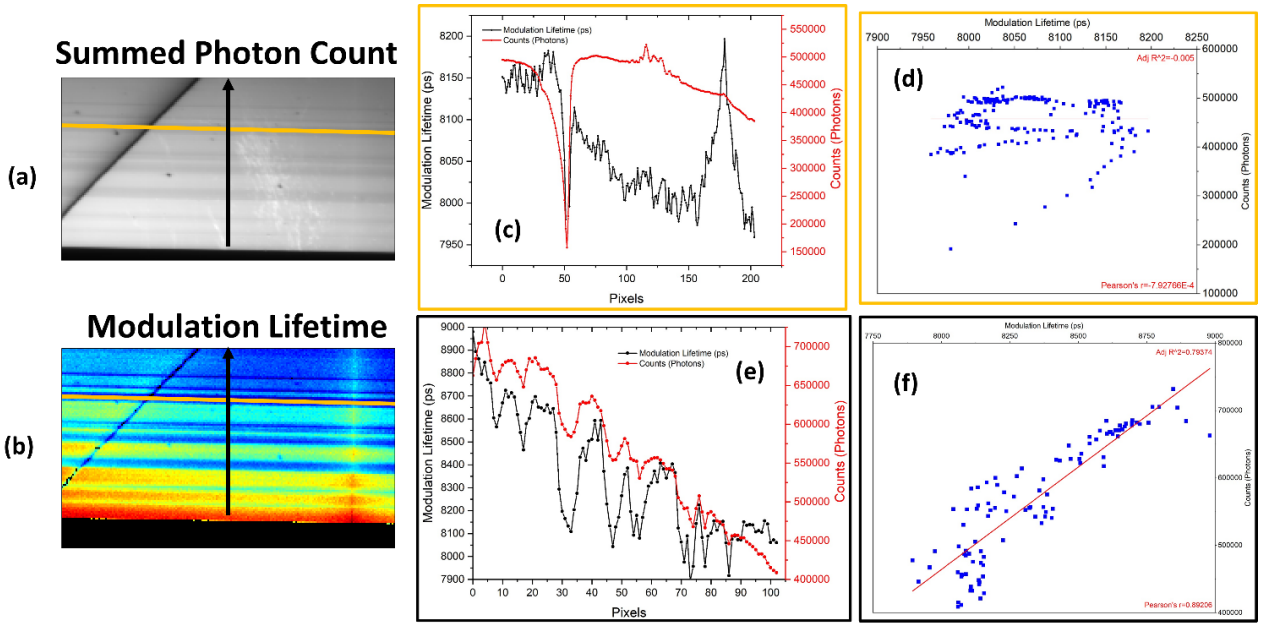



*Figure 68*[194] *– a) summed photon count and b) modulation lifetime images from the HPHT substrate. These figures show the variation in structure/composition (bands) of the HPHT substrate. c) modulation lifetime and summed photon count as a function of distance along the yellow arrow shown in a) & b), which does not show a strong correlation between lifetime and photon counts. d) scatter plot of photon count and modulation lifetime values from along the yellow line shown in a) & b) indicating that there is no correlation when moving across the bands. e) modulation lifetime and photon count as a function of distance along the black arrow shown in a) & b), indicating their correlation. f) scatter plot of photon count and modulation lifetime values from along the black arrow in a) & b) that illustrates their correlation.*

*Table 4 – A summary of the lifetime components under 500 nm excitation at 675 nm emission and their attributed defect.*

| **Lifetime Component** | **Attributed to -** |
|---|---|
| $\tau_1$ – 19 000 ps (CVD Diamond) | $NV^0$ (Based on spectrum and lifetime) |
| $\tau_2$ – 11 400 ps (HPHT Diamond) | $NV^-$ (Based on spectrum and lifetime from a quenched emitter) |
| $\tau_3$ – 4 400 ps (HPHT Diamond) | $NV^-$ (Based on spectrum and lifetime from a quenched emitter) |
| $\tau_4$ – 615 ps (HPHT Diamond) | $NV^-$ (Based on spectrum and lifetime from a quenched emitter) |

## *Spectrally resolved FLIM on a synthetic CVD diamond with HPHT substrate – 737 nm emission*

The luminescence decay was studied for an emission band at 737 nm (2 nm bandpass filter); this wavelength was selected because all the emitting defects indicated in the hyperspectral imaging data emit at this wavelength. This band is centred on the ZPL of $SiV^-$ and overlaps with the phonon side band of $NV^0$, so a double exponential luminescence decay was expected from the CVD diamond. Using the same experimental settings as used to measure the emission at 675 nm, the summed photon count (intensity), spatial phasor and fitted lifetime maps shown in Figure 69 were obtained. The summed photon count map shows that the bulk of the emission is still from the HPHT substrate.

The spatial phasor plot of Figure 69 b) indicates that the cluster corresponding to the ~19 ns lifetime component is no longer present, but the component attributed to $NV^-$ is still apparent (orange section in Figure 67). In this data set, there is a linear cluster extending from ~1.1 ns to ~19 ns on the universal circle that could represent the double exponential decay emission from $NV^0$ and $SiV^-$, which was expected in the CVD diamond. The extracted modulation lifetime map shown in Figure 69 c) indicates that there is variation in the modulation lifetime corresponding to slanted striations in the CVD diamond. This is consistent with previous measurements of this sample shown in chapter 4. The banding observed at 675 nm in the HPHT substrate is also still present.

For iterative fitting, the pixels of the image were binned to 3x3 to enable a better fit of the complex decay profiles. No photon threshold was used for the fitting or phasor lifetime analysis. The CVD diamond emission data at 737 nm fitted well to a double exponential decay model with two spatially fixed lifetime components of $\tau_1$ = 19,000 ps and $\tau_2$ = 1,100 ps. These values were determined in the same way as for the 675 nm emission FLIM maps with the phasor plot being used to set the initial guess of 19,000 ps for the first component, and 1,100 ps for the second component. The same fixed lifetime components were used to fit emission at 737 nm from the HPHT substrate with a triple exponential decay model. As with 675 nm emission, drawing a line through the cluster on the phasor plot does not provide accurate estimates for the luminescence lifetime for the HPHT substrate, so the three component lifetimes from the previous fit (at 675 nm emission in the previous section) were used when fitting the emission data at 737 nm. A total of five spatially invariant components were fixed when fitting emission data across the entire samples, with values of $\tau_1$ = 19,000, $\tau_2$ = 11,400, $\tau_3$ = 4,400, $\tau_4$ = 1,100, and $\tau_5$= 615 ps. Exemplar decay profiles and models from the fitted FLIM map are shown in Figure 70.

The modulation mean and weighted mean lifetime maps shown in Figure 69 show similar features, although the numerical values vary, because three different methods have been used to calculate the 'average' lifetime. All three maps show the same spatial features.

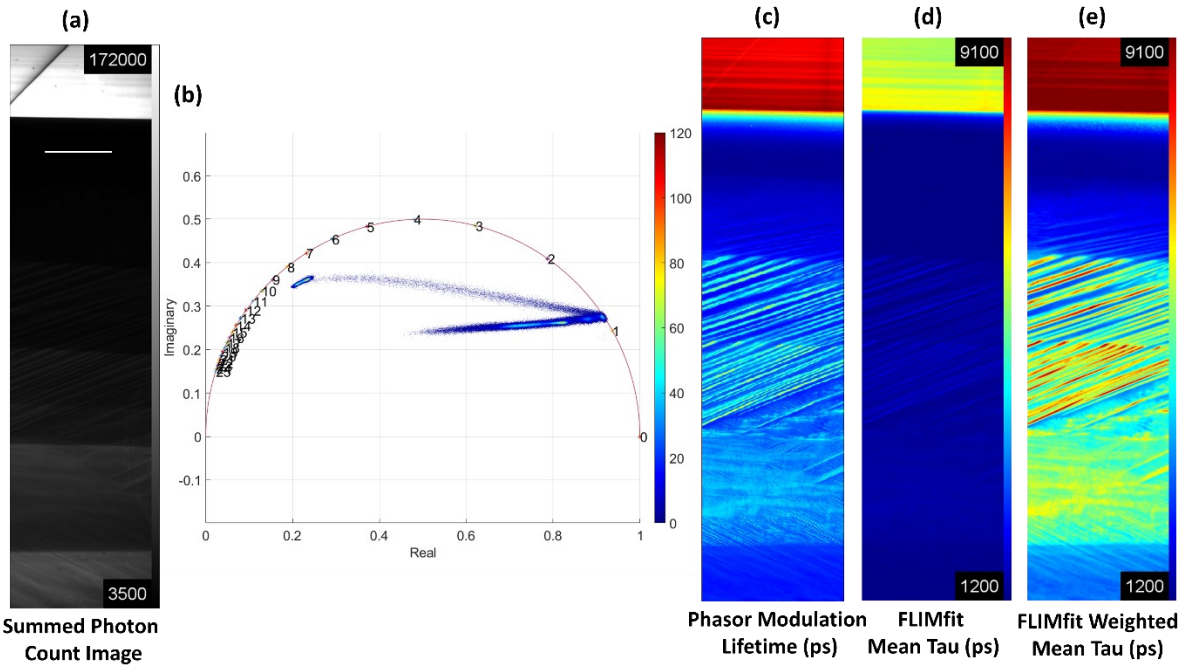



*Figure 69*[194] *- The data for this FLIM map was collected with emission centred at a wavelength of 737/2 nm with excitation at a wavelength of 500 nm (1.25 nm FWHM). Data was collected with a 40x 0.6 NA objective and point illumination with pixel dwell time of 0.275 s. The intensity (summed photon count) image in (a) shows larger than previously measured intensity from the CVD region, caused by emission from $SiV^-$. The scale bar is 0.2 mm. (b) spatial phasor plot with numbers along the outside of the universal circle representing a lifetime scale in ns. The spatial phasor plot shows several distinct regions inside the universal circle, suggesting complex decays are present. The lifetime maps in (c, d, e) show variation in the HPHT substrate as previously shown, but spatial variations in the CVD diamond are now apparent. The lifetime images use the same colour scale which is in ps.*

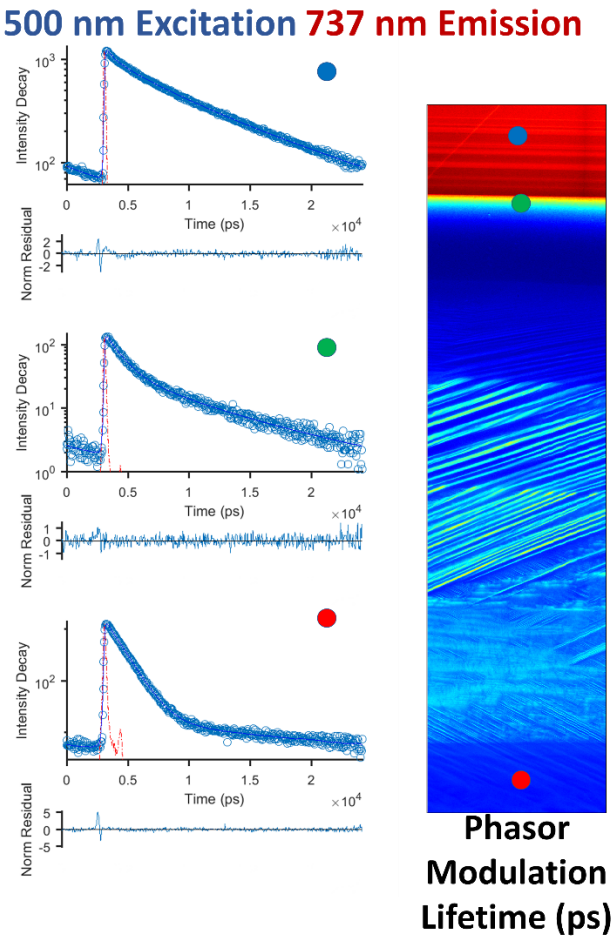



*Figure 70*[194] *- Exemplar decays and MLE quadruple-exponential fits from the FLIM data for an excitation wavelength of 500 nm and detection wavelength of 737 nm. Top graph for each panel: round points, raw data; solid blue line, fit; red line, IRF. Bottom graph of each panel: normalised fit residuals. The modulation lifetime image shows the locations where the decay originated.*

The extracted beta maps from fitting are shown in Figure 71, with a $\chi^2$ map. Beta 1 represents the slowest decay at 19,000 ns, which is attributed to $NV^0$ and is apparent in the CVD diamond. The maximum fraction of that component in a pixel is 4%, which is in good agreement with the hyperspectral data, suggesting the bulk of the emission from the CVD diamond at this wavelength should originate from $SiV^-$. The beta 4 map corresponding to the $SiV^-$ defect's lifetime indicates that at maximum, 99.3% of the emission originates from $SiV^-$. These images suggest that the difference in mean lifetime between the striations and the background is due to a variation in the concentration of $NV^0$. This is most likely related to the higher nitrogen uptake in the striation growth planes. These two lifetime components are not present in the HPHT substrate, which presents variation in the beta 2, 3, 5 parameters, apparent as horizontal bands that are similar to those previously shown in Figure

66. The $\chi^2$ map shows higher values in the HPHT substrate as previously reported in the previous section at 675 nm emission, and the bottom band of the CVD diamond has even higher values. This was due to the IRF not fitting well near t0, as shown in Figure 70.

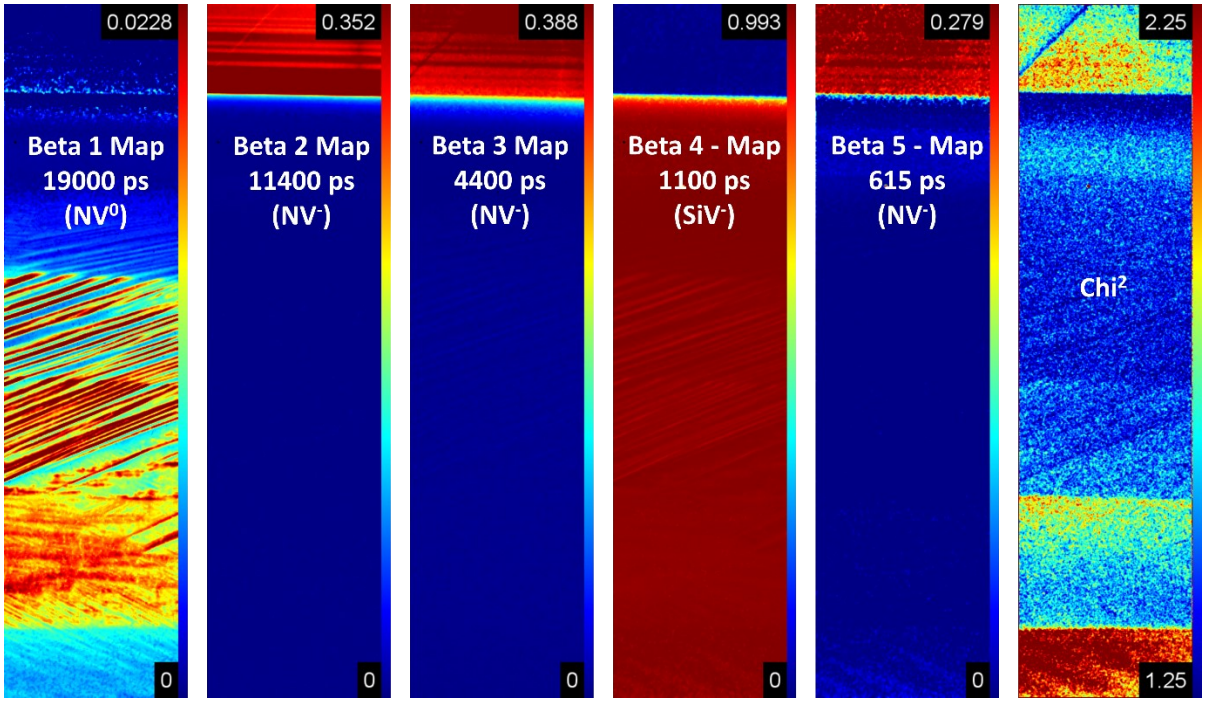



*Figure 71[194] - Beta and $\chi^2$ maps of the emission at a wavelength of 737 nm and excitation at a wavelength of 500 nm for the data in Figure 69. Components 1 & 4 are attributed to the CVD region and components 2, 3 & 5 are attributed to the HPHT region.*

In the same way as for Figure 67, ROIs on the phasor plot are mapped to pixels on the lifetime images. The red bounded linear region appears to arc from the $SiV^-$ ~1.1 ns cluster, towards a long lifetime cluster associated with $NV^-$. This appears to correspond to the region at the HPHT/CVD diamond substrate interface, as shown in the red bounded lifetime map. A modulation lifetime of 8 ns is found near the (HPHT) top of the band, decreasing to 1.3 ns near the (CVD) bottom of the band. The arc therefore suggests that $NV^-$ concentration rapidly reduces, resulting in a change from $NV^-$ to $SiV^-$ dominant lifetime components.

The green-bounded ROI on the phasor plot and corresponding lifetime image are associated to the HPHT substrate (containing $NV^-$), and a banding is apparent with similar values to the previous lifetime map for emission at 675 nm. The blue-bounded ROI on the phasor plot corresponds to the lifetime image map of the CVD diamond, excluding the interface region. There are striations apparent in the modulation lifetime map.

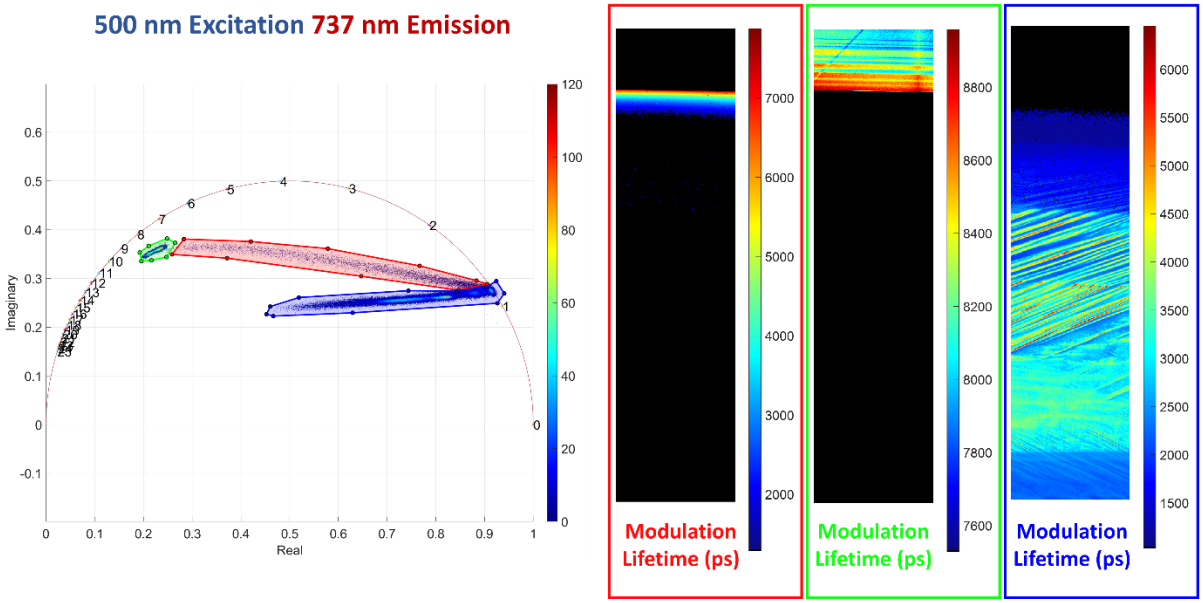



*Figure 72*[194] *- ROI selections from the phasor diagram in Figure 69, showing the variation in modulation lifetime in the CVD diamond and HPHT substrate.*

Figure 73 illustrates how ROIs in the lifetime maps can be used to find the corresponding clusters in the phasor plots. A series of ROI segmented on the luminescence intensity (summed photon count) maps are shown with their corresponding phasor plot. This technique is useful to help understand the spectroscopic (phasor lifetime) signatures of specific spatial ROIs. The difference between ROI 1 and 3 is particularly interesting because these two linear clusters both have an anchor at ~1.1 ns, but their other anchor is a different charge state of NV.

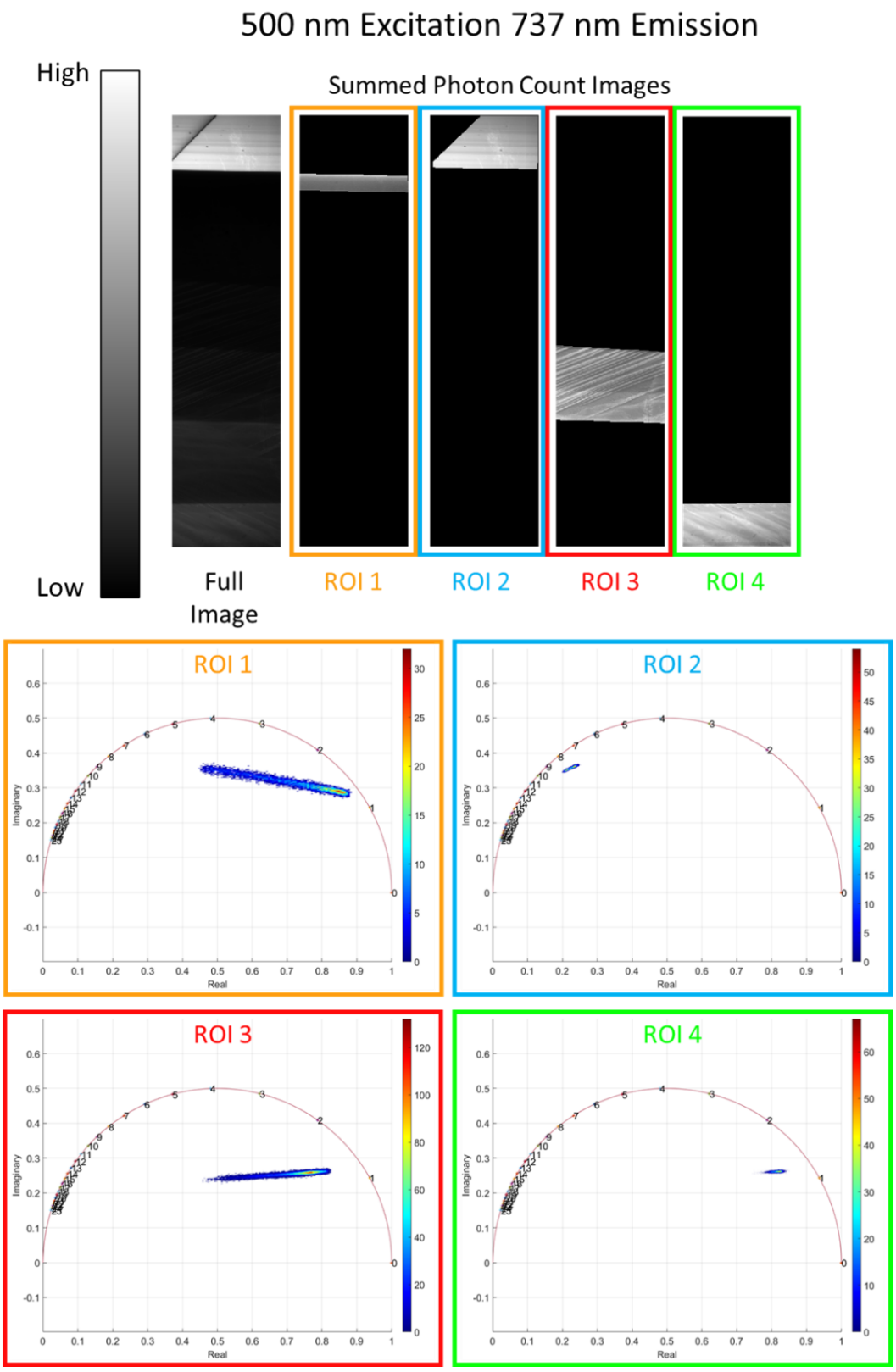



*Figure 73 – These ROI selections operate in reverse to Figure 72, and show data from Figure 69. The images were used to extract the local phasor plots for four ROIs. The phasor plot outlines correspond to the colours of the ROI photon count images. This is a useful capability if a specific region on the sample, as opposed to a lifetime cluster on the phasor plot, is of interest.*

The striations in the CVD diamond emission lifetime maps are interesting because the preferential uptake of silicon is not currently well understood[121]. Figure 74 presents line profiles were taken through the luminescence intensity (summed count) maps at a) 675 nm and b) 737 nm emission wavelengths, and c) the beta map corresponding to $NV^0$ emission ($\beta_1$) at 737 nm. The red arrow indicates the line profiles taken in each image. Figure 74 d), shows the scatter plot of the image pixels plotted against their emission intensities (total photon counts) at 675 nm and 737 nm.

Figure 74 e) presents the extracted line profiles from the three intensity maps; the coloured backgrounds and corresponding coloured data points in d) correspond to the different spatial regions in the intensity and beta images. A magnified section of the graph is presented in f), showing strong correlation between all three line plots. The peaks in the graph represent the striations where the increase of emission from $NV^0$ is probably due to higher nitrogen levels, created by the preferential uptake of nitrogen at different growth planes.

The red data points in d), which correspond to the bottom band, appear to have a different linear relationship compared to the other data points. In this region, the number of counts in the 737 nm emission band increases sharply, but the population fraction (beta) of $NV^0$ decreases, as shown in e). This contrasts with the CVD regions featuring striations where the $NV^0$ beta varies in the same direction as the intensity at 737 nm. The previously discussed decrease in mean lifetime of the 737 nm emission observed in the bottom band, suggests a higher ratio of $SiV^-$ to $NV^0$.

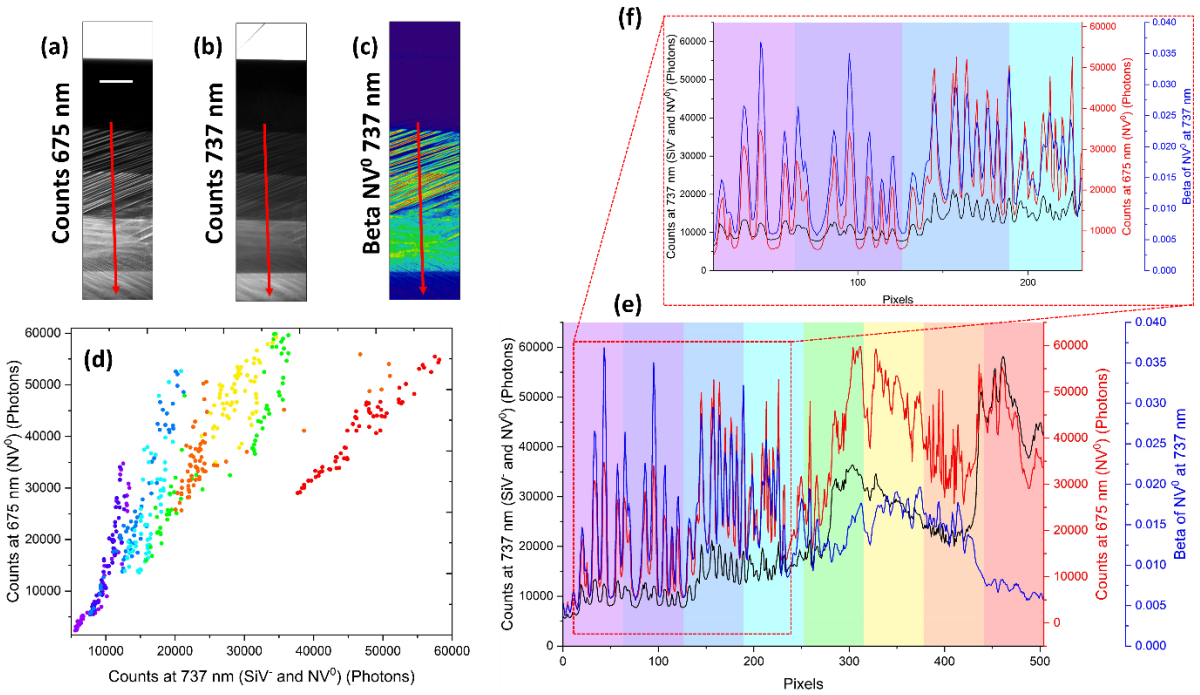



*Figure 74 - (a) Integrated photon count image from emission centred at a wavelength of 675/2 nm. The scale bar is 0.2 mm. (b) Integrated photon count image from emission centred at a wavelength of 737/2 nm. (c) Beta map of $NV^0$ from fit shown in Figure 71. The red lines through these images denote the line profile used for panels (e) and (f). (d) A scatter plot of the integrated photon counts of the two emission bands showing regions of linear correlation. (e) A full line profile of images (a)-(c) showing the change in intenisty and beta for $NV^0$. The coloured bars correspond to the colours of the data points in (d). (f) Line profile of counts at emission wavelengths of 675 and 737 nm, and beta of the $\tau_1$ = 19,000 ps component attributed to $NV^0$ showing a strong correlation in the locations of the peaks and troughs.*

Figure 75 shows the intensity (total photon counts) images of the emission at a) 675 nm and b) 737 nm with c) an indication of different ROIs. These ROIs image pixels are plotted in e) against their intensities (total photon counts) at 675 nm and 737 nm, with a black y = x line.

ROI 1 and ROI 2, which are the two upper bands in the CVD diamond, show similar gradients in the scatter plot, where the emission at 675 nm attributed to $NV^0$ is relatively high and the emission at 737 nm is low. Most of the emission at 737 nm is attributed to $SiV^-$, as shown from the spectra in Figure 71, so the emission at 737 nm can be attributed to primarily that of $SiV^-$. ROI 1 and ROI 2 are regions where the striations are well defined, compared to ROI 3, and where the data points in the graph have started to skew towards higher emission at 737 nm, along with a change in gradient. In ROI 4, where the highest emission from $SiV^-$ is expected, the data points almost follow the y = x line.

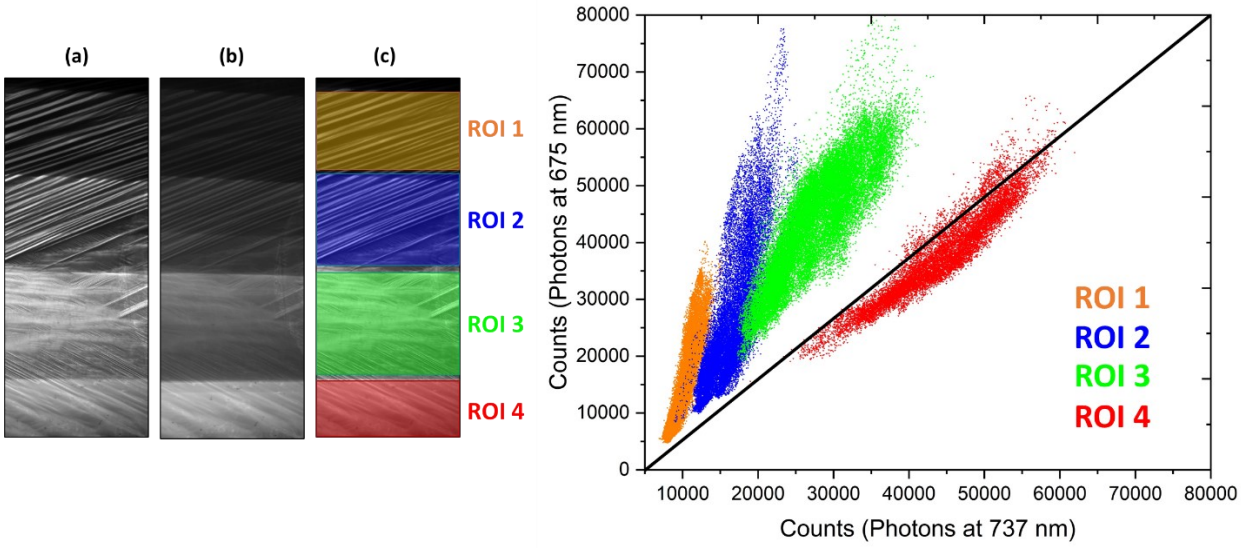



*Figure 75 – An extension of the analysis shown in Figure 74. Images a) and b) are the summed intensity images from the CVD diamond of 675 and 737 nm emission, respectively. The emission from 675 nm is caused by $NV^0$, whilst the emission at 737 nm is dominated by $SiV^-$. Image c) shows the four ROI regions which were used to plot the scatter graph. The scatter graphs show the relationship of the pixel counts for the two emission bands, where the black line indicated unity gradient. ROI 1 and 2 show similar gradients, but ROI 3 has a decreased gradient. ROI 4 shows a significant change relative to the other ROIs.*

The emission is complex, and more data, such as secondary ion mass spectroscopy (SIMS) of the various layers, is required to quantify the nitrogen and silicon concentrations. An acquisition of this region at an excitation wavelength that does not excite $NV^0$, would be useful to help confirm the $SiV^-$ emission signature. Measurement of $SiV^0$ should also be undertaken. Using these methods, a greater understanding of this sample could help explain how silicon incorporates itself into diamond. This was beyond the scope of this project. A summary of the lifetime components and their attributed defects is shown in Table 5.

*Table 5 - A summary of the lifetime components under 500 nm excitation at 737 nm emission and their attributed defect.*

| **Lifetime Component** | **Attributed to -** |
|---|---|
| $\tau_1$ – 19 000 ps (CVD Diamond) | $NV^0$ (Based on spectrum and lifetime) |
| $\tau_2$ – 11 400 ps (HPHT Diamond) | $NV^-$ (Based on spectrum and lifetime from a quenched emitter) |
| $\tau_3$ – 4 400 ps (HPHT Diamond) | $NV^-$ (Based on spectrum and lifetime from a quenched emitter) |
| $\tau_4$ – 1 100 ps (CVD Diamond) | $SiV^-$ (Based on spectrum and lifetime) |
| $\tau_5$ – 615 ps (HPHT Diamond) | $NV^-$ (Based on spectrum and lifetime from a quenched emitter) |

## *Single-point spectrally-resolved emission lifetime measurements on a synthetic CVD diamond with HPHT substrate*

Hyperspectral imaging and FLIM at two emission wavelengths can be complemented by hyperspectral lifetime spectroscopy to further resolve the emission from different emissive defects. The luminescence instrument developed provides the capability to measure spectrally resolved decay profiles, where the detection monochromator is swept over a large wavelength range and the decay is time-resolved at each wavelength. This was applied to locations in the CVD diamond and HPHT substrate. This technique will reveal any differences in the spectral profiles of the three component HPHT substrate emission decay profile. To enable phasor analysis, the frequency divider on the TCSPC card was used, as discussed in chapter 4.

The monochromator was swept to sample the emission spectrum excited at 500 nm (1.25 nm FWHM, 0.4 mW of total power) every 0.5 nm, using the same x40 0.6 NA objective lens as the FLIM measurements. For each spectral measurement, signal was integrated for 5 s and data was collected at two locations: ROI 1 in the HPHT substrate and ROI 2 in the CVD diamond, as shown in Figure 76 a). The emission intensity spectra are shown in Figure 76 b), where the CVD emission from, ROI 2 can be shown to match that of the hyperspectral data in Figure 63. For the emission spectrum of ROI 1 in the HPHT substrate, the ZPL of $NV^0$ is observed at 575 nm. This feature is relatively weak compared to the emission of $NV^-$ and was not apparent in the previous hyperspectral data. Its increased brightness may have been due to charge transfer from $NV^-$ due to the higher excitation power density for this point measurement.

When this spectrally-resolved lifetime data was analysed using iterative fitting, the lifetime components were fixed to the values previously obtained: the CVD diamond emission in ROI 1 was fitted to a double exponential decay of fixed lifetimes of $\tau_1$ = 19,000 ps and $\tau_2$ = 1,100 ps, and the HPHT emission was fitted to a quadruple decay with lifetime components fixed at τ1=19,000 ps, τ2=11,400 ps, τ3=4,400 ps, and τ4=615 ps. The beta parameters of the two ROI components are shown in Figure 76 c). Beta 1, which is the 19 ns lifetime component corresponding to $NV^0$, is relatively flat until 700 nm, where the population fraction rapidly approaches zero. This coincides with the increase of the beta 2 parameter relating to the 1.1 ns lifetime component attributed to $SiV^-$, which peaks at the ZPL of 737 nm. The spectral phasor plot in e), with colour representing emission wavelength in nm, confirms these results. Below 700 nm, the phasor points are clustered at the ~19 ns location on the universal circle. Above 700 nm, the data points follow a straight line towards ~1.1 ns on the other side of the circle, reaching the furthest extent at 737 nm. If any other defects

were emitting in this emission range, then this phasor plot would not show a linear chord between these two anchors.

The presence of $NV^0$ emission in the HPHT substrate from ROI 2 meant that four components were needed to fit the luminescence data: iterative fitting was applied using lifetime components fixed at $\tau_1$=19,000 ps, $\tau_2$=11,400 ps, $\tau_3$=4,400 ps, and $\tau_4$=615 ps, as used previously. The results are shown in Figure 76 c). Beta 1, which represents the emission from $NV^0$ is shown as blue in the graph, peaks at 575 nm, before approaching zero at 650 nm. This is expected, given the weak nature of the emission, and the much higher intensity of the $NV^-$ emission. The primary purpose of this measurement was to discover the spectral variation of the other three beta parameters, which are attributed to the emission of $NV^-$. These show no significant deviation from each other and approximately follow the same profile. This indicates that the components have similar emission profiles, or that all three components are associated with the same emitting species – presumed to be $NV^-$.

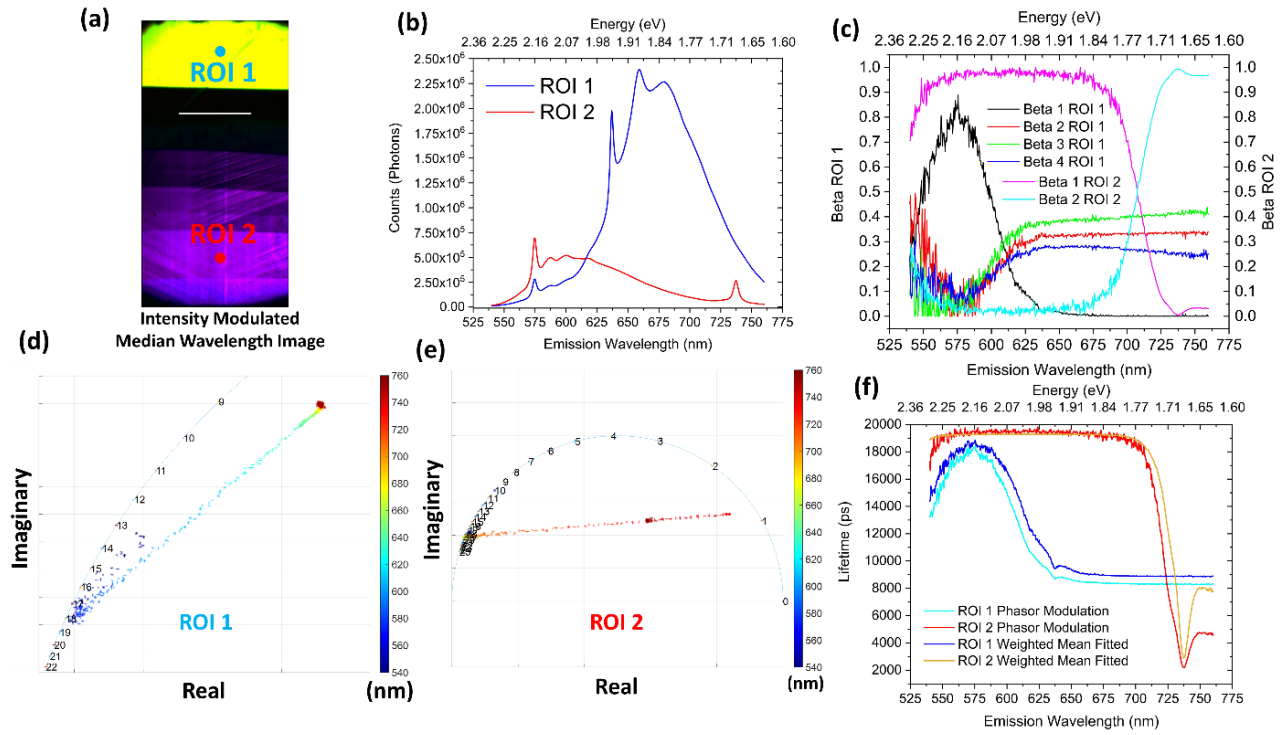



*Figure 76*[194] *– Point-spectrally resolved TCSPC data recorded using a 40x 0.6 NA objective, with an excitation wavelength of 500 nm (1.25 nm FWHM) using a integration time of 5 s per emission wavelength. (a) Intensity modulated median wavelength image from Figure 63. The scale bar is 0.5 mm. (b) Emission spectra calculated from the integrated photon count of the decay profile acquired at each emission wavelength, with a data point every 0.5 nm. The locations of the two ROIs are shown in (a). (c) population fraction (β) parameters from MLE fitting of the spectrally-resolved decay curves for ROI 1 to a quadruple exponential decay model and a double exponential for ROI 2. (d) Spectrally-resolved phasor plot of ROI 1 demonstrates a linear region between a monoexponential decay of ~19 ns ($NV^0$) for the blue end of the emission spectrum, and a point inside the universal circle for the red end of the emission spectrum. Each data point corresponds to a different emission wavelength (indicated by the colour scale). (e) Spectrally-resolved phasor plot for ROI 2 shows a similar feature as (d) between a monoexponential decay of ~19 ns for the blue end, and a point near a monoexponential decay of ~1.1 ns for the red end of the emission spectrum. Points for an emission wavelength below 700 nm are found on the universal circle at ~19 ns. (f) The phasor modulation lifetime and intensity-weighted mean lifetime from MLE fitting as a function of emission wavelength.*

More evidence for this is shown at the ZPL of $NV^-$ at 637 nm, which is unique to that defect. If the lifetime components are unrelated, a change should be noted at 637 nm, but this is not observed. This was observed in the CVD diamond for the $NV^0$ and $SiV^-$ defects at 737 nm where the emission bands overlap, however. The spectral phasor plot shown in d) shows a similar feature to the CVD diamond phasor plot in e) of Figure 76. There is a linear region from a point on the universal circle at ~19 ns to a point inside the universal circle. This point inside the circle matches the HPHT cluster in

the FLIM maps previously shown, see Figure 67 and Figure 72. Extrapolating the line to the universal circle, and fitting to a double exponential model with a lifetime with ~19 ns of the other anchor, produces a poor fit. This is because this line represents a change in population fraction between a monoexponential defect, $NV^0$, and a more complex decay of $NV^-$. The $NV^-$ anchor lays inside the universal circle instead of a point on the circle.

The emission from $NV^0$ does not extend >650 nm, which explains why in the FLIM mapping of Figure 64 no feature corresponding to $NV^0$ was detected. The modulation and intensity-weighted mean lifetimes of the two ROIs are shown in Figure 76 f). They are in good agreement with each other, suggesting that the model provides a reasonable fit for the data. This spectrally resolved analysis of the fitted decays indicates that those three components originate from the same emitter, and that the HPHT substrate has two defects under these conditions. These defects are the two emitting charge states of NV.

## *Single-point spectrally-resolved excitation-emission-lifetime measurements of a synthetic CVD diamond with HPHT substrate*

The ability to vary excitation wavelength offers a powerful method to enhance contrast of luminescence signals from different emissive defects and to preferentially excite specific emitters. Coupled with emission wavelength and lifetime measurement, an excitation-emission-lifetime matrix can be generated – at a single point or image wise via stage scanning.

The previously described spectrally-resolved lifetime measurement at a point on the HPHT substrate indicated a complex exponential decay profile (characterised by four lifetime components) that may be result from quenched $NV^-$ emission, and a monoexponential component attributed to $NV^0$. Since it is unlikely that all these emitters will have the same absorption spectrum, resolving the excitation wavelength may help distinguish their emission and help elucidate their origin.

An excitation-emission-lifetime matrix was acquired by scanning the central excitation wavelength from 430 to 750 nm, with a 2.5 nm step size, and resolving the emission scanning from 450 to 780 nm with a 2 nm step size. To enable such a broad excitation and emission band to be measured, the 50/50 beamsplitter and LVLWP (linear variable long waver pass) filter were used, with the LVLWP filter cut-on set to 20 nm longer than the excitation wavelength. This provided some blocking of the excitation light (OD4), with the spectrograph providing the remainder of the blocking (OD3). A spectral acquisition time of 0.5 s was chosen to collect sufficient photons, noting that a small

increase in spectral acquisition time leads to a large increase in total acquisition time when the luminescence signal is sampled to such precision with this many dimensions.

As previously discussed, an IRF must be measured for each excitation wavelength to account for path length differences and temporal shifts in the ultrafast supercontinuum excitation pulses. *FLIMfit* was used for the analysis of the data, applying its capability to account for spatially varying IRFs. The spectral (excitation-emission) information is encoded as an *x-y* image for analysis in *FLIMfit*, with an image for each temporal bin. The IRF measurements were collected using a mirror at the sample plane and measuring an attenuated reflection of the excitation laser at each excitation wavelength over an emission spectral detection band of 1 nm. This IRF data was then encoded as an x-y FLIM data set but with the single emission decay profile replicated across all spectral emission bins. For the excitation-resolved measurements to be useful for PLE spectroscopy, it is necessary to account for variations in the spectral power density incident at the sample plane. This was measured using a power meter at the sample plane after the objective lens, for which the results are shown in Figure 77 a). This was used to normalise the total emission intensity (summed photon count) data. It should also be noted the spectral discrimination of the prism-based monochromator for excitation varies as a function of wavelength, for which an experimental characterisation is shown in Figure 77 b).

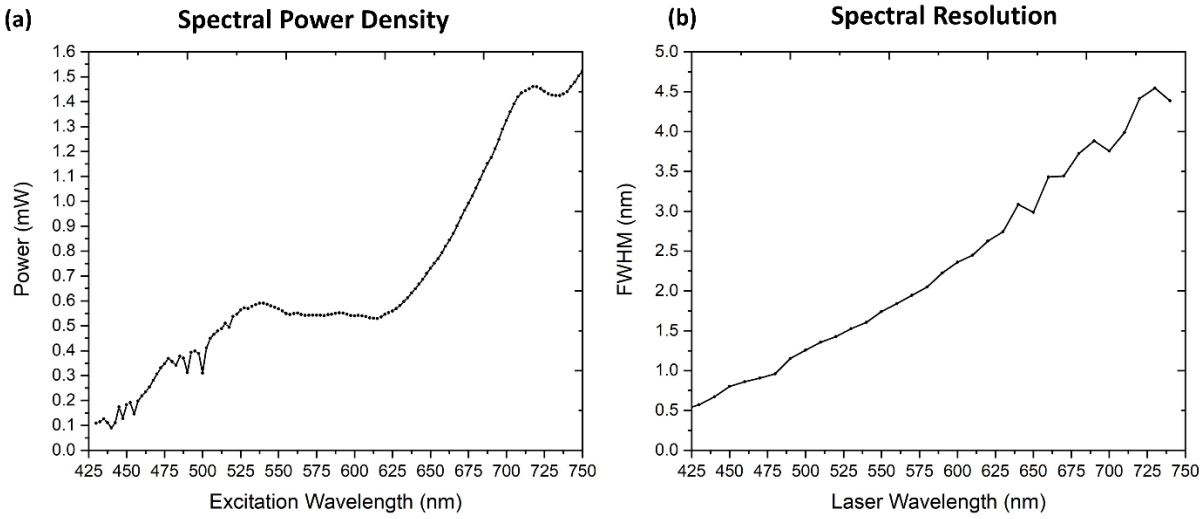



*Figure 77*[194] *- a) shows the variation in the spectral power density at the sample plane from the tuneable supercontinuum laser source. b) shows the variation in spectral resolution of the excitation source, as measured by the imaging spectrograph, with an increase in linewidth attributed to the reduced dispersion at longer wavelengths.*

The frequency divider setting was used for the TCSPC measurement to make this experiment compatible with phasor analysis. The measured region of interest on the HPHT substrate is shown in Figure 78 a), from which luminescence was collected using a 4x 0.16 NA objective lens (Olympus, UPlanAPO).

To display the lifetime information on the spectral phasor plot, the excitation-emission image was treated as an *x-y* spatial image (as shown in Figure 79 c) and d), to which phasor clusters can be mapped analogous to conventional FLIM data. The spectral phasor plot is shown in Figure 78 b), which includes an inset of the full spectral phasor plot. There are phasor data points close to zero lifetime that correspond to lines with unity gradient in the intensity (summed photon count) images in Figure 78 c) (blue region) and Figure 78 d) that result from scattered excitation light transmitted through the LVLWP filter. This bleed-through is attributed to insufficient blocking of excitation radiation by the LVLWP and could be reduced by adding an additional matching filter to the system. The most significant cluster in the spectral phasor plot maps to the yellow region in Figure 78 c) and, in addition to this cluster, there are several data points along a line from this cluster to the universal circle for a ~19 ns component, which we attribute to $NV^0$ emission. Broadly, this phasor plot is similar to the emission spectral phasor plot in Figure 76 d), with the complexity associated with the large cluster attributed to $NV^-$ emission.

The presence of $NV^0$ emission is also in the log plot of intensity (summed photon counts) in Figure 78 d), where the orange arrow indicates the ZPL of $NV^0$. In addition to the ZPL of $NV^0$, the emission ZPL of $NV^-$ is indicated by the red arrow in both intensity images. Resonant excitation of the phonon side bands associated with the $NV^-$ ZPL is indicated in both images as the green arrows. This feature is more difficult to observe for defects with weak phonon side bands, such as $SiV^-$.

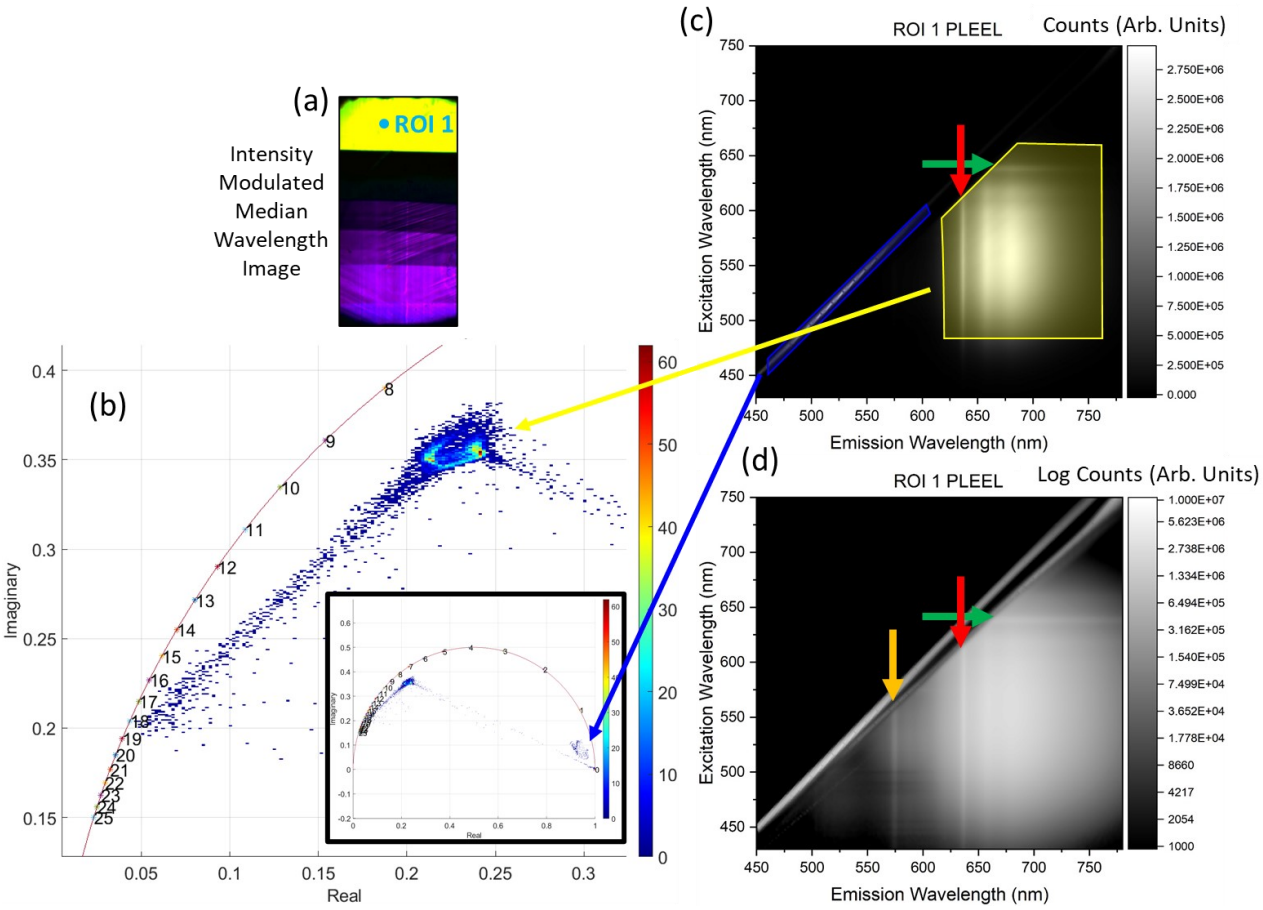



*Figure 78*[194] *– Phasor analysis of excitation-emission-lifetime data from a location on the HPHT substrate. An intensity modulated median wavelength image is shown in (a) with the marked ROI, from Figure 63. The excitation-emission phasor plot of the excitation-emission-lifetime image is shown in (b), where colour represents the number of pixels with that phasor coordinate. There is a complex region and a linear region extending from a lifetime of ~19 ns on the universal circle. (c) shows the emission intensity (summed photon count) excitation-emission matrix of the ROI in the HPHT substrate. This indicates that the bulk of the emission comes from $NV^-$ emission (>637 nm, yellow region). A log scale plot of (c) is shown in (d). See text for explanation of the coloured arrows.*

The modulation lifetimes were calculated from the spectral phasor data, and the corresponding modulation lifetime excitation-emission maps are plotted in Figure 79 using two different lifetime colour scales. In Figure 79 b), there are two distinct regions apparent, in addition to the brown diagonal line representing the excitation light bleed-through. Starting at 560 nm emission wavelength, there is a high modulation lifetime of 18 ns (shown in white), which reduces to <9 ns as the emission wavelength increases. The orange arrow indicates a slight increase in modulation lifetime at 575 nm, appearing as a white region clearer in Figure 79 b), which represents resonant excitation of $NV^0$, but this is weak. A variation in modulation lifetime with excitation wavelength in

all emission bands is apparent in Figure 80 b), which also indicates that a 500 ps modulation lifetime increase occurs for emission wavelengths >650 nm, for excitation wavelengths between 475 nm and 575 nm. This corresponds to the complex 'swirl' in the region attributed to $NV^-$ emission on the spectral phasor plot of Figure 78 b).

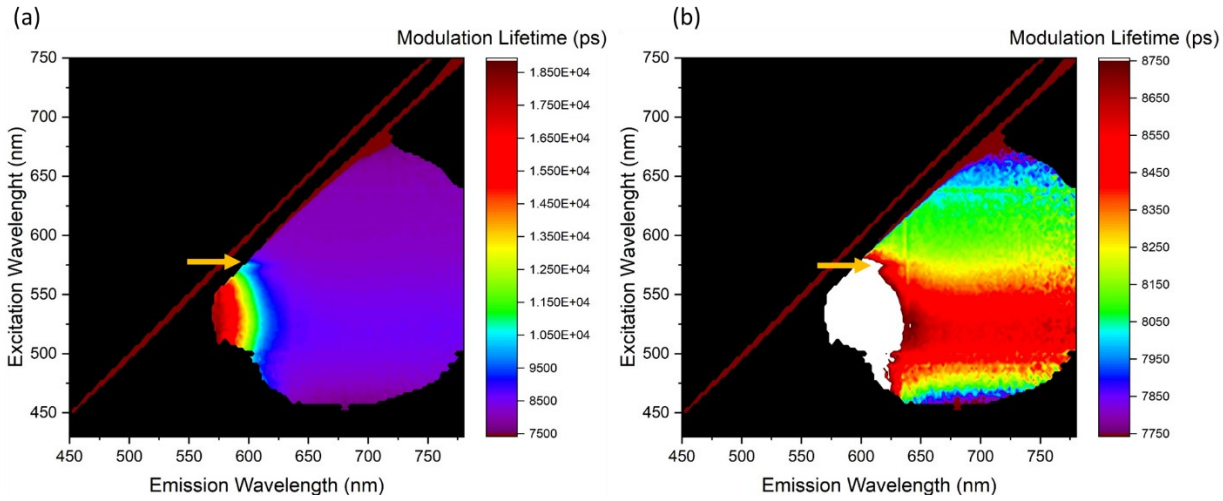



*Figure 79*[194] *- The plot in a) shows the modulation lifetime-excitation-emission matrix corresponding to the phasor plot in Figure 78 b). b) shows the same data as a) plotted on an 11x expanded lifetime scale to enhance the contrast. See text for explanation of arrow.*

Using FLIMfit to analyse this excitation-emission lifetime data, generated the weighted mean lifetimes and beta spectral maps shown in Figure 80. Data were iteratively fitted to a quadruple exponential decay model with the following fixed lifetime components (as used in the FLIM mapping data): $\tau_1$=19,000 ps, $\tau_2$=11,400 ps, $\tau_3$=4,400 ps, and $\tau_4$=615 ps. The two weighted mean lifetime maps shown in Figure 80 a) and d) show similar trends as the modulation lifetime maps in Figure 79. The beta 1 ($\beta_1$) component is again attributed to the $NV^0$ emission, with a lifetime of 19,000 ps and shows a high intensity localised near the $NV^0$ ZPL at 575 nm. Similar to the spectrally resolved lifetime measurements in Figure 76, the beta 1 emission is close to zero at emission wavelengths greater than 650 nm, and so $NV^0$ is unlikely to be responsible for any variations in lifetime observed at emission wavelengths greater than 650 nm. For the beta 2 and beta 4 components attributed to $NV^-$, the population fraction is not uniformly distributed which indicates that the three lifetime components attributed to $NV^-$ emission do not have the same spectral properties. This may be due to the wavelength dependant nature of quenching for the $NV^-$ emission, but the origin of this quenching mechanism is still not known. In addition, this model does not fully describe this complex quenched decay, and fitting can get less accurate with a reduced photon count, such as occurs at the extreme ends of the emission spectra.

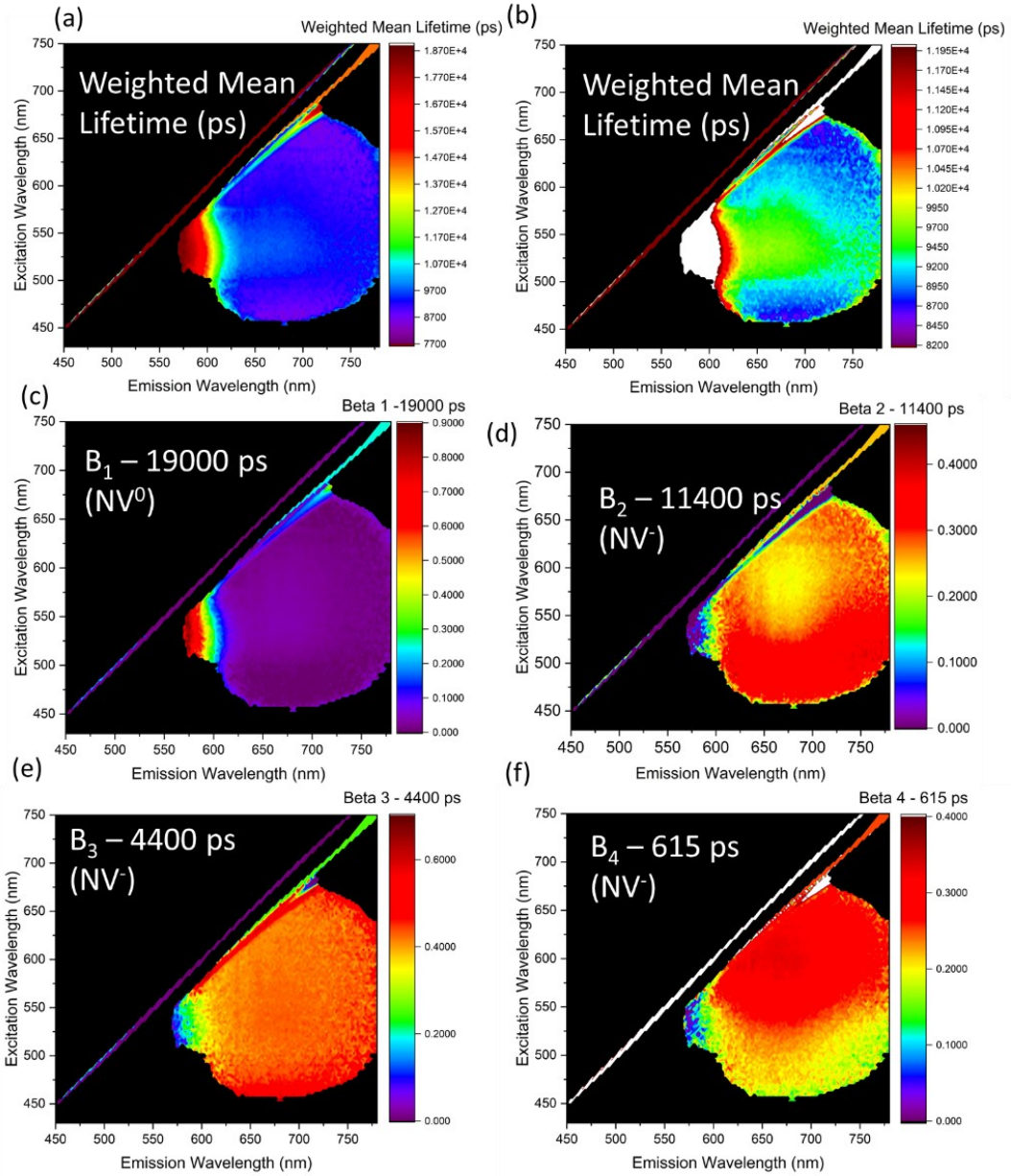



*Figure 80*[194] *- Iteratively fitted excitation-emission-lifetime plots. Plots of (a, b) intensity-weighted mean lifetime and (c, d, e, f) population fraction $\beta_i$ against excitation-emission wavelength for a fit to a quadruple-exponential decay model of luminescence from an ROI in the HPHT substrate, indicated in Figure 78 a).*

The quenching can be considered in terms of two effects: the quenching that results in the three modelled lifetime components present over the entire spectral domain, that present spatial variations in intensity, and the excitation-resolved spectral variations in lifetime between 475 and 575 nm excitation. The latter variations can be further explored comparing line profiles of the modulation and fitted weighted mean lifetimes and beta values, as shown in Figure 81.

The red-bounded graph shows the excitation-resolved lifetime spectra for emission at 706 nm and the beta plot corresponding to the emission of $NV^0$. Whilst being offset, the modulation and weighted mean lifetime excitation spectra measured at 706 nm emission present similar trends with the peaks of these two lifetime spectra corresponding to the peak of the $NV^0$ beta curve. This could indicate an interaction between the two NV charge states, with charge transfer causing a change in lifetime of $NV^-$ emission that varies as a function of excitation wavelength. As the lifetime increases in the excitation range 475 to 575 nm, it could suggest that the quenching mechanism between $NV^-$ and $NV^0$ only occurs when the $NV^0$ electron is in the ground state, since $NV^0$ is not excited at wavelengths longer than 575 nm. However, this would not explain the change in lifetime below 475 nm.

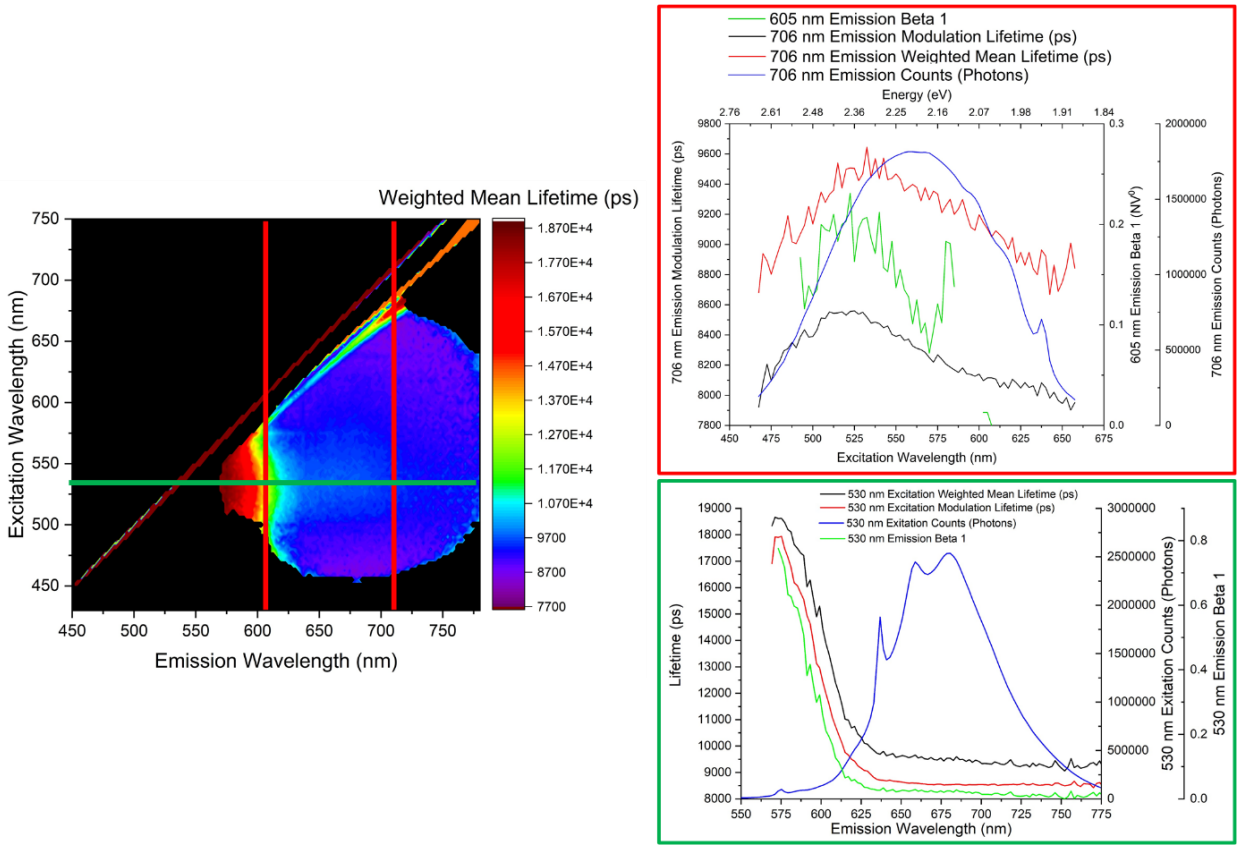



*Figure 81*[194] *- The EELM weighted mean lifetime plot shows a green and two red lines corresponding to three different wavelength measurements which are extracted in the bordered graphs. The beta corresponding to $NV^0$ (beta 1) is shown with the weighted mean lifetime from the MLE fit and the corresponding phasor modulation lifetime. The peak at 580 nm of 605 nm emission beta 1 (green line) is caused by laser bleed through in the red bordered plot.*

The green line on the lifetime map relates to the green-bounded graph, which shows the emission spectra for lifetime, beta, and intensity (total photon counts) for excitation at 530 nm. The spectrum is dominated by the emission from $NV^-$, and the modulation and weighted mean lifetimes very quickly reduce. Whilst the modulation lifetime is relatively flat from 650 nm, the weighted mean lifetime spectra slowly decrease, which indicates a discrepancy between the fitting model and the spectral phasor analysis. As previously discussed, whilst a triple-exponential model provides a reasonable fit to the emission attributed to $NV^-$, it is an approximation and may not exactly reflect the true decay profile.

The spatially varying decay profiles of the emission attributed to $NV^-$ could relate to a spatially varying quencher in the HPHT substrate. NV quenching has previously been explored[134, 197]. It has been shown that $NV^0$ can be quenched by $N_s^0$, and $NV^-$ can be quenched by $N_s$. It has also been shown that $NV^0$ can be quenched without subsequent quenching of $NV^-$, but the reverse has not been reported[197]. In this case, quenching of $NV^-$ may explain our observations, but no quenching of $NV^0$ is apparent, as the $NV^0$ emission is attributed to the monoexponential decay profile with a lifetime of 19 ns that agrees with literature values for $NV^0$. It could then be inferred that $N_s^0$ cannot be the quencher, but the other charge states cannot be ruled out. It should be noted that in the HPHT substrate $NV^0$ emission is weak, and the repetition rate of the laser does not allow accurate measurement of such long lifetime components.

The banding in the HPHT substrate, assumed to have been formed during growth, could result from variations in nitrogen incorporation during synthesis, as differences of 30°C can cause such a variation[198, 199]. It is therefore suggested that nitrogen is involved in the quenching mechanism. A detailed study of the HPHT substrate is required using secondary ion mass spectroscopy (SIMS), above bandgap excitation, FTIR absorption imaging, and potentially polarisation resolved measurements to understand the origins of the quenching mechanism. However, this is beyond the scope of this project.

Future experiments using the instrument developed for this thesis could include spatially-resolved excitation-emission-lifetime mapping of the entire sample, although this would take many days and practical considerations could require the data to be acquired at lower spectral resolution. Replacing the 50/50 beamsplitter with a more efficient method to separate excitation radiation and luminescence could improve the collection efficiency of the system, which would decrease the data acquisition times.

## *Conclusion*

The developed multidimensional luminescence instrument has been applied to a synthetic HPHT/CVD diamond, initially analysing the luminescence with respect to excitation and emission wavelength, and two spatial dimensions to realise hyperspectral imaging. This was then extended to spectrally-resolved lifetime analysis. The luminescence was observed to present decay profiles with different temporal properties as a function of spatial location. The HPHT substrate was observed to contain $NV^-$ defects, under low average excitation power at 500 nm, using line scanned hyperspectral imaging, but $NV^0$ was also observed under higher power single point excitation. In the CVD region of the diamond, emission from $NV^0$ and $SiV^-$ defects was observed from varying concentrations of defects occurring in bands, caused by intentional variation of growth conditions, and localised in striations that were not intended as a consequence of the growth conditions.

FLIM maps were acquired at two emission wavelengths with 500 nm excitation to study the spatial variation of the three emitting defects. Phasor analysis was used in conjunction with iterative fitting of the decays to reveal locations of high contrast striations in the CVD diamond. The HPHT substrate revealed a more complex decay, which was further investigated using lifetime data spectrally resolved with respect to excitation and emission wavelength. This combination of excitation-emission-lifetime matrices, with the spatial variation of intensity and lifetime, suggested that the $NV^-$ defect was quenched by an unknown quenching agent. This quenching mechanism is possibly nitrogen related.

# Chapter 6 - Spectroscopic and lifetime analysis of the $SiV^-$ defect in synthetic diamond

## Outline

In this chapter, two synthetic diamonds, chosen because of their strong emission of $SiV^-$, are investigated using several of the techniques available in the developed multidimensional luminescence microscope. This chapter discusses the application of polarisation-resolved measurements to study the fundamental photo-physics of the $SiV^-$ defect.

The measurement and understanding the $SiV^-$ energy level structure could reveal new opportunities for quantum applications using the optical manipulation of transitions. A detailed understanding of the energy level structure in relation to polarisation, lifetime and energy gaps is required. This chapter enhances existing information and provides new insight into the excited state lifetime as a function of excitation wavelength. This information may also be useful in the creation of a $SiV^-$ laser, similar to a previously reported diamond colour centre laser[200].

## Introduction

### *$SiV^-$ point-excitation-emission-lifetime matrix and PLE spectra*

The HPHT/CVD diamond sample, previously discussed in chapters 4 and 5, enables the study of $SiV^-$ due to its high concentration of this defect. PLE spectroscopy measurements of the $SiV^-$ defect have previously been reported[154, 155, 156], but with more limited measurements than this multidimensional instrument can provide. Polarisation-resolved analysis allows the orientation of excitation and emission dipoles to be studied and lifetime measurements offer a contrast mechanism that has not been widely exploited to study $SiV^-$ emission. The wide excitation wavelength range of the instrument is useful since $SiV^-$ can be excited using photon energies up to ~3.49 eV (355 nm), and the excitation-emission-lifetime resolved data can determine the optimal excitation wavelengths to study the defect.

The bottom CVD region of the diamond contains the most emission from the $SiV^-$ defect, and so this was the location of study. As shown in Figure 62, strain-induced birefringence is more common towards the periphery of the sample, so locations of minimal strain, further from the edge were chosen. Single centres cannot currently be measured as the instrument does not include a Hanbury-

brown Twiss (HBT) system (for identification of single centres); therefore all measurements are of ensembles of defects.

The first experiment to study $SiV^-$ involved the acquisition of high-resolution excitation-emission-lifetime data, centred on the ZPL of the $SiV^-$ defect at 737 nm. As this measurement was conducted at room temperature, the fine structure of the defect is not resolvable[154]. The excitation wavelength was scanned from 400 to 680 nm using the prism-based monochromator in 1 nm steps, whilst the imaging spectrograph monochromator was scanned from 725 to 750 nm in 0.2 nm steps. The entrance and exit slit of the imaging monochromator were set so the detection band at each wavelength was 1 nm, and the step size allowed sub-Nyquist sampling. Spectral integration time was set to 0.1 s, which results in a total acquisition time of ~3 hours, and this was undertaken using a 10x 0.3 NA objective lens (Olympus, UPlanFL N). The power of the excitation laser source was measured at the sample plane for each wavelength, and this was used to normalise the collected luminescence signal. The variation in the FWHM of the excitation laser source was as reported in Figure 77 for this experiment. The results of the experiment are shown in Figure 82. As the measurement was made before the variation in excitation wavelength IRF was discovered, see chapter 4, this data was analysed using a single IRF for all excitation wavelengths and the $t_0$ position was used as a fitting parameter, which shifted from -236 to + 60 ps from the lowest to highest excitation wavelength.

In Figure 82, the black projection at the back shows the excitation spectrum for this single point on the sample. Phasor analysis cannot be applied to this data because the TCSPC frequency divider setting was not used and so only a partial decay within the laser period was measured. FLIMfit was used to fit the data to a double exponential decay model, with initial guesses for lifetime components of 19 ns and 1.1 ns that resulted in good fits. 3×3 spectral binning was used to increase the accuracy of the result. The emission spectra are consistent in shape across the excitation wavelengths used, and peak at 737 nm, consistent with the $SiV^-$ ZPL. The 1.1 ns lifetime component is consistent with $SiV^-$ and the 19 ns lifetime component is attributed to $NV^0$, which is known to emit in this region of the sample and will spectrally overlap with the emission in this emission band.

For any excitation wavelengths below 600 nm, the emission spectrum peaks at 737 nm, and the intensity-weighted mean lifetime reduces to ~3 ns from 725 to 737 nm, before rising again to ~9 ns. Above 600 nm excitation, there is insufficient photon energy to excite $NV^0$, so the lifetime is monoexponential at 1.1 ns (purple colour in Figure 82). The emission band at 737-738 nm yields the most $SiV^-$ emission and so this was utilised for PLE spectroscopy studies.

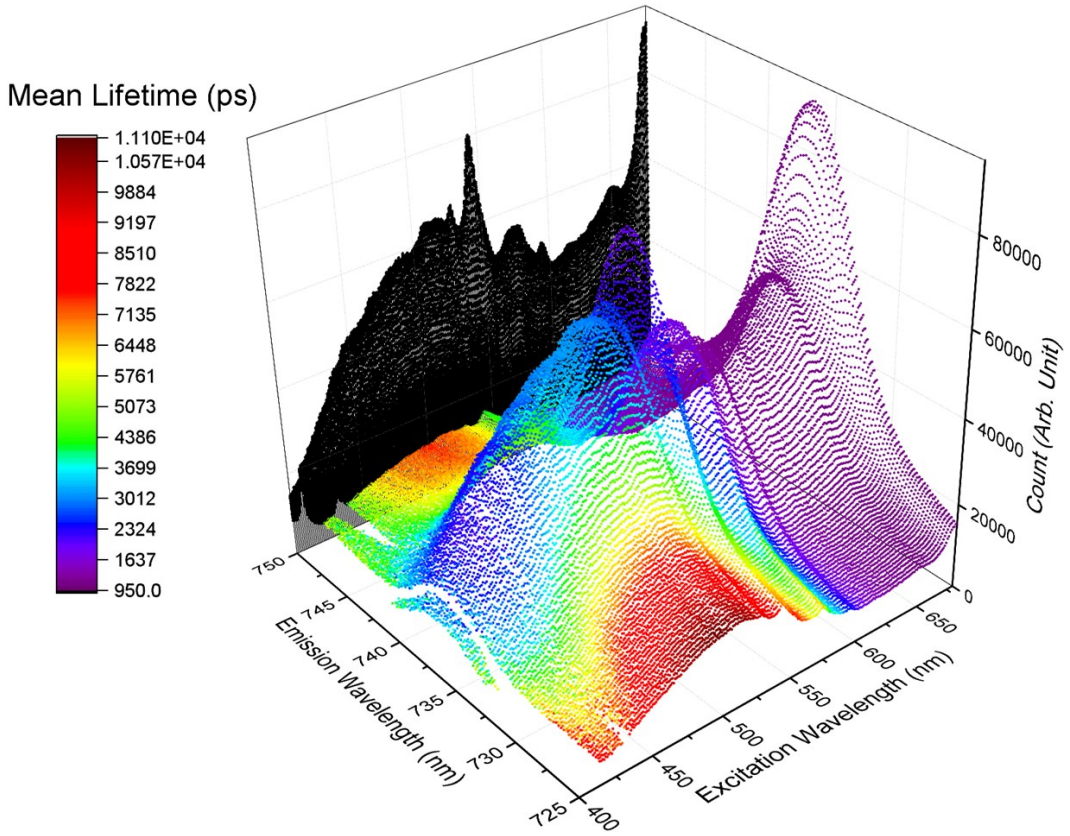



*Figure 82 – A power-corrected excitation-emission-lifetime matrix for a location containing $SiV^-$ and $NV^0$ in the CVD diamond. The black outline is a projection of the emission wavelength graphs, which produces a PLE spectrum, dominated by $SiV^-$ emission. Below excitation wavelengths of 600 nm, the weighted mean lifetime shows a more complex profile due to contributions from the $NV^0$ phonon side band, causing a variation in the weighted mean lifetime with emission wavelength. For excitation wavelengths above 600 nm, there is insufficient energy to excite $NV^0$, reducing the decay to a monoexponential with the lifetime of $SiV^-$ at 1.1 ns.*

High resolution PLE spectroscopy measurements of the sample were undertaken at the $SiV^-$ ZPL at 738 nm emission using a 2 nm bandpass filter. With 5 s spectral acquisition time using a 10x 0.3 NA objective lens (Olympus, UPlanFL N), the count rate on the detector was kept to a peak of 1.5 x $10^6$ cps to avoid pulse pile up. The excitation wavelength was scanned from 400 to 680 nm in 1 nm steps. The fluorescence filter cube comprised of an excitation 694 nm SP filter (FF02-694/SP, Semrock), a dichroic mirror at 705 nm (FF705-Di01, Semrock), and an excitation filter at 715 nm (FF01-715/LP, Semrock). For analysis using *FLIMfit*, lifetime components of 18,425 ps, attributed to $NV^0$, and 1,088 ps, attributed to $SiV^-$, were found using global fitting. An excitation wavelength-dependant IRF was acquired for this analysis.

Figure 83 presents the PLE spectra of this point measurement of the CVD diamond with results from the lifetime analysis. The black line represents the PLE spectrum at an emission wavelength of 738 nm, which presents a peak at 546 nm (2.27 eV) excitation and then rises to its highest value at 680 nm (1.82 eV). Above 680 nm the filters start to affect the overall transmission of the system. For this double exponential decay profile, the two beta parameters are a mirror image of each other and so only beta 2, corresponding to emission from $SiV^-$, is shown. In addition to the PLE spectrum, the intensity-weighted mean lifetime as a function of excitation wavelength is shown in red. This will increase as the contribution from $NV^0$, increases. The minimum beta of $SiV^-$ emission is 99.45 %, so the PLE spectra observed here is mostly that of $SiV^-$. The overall structure agrees well with previously reported $SiV^-$ PLE spectra[155].

The PLE peak at 546 nm has previously been analysed in several papers[155, 156], but this is the first time a pulsed laser source has been used to measure the PLE spectra and provide corresponding lifetime data. The lifetime data confirms that this peak corresponds to emission from $SiV^-$, and a sample with only $SiV^-$ emission is characterised later in this chapter. The peak at 546 nm is thought to originate from the central band of a 2nd excited state, above the 1st excited state where the primary emission and ZPL originates[154]. There are several other smaller features which are present at 530, 575 and 595 nm, which could represent local phonon modes[155]. A diagram showing the energy level structure of $SiV^-$ is shown in Figure 83. The dipoles of these energy levels can be explored using various polarisers, and this set of experiments is shown in the next section.

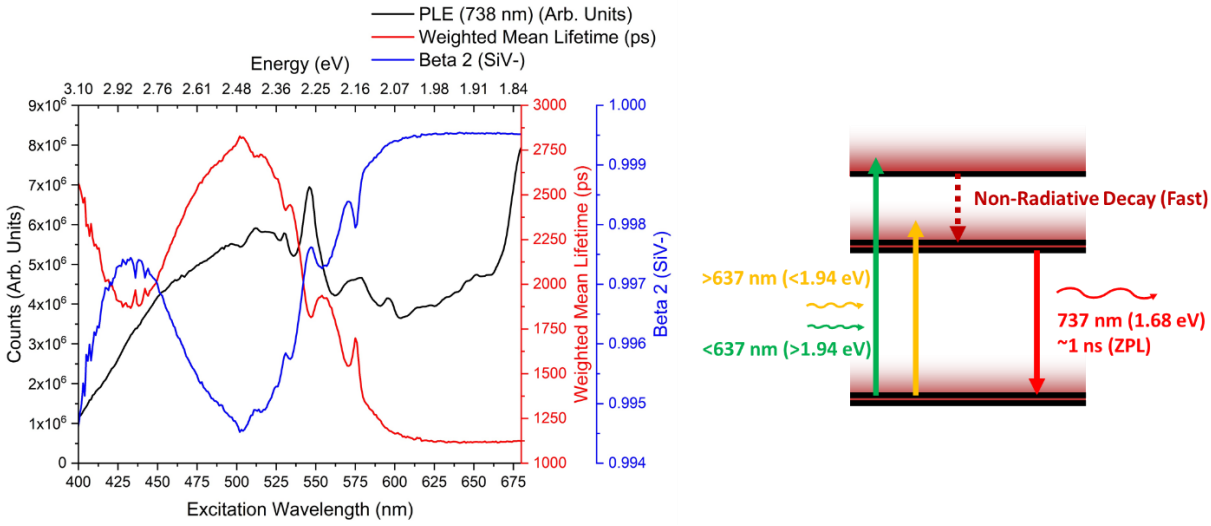



*Figure 83 – The graph shows the PLE spectrum for emission dominated by $SiV^-$ collected at 738 nm (black line), the weighted mean lifetime (red line), and the population fraction of $SiV^-$ (beta 2, blue line). The energy level diagram shows the ground and excited state, where the 737 nm ZPL originates, with a higher energy level above the excited state. Below 637 nm, the electron is excited into the 2nd excited state, whilst above 637 nm, the electron is excited directly to the first excited state, where the ZPL originates.*

## *Polarisation resolved PLE spectroscopy of SiV-*

The polarisation states of the $SiV^-$ defect have previously been studied[154], showing that all four of the fine structure transitions are polarised, where each set of two transitions from the excited state produce orthogonally polarised emitting photons. This previous study, using an optical parametric oscillator (OPO), measured the polarisation as a function of excitation wavelength, providing polarisation PLE spectroscopy data, but, due to the broad ~20 nm excitation wavelength steps, the polarisation resolved PLE spectrum was not well resolved. Using the multidimensional luminescence instrument with prism-based monochromator developed here, significantly narrower excitation resolution can be realised and, using motorised rotating polarisers, the system can be used to produce polarisation resolved PLE spectroscopy data with unprecedented resolution.

The cut of the CVD diamond with HPHT substrate is a {100} plane, which results in four different orientations of the $SiV^-$ defect, as this measurement was conducted on ensembles of SiV defects. Two different orientations of the sample were utilised: one parallel to the excitation and emission radiation polarisation states, and one at a 45° angle. These are depicted in Figure 84 as referred to as 'Parallel' and 'Diagonal' respectively, along with the layouts of the four different $SiV^-$ orientations. As both the excitation and emission polarisation state can be adjusted, the labelling of 'Ex' and 'Em' for excitation and emission respectively were chosen. The two polarisation states are horizontal and vertical (H and V), based on directions of the translation stage. A measurement of horizontal excitation and horizontal emission according to the diagram would be labelled 'Hex Hem' for example. The polarisation-resolved measurement set-up has previously been described in chapter 4. The horizontal axis was defined by the excitation polarization axis and was set to be parallel to the x-axis of the translation stage.

Each polarisation-resolved luminescence measurement entailed acquiring the four-polarisation-resolved PLE spectra for the 'Parallel' case, and then rotating the sample by 45° to measure the 'Diagonal' case. The sample was manually rotated between 'Parallel' and 'Diagonal', which means that the degree of rotation is not exact. The other consideration here is that the exact location on the sample was not the same for the next set of measurements, although markers, such as cracks, chips, and dust on the sample, were used to aid location of the sample such that a similar region was measured each time. For each excitation polarisation state and wavelength, the power was measured at the sample, although the difference between the horizontal and vertical power spectra was small (within 2%). A 10x 0.3 NA objective lens (Olympus, UPlanFl N) was used for all these measurements. The G-factor for the instrument (using the 150 lines/mm grating) was measured at the wavelength of 738 nm using a spectrally selected line from the supercontinuum laser, and

detecting the attenuated beam using the monochromator with a photomultiplier. The excitation polarisation was defined as horizontal, and the detection polariser was rotated between vertical and horizontal to acquire two orthogonal data sets. The instrument G-factor at 738 nm was then found to be 1.1.

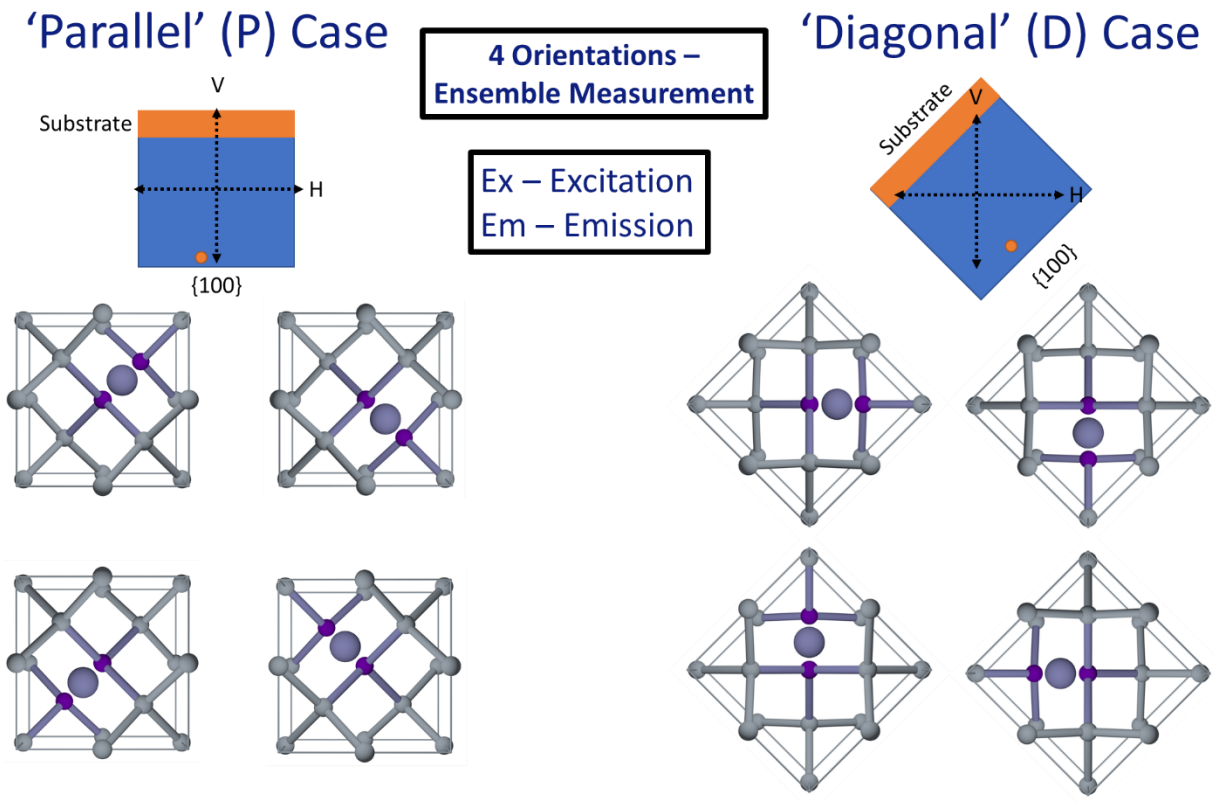



*Figure 84 – This figure describes the polarisation orientations in relation to the sample position during the polarisation-resolved PLE measurements. For a {100} sample, as shown here, there are four orientations of the SiV defect, as shown by the four images below the image representing the diamond. The orientation of the vertical and horizontal illumination and detection polarisation states are constant in all cases, and the sample is rotated to a 'parallel' case, where the edges of the sample are parallel to the polarisation states, and 'diagonal' where they are 45° offset. The location excited on the sample is shown by the orange dot.*

Data for the 'Parallel' measurement is shown in Figure 85, where the orange spot in the sample diagram denotes the approximate location measured. The excitation wavelength was scanned every 1 nm with the same spectral resolution as per Figure 77, using a 5 s acquisition time. To minimise the contribution from $NV^0$, the slit widths were set to 100 microns, resulting in a 1 nm bandwidth, centred at 738 nm and the excitation wavelength was scanned from 450 nm to 680 nm. The experiment was then repeated scanning the excitation from 680 nm to 450 nm to confirm that no charge transfer or other effects were occurring. If charge transfer was occurring, then the direction

of the wavelength/energy variation would affect the observed spectra. The colour scheme for Figure 86, and subsequent figures presenting polarisation resolved data, shows data with horizontal/vertical excitation polarisation as red/blue lines and detection polarisation represented by solid/dotted lines. Measurements for all four polarisation states for the parallel case show no significant variation in the PLE spectra. After calibrating for G-Factor, this data indicates that there is an equal contribution from all four orientations in the sample for the 'Parallel' case, regardless of excitation or emission radiation polarisation.

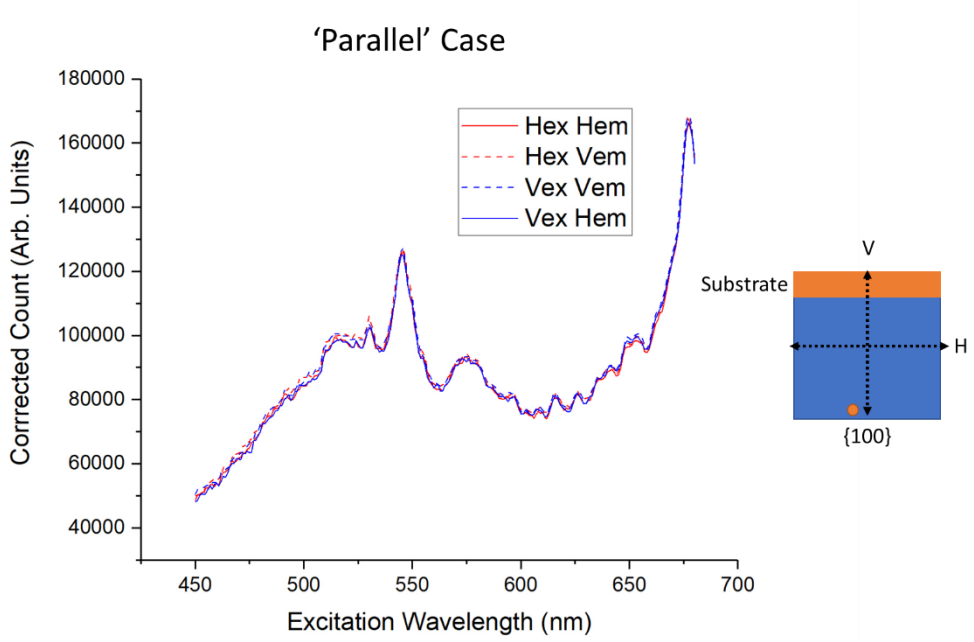



*Figure 85 – A polarisation-resolved PLE measurement of the $SiV^-$ taken at 738 nm emission in the 'parallel' case. The location excited on the sample is shown by the orange dot. All four polarisation measured spectra overlap irrespective of excitation wavelength, suggesting an equal contribution from all four orientation of the defect within the sample.*

Rotating the sample by 45° and repeating the measurement at approximately the same sample location, results in the graphs in Figure 86, designated the 'Diagonal' case, which show a more complex PLE behaviour than the 'Parallel' case. Above 637 nm excitation, measurements with parallel excitation/detection polarisation axes, i.e. Hex Hem and Vex Vem, result in more emission than measurements when the excitation/detection polarisation axes are orthogonal, i.e. Vex Hem and Hex Vem). Below 637 nm, this relationship is reversed. The features in the polarisation-resolved PLE spectra are similar, however.

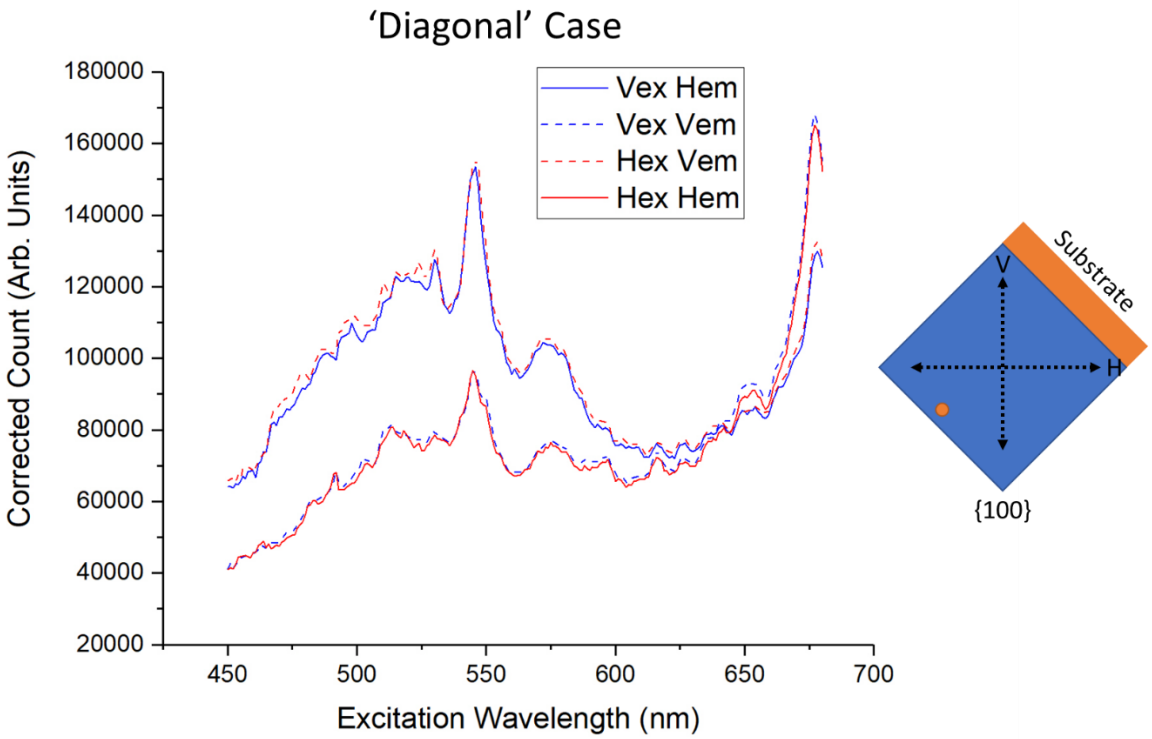



*Figure 86 - A polarisation-resolved PLE measurement of the $SiV^-$ taken at 738 nm emission in the 'diagonal' case. The location excited on the sample is shown by the orange dot. There are two pairs of spectra here for each. The two matched spectra are the opposite excitation cases, and this is explained in detail in the text. The crossover occurs at approximately 637 nm, and the large peak at 546 nm is a constant feature in all spectra.*

To determine if these measurements were dominated by spatially localised environmental effects, the experiment was repeated at a different spatial location on the sample. The sample was also rotated by 90° relative to the 'diagonal' case, to test if the same phenomena were recorded. The excitation wavelength range was extended down to 400 nm. The results are shown in Figure 87 and are similar to the results of Figure 86. It is apparent that the $SiV^-$ absorption band extends to below 400 nm. Excitation of $SiV^-$ using 355 nm excitation was found to be possible, but required higher excitation power (50 mW, against typical 0.1 - 4 mW for visible excitation). The similar PLE spectral behaviour suggests these results may be consistent across the sample, which would imply this is a fundamental measurement of the defect emission. A second sample is investigated and discussed later in this chapter.

The 530 nm peak appears in all three of the measurement sets, and would correspond to a 69 meV phonon, if it is a local phonon mode. A 64 meV peak has previously been reported in the phonon side band[154], where it was attributed to a local phonon mode and showed a polarisation contrast.

The other peaks in the PLE spectra are more complicated because they exist inside the energy gap, between the 1st excited and 2nd excited states.

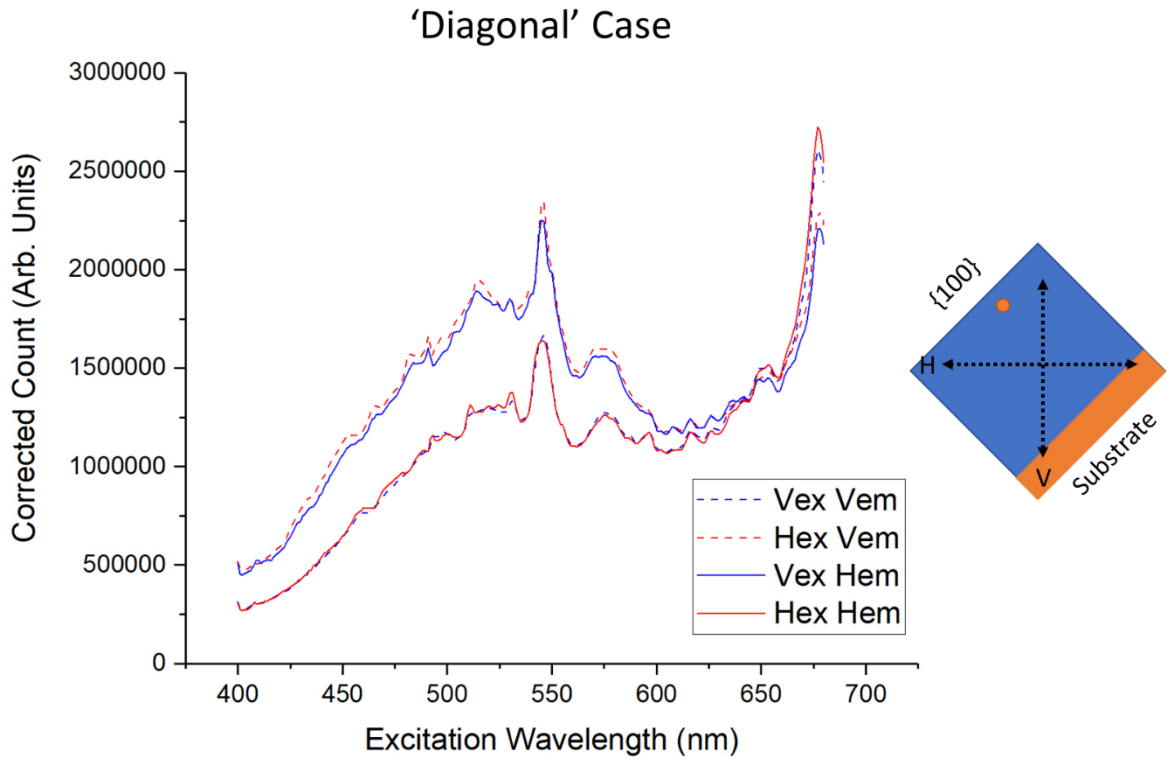



*Figure 87 - A polarisation resolved PLE measurement of the $SiV^-$ defect taken at 738 nm emission in the 'diagonal' case. The location excited on the sample is shown by the orange dot. This sample has been rotated by 90° relative to the data in Figure 86, but the spectra are similar. This measurement continues to 400 nm in excitation.*

Figure 88 shows a composite plot (where P represents the 'Parallel' case, and D the 'Diagonal') combining data presented in Figure 85 and Figure 86, with no normalisation with respect to excitation power between the two sets of data , along with two graphs showing two different contrast plots. The composite plot of Figure 88 a) shows that the features are similar across all eight measurements, with only finer detail <530 nm excitation wavelength being slightly different. This suggests that the most prominent features are consequences of the energy level structure of the defect, and local vibronic modes.

The two contrast diagrams of Figure 88 b) and c) were generated using the equations for the 'diagonal' measurements:

$$\text{Contrast}_{\text{Vertical Emission}} = \left(\frac{\text{Vertical}_{\text{Excitation}}}{\text{Horizontal}_{\text{Excitation}}}\right) - 1$$ , for graph b) and:

*Equation 29*

$$\text{Contrast}_{\text{Vertical Excitation}} = \left(\frac{\text{Vertical}_{\text{Emission}}}{\text{Horizontal}_{\text{Emission}}}\right) - 1$$ , for graph c).

*Equation 30*

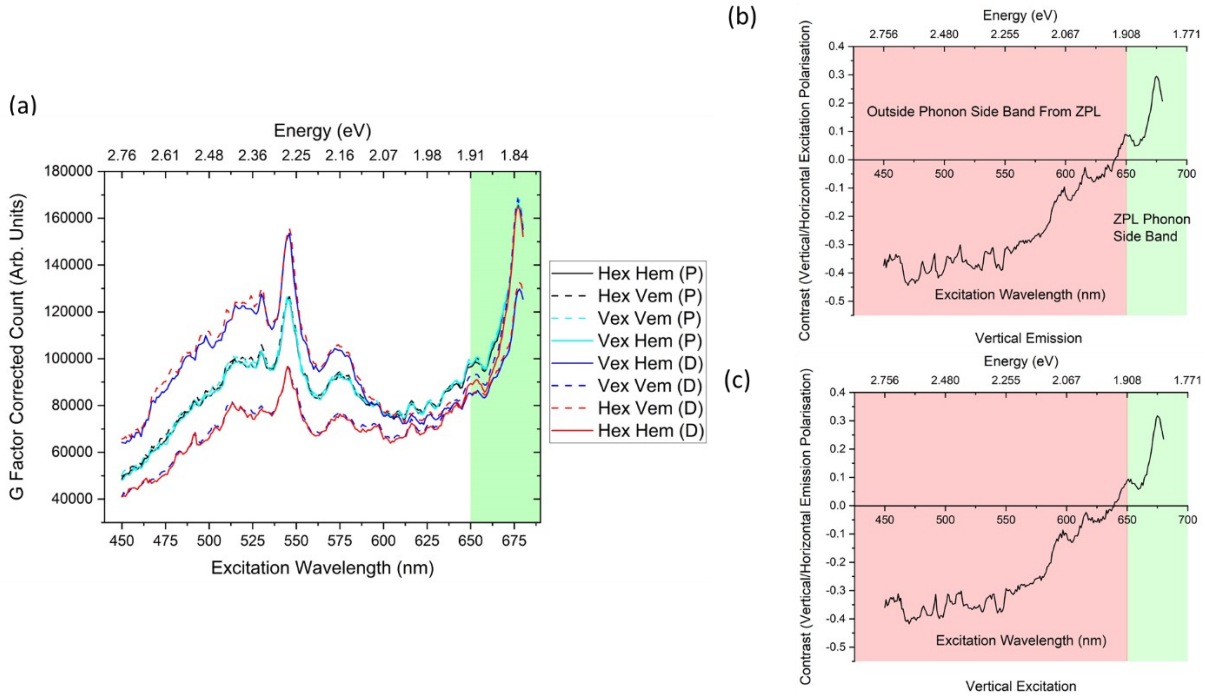



*Figure 88 – The graph in a) shows a combination of the data from Figure 85 and Figure 86 using the notation of (P) for 'parallel' and (D) for 'diagonal'. Below 600 nm the 'parallel' spectra are approximately averaged positions of the 'diagonal' spectra. Graphs b) and c) show the 'diagonal' case contrasts described by Equation 29 and Equation 30 respectively. The zero-point crossover for contrast in b) and c) is shown to be 637 nm in both cases. In all graphs the green region represents the ZPL phonon side band maximum extension.*

At 637 nm, the contrast between the vertical and horizontal polarisation states, irrespective of emission or excitation axis orientation, reaches zero. This suggests that it is the transition between excitation into the second excited state, however, due to factors explained later, the exact transition is less well defined. Previous experiments have studied the extent of the $SiV^-$ phonon side band, and it has been shown to extend ~200 meV from the bottom of the ground state and to vary with polarisation state[154]. In all three graphs, this region is coloured green, indicating where the end of

this phonon side band lies at 650 nm. Red represents the outside of this region in the two contrast graphs. The transition between positive and negative contrast does not occur for another 40 meV above the ZPL, which could suggest the energy levels overlap. At 550 nm, the reduction to negative contrast has completed, suggesting that 546 nm, corresponding to the peak in the PLE spectra, is the centre of the 2$^{nd}$ excited energy band[156].

The following analysis and modelling were conducted with the help of Dr Ben Green from the University of Warwick[199]. The SiV defect has been shown to have $D_{3d}$ inversion symmetry in several studies and this is now considered to be the dominant theory on its structure[15, 154]. The emitting dipole of the negative charge state for the ZPL at 737 nm has also been shown to lie parallel to the bond axis of the defect, i.e. along the bond between the two vacancies[154]. Looking along this [111] axis, we are therefore looking along the axis of emission dipole for the 1$^{st}$ excited state. We can then define the bond axis/1$^{st}$ excited state as the z-axis, and the orthogonal planes to be the x and y-axis.

In Figure 89 b), we can see the expected relative intensity of each of the four orientations of $SiV^-$ (we measure an ensemble in these experiments), which consist of two different pairs of dipoles as they appear in a {100} plane. It should be noted here that the definition of horizontal and vertical correspond to 0°, 90°, 180°, and 270° for the 'Parallel' case, whilst they are rotated by 45° for the 'Diagonal' case. This is visualised by the black dotted line for 'Parallel' and the red dotted line for 'Diagonal'. The model in b) is consistent with the PLE data acquired for excitation >637 nm. An example is shown as the green dot, where in the 'Parallel' configuration, an equal response from all four orientations of dipoles is observed. In addition, considering the 'Diagonal' case, all four orientations again provide an equal response, which agrees well with the data >637 nm shown in Figure 85 and Figure 86.

For excitation <637 nm, the model shown in Figure 89 b) is inconsistent with the observations. At any point, an equal response of the dipole is expected for any variation of vertical and horizontal excitation. To explain the change in contrast, a different dipole orientation must be present in the 2$^{nd}$ excited state. For a defect with $D_{3d}$ symmetry, a dipole orientated to the XY axis (using the notation previously introduced 2 paragraphs previously) is the only other option allowed by symmetry[199]. A model for this is shown in Figure 89 a). This model must explain the following observations:

1 – provide an equal response for the 'Parallel' case independent of excitation and emission polarisation (to explain the results shown in Figure 85).

2 – modify the response of the system so the polarisation state of excitation <637 nm can result in a higher intensity of emission in the opposite polarisation state (Hex, Vem for example).

In Figure 89 a), the green dot corresponds to excitation of horizontally polarised light to the 'Parallel' case. This excites the electron to the 2nd excited state, where it rapidly decays to the 1st excited state and then decays to the grounds state emitting a photon at 737 nm, corresponding to the green dot in b). For either case of horizontally or vertically polarised excitation light, the response of the emission will be the same, explaining observation 1. Rotating the sample to the diagonal case, and exciting <637 nm so the blue dot represents the excitation polarisation shown along with the orange dipole in a), the corresponding orange dipole in b) is 90° rotated from the initial excitation state. This corresponds to excitation with Vex and detecting more emission in Hem than in Vem, which is consistent with the observations in Figure 86. Therefore point 2 has been explained. It should be noted here that the emission is assumed to be solely along the Z-Axis (bond axis [111]) (corresponding to plot b), and this is explored later.

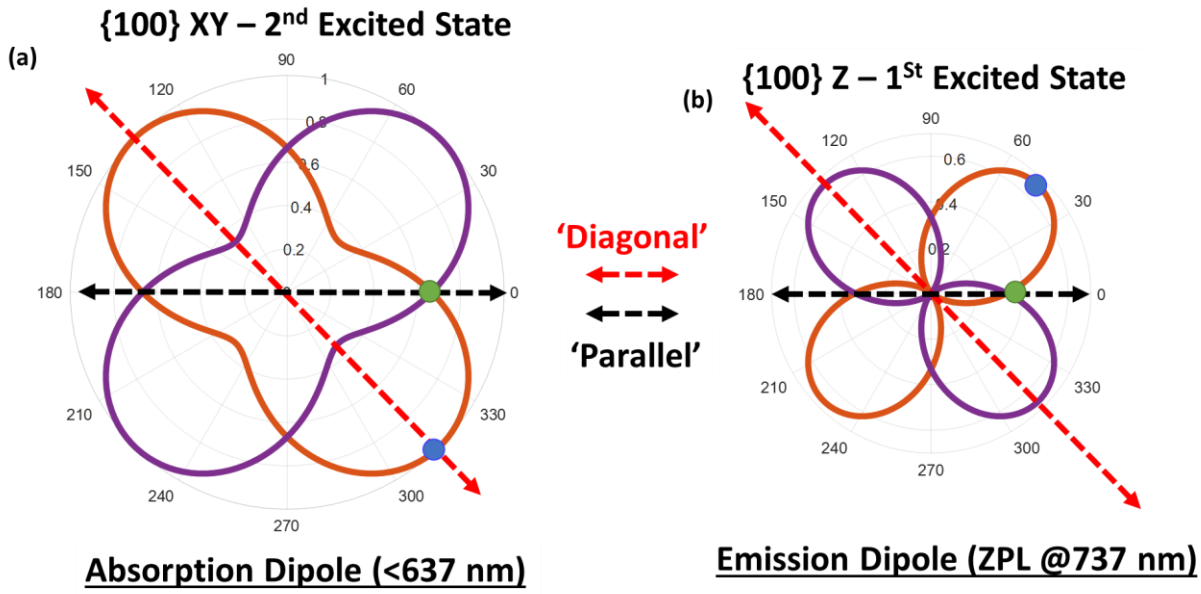



*Figure 89 – Theoretical models showing the projection of the expected contrast for the XY dipole in a) and Z dipole b) for a {100} plane. The orange and purple plots show the expected contrast for the two pairs of SiV orientations in the lattice. The vertical and horizontal polarisation states are 0°, 90°, 180°, and 270°, noting that that for 'diagonal' case data these positions are rotated by 45°.*

An XY-dipole fits the experimental evidence, for excitation below 637 nm. The graphs in Figure 90 highlight the contrast conundrum more clearly. Here it is shown that the XY-dipole gives the opposite contrast, which is shown as colour, to the Z-dipole. We therefore have shown that the

excitation and emission dipole are not the same for excitation <637 nm, which is in good agreement with the literature[154]. In addition to this, we postulate that only the other viable dipole orientation is an XY-dipole for the 2nd excited state[199].

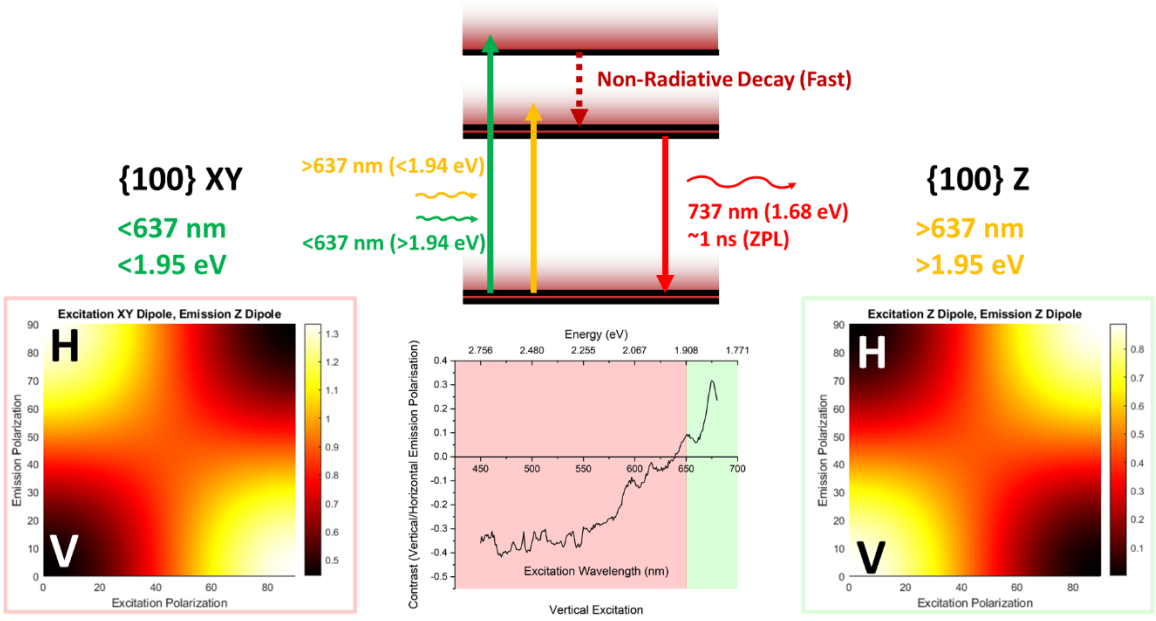



*Figure 90 – Excitation below 650 nm has theoretical contrast shown (left), and represents a XY dipole, whilst the data (right) shows the theoretical contrast for the Z dipole, the colour scale bar denotes the contrast. Excitation and emission polarisation run from 0 to 90°. The exact contrasts are not achieved due to effects discussed in the text. The central graph shows the measured data from Figure 88, with an energy level diagram above showing the main transitions.*

One important assumption is made in the model; that all the emission is originating from the Z-dipole, i.e. along the bond axis of the defect. The contrast values measured, do not reach the values anticipated in Figure 90, and suggests this assumption is not accurate enough to describe the observations. This experiment was conducted at room temperature, so phonons will cause depolarisation of the emission, and the excited state may overlap with the 2nd excited state. Previous measurements conducted at 8 K also did not reach the theoretical contrasts in polarisation[154]. In the reported measurement here, birefringence will also affect the results, although a region of comparatively low birefringence was chosen specifically to mitigate this effect.

Another measurement was conducted on a region of comparatively high birefringence, for which the data is presented in Figure 91 for a 'Parallel' case. This measurement should have produced four identical PLE spectra, however, the results show variations <560 nm, and more subtle variations in the 600-680 nm band. The PLE spectra are split into pairs of common emission polarisation states.

There are two potential explanations for this variation. The birefringence in the sample could be causing variations in the emission, which will affect the results. This predominantly appears in the blue part of the PLE spectra, however, which may indicate the birefringence is stronger in that region of the spectrum. An alternative explanation is that this experiment is probing vibronic energy levels above the 2nd excited state. In addition, birefringence in diamond is caused by strain, breaking symmetry. This strain could induce splitting of energy levels, and SiV is a 'soft' defect, which results in larger energy changes for a given stress. 'Soft' defects typically contain vacancies, which allow a greater deformation of the surrounding lattice. This increases the degree of energy level migration for a given stress. The splitting causes energy levels to shift, causing broadening and peak shifts. In particular, the central 546 nm peak appears to split into an intensity arrangement of ~1:2:1 for vertical emission, and ~2:2 for horizontal emission. The excited state and ground state are doubly degenerate, which may indicate this strain is inducing preferential decay paths in the 2nd excited state for a given polarisation, which gives rise to the variation in the PLE structure with polarisation and wavelength.

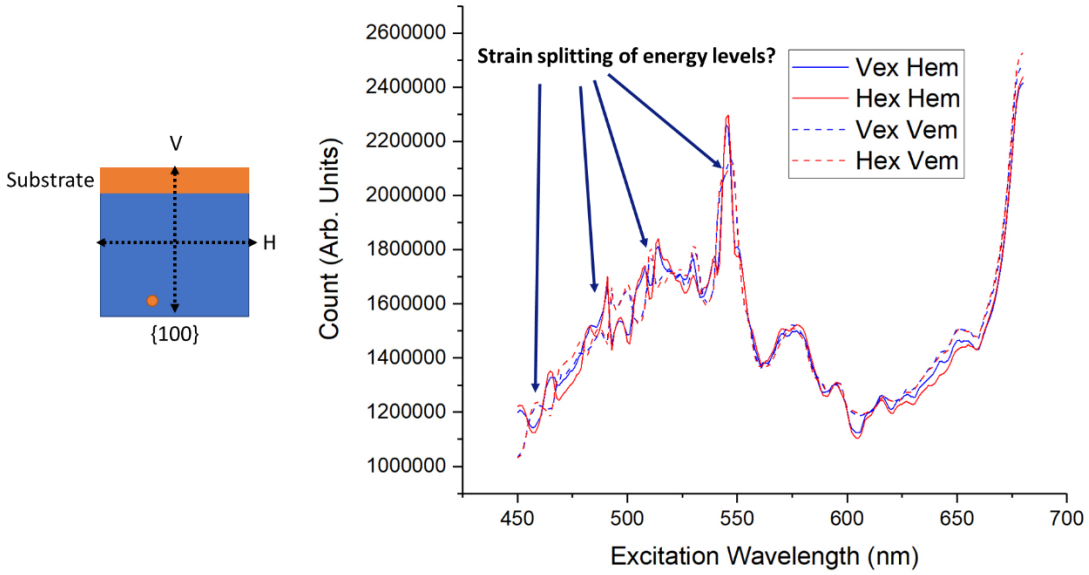



*Figure 91 – Data collected using the same parameters as Figure 85 for a 'parallel' case, on a high birefringent region (high strain). As shown in the data from Figure 85, this should be four identical spectra. This data shows variation in the PLE spectra below 560 nm. This splits into two pairs, with common emission polarisation. This could suggest strain splitting of energy levels, or wavelength dependant birefringence.*

## *SiV- spectroscopic and lifetime analysis on a second CVD diamond sample*

To gain confidence that the observations discussed in the previous section are generally applicable to the SiV- defect, it is important to study more than one sample. A second CVD diamond was sourced, which was synthesised at the same time as the previous sample (same batch/family) but had been subsequently HPHT treated. The HPHT process removed the NV defects through aggregation to form $N^2V$ etc. This should allow a more specific lifetime analysis of $SiV^-$ to be conducted, as no other species emitting in the same spectral region should be detected. Example birefringence and white-light transmission images from this second sample are shown in Figure 92, which were taken using the side port mounted colour CMOS camera. In addition, a colour image was taken during excitation to show the location of the emission in the sample. The visible light is the emission of $SiV^-$ from the sample, as the excitation radiation was blocked using filters. A region of comparatively low birefringence was again chosen for these measurements.

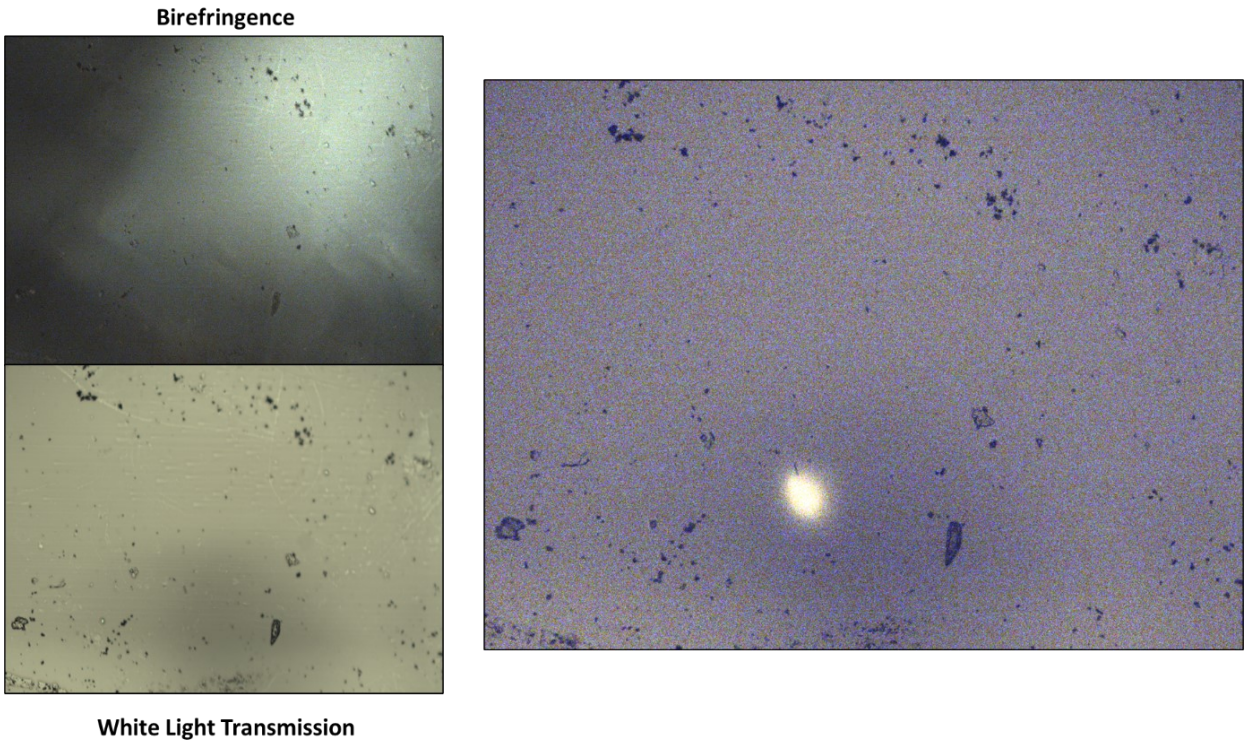



*Figure 92 – Images (left) show the colour white-light transmission and birefringence of the sample. The sample does exhibit some strain induced birefringence. In the image (right) the emission spot can be seen when the excitation source is blocked by filters. Images were taken with the side port colour CMOS camera, on the CVD diamond.*

For the ‘Parallel’ case data presented in Figure 93, we expect the PLE spectra to look similar to those shown in Figure 85. The PLE spectra do match well, with some small differences between the spectra that may be due to the slight birefringence, and therefore strain indicated in Figure 92. It is also possible the sample was not exactly parallel to the stage. This diamond was cut and grown the same way as the previous sample, so the sample also presents a {100} plane.

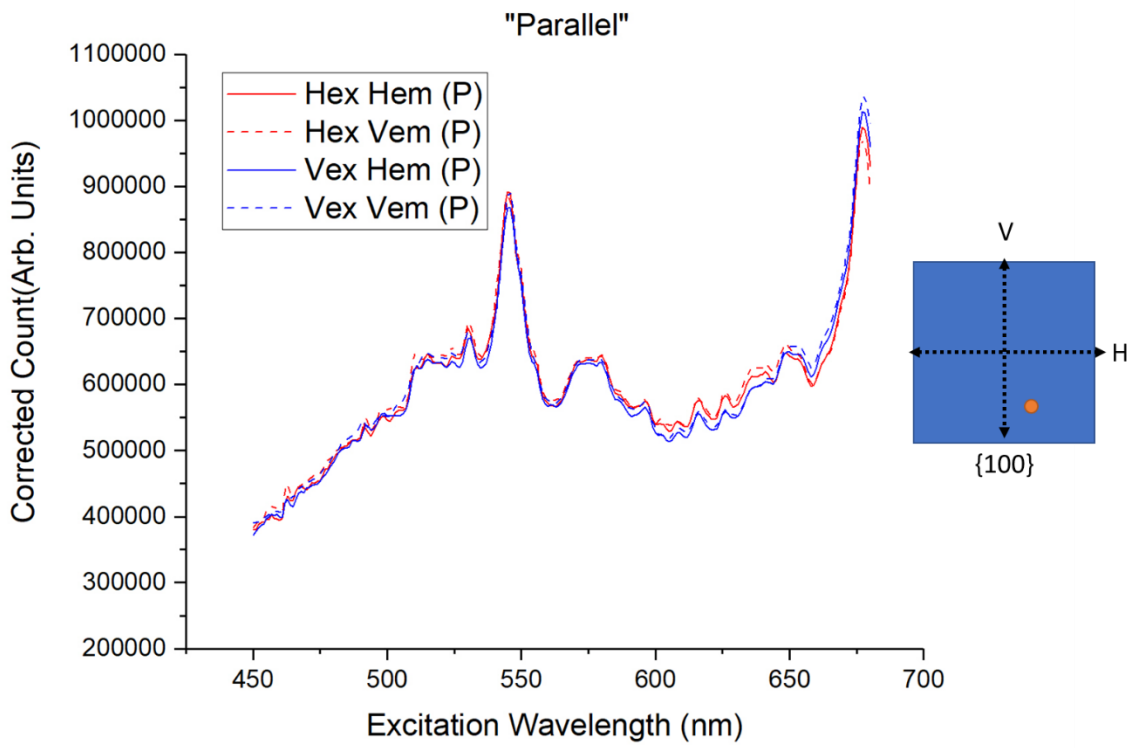



*Figure 93 - A polarisation resolved PLE measurement of the $SiV^-$ defect taken at 738 nm emission in the ‘parallel’ case. The location excited on the sample is shown by the orange dot. This is a CVD diamond with the same cut ({100}), and shows the same spectral features seen in Figure 85.*

For the ‘Diagonal’ case shown in Figure 94, similar spectra were observed as those shown in Figure 86. This suggest that the splitting phenomena and polarisation contrast previously shown is a general property of the $SiV^-$ defect in diamond. A cross-over between the two pairs of spectra occurs at 637 nm, which is consistent with the previous measurements.

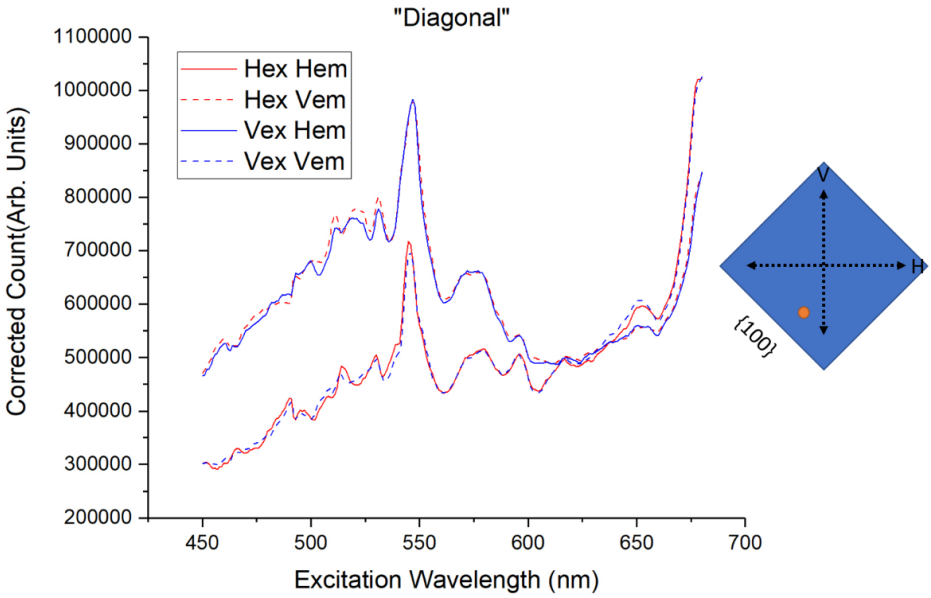



*Figure 94 - A polarisation resolved PLE measurement of the SiV⁻ defect taken at 738 nm emission in the 'diagonal' case. The location excited on the sample is shown by the orange dot. This is a CVD diamond with the same cut ({100}), and shows the same spectral features seen in Figure 86.*

Without the $NV^0$ decay in the emission, this sample enables a cleaner measurement of the $SiV^-$ lifetime. Examples of the observed monoexponential decay profiles of $SiV^-$ are shown in Figure 96. These measurements were polarisation-resolved, with a slight difference in position between the 'Parallel' (P) and 'Diagonal' (D) cases, due to manual sample rotation. The decay data was fitted to a monoexponential model and the variation of lifetime with excitation wavelength is shown in Figure 95 for the different polarization-resolved measurement configurations. A PLE spectra of an exemplar polarisation state (Hex Hem) is also shown. When this measurement was undertaken, the temporal shift of the IRF with excitation wavelength was not known, and this caused a variation in the $t_0$ in the fitting. To counter this, $t_0$ was included as a fitting parameter and the result of this is presented in Figure 96. The data was acquired scanning the excitation wavelength in 1 nm steps but was subsequently averaged over 10 adjacent wavelength steps to smooth out noise in the lifetime values.

Figure 97 shows the $SiV^-$ defect lifetime values of ~1.1 ns are in good agreement with previous measurements of the $SiV^-$ defect in CVD diamond[152]. There is a 20 ps divergence from the 'Parallel' and 'Diagonal' cases, which could originate from measurements being taken at slightly different regions on the sample. An explanation for this could be a quenching species with a weak effect, that in this sample is spatially variant. The same fitting parameters were used to fit all eight sets of decay

data, and this produced similar $t_0$ variations, as shown in Figure 96 c). The lifetime is approximately constant between 550 and 680 nm, apart from a discrepancy at 595 nm that appears to show a slight increase in lifetime for the 'Diagonal' case, and a decrease of lifetime for the 'Parallel' case. This feature corresponds to a peak in the PLE spectra in Figure 97, indicated by the dotted blue line. This is interesting because it could suggest a fluorescence lifetime anisotropy. If the 595 nm feature in the PLE spectra is phonon related, then this could potentially be involved in the mechanism resulting in this anisotropy. The difference in lifetime is also very small 10 ps, suggesting a rapid mechanism.

For all eight measurements, below 550 nm (546 nm indicated by the red dotted line), the lifetime slowly starts to increase with photon energy, and in the 'Diagonal' measurements, there is a small divergence of 10-15 ps between the data acquired with parallel and orthogonal excitation/emission polarization axes. The 546 nm peak on the PLE spectrum has been attributed to the centre of the 2$^{nd}$ excited state band. This could indicate that the mechanism being probed in this region is the phonon side band of the 2$^{nd}$ excited state, and the relaxation time scales involved change with excitation wavelength. This change in lifetime is 30 ps, which is near the temporal precision of the TCSPC system (estimated to be ~5 ps). Measurement of this behaviour as a function of temperature could help elucidate the role of phonon mediated mechanisms.

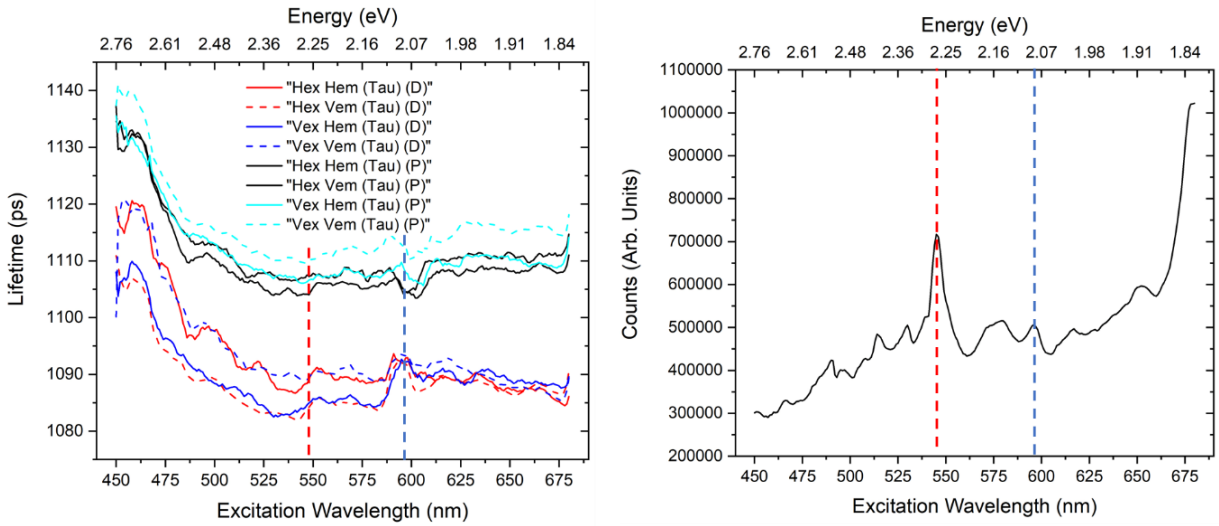



*Figure 95 – The graph (left) shows the PLE lifetime data fitting of the SiV- defect with a monoexponential decay for eight different polarisation and sample orientation measurements. The graph (right) is an extracted PLE spectrum one of the decays. The red dotted lines at 546 nm indicate where the large feature in the PLE spectra is, whilst the blue dotted line shows a region of fluorescence lifetime anisotropy in the lifetime data. This blue line corresponds to a feature in the PLE spectra. Below 546 nm the lifetime slowly increases and is discussed in the text. The lack of $NV^0$ in this sample enabled this measurement to be more accurate.*

Figure 96 shows an exemplar set of luminescence decays from one of the eight polarisation-resolved PLE spectroscopy measurements. Here, the purple curves represent 450 nm excitation and the dark red curves 680 nm excitation with other colours representing intermediate excitation wavelengths. The decay curves have been normalised to the peak of each curve. The graph in Figure 96 a) shows there is only a monoexponential decay present, with a background that varies due to the normalisation. The decay profiles are shown at higher magnification in Figure 96 b), which reveals how the decay profiles have shifted due to changes in their $t_0$ positions, which was later found to be due to an excitation wavelength-dependent IRF. To address this, the $t_0$ parameter was included as a variable in the iterative fitting procedure, and the resulting $t_0$ values are plotted in Figure 96 c). While there are a few outliers, the trend of the shift in $t_0$ is the same for all eight measurements, which suggests this is a reasonable approach to mitigate the IRF shift with wavelength.

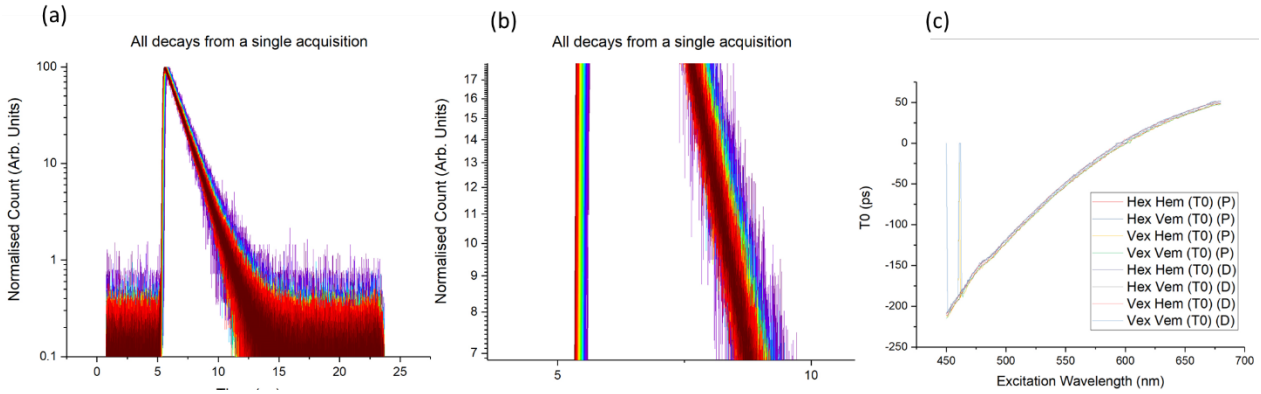



*Figure 96 – Luminescence decays for SiV- defect. Graphs a) and b) show the example decays normalised to 100. The colour of each line indicates the emission wavelength from dark red (680 nm) to purple (450 nm). The variation in t0 with excitation wavelength due to path differences in the prism based monochromator causes a 'rainbow' effect where the curves are increasingly shifted in time for increasing excitation wavelength. For fitting, t0 was included as a fitting parameter, and the results for all eight measurement as a function of excitation wavelength are shown in graph c). Note that in c) a negative value corresponds to the decay being shifted further in time (to the right).*

An example $SiV^-$ luminescence decay profile is shown in Figure 97 with the IRF included in the fit. The normalised residuals are generally randomly distributed about zero, but there is a discrepancy near the $t_0$ time, which is also shown in the expanded view of this data. Closer inspection of the IRF reveals a small feature before the main peak. Since this feature is not present in the decay, so the convolution of the model and IRF does not fit the decay properly. The origin of this feature in the IRF was not confirmed, but measurements of the IRF using an OD filter after the filter cube, just before the entrance slit to the spectrograph did limit its presence. This may be a source of error in the

calculated lifetimes, but because this decay is monoexponential with low background signal then this effect is minimised.

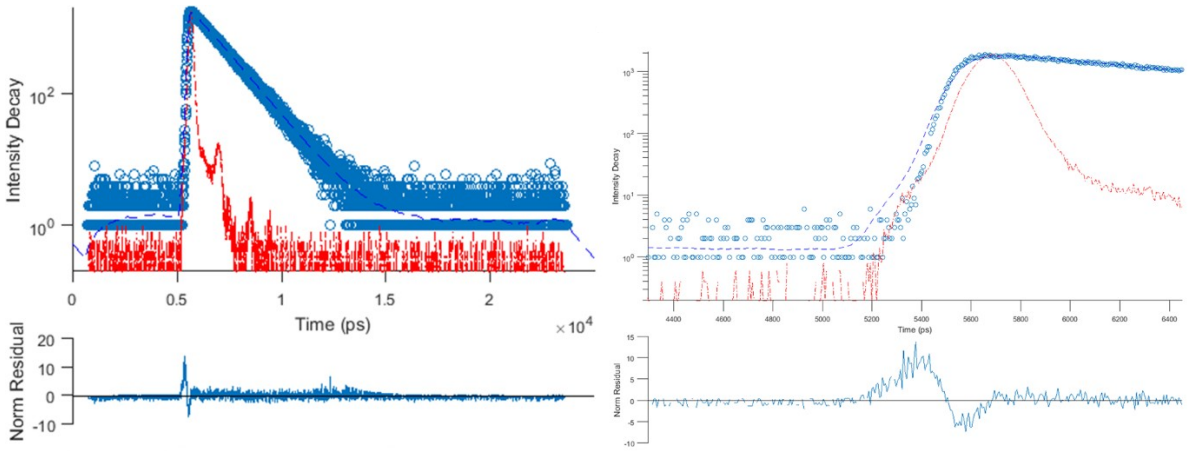



*Figure 97 – SiV- luminescence decay profile for an excitation wavelength of 546 nm and an emission wavelength of 738 nm. A monoexponential decay fit (blue dashed line) to the data (blue circles) is shown together with the IRF (red line). The plot on the right shows a zoom of the region near the rising edge.*

## *Comparison with absorption data*

An absorption measurement was conducted at the University of Warwick at liquid nitrogen temperatures on a third CVD diamond sample that contained a high concentration of $SiV^-$ [199]. The absorption spectrum for this third sample and the (non-polarisation-resolved) PLE spectroscopy data presented in Figure 83 are similar, suggesting that phonon broadening at room temperature is not a significant effect. The data from these two measurements is plotted together in Figure 98. Below ~500 nm, the absorption due to nitrogen is high, and so the absorption measurement shows an increase of total sample absorption. Whereas the PLE spectroscopy data shows a decrease in the emission intensity, which is caused by lower absorption of the $SiV^-$ defect.

The primary advantage PLE spectroscopy has over absorption measurements is illustrated here, as absorption will integrate contributions from multiple defect species in the sample. In PLE spectroscopy, the emission is measured and spectral and/or lifetime analysis can distinguish contributions from different defect species. Furthermore, absorption measurements typically require a significant amount of material, or absorbing species, to make accurate measurements. In addition, the technique is not easily spatially sensitive at high spatial resolutions, and requires two flat, non-scattering parallel sides to minimise errors.

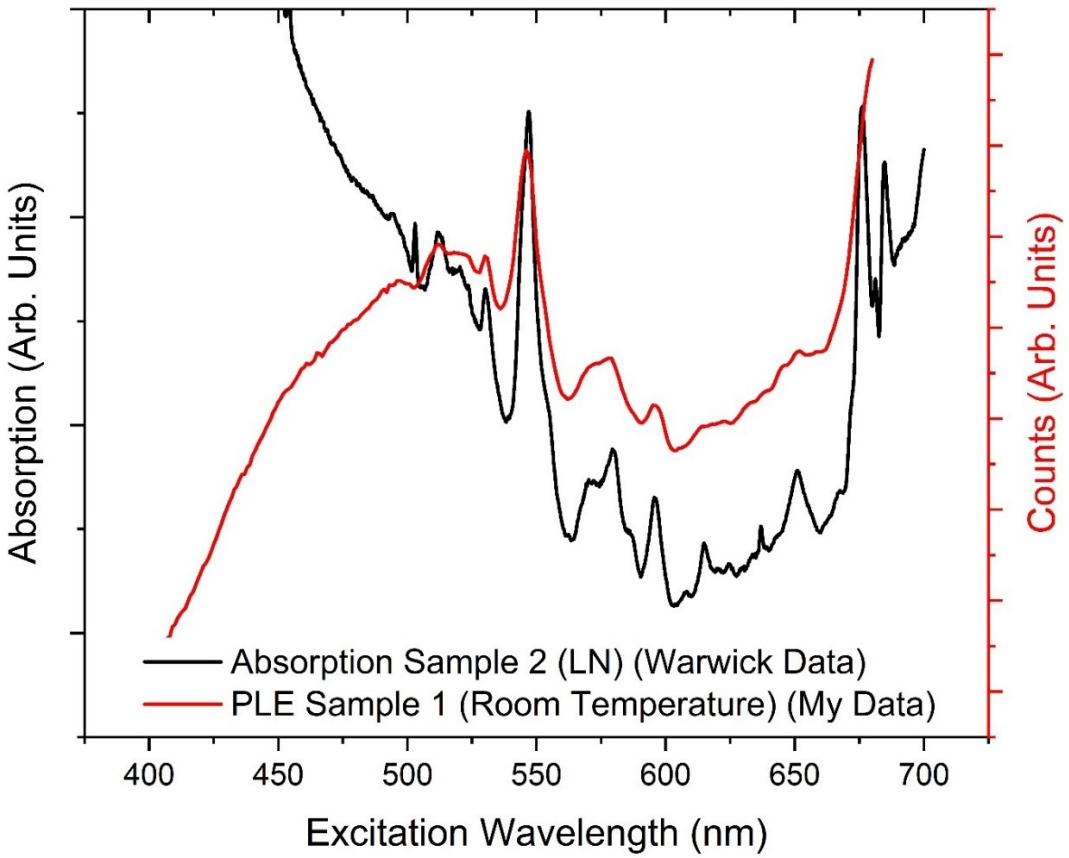



*Figure 98 – A comparison between PLE data taken from Figure 83 at room temperature (red line) and absorption data from the University of Warwick (black line) at liquid nitrogen temperatures. Despite the large temperature difference most of the features are resolvable in the PLE measurement, and they align well, which strongly suggests this is a fundamental measurement of the $SiV^-$ defect.*

## Conclusion and outlook

The photo-physics of the $SiV^-$ defect has been investigated on a HPHT/CVD diamond. The broad capabilities of the developed instrument allowed ensembles of defects to be examined. Polarisation resolved PLE spectroscopy measurements were undertaken on two samples containing $SiV^-$. The change in polarisation of the excitation spectra with rotation of the sample indicated the existence of an 2nd excited state with a different dipole orientation (XY axis) to that of the emission dipole (Z axis, aligned to [111], the bond axis). This had previously been noticed in other works[154, 155, 156], but the high-resolution data produced here allowed this to be identified more accurately. PLE lifetime spectroscopy data of the $SiV^-$ defect was also collected, which has not previously been accomplished in diamond, and this revealed a change in lifetime towards shorter excitation wavelengths. The origin of this could be phonon related transitions.

In the next chapter, the instrument was applied to natural diamond, which can have significantly different properties to that of synthetic diamond.

# Chapter 7 – Application of multidimensional imaging and spectroscopy to natural diamond

## Outline

This chapter reports the application of the developed multidimensional luminescence microscope to natural diamond. Hyperspectral image data, lifetime image data and single point-spectrally resolved lifetime data were acquired using excitation wavelengths below 410 nm. Three natural diamonds were investigated, consisting of one faceted sample, and two polished natural diamond plates. Quenched emission from the N3 defect was observed from all three samples, which the lifetime imaging revealed varied spatially. This luminescence spectroscopy has potential applications for determining if a diamond is natural or synthetic, and measuring A-centres without absorption spectroscopy.

## Overview

The emission from natural diamond is significantly more complex to analyse than emission from synthetic diamond[145]. The growth of synthetic diamonds is precisely controlled, especially in CVD diamond synthesis where the conditions are held constant over long periods, and any changes in conditions, elemental composition of the raw materials, and timescales are documented. Conversely, during the growth of natural diamonds over a vastly different timescale (millions of years), the elemental composition of the Earth can vary, leading to impurities introduced at various stages of growth, such as nitrogen. The range of processes and conditions to which the diamond will have been exposed to by the time it reaches the surface can result in complex structures with complex luminescence properties. Natural diamond has been extensively studied, resulting in stones being categorised into 'types', based on their nitrogen aggregation and concentration[123]. Luminescence measurements can also be made to elucidate defect information, and the spatial variation of these defects could be used to separate natural and synthetic diamond.

The developed multidimensional luminescence instrument provides unprecedented capabilities to characterise natural diamond luminescence in a single instrument and to address the potential variety in the emission caused by different defects. For example, the timescales of the growth of natural diamonds can result in spatially varying differences in, e.g. nitrogen aggregation, as is explored further in this chapter, and result in spatial variations in lifetimes due to different degrees of quenching[129].

## Faceted natural diamond

The study of faceted, cut, diamonds is of particular interest to the gemstone community. Typically, bulk measurements such as absorption are used to quickly classify a diamond into a 'type', based on the nitrogen concentration and aggregation. With a faceted diamond, this is relatively straightforward. Imaging cut diamonds is more challenging, especially in 3D, due to the spherical aberration caused by the high refractive index of diamond and the reflections from the facets[201]. Reflections are typically mitigated in instruments such as DiamondView$^{tm}$ by using above-bandgap excitation from a flash lamp, ensuring only the surface emission is excited due to the very high absorption, thus removing any internal reflections. Coupling this with a three axis goniometer enables a sample's spatially varying emission to be characterised, even for a faceted or rough natural diamond. However, the DiamondView$^{tm}$ provides limited spectroscopic information, which makes identification of specific defects challenging without subsequent secondary analysis, for example, point-spectra. These subsequent measurements are rarely performed using above bandgap excitation, due to the scarcity of affordable laser sources in the deep UV. This means a direct comparison between the two excitation methods is challenging. Using a single system to measure all of these properties, and more, is therefore beneficial.

If a faceted diamond is to be imaged, this is best undertaken through one of the flat faces. The table of a brilliant cut diamond is the largest single flat area. Using optical sectioning provided by the narrow slit in the multidimensional luminescence instrument developed during this thesis, hyperspectral imaging of the table of a diamond can be undertaken without the need for above band-gap excitation to remove internally reflected light. This can provide the spectral luminescence fingerprints of emissive defects and lifetime mapping can reveal quenched emission, indicative of defects with no optical emission such as A-centres.

### *Hyperspectral and lifetime imaging*

The multidimensional luminescence instrument was applied to study a faceted natural diamond that was classified as a type IaAB, meaning it contained A-centres and B-centres, which are nitrogen related defects. The sample weighs 0.22 carats and measured 3.9 x 3.9x 2.4 mm$^3$. Many defects commonly occurring in natural diamond are excited in the UV or blue parts of the spectra[19], and this makes the supercontinuum excitation source a less useful excitation source due to the weak spectral power density in this region. The 355 nm laser in this system is useful for studying natural diamond luminescence because of the high average output (100 mW at stable output), and pulsed output (ps

pulses). However, when using this laser, the excitation optics after the cylindrical lens must be modified: the achromatic doublets were replaced with best-form singlet lenses (LBF254-100 and LBF254-200, Thorlabs), to avoid any fluorescence from the optical cement found in achromatic doublet lenses.

A set of luminescence data acquired from a section of the table of the cut natural diamond is shown in Figure 99. Line scanning hyperspectral imaging data excited at 355 nm are shown in Figure 99a). A 4x 0.16 NA objective lens (Olympus, UPlanAPO) was used in conjunction with the EMCCD camera, and the 150 line/mm grating in the image spectrometer. This led to 1 nm spectral resolution when using a 10 micron width entrance slit. The colour scheme used to display this hyperspectral image data is different to others in this thesis. Here, each pixel in the emission wavelength dimension was assigned an RGB colour corresponding to an approximate RGB space formula, and then the mean RGB value was calculated for each x-y position by averaging in the emission wavelength dimension. However, this sample displayed no variation in spectral components, and all the emission was attributed to the N3 defect, which has a ZPL at 415 nm – as is evident in the spectrum in Figure 99e), obtained from averaging over the whole image. Due to the lack of spectral variation in the emission, this intensity-weighted mean wavelength map is uniformly coloured.

Lifetime imaging for this sample was performed at a single emission band at 430 nm, with a 5 nm bandpass. A 40x 0.55 NA objective lens (Olympus) was used with the PMT, using a pixel size of 5 microns set to a pixel dwell time of 0.15 s. At the time of this measurement, the change in FOV with each objective lens had not been calibrated and so the hyperspectral image region was shifted with respect to the lifetime imaged region. The lifetime imaged region is shown by the red dotted box in Figure 99a). Figure 99c) shows the temporally integrated intensity image from the emission detected with a 430/5 nm emission filter. Several features are apparent, which were not clear in the hyperspectral image, possibly due to the better spatial sampling and stronger optical sectioning (due to the higher NA). Some structure, attributable to rectangular growth is apparent in the intensity image. Following 3 x 3 spatial binning, the lifetime data was fitted pixel-wise to a triple exponential decay model with two lifetime components fixed to $\tau_3$ = 342 ps, and $\tau_2$ =2.9 ns, and the third lifetime component was determined by the fit. The fixed components, $\tau_3$ and $\tau_2$, were set after summing all the pixel decay profiles to create a single decay profile and fitting this to a triple exponential decay model, using initial conditions of $\tau_3$ = 400 ps and $\tau_2$ = 3.5 ns. Fixing $\tau_3$ and $\tau_2$ to the values from this single image summed decay, and fitting $\tau_1$ produced a better fit ($\chi^2$ = 1.0) over all the lifetime image pixels than freely fitting all three components. The average value of the fitted component, $\tau_1$, is 23.6 ns, which is attributed to the emission from the N3 defect.

The resultant intensity-weighted mean lifetime image is shown in Figure 99 d) and presents a variation in lifetime, which could be caused by variations in growth conditions. To explore these lifetime differences, two spectrally varying lifetime point-measurements (where the diameter of the point was 1 μm) were taken at the locations indicated by the two ROI circles with the same 355 nm excitation. The resulting lifetime data was fitted to a triple exponential decay model with the two components, $\tau_3$ and $\tau_2$, fixed to the values stated previously, and the variation of the intensity-weighted mean lifetime with emission wavelength is shown in Figure 99 f). This data also indicates that for emission at 430 nm, the intensity-weighted mean lifetime is different between these two regions. The increase in intensity-weighted mean lifetime towards longer emission wavelengths is explored later in this chapter. The slowest component $\tau_1$ (23.6 ns on average), has been attributed to the emission from the N3 defect, however, the natural N3 defect lifetime is 41 ns according to literature[128]. It is known this defect can be quenched by nearby A-centres, and this sample does contain A-centres.

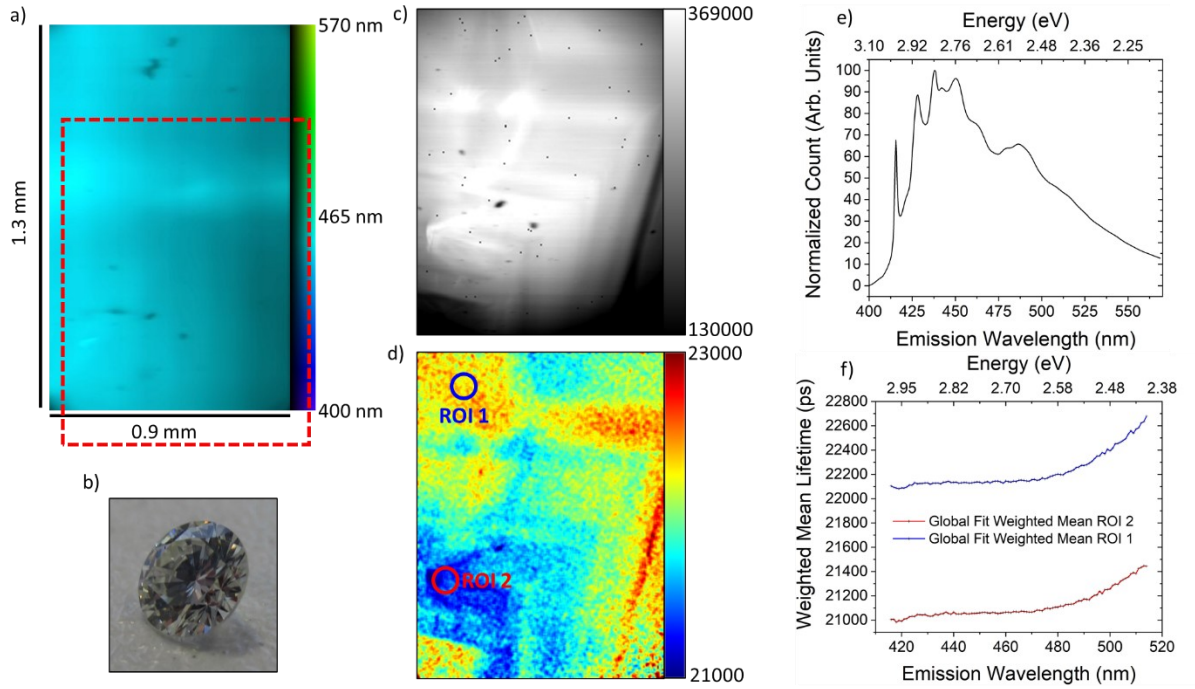



*Figure 99*[190] *- a) Intensity-modulated false-colour mean wavelength hyperspectral image of a natural cut and polished diamond, taken under 355 nm excitation, using a 4X, 0.16 NA objective of a 170 nm spectral band from 400 nm, with spectral resolution of 1 nm. The red dotted box indicates the region imaged with FLIM. b) White-light colour image of the sample 0.25 carat cut natural diamond. c) Integrated intensity point-scanned image of the emission at 430/5 nm, acquired with a 40x 0.55 NA objective in a). d) 3x3 binned intensity weighted mean lifetime luminescence lifetime map (ps), fitted pixelwise with a triple exponential decay, showing spatial variations in intensity weighted mean lifetime. e) Luminescence emission spectrum of the sample integrated across the whole hyperspectral image. The ZPL at 415.2 nm indicates this is the emission from the N3 defect and its lifetime has been significantly quenched to an average of 23.6 ns. f) Spectrally resolved intensity weighted mean lifetimes of two regions on the sample that showed a variation in lifetime in the luminescence lifetime map d).*

The $\tau_1$ lifetime, beta population fraction and $\chi^2$ maps are shown in Figure 100. The $\chi^2$ map shows no structure, which indicates that the model provides a good fit within the noise level of the measurement. The β maps associated with the longest ($\beta_1$) and shortest ($\beta_3$) lifetime components show an anti-correlation. This could indicate that these two lifetime components are related, and this is explored later. β2, corresponding to the intermediate (2.9 ns) lifetime component presents less spatial variation and therefore may not be associated with the emission from N3 defects. The intensity merged and non-merged images are shown not to obscure some differences in lifetime, primarily near the bottom of the images.

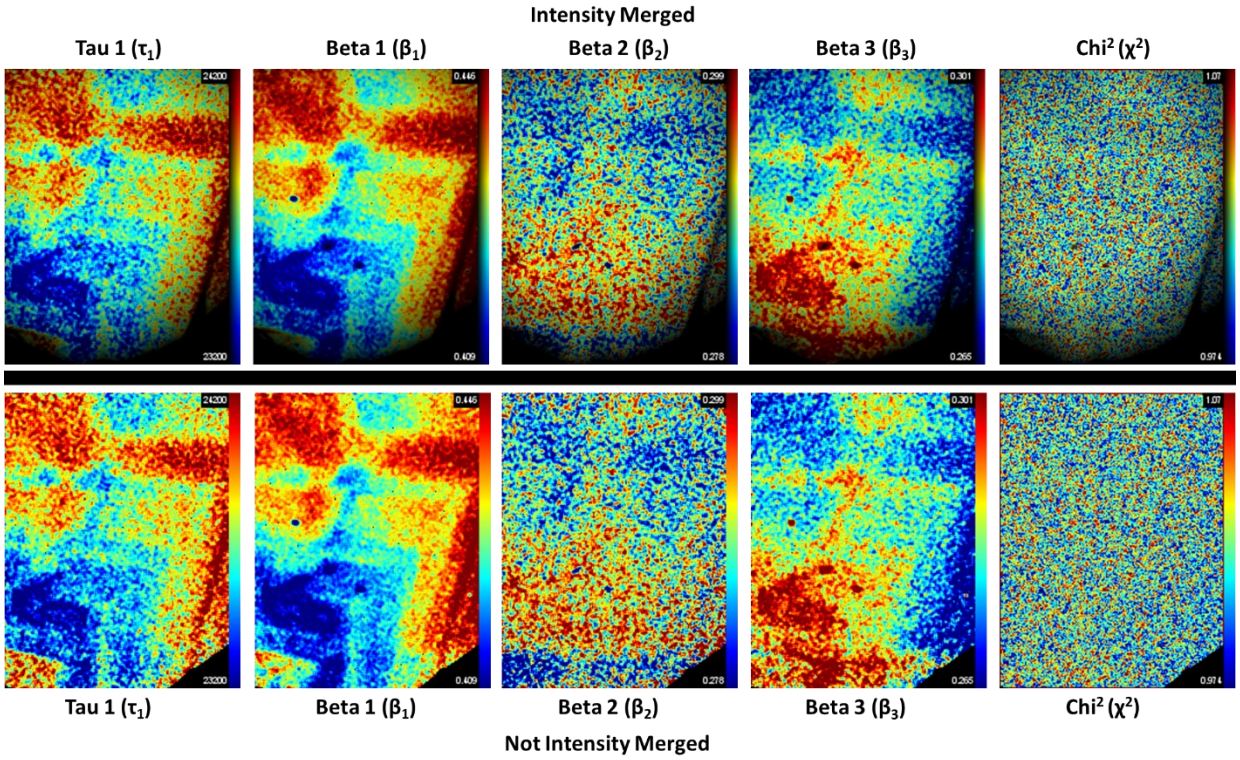
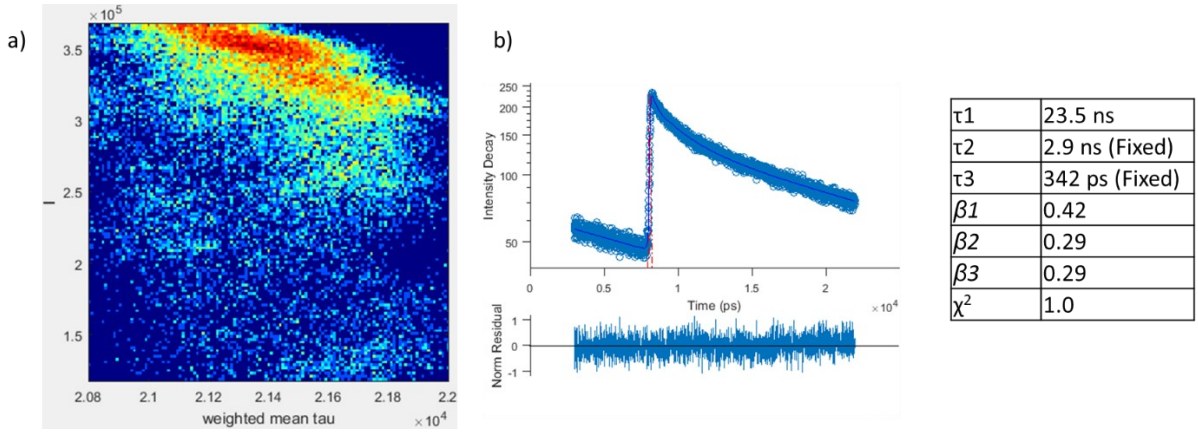



*Figure 100*[190] *– A set of intensity-merged and not intensity-merged images showing the spatial variations of various parameters. $T_2$ and $\tau_3$ had fixed lifetimes and so the images are not shown here. The $\chi^2$ map shows no obvious structure, suggesting the model is a good fit for the data to within the noise level for all regions of the image. This data corresponds to the model from Figure 99 d).*

The relationship between intensity (summed photon counts) and lifetime needs to be explored in lifetime measurements, because it can indicate a potential instrument-related artefact. In Figure 101 a), a 2D histogram showing the relationship between the intensity-weighted mean lifetime and summed intensity is shown. Broadly, as the lifetime decreases, the intensity increases. Both the emitting defect, N3, and the quenching agent, A-centres, are nitrogen related. This is a natural diamond, so the growth timescales can result in significant variations in nitrogen incorporation and aggregation. Typical luminescence quenching results in a shorter lifetime and fewer emitted photons. However, both the emitters and quenchers are associated with the incorporation of nitrogen and it is possible that the increase in nitrogen incorporation results in an increase in the number of (quenched) emitters, resulting in higher intensity, but lower lifetime in some regions. An exemplar luminescence decay profile from a region of the sample is shown in Figure 101 b), with a table showing the different parameters fitted obtained from the fitting.




| | |
|---|---|
| τ1 | 23.5 ns |
| τ2 | 2.9 ns (Fixed) |
| τ3 | 342 ps (Fixed) |
| *β1* | 0.42 |
| *β2* | 0.29 |
| *β3* | 0.29 |
| $\chi^2$ | 1.0 |

*Figure 101*[190] *- Analysis of luminescence lifetime data from the natural diamond sample excited at 355 nm with a 430/5 nm detection band for pixelwise fitting: a) shows a 2D false-colour histogram of the intensity-weighted mean lifetime plotted against the total photon count (I), presenting a linear relationship between the total photon count and weighted mean lifetime; b) is an exemplar single pixel luminescence decay profile showing the fit to the triple exponential decay model. The table shows the fitted parameters*[190].

## *Single point-spectrally resolved lifetime*

The increase of the weighted mean lifetime at longer wavelengths shown in Figure 99 f) and the reduced spatial variation for the $\beta_2$ component shown in Figure 100 indicate that not all the emission lifetime components are related to the N3 defect. To further explore this, single-point spectrally resolved lifetime measurements were undertaken to investigate how the weighted mean lifetime vary as a function of emission wavelength. The same excitation wavelength of 355 nm was used with a 4x 0.16 NA (Olympus, UPlanAPO) objective lens was used to collect the data, sampling the emission wavelength every 0.05 nm. This data was then spectrally binned to realise 0.5 nm spectral sampling. The resulting spectrum is shown in Figure 102 a) on a linear and logarithmic intensity scale. The spectrum exhibits the ZPL of N3 at 415 nm and the log plot reveals a peak at 372 nm, corresponding to first order Raman scattering. At each wavelength, a luminescence decay profile was measured, and this is presented in Figure 102 b). Fast decay profiles (attributed to scattering as they match the IRF profile) are indicated at 372 nm and 392 nm, which correspond to 1$^{st}$ and 2$^{nd}$ order Raman scattering.

Figure 102 c) presents a plot of the intensity-weighted mean lifetime as a function of wavelength, for which the decay profiles were globally fitted to a triple exponential decay model, producing component lifetimes of $\tau_1$ = 23.5 ns, $\tau_2$ = 3.0 ns, and $\tau_3$ = 0.45 ns, using initial conditions from the FLIM data. The intensity-weighted mean lifetime decreases below 400 nm and is reasonably constant between 400 and 500 nm, before slowly increasing with wavelength. The three globally

fitted population fractions are shown in Figure 102 d). The β2 population fraction decreases from 370 nm before plateauing from 420-500 nm, after which it decreases. The τ2 lifetime component could originate from A-band emission in diamond, which is thought to originate from dislocations, and is efficiently excited at 355 nm[19]. This A-band emission, which overlaps spectrally with N3 emission, does not depend on nitrogen incorporation and this could explain why no significant spatial variation in τ2 was observed in the lifetime images. The other two components follow similar trends, suggesting that they are associated with the same emitting species. The short component may be attributed to quenching of the N3 emission[128]. The lack of structure in the residuals in Figure 101 b) suggest that these the components are sufficient to represent the N3 and attributes A-band decay profile, within the noise level of the decay.

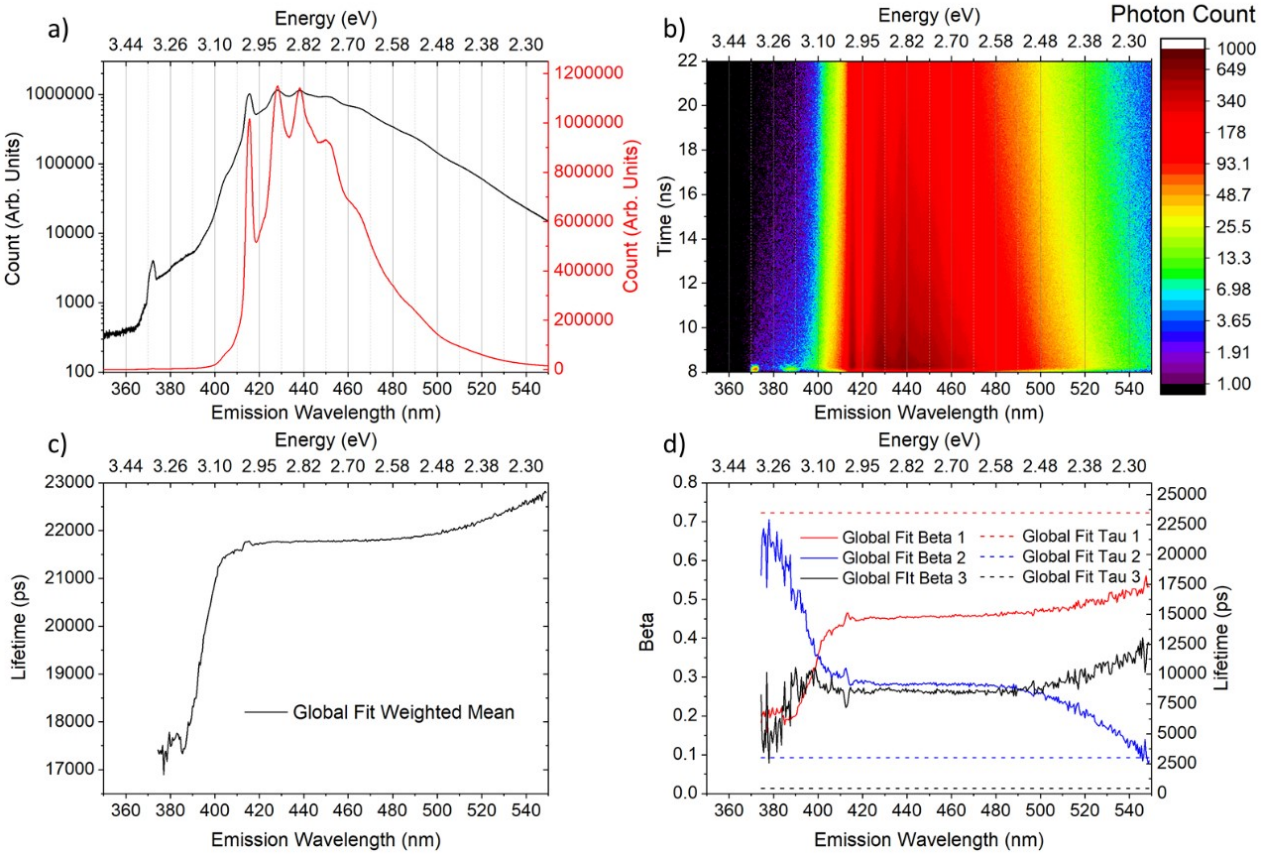



*Figure 102*[190] *- a) Spectrum of a point on the natural cut sample under 355 nm excitation using a 4X, 0.16 NA objective, with a log scale indicating the presence of the 1st and 2nd order Raman shift at 372 and 392 nm respectively. b) Spectrally resolved decay profiles from same region with a decay plotted every 0.05 nm. c) Spectrally resolved intensity-weighted mean lifetimes globally fitted with three exponential decays, binned to 0.5 nm resolution. d) Spectrally resolved β and τ values of each decay component globally fitted, binned to 0.5 nm resolution.*

## Natural diamond plate

Faceted diamonds are harder to image than polished natural diamond plates, due to the reflections from other faces. In addition, absorption mapping is more difficult with a faceted diamond, because reflections off multiple angled faces could occur, complicating absorption measurements. This is one reason why only bulk absorption measurements are undertaken of faceted natural diamonds. For research purposes, diamonds are often machined to be thin plates with two parallel faces, but this is not possible in the diamond gemstone industry, e.g. for identification purposes. This section reports measurements of a different natural diamond that has been cut and polished to produce a plate that was thin enough to make dimensional measurements impossible due to the physical integrity of the sample. The sample was too thin to safely measure accurately. Since diamond growth occurs in 3D, this diamond plate is expected to present some variation of optical properties with depth.

A blue light transmission image with a blue filter (with unknown bandwidth and centre), and a DiamondView™ image (of luminescence from above band gap excitation) is shown in Figure 103. The transmission image reveals some variation in absorption, which is identifiable in this blue region. The DiamondView™ image presents spatial and spectral variation in emission. This variation can be further analysed through the various capabilities available with the multidimensional instrument. These spatial/spectroscopic properties could be useful for determining whether a diamond is synthetic or natural, which is of importance to the gemmology community. This sample appears to be similar to diamonds referred to as 'Chameleon diamonds', which show a complex spatial distribution of defects[202] and have been known to include an absorption feature at 480 nm[203]. Luminescence lifetime analysis has not previously been used to investigate a 'Chameleon diamond'.

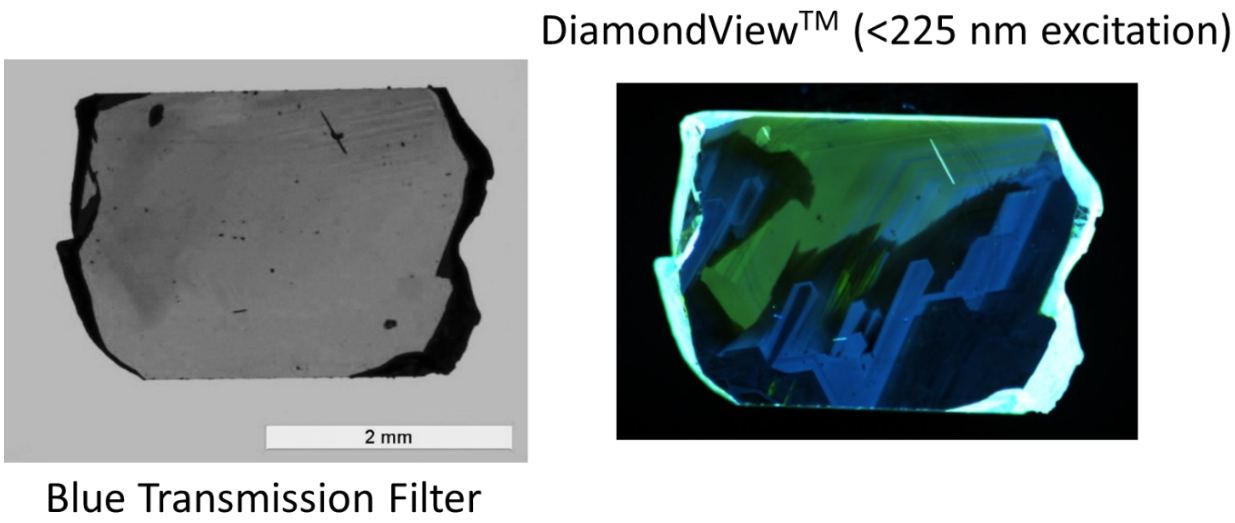



*Figure 103 – Images taken by De Beers showing a blue transmission filter light transmission image (left), and a DiamondView™ image of the same sample (right) of a natural diamond plate. The emission colours indicate blue and green emitters, potentially indicating N3 and H3 defects.*

## *Hyperspectral imaging*

Hyperspectral emission data was acquired with an excitation wavelength of 405 nm using a gain-switched diode laser (PicoQuant, LDH-D-C-405M), which was chosen to preferentially excite the N3 defect that was expected to be present in this sample. Although this defect can be excited at 355 nm, this would also excite other defects[190], which could add unnecessary complexity to luminescence lifetime analysis. Excitation at 405 nm is not expected to excite emission from other defects. A 4x 0.16 NA objective lens (Olympus, UPlanAPO) was used with line illumination for the hyperspectral imaging using the 150 lines/mm grating to achieve 0.28 nm spectral resolution over a 355 nm bandwidth. The sCMOS (Zyla 5.5, Andor) was used for detection.

As shown in Figure 104 a), white-light transmission through this sample shows some spots (possibly dust or small inclusions) and visible cracks, along with some angled parallel lines that could have originated from mechanical polishing. Through crossed polarisers, white-light transmission presents several brighter regions, as shown in Figure 104 b), which are indicative of strain in the lattice from symmetry breaking, causing birefringence. Some of these bright regions are bounded by lines at angles of 106°, suggesting they are related to the tetrahedral structure of diamond, for which the bond angle is 106.7°. The median wavelength of the hyperspectral emission data excited at 405 nm is displayed in grey scale in Figure 106 c). The upper region of the sample shows little variation in median wavelength, suggesting the presence of only a single emitting species. The lower region

shows more structure in the median wavelength, varying as bands in places, indicating that multiple emitting species are present. The spectrally-integrated intensity image calculated from the hyperspectral data is combined with the median wavelength image to produce image Figure 106 d).

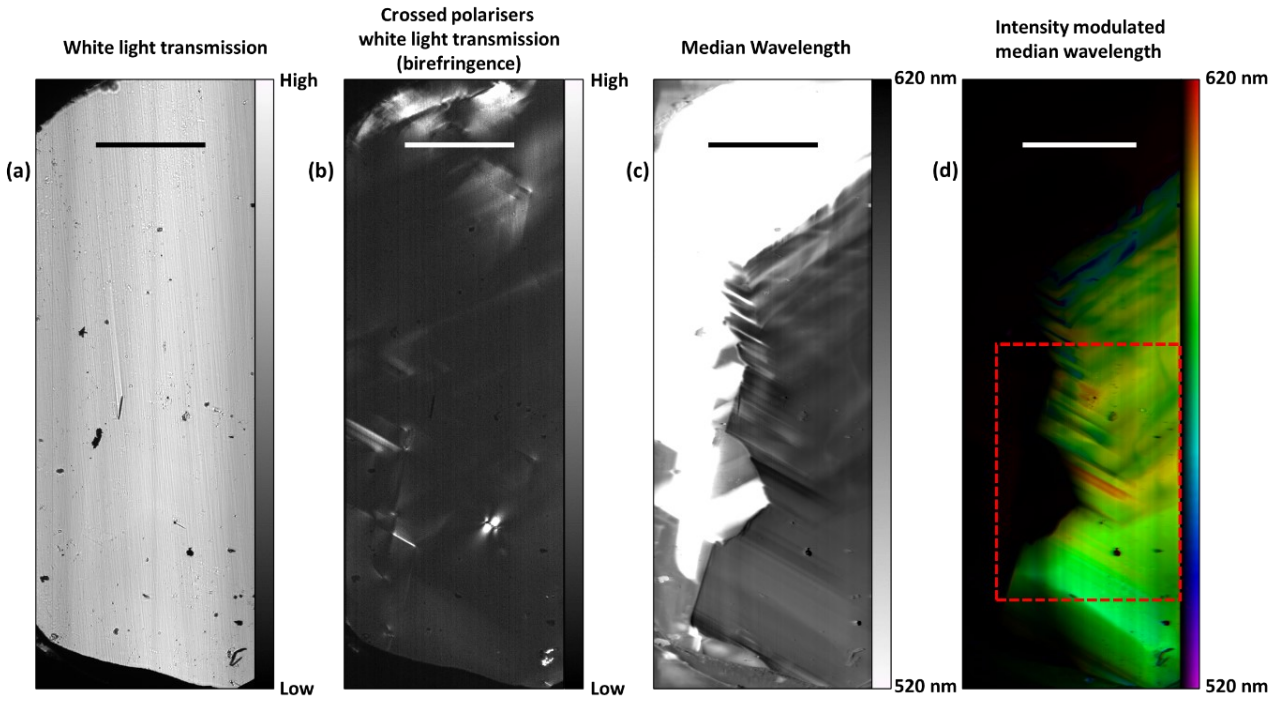



*Figure 104 – Hyperspectral data from the natural diamond plate under 405 nm excitation using a 4x 0.16 NA objective. A white-light transmission image of the sample is shown in a) and does not reveal anything significant about the sample. Crossed polarisers were used in conjunction with white-light transmission to form the birefringence image of the sample in b). This reveals regions of strain in the lattice, which causes birefringence. The median wavelength from the hyperspectral data was calculated and a grey scale map is shown in c). The diamond is split into two distinct regions. One region to towards the top of the image is uniform with a median wavelength of 520 nm, whilst the bottom right of the sample shows a more structured and complex profile, with varying median wavelengths. Combining a summed intensity image (not shown) with the median wavelength (as colour), the image in d) reveals that the more complex region of the sample is the brightest. The scale bar is 500 µm.*

The emission spectral data from three different ROIs on this thin natural diamond sample are shown in Figure 105. For excitation at 405 nm, the filter cube does not enable emission <430 nm to reach the detector. This means that the ZPL from N3 at 415 nm is not observed, but its extended phonon side band is present[19]. Excitation at 355 nm was undertaken to confirm the presence of the N3 415 nm ZPL, but this data is not shown here. Emission below 500 nm can be attributed to emission from the N3 defect. The emission above 500 nm appears complex, with the median wavelength

varying with spatial position on the sample, which suggests multiple overlapping defects. There are no obvious sharp features that can be attributed to a ZPL of other defects.

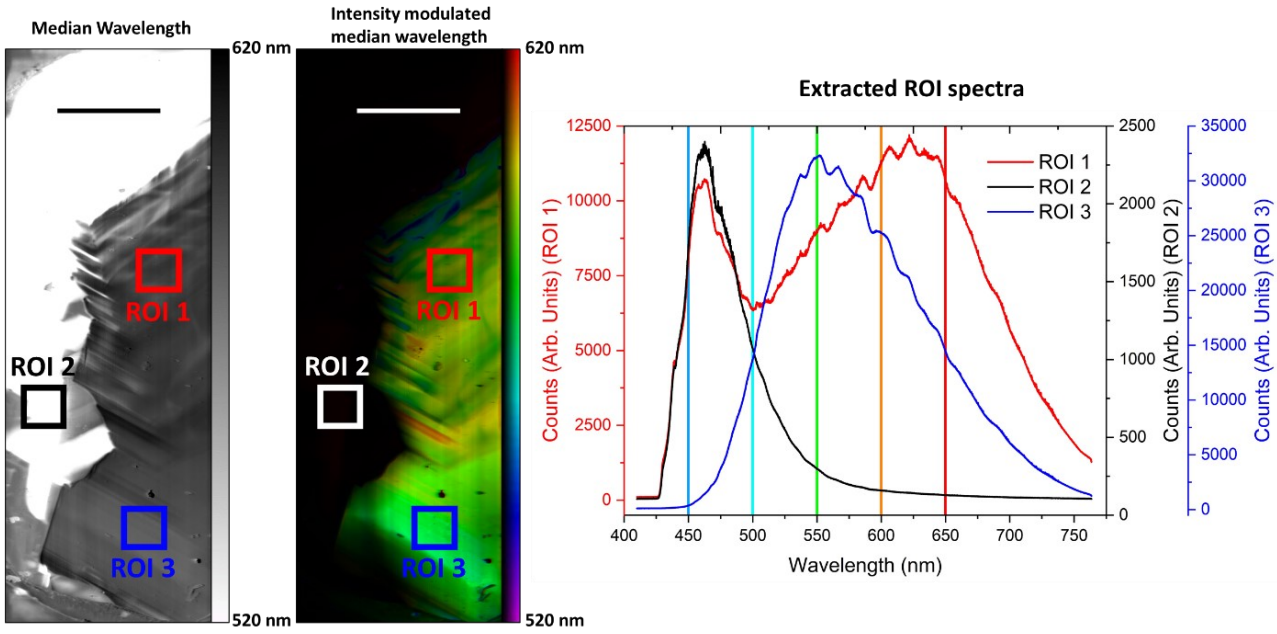



*Figure 105 – The median wavelength (left) and intensity modulated median wavelength images (middle) are shown here with various regions of interest highlighted, under 405 nm excitation. The averaged spectra from these regions have been highlighted on the graph (right), which show the variation in spectral features. The vertical coloured lines in the graph indicate the emission bands used for the FLIM experiments discussed below. The scale bar is 500 µm.*

## *Single point-spectrally resolved lifetime*

Spectrally resolved lifetime analysis was undertaken to further explore the photo-physics underlying the emission spectra shown in Figure 105. Measurements were made at five locations on the sample within the red dashed rectangle shown in Figure 104 d). These locations, which are indicated in the intensity-modulated median wavelength and median wavelength (grey scale) images in Figure 107, were chosen because they showed variation in their spectra from the hyperspectral data set. For each measurement, the monochromator was stepped in 0.25 nm increments from 420 to 700 nm, with a spectral dwell time of 5 s. This data was collected using the 40x 0.6 NA objective lens (Olympus, LUCPlanFL N) using the 405 nm gain-switched diode laser (PicoQuant, LDH-D-C-405M) operated at 2.5 MHz pulse repetition rate.

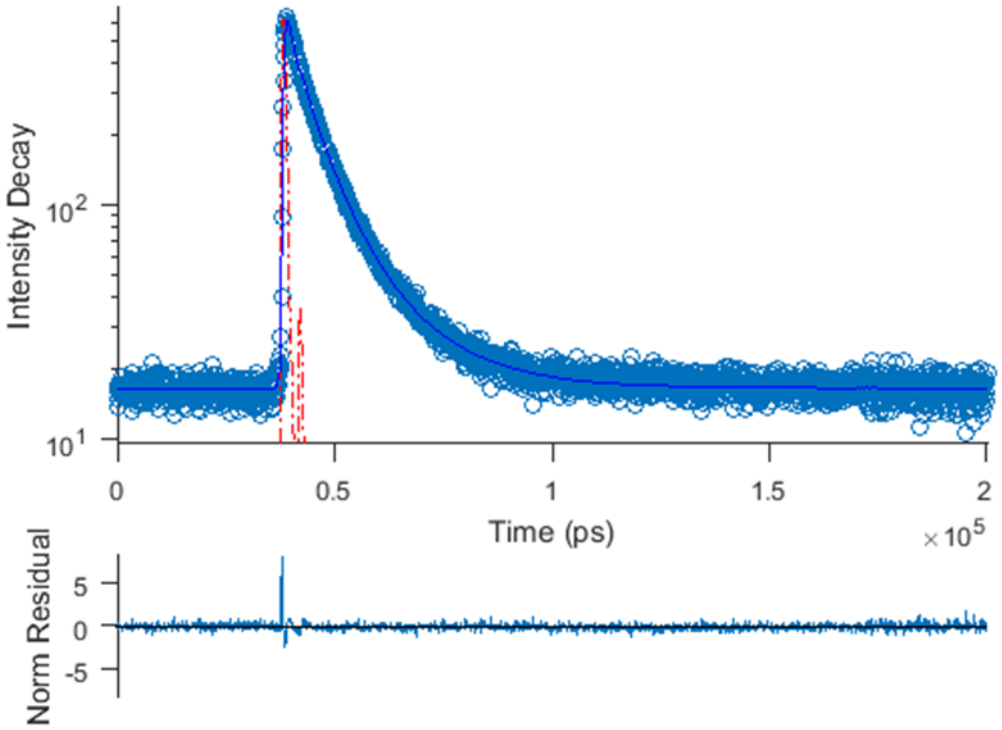



*Figure 106 – An example decay from the natural diamond plate, measured at 600 nm emission using 405 nm excitation. The fluorescent component of this measurement decays to the noise floor inside the pulse period of the laser. The large offset observed here originates from long lived emission/phosphorescence, not from dark counts on the detector. This decay was fitted with a quadruple exponential model from a 3x3 binned pixel from FLIM data.*

The resulting luminescence lifetime data included a large apparent offset, which is attributed to a background of long-lived phosphorescence emission, and this is shown in the example decay in Figure 106. This phosphorescence background was briefly explored in chapter 4, using the (micro-time) photon time-tagging capability of the TCSPC system. This background was subtracted from the decay profiles, so that subsequent phasor analysis only considered the fluorescence components of the signal. This phosphorescence background subtraction was achieved by averaging the photon count just before the onset of the IRF and subtracting that value from each time bin in the spectrally resolved decay data. A phosphorescence background spectrum was also calculated from this data, which is shown as the black line in Figure 107, whereas the fluorescence intensity (summed photon count before subtraction of background) is plotted in red, and the net fluorescence intensity (summed photon count after subtraction of phosphorescence background) is plotted in green. The phase lifetime was calculated using phasor analysis applied to the net fluorescence decay data and this is plotted in blue.

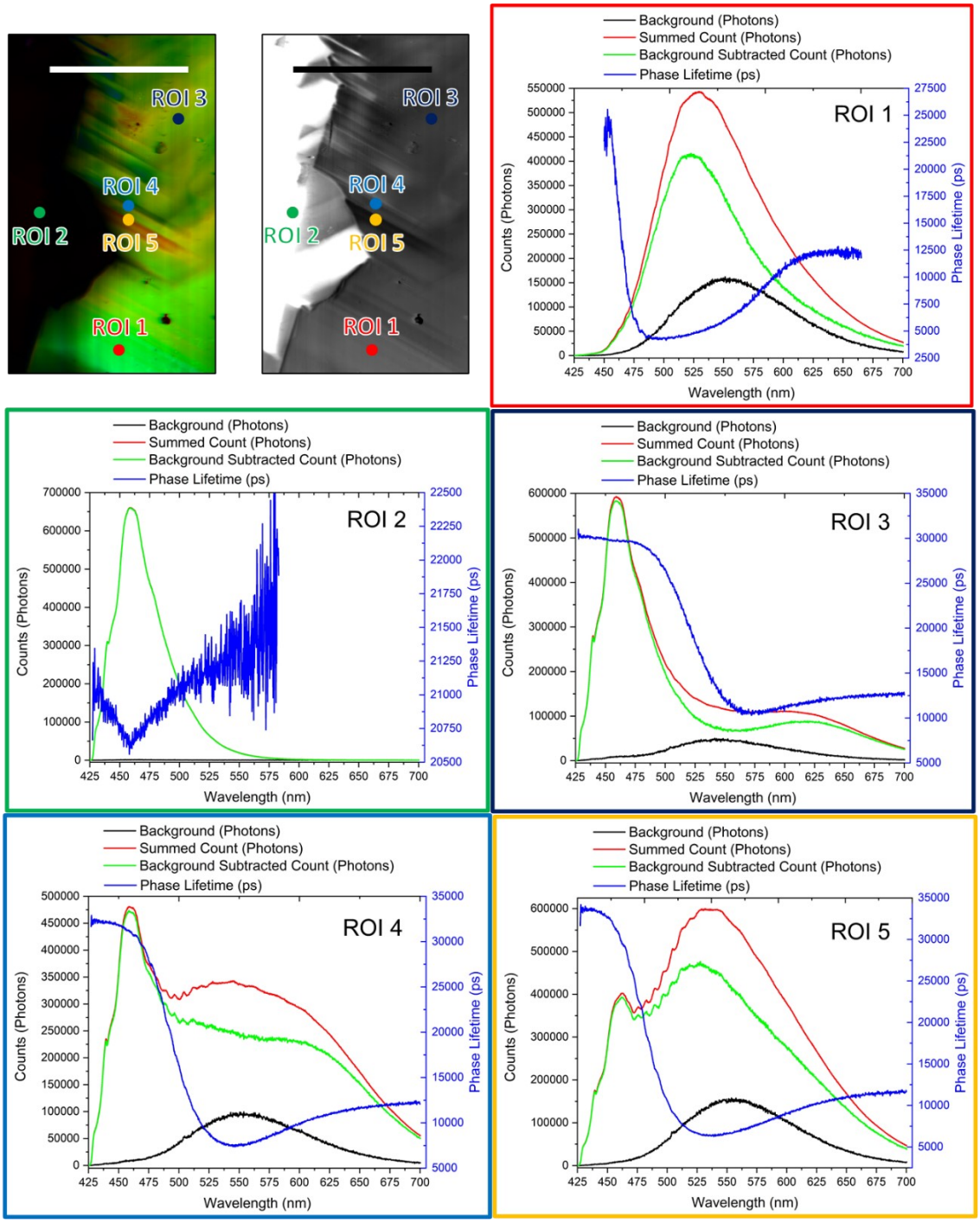



*Figure 107 – Five locations on the sample were measured using the single-point spectrally resolved lifetime technique, using 405 nm excitation. The median wavelength intensity modulated and median wavelength images are shown, with the five locations indicated. Each coloured ROI has a corresponding graph, and these are analysed in the text. Each graph contains a summed background phosphorescence photon count line (phosphorescence, black), a total summed photon count line (including background phosphorescence, red), a background subtracted summed photon count line (after background phosphorescence subtraction, green), and a phase lifetime line (after background phosphorescence subtraction, blue). The scale bar is 500 µm.*

Measurement of the luminescence decay profiles allows the spectral profile of the phosphorescence background to be separated from that of the fluorescence. ROI 1 is located near the bottom of the sample and is in a region with a high background phosphorescence photon count, peaking near 150,000 photons at 535 nm. The peak of the (green) net fluorescence emission spectrum was found to be at 525 nm after subtraction of the phosphorescence background. The decay of the phosphorescence was previously measured in chapter 4. One component of the phosphorescence has been attributed to the NE3 defect, with the decay shown in Figure 48. The other components in this phosphorescence decay did not have a known origin. The variation in phase lifetime as a function of emission spectrum suggests at least three emission bands/different fluorescent emitters are present in ROI 1. The peak at 450 nm in phase lifetime could indicate that a small component of N3 is present at this location, although N3 emission is not apparent in the fluorescence intensity spectrum. The phase lifetime decreases to a minimum of 4.3 ns at 490 nm and then increases with wavelength to 12.1 ns at 660 nm. This variation in phase lifetime could be due to a mixture of at least two lifetime components, in addition to the small component of possible N3 emission centred at 450 nm.

ROI 2 is located in a dark region of the image that shows no variation in median wavelength, as shown in Figure 104 and Figure 105. The background photon counts for emission from this location peak at 1525 photons at 462.25 nm, suggesting that phosphorescence is not significant relative to the peak intensity (summed photon count) of 659,000 photons at 459 nm. The fluorescence may be due to the phonon side band of N3; however, the phase lifetime is much less than 41 ns, the natural lifetime of this defect[128]. This may be explained by quenching of emission from the N3 defect. There is some wavelength-dependant structure to the phase lifetime with a range up to 750 ps through the main part of the emission spectrum. The cause of this is unknown but could indicate the presence of another emitting or quenching defect. This is further explored in the discussion of FLIM data later in this chapter.

The emission from ROIs 3, 4 and 5 show similar spectral features, albeit with different concentrations of the main components. All three locations present a phosphorescence background with varying intensity, peaking at 550 nm. Also apparent is a small peak at 504 nm on top of the broader phosphorescence (background) spectrum. This could be a weak ZPL of the defect responsible for the phosphorescence but does not correspond to anything in literature. The NE3 defect, which was attributed to a component of the phosphorescence decay in chapter 4, has a ZPL at 523.3 nm[19], which does not match this feature. There were other lifetime components measured in the phosphorescence decay, shown in chapter 4, which could be related to this feature at 504 nm. H3 and 3H have a ZPL near this feature, but H3 has a fluorescence lifetime of 16.7 ±0.5 ns,

whereas 3H is thought to decay very rapidly (below 1 ns)[145], and neither are in the microsecond time domain. Investigation at cryogenic temperatures using spectrally resolved micro-time lifetime spectroscopy could reveal more information about the components of this phosphorescence background.

The net fluorescence (green line in Figure 107) from ROI 3 shows a peak at 460 nm and a weaker feature peaking at 625 nm. The (green) net fluorescence spectra from ROI 5 and ROI 5 also present the emission peak near 460 nm, although this is obscured at ROI 5, for which the spectrum also presents a broad peak around 530 nm. The spectral and phase lifetime information of ROI 1, 3, 4 and 5 indicate emission from at least three different lifetime components. This is consistent with a longest lifetime component emitting near 460 nm, attributed to N3 with varying lifetime due to quenching: a shortest lifetime component with an emission peak between 500 and 550 nm and a lifetime of ~4.3 ns (evidence from ROI 1), and an intermediate lifetime component of ~12.5 ns, with an emission peak near 625 nm. There is insufficient information available to attribute the two shorter lifetime components to specific defects without spectra presenting ZPLs. Cryogenic luminescence measurements may provide improved spectral discrimination between emitting species, although it can be challenging to correlate spectra measured at room temperature with cryogenic measurements. Figure 108 presents for each ROI the variation of phase lifetimes (phosphorescence background subtracted) and the luminescence modulation lifetimes, for which the phosphorescence background was not subtracted. The modulation lifetime shows the weak phosphorescence feature at 504 nm, and this is the reason why the background phosphorescence was not subtracted.

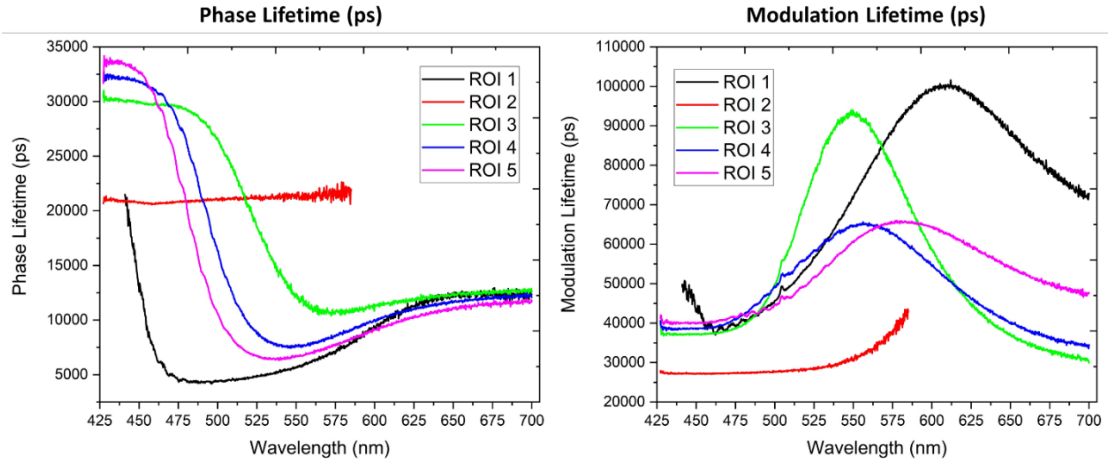



*Figure 108 – The phase lifetime (phosphorescence background removed) and modulation lifetime (phosphorescence background included) for each of the five ROIs in Figure 107 under 405 nm excitation are shown in the two graphs. The complex profiles indicate multiple emitting species, of which, one attributed to N3 emission is quenched*

## *Luminescence lifetime imaging*

Luminescence lifetime imaging was undertaken using emission detection bands of 0.5 nm FWHM at the five different wavebands indicated on Figure 105, ranging from 450 nm to 650 nm in 50 nm increments, and applied to the region shown as the red dashed box on the hyperspectral image in Figure 104. A 40x 0.6 NA objective lens (Olympus, LUCPlanFL N) was used with 405 nm excitation at 2.5 MHz pulse repetition rate for measurements in the 450 nm emission band, and at 5 MHz pulse repetition rate for measurements in the 500-650 nm emission bands (to enable complete measurements of the longest lifetime components. A step size of 3 µm was used for the point stage scanning with a pixel dwell time of 0.5 s. Two full excitation periods were measured using the frequency divider setting, allowing phasor analysis to be applied, as previously described in chapter 4.

The phosphorescence background, which was present in most of the decay data, was subtracted as described in the previous section and the phosphorescence background image was calculated. For each emission band, the net fluorescence intensity (time-integrated photon count after background subtraction) and background phosphorescence images are shown in Figure 109.

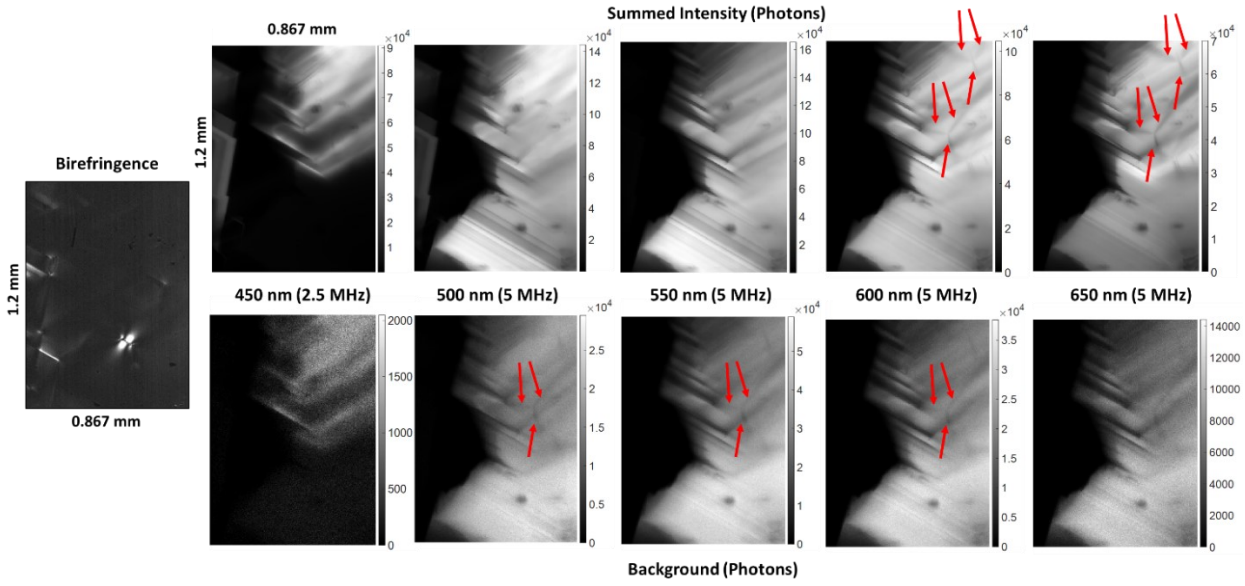



*Figure 109 – Summed intensity and background phosphorescence photon count images of a natural diamond plate at five emission wavelengths, under 405 nm excitation. The structure of the emission varies as a function of wavelength, whilst the background emission structure is mostly consistant, with the exception of 450 nm emission. The red arrows inidcate the locations of the three-finned structure discussed in the text.*

The 450 nm intensity images present a small region of fluorescence to the left of the field of view and a spatially varying (banded) intensity distribution in the top right quadrant. This banded emission could originate from different concentrations of emitters. At this emission wavelength, the background intensity image presents very low photon counts (2000 at peak vs 90 000 at peak of fluorescence) and matches the spatial distribution in the corresponding fluorescence intensity image. This background is unlikely to be phosphorescence in this case (as discussed later) but may result from late-arriving photons from the tail end of the fluorescence decay excited by the previous excitation pulse – noting that the phase lifetime of this region is ~34 ns. The region to the left does not present a background image matching the fluorescence image, but the phase lifetime of this region is lower, peaking at ~25 ns, and so there would be a much smaller contribution from the fluorescence decay to the background signal.

At 500 nm emission, the fluorescence and background intensity images present additional structures in the bottom half of the field of view, which suggests at least one additional emitter is present. The peak photon count is higher at 140,000 photons, and banding is also shown, that could be due to a variation in emitter concentration(s). The background image at 500 nm emission is present over much of the field of view and contains significantly more photons (29,000 at peak) compared to the background image at 450 nm emission (2000 peak). The intensity and background images for emission at 500, 550, 600 and 650 nm are similar, suggesting the emission originates from the same set of emitters, which is consistent with the spectrally resolved information previously shown in Figure 107.

At 550 nm the summed intensity image is spatially similar to 500 nm, with slight reduction in photon count in some regions at the top of the image. This is consistent with a reduction in N3 emission photons, for which this has been attributed, and is prevalent in the top section of the image. Emission at 600 and 650 nm is similar spatially, with the primary differences compared to 550 nm being a reduction in contrast of the banding at the bottom of the image, and prominent three-finned features (red arrows) becoming apparent near the centre of the image (clearest at 650 nm). The complexity of these spatial features, and the emission bands at which they become prominent suggests multiple emitting defects.

Using phasor analysis, the modulation lifetime (before background subtraction) and phase lifetime (after background subtraction) were calculated using a photon threshold of 1500 photons. This is to show the spatial variation of both the fluorescence and phosphorescence emission. The resulting lifetime maps are shown in Figure 110 for each emission wavelength, where a false colour scale is used to indicate the lifetime in ps.

The emission at 450 nm can be attributed to N3 emission, which is the dominant emitter in this band. The 450 nm intensity images in Figure 109 show that most of the photons originate from the region towards the top right of the field of view, which appears red in the phasor lifetime map in Figure 110, or from the region to the left of the field of view, which presents multiple phasor lifetime values. The range of phase lifetimes attributed to N3 thus ranges from 35 ns to 17 ns, with no regions presenting the N3 natural lifetime of 41 ns. This suggests a large varying concentration of quenching defects (A-centres). The two regions with different lifetimes could indicate that this diamond grew in two stages under very different conditions.

Emission at 500 nm and longer wavelengths is more complex than at 450 nm, including an additional component, emitted from the bottom half of the phase lifetime image in Figure 110. The mean phase lifetime of this blue region in the 500 nm emission phase lifetime map is 4.15 ±0.13 ns (standard deviation), which is close to the 4.3 ns value acquired from the spectrally resolved lifetime data in Figure 107. The uniformity of this region helps to more accurately determine the lifetime of this (unknown) emitting defect, as it appears to be the only component present. The upper section of this phase lifetime image presents both components, a long lifetime component attributed to quenched N3 emission and the 4.15 ns component, with more spatial variation than was apparent at 450 nm. The region to the left hand edge of the image for emission at 500 nm shows lifetime ranging from 16.5 ns to ~35 ns (compared to 15 – 18 ns for emission at 450 nm) which could indicate the presence of a further defect.

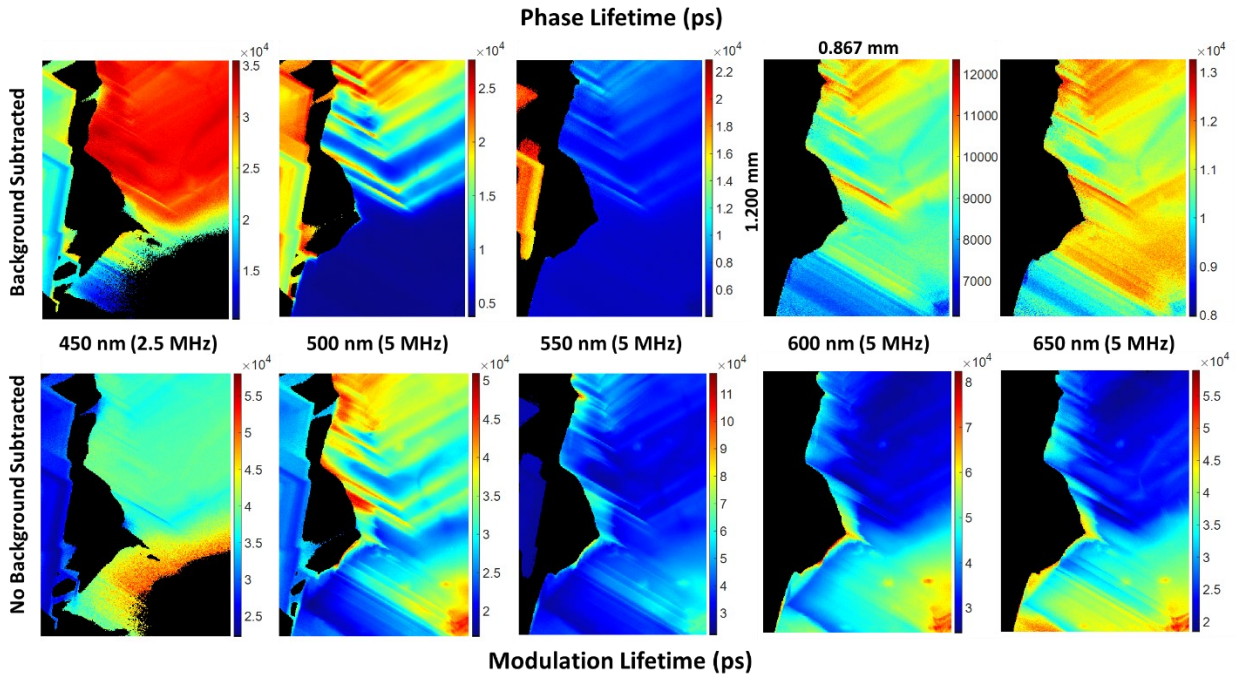



*Figure 110 – Phase lifetime (with background photons subtracted) and modulation lifetime (without background photons subtracted) at five emission wavelengths under 405 nm excitation, extracted from phasor analysis. Corresponding phasor diagrams are shown in Figure 111. The phase lifetime images represent only the fluorescent components of the emission, whilst the modulation lifetime images show the total variation of lifetime of both the fluorescent and phosphorescent emission. These images are discussed in the text.*

For emission detected at 550 nm, the phase lifetime image shown in Figure 110 shows only small variations in lifetime, primarily towards the top and at the left hand side of the image. This may be because the emission from N3 is very weak this far from its 415 nm ZPL and so there is less spatial variation in lifetime, with any variation existing due to spatial variation in nitrogen incorporation. The region to the left, attributed to quenched N3 emission, presents the same lifetime of 16.5 ns observed in the 500 nm emission image. The tail end of the emission does extend to 550 nm as shown in Figure 102. The emission at 600 nm for the phase lifetime in Figure 110 shows more complex lifetime contrast, which may originate from two unknown defects presenting lifetime components of ~4.15 ns, and ~12.5 ns. Both defects present emission with varying spatial distribution and there is no region where only one of these lifetime components is present. For emission at 650 nm, the phase lifetime image shows similar spatial distributions of lifetime as the phase lifetime image for emission at 600 nm, but with a shift towards longer lifetime values. This is consistent with the spectral lifetime information shown in Figure 107.

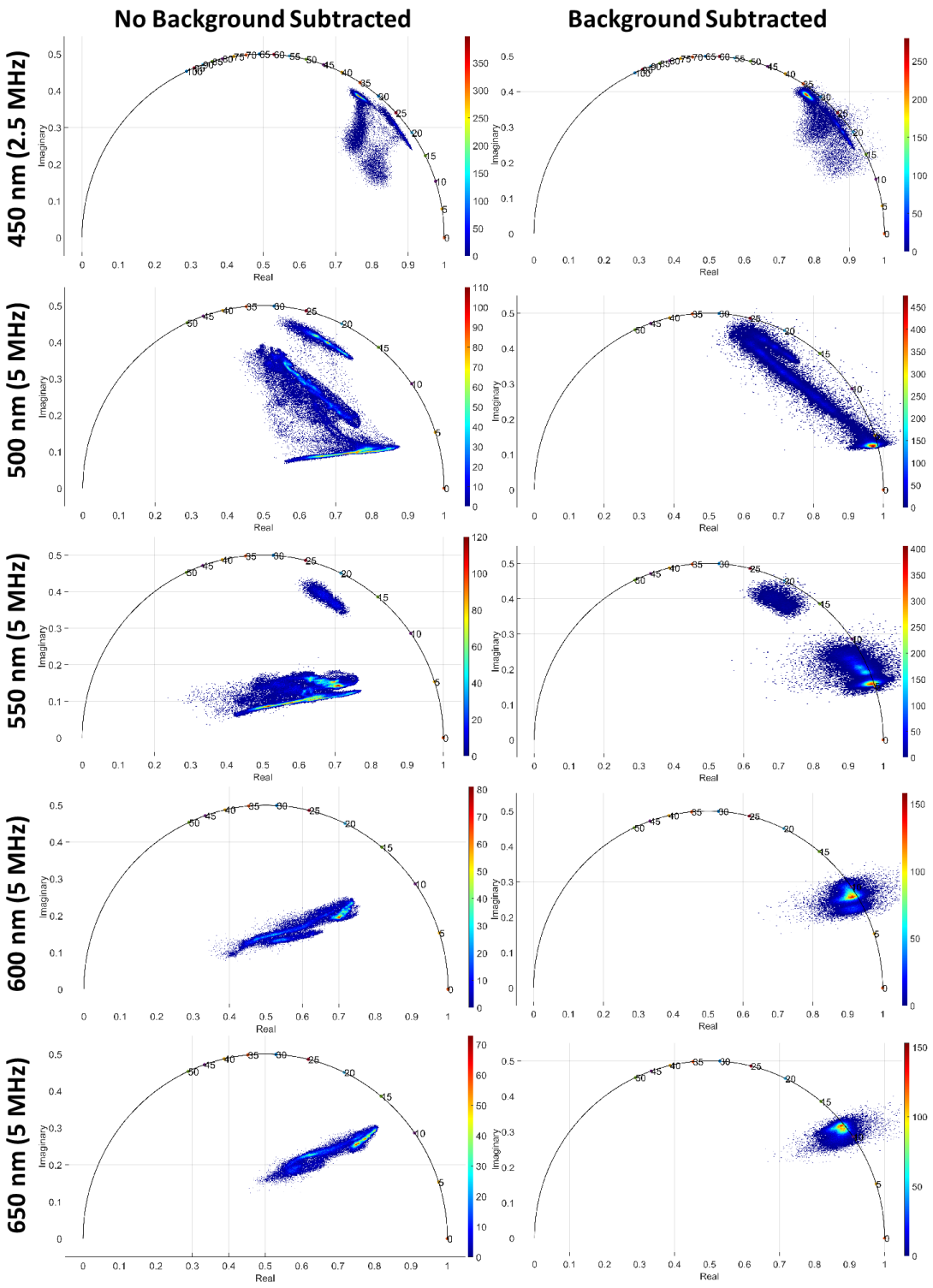



*Figure 111 – These phasor plots correspond to the images in Figure 110. The non-background-subtracted phasor plots were used to extract the modulation lifetimes, and the background-subtracted phasor plots were used to extract the phase lifetimes. The background has a significant impact on the distribution of the data points in the phasor plot, due to the contribution of the background to total photon count. The coloured data points represent the number of pixels in the image.*

The modulation lifetime images are more complex, due to the presence of both fluorescence and phosphorescence components. The impact of correct background subtraction is further illustrated in the phasor plots shown in Figure 111, where it is more straightforward to determine the lifetime components that are present using the background subtracted data.

Overall, the lifetime variations highlight spatial structure, consisting of angular bands of lifetime contrast that may be due to preferential incorporation of defects into specific growth planes. Alternatively, it could represent different growth or annealing conditions, which were present at different times, or at different depths in the Earth. Direct identification of the emitting defects could help in determining which of these possibilities is the most probable, with applications for underground geology or diamond identification being possible outcomes.

The luminescence decay profiles observed from this sample could not be unambiguously modelled due to the number of spectrally overlapping lifetime components, and insufficient prior knowledge about the sample. The complexity of the quenched N3 decay required a total of five components to reach an adequate fit (no structure in residual and $\chi^2$ ~1): three for the longer (less quenched) decay region (right of image Figure 109 450 nm) and two for the shorter (more quenched) decay region (left of image Figure 109 450 nm). For emission at 500 nm, where multiple lifetime components overlap spectrally, the number of parameters required exceeded the maximum allowed by the *FLIMfit* programme, making it impossible to determine all the component lifetimes for both the FLIM and single point spectrally resolved lifetime data sets. In future, the use of additional excitation wavelengths, with an adjustable excitation pulse repetition rate, could be used to excite specific defects more selectively. The lifetimes of these components could then be used to reduce the number of variables when fitting the data sets with multiple lifetime components.

The study of this sample has illustrated the complexity of natural diamond luminescence. This sample is thought to be a 'Chameleon diamond' – a type whose luminescence has not previously been measured with these techniques. Some of the limitations of the developed instrument are apparent in this work, including the lack a variable repetition rate excitation laser above 405 nm. The ability to make measurements at different temperatures, including cryogenic experiments, could help to reduce the complexity and overlap of the defects' luminescence. This sample exhibited the shortest lifetime (16.5 ns) attributed to N3 emission yet reported to my knowledge, well below the natural lifetime of 41 ns. This could suggest a high concentration of A-centres, or another new quenching mechanism.

## Natural diamond plate with mapped varying A-centre concentrations

The measurement of A-centre distribution is potentially important in the gemmology industry, as it could be used to determine if a diamond is natural or synthetic. A-centres are non-emissive and therefore only visible via absorption measurements, which have limitations including the need for well-controlled sample geometries (such as parallel flat sides) [19]. The previous analysis of natural diamond luminescence using lifetime imaging and spectrally resolved lifetime measurements revealed complex luminescence decays, with multiple spectrally overlapping components attributed to multiple unknown defects that could not be resolved without more prior information. It is not generally possible to use literature values to constrain the analysis because not all defects have been characterised and because quenching can reduce the lifetime of any defects present. Without prior knowledge to inform a fitting model, lifetime data analysis may be undertaken using phasors, which can provide at least a qualitative visualisation of luminescence dynamics including quenching. This could help to map the quenching of emissive defects, such as the quenching of N3 emission by A-centres in natural diamonds.

To explore this approach, another thin natural diamond plate exhibiting only N3 emission under 405 nm excitation was measured using lifetime mapping and analysed using phasor analysis. Figure 112 shows DiamondView™ images from both sides of this sample, presenting differences in emission intensity from each side. Absorption mapping would measure the total absorption through the sample thickness.

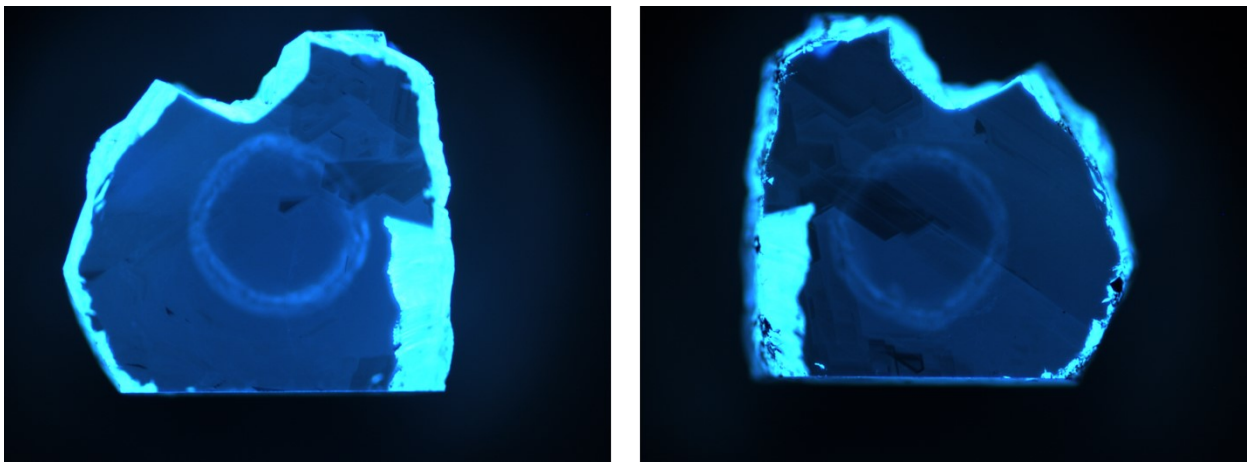


*Figure 112 – Two images from DiamondView™ taken by De Beers of a natural diamond plate showing emission from opposite sides of the sample. There is some structure present, but the sample primarily emits in the blue spectrum, attributed to N3 emission.*

Absorption mapping was conducted by Dr Phil Diggle (De Beers Technology group), using a Thermo Scientific Nicolet iN10 MX, with 4 $cm^{-1}$ spectral resolution. The Images shown in Figure 113 are the fitted concentration distributions for substitutional nitrogen, A-centres, and B-centres. The red circle denotes the aperture, which was used to hold the sample. A-centre concentration varies throughout the sample, from ~150 ppm, to >300 ppm. The image was sampled at 75 µm pixel spacing over a ~2 x 2 $mm^2$ area.

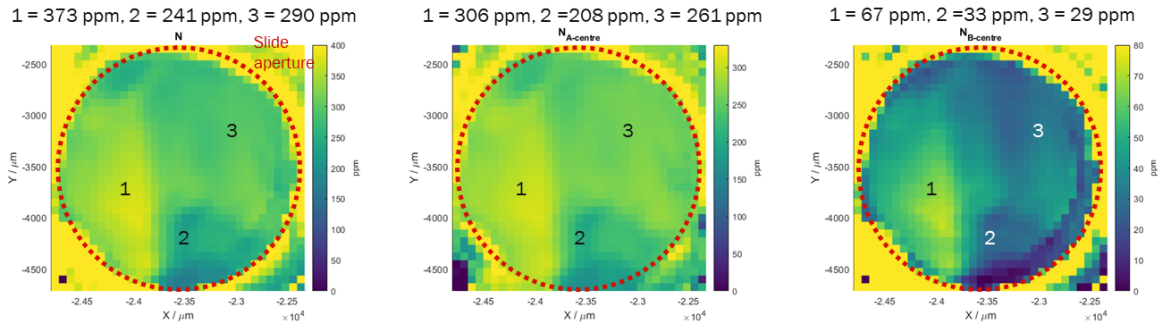



*Figure 113 – Concentration data for three nitrogen related defects taken by Dr Phil Diggle (De Beers) using spatially mapping IR absorption spectroscopy. There is variation in all three defects, and the A-centre and nitrogen spatial variation are similar.*

## *Luminescence lifetime mapping with phasor analysis*

The FLIM data presented in Figure 114 were acquired before the absorption data was received and was acquired over a smaller region with higher (1.5 µm) spatial sampling. It is difficult to co-register the lifetime images with both the DiamondView™ and absorption images because they were acquired on different instruments. This illustrates why a single instrument providing co-registered image modalities is useful. The luminescence lifetime data was collected using a 40x 0.6 NA objective lens (Olympus, LUCPlanFL N), with a 450/3 nm emission filter, excited at 405 nm using a gain-switched laser diode (PicoQuant, LDH-D-C-405M) operating at 5 MHz pulse repetition rate. The frequency divider setting was used to acquire data over two laser pulse periods, which enabled phasor analysis of longer lifetimes.

The spatial phasor plot, intensity (temporally integrated photon count), and modulation lifetime images are shown in Figure 114. The phasor plot presents a complex arcing “comet-shaped” cluster, which may represent decay profiles emitted from N3 defects with varying degrees of quenching – noting that this was the only defect expected to be excited in this sample at 405 nm. The intensity image shows significant variation, and the spatial distribution is not easily recognisable in the images from Figure 112 or Figure 113. This may be due to the difference in excitation wavelength compared

to the DiamondView™ images and the lack of optical sectioning in the absorption images. The modulation lifetime image presents a spatial variation in lifetime, which corresponds to many of the spatial features in the intensity image. The modulation lifetime varies by 6-7 ns, which is a large range[145] and these lifetimes are much lower than the natural lifetime for N3 of 41 ns.

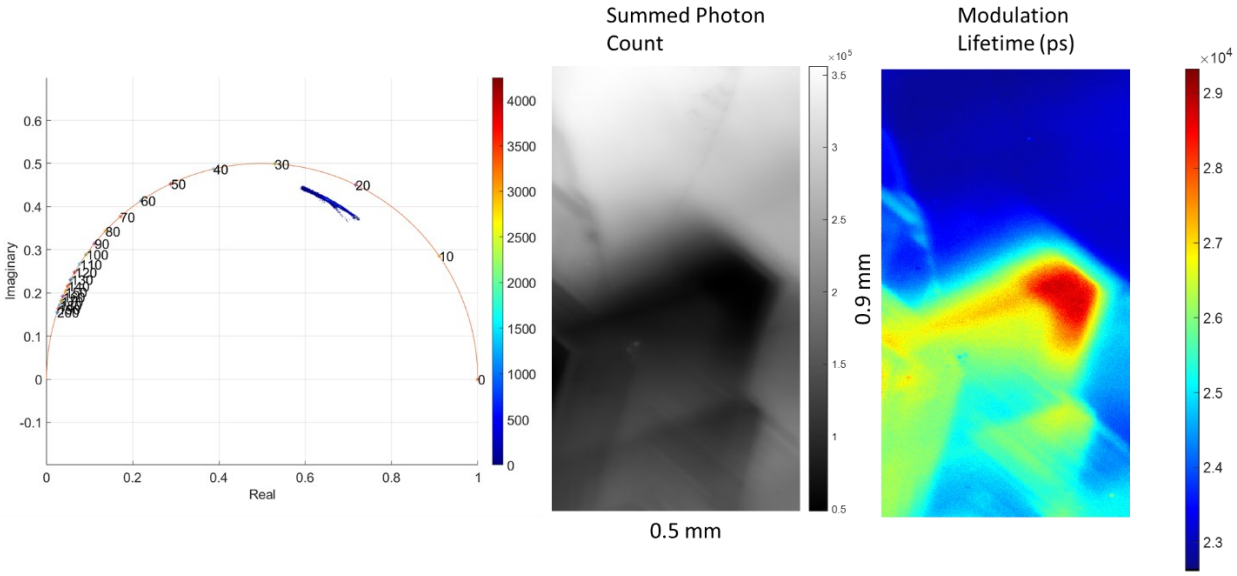



*Figure 114 – FLIM of the natural diamond plate sample was taken using a 405 nm laser, 40x 0.6 NA objective and 5 MHz to collect the data shown above. The emission wavelength was 450/3 nm. The frequency divider setting was used to allow phasor analysis to be utilised. The phasor plot (left) shows an arcing cluster, with many pixels centred at one end of the "comet" and the rest of the pixels spread along a "tail". The summed intensity and modulation lifetime images show a clear correlation between intensity and lifetime. This emission is dominated by N3 defects, and the modulation lifetime reveals the defect is quenched and shows significant variation.*

Figure 115 and Figure 116 show how the phasor plot can be used to segment the images with respect to lifetime. The 'nucleus' or 'head' of the 'comet' cluster in the phasor plot corresponds to the brightest pixels in the intensity image. The modulation lifetime varies by less than 1 ns across this region. It would be interesting to correlate this region with the absorption map to better understand the observed quenching.

The tail of the comet cluster represents the remaining region on the intensity and lifetime images and presents a much larger variation in modulation lifetime. Most of the structures that are attributed to variations in growth conditions are in this region of the diamond. The ability to segment the image by lifetime allows such regions to be readily graphically identified.

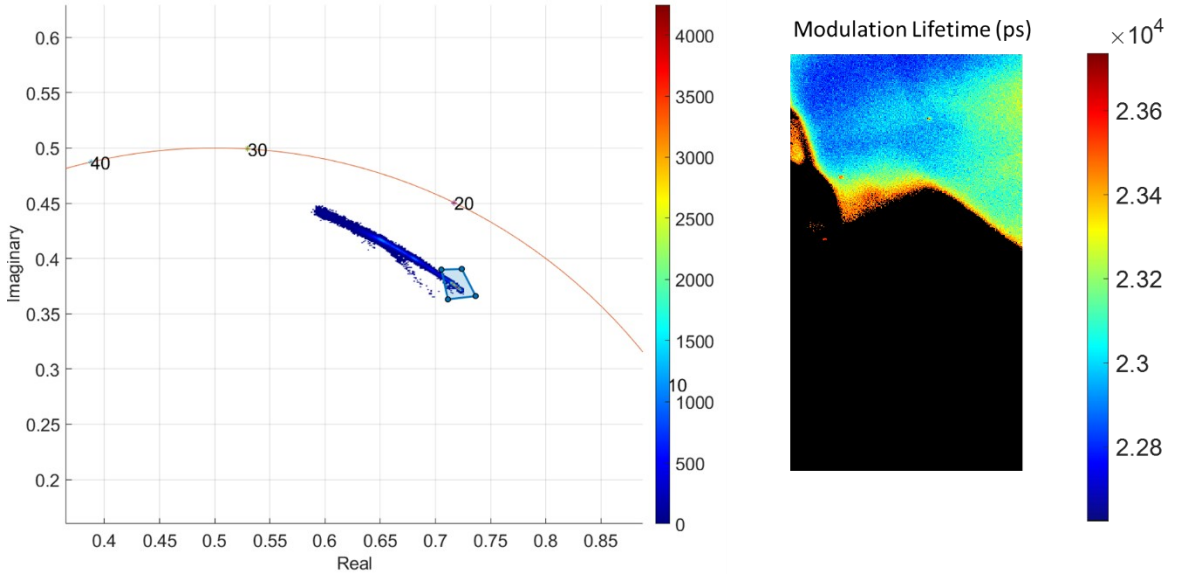



*Figure 115 – A zoomed in region of the phasor plot is shown, with a region of interest centred at the "head" of the "comet". The extracted modulation lifetime image for this region reveals that it is the top part of the sample that has the lowest modulation lifetime.*

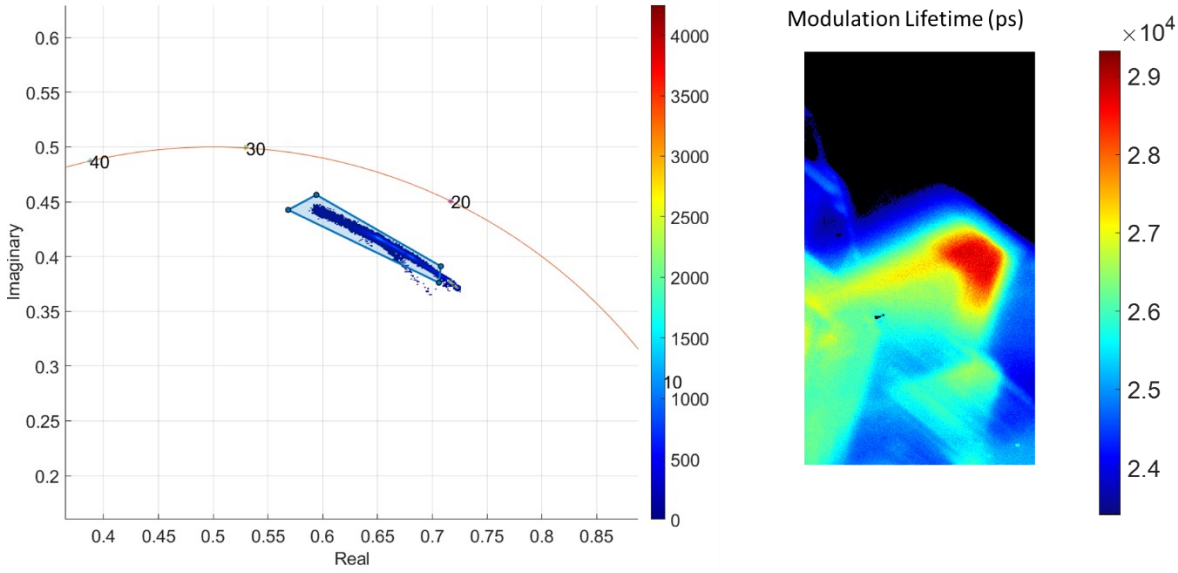



*Figure 116 - A zoomed in region of the phasor plot is shown, with a region of interest centred at the "tail" of the "comet". This shows a much larger variation in modulation lifetime and contains significantly more structure in the resultant modulation lifetime image.*

The modulation lifetime values from the phasor plots were applied to determine the initial parameters for iterative fitting of the lifetime data. However, these quenched decays were found to

be not accurately fitted using a double or triple exponential decay model and iterative fitting of the luminescence decays in this case did not offer any additional insights beyond those from the phasor analysis.

There is clear correlation between the calculated modulation lifetime and the pixel intensity (total photon count). A 2D histogram of the photon count and modulation lifetime images is shown in Figure 117, where the modulation lifetime is seen to reduce with increasing emission intensity. This was observed previously in Figure 101 on a different natural diamond and may again be explained by variations in nitrogen incorporation. It is interesting to note that towards higher photon counts, the rate of decrease of lifetime tends to zero, possibly indicating saturation of the quenching mechanism.

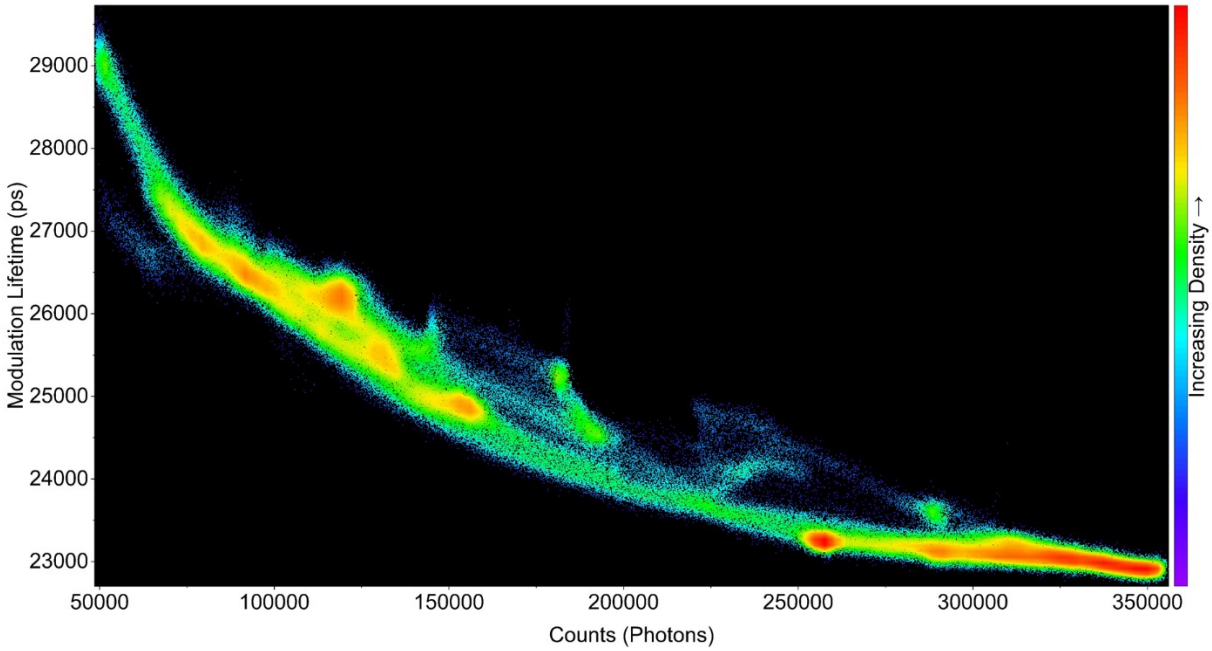



*Figure 117 – The graph above shows the relationship between photon counts and modulation lifetime across the entire image. This is a complex profile that requires additional data to be analysed accurately. Broadly, there is a relationship between photon count and modulation lifetime, where the lifetime variation is due to quenching.*

Thus phasor analysis can provide a direct method for visualising the distribution of quenched emissive defects such as N3. It may be possible to estimate the concentration of A-centres from luminescence lifetime data using phasor analysis. This could be facilitated by quantitative lifetime imaging of reference samples, i.e. diamonds with known A-centre concentrations. A key advantage of luminescence imaging is that it can be applied to faceted diamonds when implemented using optical sectioning, which provides a clear advantage over absorption mapping of A-centres.

## Conclusion and outlook

In this chapter, the luminescence from three natural diamonds has been analysed with hyperspectral imaging, spectrally-resolved lifetime measurements and lifetime imaging. This has revealed the complexity of natural diamond luminescence that originates from multiple defects whose emission overlaps spectrally at room temperature. Lifetime analysis is further complicated by the quenching of emission that makes it difficult to utilise prior knowledge to identify specific lifetime components. Where the lack of prior knowledge and the complexity of the emission decay profiles render iterative fitting of lifetime data non-viable, phasor analysis can provide graphical insights into emission dynamics such as quenching. The work reported here could be extended by using additional excitation sources and by making measurements at cryogenic temperatures to reduce the width of emission spectra. Quantification of lifetime data could be improved by using excitation sources with variable pulse repetition rates to accommodate longer lifetime decays, In the current instrument this facility was only available at 405 nm using the gain-switched diode laser.

Phasor analysis was found to be useful to explore the quenching of N3 defects by A-centres. Ultimately this work could be extended to utilise the quenching of N3 emission lifetime to calculate the concentration of A-centres. Compared to absorption measurements, this approach could provide 3D data through optical sectioning and would be applicable to a wide range of samples including faceted gemstones.

# Chapter 8 – Conclusions and future work

## Introduction

This thesis presents the development of a novel multidimensional luminescence microscope, its characterisation, and its application to diamond luminescence. Hyperspectral imaging, luminescence lifetime imaging, and advanced spectroscopy techniques involving excitation, emission, lifetime, and polarisation resolved measurements were applied to diamond. This enabled the study of $NV^-$ defects, dipole orientations of the $SiV^-$ defect, and complex emission from several diamonds of different origins.

The developed instrument provides multiple measurement modalities that can be considered for any specific experiment. The flow chart in Figure 118 illustrates a strategy to use the developed instrument. Initial characterisation with white-light and crossed polariser transmission measurements can provide useful reference images but does not provide information about defects present in a sample, for which luminescence measurements are necessary. Luminescence studies may begin with spectrally resolved point-measurement at a few key excitation wavelengths, or PLE and/or hyperspectral imaging may be undertaken, e.g. to determine the excitation and emission wavelength or wavelength bands required for subsequent time-consuming luminescence lifetime measurements.

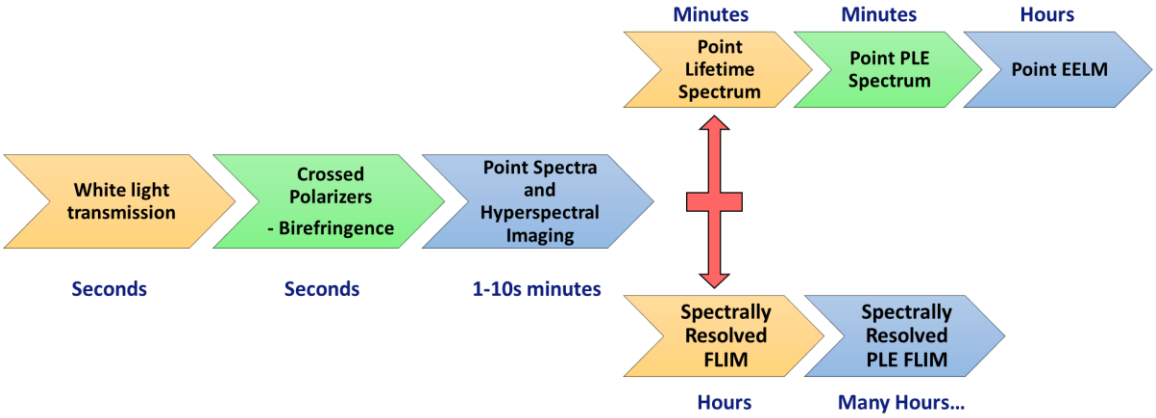



*Figure 118 – A flow chart showing a possible strategy to analyse an unknown sample using the developed multidimensional luminescence microscope. Typical data acquisition times are given, although these are heavily dependent on the acquisition parameters, including dwell time, spectral ranges, and sampling.*

This strategy splits into two branches, dependant on what is required from the sample. In some cases, only the spatial information is of interest, possibly for screening purposes of natural and synthetic diamond. In other cases, the fundamental photo-physics is of interest and full excitation-emission-lifetime matrices (EELM) may be useful. EELM imaging of diamond luminescence can be prohibitively costly in time and so practical measurements may be limited in terms of spatial or spectral resolution.

## Conclusions

In chapter 2, the photo-physics of luminescence were discussed, including an outline of the different luminescence parameters and how they can be used to provide or enhance contrast. The optical microscopy and spectroscopy techniques used in this thesis were also reviewed. Chapter 3 discussed the properties of diamond, including mechanical and thermal properties, as well as the spectroscopy of the microscopic defects studied for this thesis. An overview of the more common luminescent defects was presented, with an overview of their emission and lifetime parameters, and their structural diagrams.

A large component of this thesis covered the development of the multidimensional luminescence microscope, as described in chapter 4. Initially, a pre-existing spectrofluorometer was modified for use with diamond, and luminescence was analysed with respect to lifetime, emission wavelength and polarisation. This provided evidence of the value of spectrally and polarisation resolved lifetime measurements of luminescence for diamond defect analysis. A simple line scanning hyperspectral imaging microscope utilising a grism-based spectrometer was then developed. A single instrument combining hyperspectral imaging and time-resolved spectroscopy was then developed that provided improved spatial and spectral resolution compared to the grism spectrometer-based instrument, and higher light collection efficiency than the spectrofluorometer.

Using a linear variable emission filter and 50/50 beamsplitter in place of a dichroic beamsplitter enabled this instrument to be used with a broad range of excitation and emission wavelengths. Spectrally resolved lifetime was achieved using TCSPC detection with a photomultiplier at the monochromator port on the imaging spectrograph. Excitation-emission-lifetime matrix data could be acquired using the tuneable excitation radiation provided by a custom-built prism-based monochromator and ultrashort pulsed supercontinuum laser source. Rotatable polarisers allowed polarisation-resolved measurements that could be combined with the above modalities. The co-registration of data from these different measurement techniques makes this multidimensional luminescence microscope useful to determine the properties of emitting samples.

Data analysis, in particular analysis of lifetime data, is an important aspect of this thesis, and chapter 4 also explains the two techniques used for analysing the luminescence decay data. The issue of missing decay data from TCSPC measurements was described, and a solution measuring two sequential decay profiles was presented, which allowed phasor analysis to be used. The use of both phasor analysis and iterative fitting of lifetime data to exponential decay models to analyse spectrally resolved lifetime and FLIM data was discussed. Chapter 4 also addresses the presentation of hyperspectral data, for which displaying the median wavelength as an HSB image proved useful.

Chapter 5 reported the application of the instrument to synthetic diamond, where the emitting species are often anticipated because the growth parameters are known. In general, there are common defects expected to be present in CVD and HPHT diamond. A single crystal CVD diamond, with a HPHT substrate, was chosen to evaluate the multidimensional luminescence microscope because of its interesting growth history, and its well-studied two principal defects, NV and SiV. Hyperspectral imaging revealed the variations in CVD growth that had been engineered into the sample, by varying the nitrogen incorporation rate during synthesis. ROI selection on and off striations showed variations in NV and SiV emission. FLIM analysis of the sample revealed strong contrast in the striations, due to those variations in NV concentrations, but also quenched emission from $NV^-$ in the HPHT substrate. Using a combination of iterative fitting, phasor analysis and point-spectrally resolved lifetime measurements, the emission decay information was found to originate from quenched $NV^-$. Excitation-emission-lifetime data taken from the HPHT substrate then revealed, with combined phasor and iterative fitting analysis, that the quenching was excitation wavelength dependant.

In chapter 6, the application of the instrument to study emission from the $SiV^-$ defect in the same synthetic diamond sample was reported. Polarisation-resolved PLE spectroscopy was used to measure the energy level structure of the defect and $2^{nd}$ excited state, with a peak at 546 nm, has a different dipole orientation to that of the lower excited state. In addition, a variation in lifetime of the defect was observed when excited <550 nm.

Chapter 7 reports the application of the instrument to natural diamond, which is more challenging since there is no a priori information about the diamond growth. The measurements were conducted at room temperature, resulting in spectral overlap of the defect emission. Three separate samples were measured: a faceted natural diamond, a plate, and another plate containing N3 and A-centre defects. The faceted diamond was measured using hyperspectral imaging, which revealed only emission from N3 at 355 nm excitation. FLIM then revealed a complex emission profile, and quenched emission from N3. A point-spectrally resolved lifetime measurement indicated three

lifetime components, two of which were assigned to N3. The first of the two diamond plates presented the most complex emission observed from any diamond sample investigated, attributed to quenched emission processes from multiple emitters presenting decays over a wide timescale. Initial mapping of the second diamond plate also revealed variations in N3 lifetime attributed to quenching. These complex luminescence signatures require further study to determine their origins. Their spatial variation in lifetime could potentially provide a means for identification of specific natural diamonds, e.g., to track a particular diamond through the cutting and polishing process.

## Future luminescence studies

The measurements of diamond luminescence presented in this thesis could be extended to further study the underlying photo-physics. There are many optical signatures of diamond luminescence whose origin are currently unknown, and this multidimensional luminescence instrument can aid in their characterisation, using its flexibility. A recently published study reported a series of synthetic diamonds that had been irradiated/implanted with unusual elements, and subsequently measured using several instruments, generated many new optical signatures[22]. These optical signatures have not yet been studied in depth, and the instrument developed here could be applied to search for new defects that could enable new potential applications, in particular for quantum optical applications.

The instrumentation developed can be applied to study quenching mechanisms, as studied here for $NV^-$ and N3 defects, which are interesting for multiple applications. Quenching of $NV^-$ is important for quantum optical applications of this defect, which are dependent on excited-state lifetimes. The variation of quenching with excitation wavelength could be studied with a view to improving the performance of quantum optical devices. The quenching of emission from the N3 defect, as measured with FLIM, could be used for the differentiation of synthetic and natural diamonds, noting that phasor analysis of luminescence decays could provide a graphical method for rapidly determining the degree of quenching. The relationship between the quencher (A-centre) concentration and N3 lifetime could be used to determine the concentration of A-centres without resorting to absorption spectroscopy and its requirement for thin polished samples with parallel faces.

The instrumentation developed could be applied to annealing studies of diamonds, which can be used to determine when specific optical signatures appear or disappear as a function of temperature[134]; this can provide a greater understanding of the elements involved since different defects become mobile at different temperatures.

In addition, the multidimensional luminescence instrument could be applied to many other materials, including emerging “2D semiconductors” such as graphene and hBN, and to biological samples, where the multiple spectroscopic readouts could be used to unmix contributions from multiple components in the emission.

## Future instrument improvements

Whilst the instrument can provide multiple measurement modalities, it has several limitations that could be addressed. When a 50/50 beamsplitter is used to separate excitation and luminescence (instead of a dichroic beamsplitter) to allow for broad band operation, the light collection efficiency at the detector is reduced to 25% before considering further losses, e.g. from the lenses and filters. Broadband operation is important when measuring excitation-emission matrices, as a standard dichroic beamsplitter would not enable the NV and $SiV^-$ defects spectra to be acquired in a single measurement for example. A potential solution to this problem would be to use an ‘achrogate’[204], or similar approach, to separate the excitation and emission light when using line (or point) illumination. This involves placing a small, mirrored line or spot on an otherwise transparent beam deflecting (e.g., 45°) substrate at in the back focal plane of the objective lens – or in a conjugate plane of an image relay. The excitation source is then reflected at the mirrored surface and focussed to a line (or point) at the sample. The resulting incoherent luminescence passes through the transparent substrate, with a small loss at the mirrored surface. An example diagram of such a system is shown in Figure 119. If point illumination is used, the small diameter of the beam at the back aperture of the objective reduces the effective NA, causing the focused spot to be much larger than for a beam fully filling the back aperture.

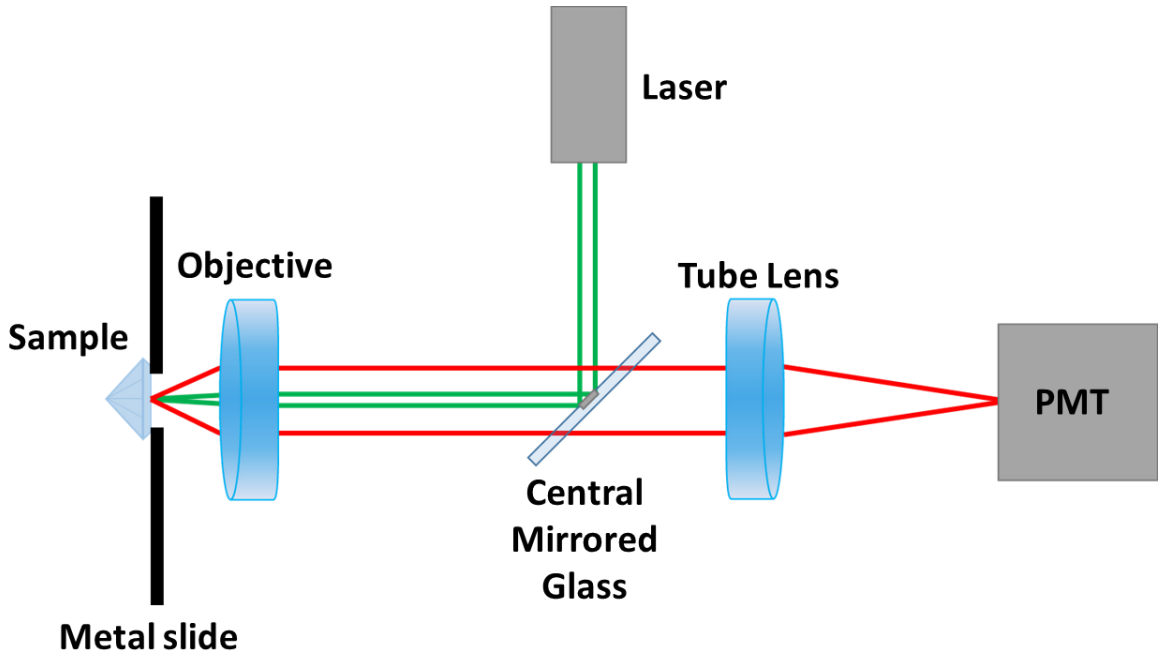



*Figure 119 – An optical diagram showing the excitation and emission paths using a small, mirrored region on a glass substrate. The excitation light is reflected by this mirror onto the sample, whilst the emission passes through the glass into the detector. The mirrored region blocks the emission light creating a mask. This would be wavelength independent, unlike dichroic mirrors. The above design works for point scanning, such as employed for FLIM measurements.*

The large wavelength range of broadband measurements may also be limited by the achromatic performance of the lenses. The current system uses several standard achromatic doublets with a typical operational range of ~300 nm (typically 400-700 nm for the visible part of the spectrum). This could be improved by employing apochromats, or super achromats, which can be corrected over larger wavelength ranges, and provide smaller deviations of focus. They may be prohibitively expensive and provide low transmission due to the increased number of optical elements. A more complete solution could be to use reflective optical components that can be free of significant chromatically dependent aberrations, but efficiency depends on the reflectivity of the mirrored surface. However, the metallic coatings required for broadband operation may present additional losses and using off-axis spherical mirrors for focusing may introduce unacceptable aberrations, particularly over large FOVs. Reflective microscope objective optics suffer from central obscuration, which limits the acceptance of excitation beams to an annular beam profile, and the multiple reflections required further limits performance of these optical elements.

Aberrations are a particular problem for hyperspectral imaging (as implemented in this developed system), due to chromatic aberrations in refractive optical components and further aberrations in

the spectrograph. Czerny-Turner spectrographs use toroidal mirrors, which can provide images mostly free of aberrations but only over a limited FOV. Practically, masks are used to block the aberrated light from the detector, reducing the FOV. This challenge may be addressed using a reflective Schmitt correction plate, which corrects the wavefront for the induced aberration of the toroidal mirrors, as currently employed by the IsoPlane series of spectrographs[205].

Achromatic/Apochromatic based objective lenses are unsuitable for broadband hyperspectral imaging, as only 2, 3 or 4 wavelengths – typically within the visible spectral range and dependant on achromatic, apochromatic or superachromatic design respectively – will be in focus. Reflective objectives inherently provide achromatic operation over the full spectral range of the mirror coating.

Spectroscopy of diamond luminescence is often conducted at low temperatures using L-$N_2$ or even L-He. This is because of the thermal broadening of emission lines at room temperature and the decrease in quantum coherence times. The ability of low temperature measurements to resolve any thermal shelving states/transitions when measuring new defects is also useful to elucidate the energy level structure. Thus, the ability to undertake low temperature luminescence studies would be desirable, but this requires the use of cryostats or cold stages, which can be difficult to integrate with translation stages for imaging. Furthermore, vibrations caused by pumps can reduce the spatial resolution caused by phase changing liquids/gases, large distanced between windows and sample can increase the required working distance and therefore reduce the spatial resolution achievable, and condensation/ice is also a problem because it can reduce collection efficiency.

The supercontinuum excitation source used to provide broad band tuneable excitation for the work reported here offers a low spectral density compared to many CW laser sources and the lack of emission <400 nm limits its applicability to some diamond luminescence, since some defects can only be excited in the ultraviolet. Furthermore, the inability to vary the excitation pulse repetition rate (of the specific supercontinuum source used here) below 40 MHz limits the ability to measure lifetimes much longer than 10 ns – although supercontinuum lasers with variable repetition rates down to a few MHz are available. Tuneable pulsed excitation can be also provided from a Ti:Sapphire laser, but there are gaps in the spectrum, even when using harmonic generation. These limitations can now be addressed, however, using optical parametric oscillator-based ultrafast laser sources. Above bandgap excitation (i.e., below 225 nm) could be provided through multiphoton excitation of blue radiation or by mixing the 2nd (532 nm) and 3rd harmonic (355 nm) outputs of an ultrafast laser at 1064 nm laser in a multicolour multiphoton process. Above bandgap excitation is important to compare directly with standard imaging systems such as DiamondView™ already in use by the gem industry.

Some samples are thick plates which means it is usually only possible to image near the two flat surfaces and therefore only growth features at the surface are apparent. To see internal structure, 3D imaging of diamond is desirable, but this is challenging due to the high refractive index mismatch with air that leads to significant spherical aberration. The use of adaptive optics (AO) to correct this, as previously demonstrated[87], could be incorporated in the luminescence microscope reported here. A fast AO system coupled with a scanning mirror could create a pseudo line illumination for axially resolved hyperspectral imaging.

# Published work and proceedings

**Daniel C. Jones**, Yuriy Alexandrov, Nathan Curry, Sunil Kumar, Peter M. P. Lanigan, Colin D. McGuinness, Matthew W. Dale, Daniel J. Twitchen, David Fisher, Mark A. A. Neil, Christopher Dunsby, Paul M. W. French – "*Multidimensional spectroscopy and imaging of defects in synthetic diamond: excitation-emission-lifetime luminescence measurements with multiexponential fitting and phasor analysis*" *J. Phys. D. Appl. Phys.* **54**, (2021).

Peter M. P. Lanigan, Colin D. McGuinness, Mark Rendle, Peter A. Aked, Christopher G. Bearcroft, **Daniel C. Jones**, Simon C. Lawson - *"Real-time detection of long lived near infrared luminescence from colourless cubic zirconia by time-gated imaging" Minerals* **10**, 1–9 (2020).

**Daniel C. Jones**, Yuriy Alexandrov, Nathan Curry, Sunil Kumar, Peter M. P. Lanigan, Colin D. McGuinness, Matthew W. Dale, Daniel J. Twitchen, David Fisher, Mark A. A. Neil, Christopher Dunsby, Paul M. W. French - *"A Multidimensional Imaging and Spectroscopic Microscope"* **2020**, JF4E.5 (2020).

**Daniel C. Jones**, Sunil Kumar, Peter M. P. Lanigan, Colin D. McGuinness, Matthew W. Dale, Daniel J. Twitchen, David Fisher, Philip M Martineau, Mark A. A. Neil, Christopher Dunsby, Paul M. W. French *"Multidimensional luminescence microscope for imaging defect colour centres in diamond*" *Methods Appl. Fluoresc.* **8**, 014004 (2019).

# References


[1] Lakowicz, J. R. *Principles of Fluorescence Spectroscopy*. **33**, (Springer US, 2006).

[2] Shinde, K. N., Dhoble, S. J., Swart, H. C. & Park, K. Basic Mechanisms of Photoluminescence. in 41–59 (2012). doi:10.1007/978-3-642-34312-4_2

[3] Kasha, M. Characterization of electronic transitions in complex molecules. *Discuss. Faraday Soc.* **9**, 14 (1950).

[4] Collins, A. T. The characterisation of point defects in diamond by luminescence spectroscopy. *Diam. Relat. Mater.* **1**, 457–469 (1992).

[5] Su, Z. *et al.* Luminescence landscapes of nitrogen-vacancy centers in diamond: quasi-localized vibrational resonances and selective coupling. *J. Mater. Chem. C* **7**, 8086–8091 (2019).

[6] Swinehart, D. F. The Beer-Lambert Law. *J. Chem. Educ.* **39**, 333 (1962).

[7] White, A. M., Williams, E. W., Porteous, P. & Hilsum, C. Applications of photoluminescence excitation spectroscopy to the study of indium gallium phosphide alloys. *J. Phys. D. Appl. Phys.* **3**, 312 (1970).

[8] Koller, E., Quehenberger, O., Jürgens, G., Wolfbeis, O. S. & Esterbauer, H. Investigation of human plasma low density lipoprotein by three-dimensional flourescence spectroscopy. *FEBS Lett.* **198**, 229–234 (1986).

[9] Wang, W., Wu, Z., Zhao, J., Lui, H. & Zeng, H. A rapid excitation-emission matrix fluorometer utilizing supercontinuum white light and acousto-optic tunable filters. *Rev. Sci. Instrum.* **87**, (2016).

[10] *Fluorescence Lifetime Spectroscopy and Imaging*. (CRC Press, 2014). doi:10.1201/b17018

[11] Warren, S. C. Development and application of multiplexed fluorescence imaging to chemotaxis signalling pathways - Thesis. (2014). doi:10.25560/25117

[12] Berezin, M. Y. & Achilefu, S. Fluorescence Lifetime Measurements and Biological Imaging. *Chem. Rev.* **110**, 2641–2684 (2010).

[13] Inoue, S., Shimomura, O., Goda, M., Shribak, M. & Tran, P. T. Fluorescence polarization of green fluorescence protein. *Proc. Natl. Acad. Sci.* **99**, 4272–4277 (2002).

[14] Saani, M. H., Vesaghi, M. A. & Esfarjani, K. Oscillator strength calculations in color centers of diamond and the role of spin. *Eur. Phys. J. B* **39**, 441–446 (2004).

[15] Green, B. L. *et al.* Electronic structure of the neutral silicon-vacancy center in diamond. 1–6 (2018). doi:10.1103/PhysRevB.99.161112

[16] Manning, H. B. Development of multi-dimensional fluorescence metrology and application to cartilage degradation in arthritis. (Thesis) *Chemical Biology* (2010).

[17] *Dye Lasers*. **1**, (Springer Berlin Heidelberg, 1973).

[18] Lichtenstein, N., Geiger, B. & Kam, Z. Quantitative Analysis of Cytoskeletal Organization by Digital Fluorescent Microscopy. *Cytom. Part A* **54**, 8–18 (2003).

[19] Zaitsev, A. M. *Optical Properties of Diamond*. **14**, (Springer Berlin Heidelberg, 2001).

[20] Ghauharali & Brakenhoff. Fluorescence photobleaching-based image standardization for fluorescence microscopy. *J. Microsc.* **198**, 88–100 (2000).

[21] Khan, R. U. A., Martineau, P. M., Cann, B. L., Newton, M. E. & Twitchen, D. J. Charge transfer effects, thermoand photochromism in single crystal CVD synthetic diamond. *J. Phys. Condens. Matter* **21**, (2009).

[22] Lühmann, T. *et al.* Screening and engineering of colour centres in diamond. *J. Phys. D. Appl. Phys.* **51**, (2018).

[23] Inoué, S. Foundations of Confocal Scanned Imaging in Light Microscopy. in *Handbook Of Biological Confocal Microscopy* 1–19 (Springer US, 2006). doi:10.1007/978-0-387-45524-2_1

[24] Boardman, J. W. Inversion of high spectral resolution data. *Imaging Spectrosc. Terr. Environ.* **1298**, 222–233 (1990).

[25] Pour, A. B. & Hashim, M. Hydrothermal alteration mapping from Landsat-8 data, Sar Cheshmeh copper mining district, south-eastern Islamic Republic of Iran. *J. Taibah Univ. Sci.* **9**, 155–166 (2015).

[26] Dong, X. *et al.* Line-Scan Hyperspectral Imaging Microscopy with Linear Unmixing for Automated Two-Dimensional Crystals Identification. *ACS Photonics* **7**, 1216–1225 (2020).

[27] Wang, X., Zhang, Y., Ma, X., Xu, T. & Arce, G. R. Compressive spectral imaging system based on liquid crystal tunable filter. *Opt. Express* **26**, 25226 (2018).

[28] Inoue, Y., Penuelas, J. & Penuelas, J. An AOTF-based hyperspectral imaging system for field use in ecophysiological and agricultural applications. *Int. J. Remote Sens.* **22**, 3883–3888 (2001).

[29] Gat, N. Imaging spectroscopy using tunable filters: a review. *Wavelet Appl. VII* **4056**, 50–64 (2000).

[30] Halicek, M., Fabelo, H., Ortega, S., Callico, G. M. & Fei, B. In-vivo and ex-vivo tissue analysis through hyperspectral imaging techniques: Revealing the invisible features of cancer. *Cancers (Basel).* **11**, 1–30 (2019).

[31] Uto, K., Seki, H., Saito, G., Kosugi, Y. & Komatsu, T. Measurement of a coastal area by a hyperspectral imager using an optical fiber bundle, a swing mirror and compact spectrometers. *Work. Hyperspectral Image Signal Process. Evol. Remote Sens.* **0**, 3909–3925 (2016).

[32] Chaudhary, S., Ninsawat, S. & Nakamura, T. Non-destructive trace detection of explosives using pushbroom scanning hyperspectral imaging system. *Sensors (Switzerland)* **19**, 1–15 (2019).

[33] Yokoya, N., Miyamura, N. & Iwasaki, A. Preprocessing of hyperspectral imagery with consideration of smile and keystone properties. *Multispectral, Hyperspectral, Ultraspectral Remote Sens. Technol. Tech. Appl. III* **7857**, 78570B (2010).

[34] Richter, R., Schlapfer, D. & Muller, A. Operational atmospheric correction for imaging spectrometers accounting for the smile effect. *IEEE Trans. Geosci. Remote Sens.* **49**, 1772–1780 (2011).

[35] Ceamanos, X*., et al*. Spectral smile correction in crism hyperspectral images *Channels* 9–12 (2010).

[36] Wilson, N. C., MacRae, C. M., Torpy, A., Davidson, C. J. & Vicenzi, E. P. Hyperspectral cathodoluminescence examination of defects in a carbonado diamond. *Microsc. Microanal.* **18**, 1303–1312 (2012).

[37] Cross, R. E. Optical Spectroscopy Instrumentation for the Characterisation of Wide Band Gap Materials (Thesis). (2015).

[38] Bugiel, I., Konig, K. & Wabnitz, H. Investigation of cells by fluorescence laser scanning microscopy with subnanosecond time resolution. *Lasers in the Life Sciences* **3**, 47–53 (1989).

[39] Dowling, K., Hyde, S. C. W., Dainty, J. C., French, P. M. W. & Hares, J. D. 2-D fluorescence lifetime imaging using a time-gated image intensifier. *Opt. Commun.* **135**, 27–31 (1997).

[40] Sparks, H. *et al.* Characterisation of new gated optical image intensifiers for fluorescence lifetime imaging. *Rev. Sci. Instrum.* **88**, (2017).

[41] Ryderfors, L., Mukhtar, E. & Johansson, L. B. A. Two-photon excited fluorescence depolarisation experiments: II. the proper response function for analysing TCSPC data. *Chem. Phys. Lett.* **411**, 51–60 (2005).

[42] Esposito, A., Oggier, T., Gerritsen, H. C., Lustenberger, F. & Wouters, F. S. All-solid-state lock-in imaging for wide-field fluorescence lifetime sensing. *Opt. Express* **13**, 9812 (2005).

[43] Characterisation of new gated optical image intensifiers for fluorescence lifetime Imaging, H. Sparks, F. Görlitz, D. J. Kelly, S. C. Warren, P. A. Kellett, E. Garcia, A. K. L. Dymoke-Bradshaw, J. D. Hares, M. A. A. Neil, C. Dunsby, and P. M. W. French. *Rev Sci Inst.* **88**, 013707 (2017);

[44] Becker, W. The Becker and Hickl TCSPC Handbook. *Scanning* 1–566 (2010).

[45] Arlt, J. *et al.* A study of pile-up in integrated time-correlated single photon counting systems. *Rev. Sci. Instrum.* **84**, (2013).

[46] Peronio, P., Acconcia, G., Rech, I. & Ghioni, M. Improving the counting efficiency in time-correlated single photon counting experiments by dead-time optimization. *Rev. Sci. Instrum.* **86**, 1–8 (2015).

[47] Talbot, C. B. *et al.* Application of ultrafast gold luminescence to measuring the instrument response function for multispectral multiphoton fluorescence lifetime imaging. *Opt. Express* **19**, 13848 (2011).

[48] Praktikum, P. & Quenching, F. Fluorescence Quenching Studies. *Phys. Prakt.* 1–14 (2016).

[49] Glasgow, B. J. Fluorescence lifetime imaging microscopy reveals quenching of fluorescein within corneal epithelium. *Exp. Eye Res.* **147**, 12–19 (2016).

[50] Melnikau, D., Elcoroaristizabal, S. & Ryder, A. G. An excitation emission fluorescence lifetime spectrometer using a frequency doubled supercontinuum laser source. *Methods Appl. Fluoresc.* **6**, (2018).

[51] Owen, D. M. *et al.* Excitation-resolved hyperspectral fluorescence lifetime imaging using a UV-extended supercontinuum source. *Opt. Lett.* **32**, 3408 (2007).

[52] Alfano, R. R. *The Supercontinuum Laser Source*. (Springer New York, 2016). doi:10.1007/978-1-4939-3326-6

[53] Janesick, J. R., Elliott, T., Andrews, J., Tower, J. & Pinter, J. Fundamental performance differences of CMOS and CCD imagers: part V. in (eds. Widenhorn, R. & Dupret, A.) 865902 (2013). doi:10.1117/12.2008268

[54] Chambers, S. & Cameras, A. White paper on the merits of CCD and CMOS technology in Gel Documentation Applications. 1–4

[55] Cova, S., Ghioni, M., Lacaita, A., Samori, C. & Zappa, F. Avalanche photodiodes and quenching circuits for single-photon detection. *Appl. Opt.* **35**, 1956 (1996).

[56] The Properties of Natural and Synthetic Diamond. Academic Press, London 1992. *Cryst. Res. Technol.* **28**, 602–602 (1993).

[57] The structure of the diamond. *Proc. R. Soc. London. Ser. A, Contain. Pap. a Math. Phys. Character* **89**, 277–291 (1913).

[58] The structure of graphite. *Proc. R. Soc. London. Ser. A, Contain. Pap. a Math. Phys. Character* **106**, 749–773 (1924).

[59] *Springer Handbook of Electronic and Photonic Materials*. (Springer International Publishing, 2017). doi:10.1007/978-3-319-48933-9

[60] Gracio, J. J., Fan, Q. H. & Madaleno, J. C. Diamond growth by chemical vapour deposition. *J. Phys. D. Appl. Phys.* **43**, (2010).

[61] Reina, G., Zhao, L., Bianco, A. & Komatsu, N. Chemical Functionalization of Nanodiamonds: Opportunities and Challenges Ahead. *Angew. Chemie Int. Ed.* **58**, 17918–17929 (2019).

[62] Chauhan, S., Jain, N. & Nagaich, U. Nanodiamonds with powerful ability for drug delivery and biomedical applications: Recent updates on in vivo study and patents. *J. Pharm. Anal.* **10**, 1–12 (2020).

[63] Ye, Y., Li, J., Zhou, H. & Chen, J. Microstructure and mechanical properties of High- Hardness Nano-Polycrystalline Diamonds. **34**, 1797–1803 (2008).

[64] Cleri, F., Keblinski, P., Colombo, L., Wolf, D. & Phillpot, S. R. On the electrical activity of sp 2 -bonded grain boundaries in nanocrystalline diamond. *Europhys. Lett.* **46**, 671–677 (1999).

[65] May, P. W., Ashfold, M. N. R. & Mankelevich, Y. A. Microcrystalline, nanocrystalline, and ultrananocrystalline diamond chemical vapor deposition: Experiment and modeling of the factors controlling growth rate, nucleation, and crystal size. *J. Appl. Phys.* **101**, 053115 (2007).

[66] Williams, O. A. Nanocrystalline diamond. *Diam. Relat. Mater.* **20**, 621–640 (2011).

[67] Frank, F. C. *et al.* Orientation-dependent nitrogen incorporation on vicinals on synthetic diamond cube growth surfaces. *J. Cryst. Growth* **100**, 354–376 (1990).

[68] Haggerty, S. E. Carbonado Diamond: A Review of Properties and Origin. *Gems Gemol.* (2017). doi:10.5741/GEMS.53.2.168

[69] Williams, O. A. & Nesládek, M. Growth and properties of nanocrystalline diamond films. *Phys. status solidi* **203**, 3375–3386 (2006).

[70] Barreto, L. P. P. *et al.* Preparation and characterization of sintered polycrystalline diamond (PCD) with 15 wt% Nb binder. *Diam. Relat. Mater.* **106**, 107867 (2020).

[71] Dahl, J. E. Isolation and Structure of Higher Diamondoids, Nanometer-Sized Diamond Molecules. *Science (80-.).* **299**, 96–99 (2003).

[72] Laube, C. *et al.* Controlling the fluorescence properties of nitrogen vacancy centers in nanodiamonds. *Nanoscale* **11**, 1770–1783 (2019).

[73] Alkahtani, M. H. *et al.* Fluorescent nanodiamonds: past, present, and future. *Nanophotonics* **7**, 1423–1453 (2018).

[74] Uddin, M. S., Seah, K. H. W., Li, X. P., Rahman, M. & Liy, K. Effect of crystallographic orientation on wear of diamond tools for nano-scale ductile cutting of silicon. *Wear* **257**, 751–759 (2004).

[75] Frost, M. J. Mohs scale of hardness. in *Mineralogy* 283–284 (Kluwer Academic Publishers). doi:10.1007/0-387-30720-6_84

[76] Balmer, R. S. *et al.* Chemical vapour deposition synthetic diamond: materials, technology and applications. *J. Phys. Condens. Matter* **21**, 364221 (2009).

[77] Ramaseshan, S. The cleavage properties of diamond. *Proc. Indian Acad. Sci. - Sect. A* **24**, 114–121 (1946).

[78] Miess, D. & Rai, G. Fracture toughness and thermal resistance of polycrystalline diamond compacts. *Mater. Sci. Eng. A* **209**, 270–276 (1996).

[79] Anthony, T. R. *et al.* Thermal diffusivity of isotopically enriched C12 diamond. *Phys. Rev. B* **42**, 1104–1111 (1990).

[80] Coe, S. . & Sussmann, R. . Optical, thermal and mechanical properties of CVD diamond. *Diam. Relat. Mater.* **9**, 1726–1729 (2000).

[81] Morelli, D. T., Hartnett, T. M. & Robinson, C. J. Phonon-defect scattering in high thermal conductivity diamond films. *Appl. Phys. Lett.* **59**, 2112–2114 (1991).

[82] Rabeau, R. P. M. and J. R. *Optical Engineering of Diamond, Wiley, first ed.,*. (2013).

[83] Thomas, M. E. et al. Optical Properties of Diamond. *SPIE 2286, Wind. Dome Technol. Mater. IV* **2286**, (1994).

[84] Gilbertson, A. *et al.* Cutting Diffraction Gratings to Improve Dispersion ('Fire') in Diamonds. *Gems Gemol.* **45**, 260–270 (2009).

[85] Dispersion in diamond. in *Dictionary of Gems and Gemology* 270–270 (Springer Berlin Heidelberg). doi:10.1007/978-3-540-72816-0_6647

[86] Turri, G. *et al.* Index of refraction from the near-ultraviolet to the near-infrared from a single crystal microwave-assisted CVD diamond. *Opt. Mater. Express* **7**, 855 (2017).

[87] Salter, P. S. & Booth, M. J. Adaptive optics in laser processing. *Light Sci. Appl.* **8**, 1–16 (2019).

[88] Lenz, M. O. *et al.* 3-D stimulated emission depletion microscopy with programmable aberration correction. *J. Biophotonics* **7**, 29–36 (2014).

[89] LANG, A. R. Causes of Birefringence in Diamond. *Nature* **213**, 248–251 (1967).

[90] Breeding, C. & Shigley, J. The 'type' classification system of diamonds and its importance in gemology. *Gems Gemol.* **45**, 96–111 (2009).

[91] Mildren, R. P. & Sabella, A. Highly efficient diamond Raman laser. *Opt. Lett.* **34**, 2811 (2009).

[92] Pu, M., Zhang, F., Liu, S., Irifune, T. & Lei, L. Tensile-strain induced phonon splitting in diamond. *Chinese Phys. B* **28**, (2019).

[93] Jasbeer, H. *et al.* Birefringence and piezo-Raman analysis of single crystal CVD diamond and effects on Raman laser performance. *J. Opt. Soc. Am. B* **33**, B56 (2016).

[94] Lapp, M. & Penney, C. M. 3.2. Analysis of Raman and Rayleigh Scattered Radiation. in 408–433 (1981). doi:10.1016/S0076-695X(08)60873-X

[95] Koizumi, S. Ultraviolet Emission from a Diamond pn Junction. *Science (80-. ).* **292**, 1899–1901 (2001).

[96] Pinault, M.-A., Barjon, J., Kociniewski, T., Jomard, F. & Chevallier, J. The n-type doping of diamond: Present status and pending questions. *Phys. B Condens. Matter* **401–402**, 51–56 (2007).

[97] Palyanov, Y. N., Kupriyanov, I. N., Khokhryakov, A. F. & Ralchenko, V. G. Crystal Growth of Diamond. in *Handbook of Crystal Growth* 671–713 (Elsevier, 2015). doi:10.1016/B978-0-444-63303-3.00017-1

[98] Bundy, F. P. *et al.* The pressure-temperature phase and transformation diagram for carbon; updated through 1994. *Carbon N. Y.* **34**, 141–153 (1996).

[99] Palyanov, Y. N. The many facets of diamond crystals. *Crystals* **8**, 1–9 (2018).

[100] Welbourn, C. M., Cooper, M. & Spear, P. M. De Beers Natural versus Synthetic Diamond Verification Instruments. *Gems Gemol.* **32**, 156–169 (1996).

[101] SUTTON, J. R. The Relationship between Diamonds and Garnets. *Nature* **75**, 488–488 (1907).

[102] Bundy, F. P., Bovenkerk, H. P., Strong, H. M. & Wentorf, R. H. Diamond-Graphite Equilibrium Line from Growth and Graphitization of Diamond. *J. Chem. Phys.* **35**, 383–391 (1961).

[103] Hall, H. T. Ultra-High-Pressure, High-Temperature Apparatus: the 'Belt'''. *Rev. Sci. Instrum.* **31**, 125–131 (1960).

[104] Shea, J. J. *Properties, Growth and Applications of Diamond*. *IEEE Electrical Insulation Magazine* **18**, (2002).

[105] Palyanov, Y. N., Kupriyanov, I. N., Khokhryakov, A. F. & Borzdov, Y. M. High-pressure crystallization and properties of diamond from magnesium-based catalysts. *CrystEngComm* **19**, 4459–4475 (2017).

[106] Liu, X., Jia, X., Fang, C. & Ma, H. A. Diamond crystallization and growth in N-H enriched environment under HPHT conditions. *CrystEngComm* **18**, 8506–8515 (2016).

[107] Strong, H. M. & Chrenko, R. M. Further studies on diamond growth rates and physical properties of laboratory-made diamond. *J. Phys. Chem.* **75**, 1838–1843 (1971).

[108] Matsumoto, S., Sato, Y., Tsutsumi, M. & Setaka, N. Growth of diamond particles from methane-hydrogen gas. *J. Mater. Sci.* **17**, 3106–3112 (1982).

[109] Piekarczyk, W. & Prawer, S. Role of atomic hydrogen in preventing surface reconstruction and sp2 bond formation during chemical vapour deposition of diamond. *Diam. Relat. Mater.* **2**, 41–47 (1993).

[110] Yiming, Z., Larsson, F. & Larsson, K. Effect of CVD diamond growth by doping with nitrogen. *Theor. Chem. Acc.* **133**, 1–12 (2014).

[111]Schreck, M., Gsell, S., Brescia, R. & Fischer, M. Ion bombardment induced buried lateral growth: the key mechanism for the synthesis of single crystal diamond wafers. *Sci. Rep.* **7**, 44462 (2017).

[112] Lee, S.-T., Lin, Z. & Jiang, X. CVD diamond films: nucleation and growth. *Mater. Sci. Eng. R Reports* **25**, 123–154 (1999).

[113] Gallheber, B.-C., Fischer, M., Mayr, M., Straub, J. & Schreck, M. Growth, stress, and defects of heteroepitaxial diamond on Ir/YSZ/Si(111). *J. Appl. Phys.* **123**, 225302 (2018).

[114] Afandi, A., Howkins, A., Boyd, I. W. & Jackman, R. B. Nanodiamonds for device applications: An investigation of the properties of boron-doped detonation nanodiamonds. *Sci. Rep.* **8**, 17–19 (2018).

[115] Williams, O. A. *et al.* Size-dependent reactivity of diamond nanoparticles. *ACS Nano* **4**, 4824–4830 (2010).

[116] Zhou, L. Q. *et al.* Imaging Damage in Steel Using a Diamond Magnetometer. *Phys. Rev. Appl.* **15**, 1–10 (2021).

[117] Kaiser, W. & Bond, W. L. Nitrogen, a major impurity in common type I diamond. *Phys. Rev.* **115**, 857–863 (1959).

[118] Ashfold, M. N. R. *et al.* Nitrogen in Diamond. *Chem. Rev.* (2020). doi:10.1021/acs.chemrev.9b00518

[119] Burns, R. C. *et al.* HPHT growth and x-ray characterization of high-quality type IIa diamond. *J. Phys. Condens. Matter* **21**, (2009).

[120] Woods, G. S., Van Wyk, J. A. & Collins, A. T. The nitrogen content of type lb synthetic diamond. *Philos. Mag. B Phys. Condens. Matter; Stat. Mech. Electron. Opt. Magn. Prop.* **62**, 589–595 (1990).

[121] Moore, S. L. & Vohra, Y. K. Nitrogen and silicon defect incorporation during homoepitaxial CVD diamond growth on (111) surfaces. *Mater. Res. Soc. Symp. Proc.* **1734**, 26–31 (2015).

[122] Tallaire, A. *et al.* Characterisation of high-quality thick single-crystal diamond grown by CVD with a low nitrogen addition. *Diam. Relat. Mater.* **15**, 1700–1707 (2006).

[123] Two types of diamond. *Philos. Trans. R. Soc. London. Ser. A, Contain. Pap. a Math. or Phys. Character* **232**, 463–535 (1933).

[124] Lawson, S. C., Fisher, D., Hunt, D. C. & Newton, M. E. On the existence of positively charged single-substitutional nitrogen in diamond. *J. Phys. Condens. Matter* **10**, 6171–6180 (1998).

[125] Smith, W. V., Sorokin, P. P., Gelles, I. L. & Lasher, G. J. Electron-spin resonance of nitrogen donors in diamond. *Phys. Rev.* **115**, 1546–1552 (1959).

[126] Davies, G. The A nitrogen aggregate in diamond-its symmetry and possible structure. *J. Phys. C Solid State Phys.* **9**, L537–L542 (1976).

[127] Crossfield, M. D., Davies, G., Collins, A. T. & Lightowlers, E. C. The role of defect interactions in reducing the decay time of H3 luminescence in diamond. *J. Phys. C Solid State Phys.* **7**, 1909–1917 (1974).

[128] Thomaz, M. F. & Davies, G. The decay time of N3 luminescence in natural diamond. *Proc. R. Soc. London. A. Math. Phys. Sci.* **362**, 405–419 (1978).

[129] Liaugaudas, G., Collins, A. T., Suhling, K., Davies, G. & Heintzmann, R. Luminescence-lifetime mapping in diamond. *J. Phys. Condens. Matter* **21**, 364210 (2009).

[130] Doherty, M. W. *et al.* The nitrogen-vacancy colour centre in diamond. *Phys. Rep.* **528**, 1–45 (2013).

[131] Davies, G. Dynamic Jahn-Teller distortions at trigonal optical centres in diamond. *J. Phys. C Solid State Phys.* **12**, 2551–2566 (1979).

[132] Meara, C. J., Rayson, M. J., Briddon, P. R. & Goss, J. P. Density functional theory study on magnetically detecting positively charged nitrogen-vacancy center in diamond. *Phys. Rev. B* **100**, 1–8 (2019).

[133] Zhao, H.-Q., Fujiwara, M. & Takeuchi, S. Suppression of fluorescence phonon sideband from nitrogen vacancy centers in diamond nanocrystals by substrate effect. *Opt. Express* **20**, 15628 (2012).

[134] Liaugaudas, G., Davies, G., Suhling, K., Khan, R. U. A., & Evans, D. J. F. (2012). Luminescence lifetimes of neutral nitrogen-vacancy centres in synthetic diamond containing nitrogen. *Journal of Physics Condensed Matter*, *24*(43). https://doi.org/10.1088/0953-8984/24/43/435503

[135] Robledo, L., Bernien, H., Sar, T. Van Der & Hanson, R. Spin dynamics in the optical cycle of single nitrogen-vacancy centres in diamond. *New J. Phys.* **13**, (2011).

[136] Riedel, D. *et al.* Deterministic enhancement of coherent photon generation from a nitrogen-vacancy center in ultrapure diamond. *Phys. Rev. X* **7**, 1–8 (2017).

[137] Deák, P., Aradi, B., Kaviani, M., Frauenheim, T. & Gali, A. Calculation ofthe transitions and migration of nitrogen and vacancy related defects,with implications on the formation of NV centers in bulk diamond. 20 (2013).

[138] Chen, Y. C. *et al.* Laser writing of coherent colour centres in diamond. *Nat. Photonics* **11**, 77–80 (2017).

[139] Chen, Y.-C. *et al.* Laser writing of individual nitrogen-vacancy defects in diamond with near-unity yield. *Optica* **6**, 662 (2019).

[140] Aslam, N., Waldherr, G., Neumann, P., Jelezko, F. & Wrachtrup, J. Photo-induced ionization dynamics of the nitrogen vacancy defect in diamond investigated by single-shot charge state detection. *New J. Phys.* **15**, (2013).

[141] Maze, J. R. *et al.* Nanoscale magnetic sensing with an individual electronic spin in diamond. *Nature* **455**, 644–647 (2008).

[142] Rondin, L. *et al.* Magnetometry with nitrogen-vacancy defects in diamond. *Reports Prog. Phys.* **77**, (2014).

[143] Pfender, M. *et al.* Single-spin stochastic optical reconstruction microscopy. *Proc. Natl. Acad. Sci. U. S. A.* **111**, 14669–14674 (2014).

[144] Jaskula, J.-C. *et al.* Superresolution optical magnetic imaging and spectroscopy using individual electronic spins in diamond. *Opt. Express* **25**, 11048 (2017).

[145] Eaton-Magaña, S. Comparison of luminescence lifetimes from natural and laboratory irradiated diamonds. *Diam. Relat. Mater.* **58**, 94–102 (2015).

[146] Van Wyk, J. A. Carbon-12 hyperfine interaction of the unique carbon of the P2 (ESR) or N3 (optical) centre in diamond. *J. Phys. C Solid State Phys.* **15**, (1982).

[147] Bradac, C., Gao, W., Forneris, J., Trusheim, M. E. & Aharonovich, I. Quantum nanophotonics with group IV defects in diamond. *Nat. Commun.* **10**, 1–13 (2019).

[148] Görlitz, J. *et al.* Spectroscopic investigations of negatively charged tin-vacancy centres in diamond. *New J. Phys.* **22**, (2020).

[149] D'Haenens-Johansson, U. F. S. *et al.* Optical properties of the neutral silicon split-vacancy center in diamond. *Phys. Rev. B* **84**, 245208 (2011).

[150] Breeze, B. G. *et al.* Doubly charged silicon vacancy center, Si-N complexes, and photochromism in N and Si codoped diamond. *Phys. Rev. B* **101**, 1–10 (2020).

[151] Green, B. L. *et al.* Neutral Silicon-Vacancy Center in Diamond: Spin Polarization and Lifetimes. *Phys. Rev. Lett.* **119**, 2–6 (2017).

[152] Rogers, L. J. *et al.* Multiple intrinsically identical single-photon emitters in the solid state. *Nat. Commun.* **5**, 4739 (2014).

[153] Rose, B. C. *et al.* Observation of an environmentally insensitive solid-state spin defect in diamond. *Science (80-. ).* **361**, 60–63 (2018).

[154] Rogers, L. J. *et al.* Electronic structure of the negatively charged silicon-vacancy center in diamond. *Phys. Rev. B - Condens. Matter Mater. Phys.* **89**, 1–8 (2014).

[155] Ekimov, E. A. *et al.* Photoluminescence excitation study of split-vacancy centers in diamond. *Phys. Rev. B* **97**, (2018).

[156] Häußler, S. *et al.* Photoluminescence excitation spectroscopy of SiV- and GeV- color center in diamond. *New J. Phys.* **19**, 063036 (2017).

[157] Dhomkar, S., Zangara, P. R., Henshaw, J. & Meriles, C. A. On-Demand Generation of Neutral and Negatively Charged Silicon-Vacancy Centers in Diamond. *Phys. Rev. Lett.* **120**, 117401 (2018).

[158] Thiering, G. & Gali, A. Ab Initio Magneto-Optical Spectrum of Group-IV Vacancy Color Centers in Diamond. *Phys. Rev. X* **8**, 1–17 (2018).

[159] Srikanth, V. V. S. S., Sampath Kumar, P. & Kumar, V. B. A Brief Review on the In Situ Synthesis of Boron-Doped Diamond Thin Films . *Int. J. Electrochem.* **2012**, 1–7 (2012).

[160] Kato, H., Futako, W., Yamasaki, S. & Okushi, H. Growth of phosphorus-doped diamond using tertiarybutylphosphine and trimethylphosphine as dopant gases. *Diam. Relat. Mater.* **14**, 340–343 (2005).

[161] Gajewski, W. *et al.* Electronic and optical properties of boron-doped nanocrystalline diamond films. *Phys. Rev. B - Condens. Matter Mater. Phys.* **79**, 1–14 (2009).

[162] Ekimov, E. A. *et al.* Superconductivity in diamond. *Nature* **428**, 542–545 (2004).

[163] Mandal, S. *et al.* The diamond superconducting quantum interference device. *ACS Nano* **5**, 7144–7148 (2011).

[164] Watanabe, M. *et al.* Stacked SNS Josephson junction of all boron doped diamond. *Phys. C Supercond. its Appl.* **470**, S613–S615 (2010).

[165] Goss, J. P., Briddon, P. R., Hill, V., Jones, R. & Rayson, M. J. Identification of the structure of the 3107 cm −1 H-related defect in diamond. *J. Phys. Condens. Matter* **26**, 145801 (2014).

[166] Manning, H. B. *et al.* A compact, multidimensional spectrofluorometer exploiting supercontinuum generation. *J. Biophotonics* **1**, 494–505 (2008).

[167] Barjon, J. *et al.* Silicon incorporation in CVD diamond layers. *Phys. Status Solidi Appl. Mater. Sci.* **202**, 2177–2181 (2005).

[168] Lai, N. D., Zheng, D., Treussart, F. & Roch, J. F. Optical determination and magnetic manipulation of a single nitrogen-vacancy color center in diamond nanocrystal. *Adv. Nat. Sci. Nanosci. Nanotechnol.* **1**, (2010).

[169] Dunsby, C. *et al.* An electronically tunable ultrafast laser source applied to fluorescence imaging and fluorescence lifetime imaging microscopy. *J. Phys. D. Appl. Phys.* **37**, 3296–3303 (2004).

[170] Owen, D. M. *et al.* Excitation-resolved hyperspectral fluorescence lifetime imaging using a UV-extended supercontinuum source. *Opt. Lett.* **32**, 3408 (2007).

[171] https://www.deltaopticalthinfilm.com/ (04-09-2020)

[172] Jullien, A., Scarangella, A., Bortolozzo, U., Residori, S. & Mitov, M. Nanoscale hyperspectral imaging of tilted cholesteric liquid crystal structures. *Soft Matter* **15**, 3256–3263 (2019).

[173] Jeon, D. S. *et al.* Compact snapshot hyperspectral imaging with diffracted rotation. *ACM Trans. Graph.* **38**, (2019).

[174] Warren, S. C. *et al.* Rapid Global Fitting of Large Fluorescence Lifetime Imaging Microscopy Datasets. *PLoS One* **8**, e70687 (2013).

[175] Clayton, A. H. A., Hanley, Q. S. & Verveer, P. J. Graphical representation and multicomponent analysis of single-frequency fluorescence lifetime imaging microscopy data. *J. Microsc.* **213**, 1–5 (2004).

[176] Redford, G. I. & Clegg, R. M. Polar plot representation for frequency-domain analysis of fluorescence lifetimes. *J. Fluoresc.* **15**, 805–815 (2005).

[177] Digman, M. A., Caiolfa, V. R., Zamai, M. & Gratton, E. The phasor approach to fluorescence lifetime imaging analysis. *Biophys. J.* **94**, L14–L16 (2008).

[178] Ranjit, S., Malacrida, L., Jameson, D. M. & Gratton, E. Fit-free analysis of fluorescence lifetime imaging data using the phasor approach. *Nat. Protoc.* **13**, 1979–2004 (2018).

[179] Weber, G. Resolution of the fluorescence lifetimes in a heterogeneous system by phase and modulation measurements. *J. Phys. Chem.* **85**, 949–953 (1981).

[180] Jameson, D. M., Gratton, E. & Hall, R. D. The Measurement and Analysis of Heterogeneous Emissions by Multifrequency Phase and Modulation Fluorometry. *Appl. Spectrosc. Rev.* **20**, 55–106 (1984).

[181] Laine, R. Fluorescence lifetime rspectroscopy and imaging of FRET probes for the study of cell signalling. ATh1N.4 (Thesis) (2013). doi:https://doi.org/10.25560/14272

[182] Hanley, Q. S. Spectrally resolved fluorescent lifetime imaging. *J. R. Soc. Interface* **6**, (2009).

[183] Colyer, R. *et al.* Phasor-based single-molecule fluorescence lifetime imaging using a wide-field photon-counting detector. *Single Mol. Spectrosc. Imaging II* **7185**, 71850T (2009).

[184] Redford, G. I. & Clegg, R. M. Polar plot representation for frequency-domain analysis of fluorescence lifetimes. *J. Fluoresc.* **15**, 805–815 (2005).

[185] Martelo, L., Fedorov, A. & Berberan-Santos, M. N. Fluorescence Phasor Plots Using Time Domain Data: Effect of the Instrument Response Function. *J. Phys. Chem. B* **119**, 10267–10274 (2015).

[186] Sun, Y. & Liao, S. The Ultimate Phasor Plot and beyond. *ISS Application Note* 1–9 (2014). Available at: http://www.iss.com/resources/pdf/appnotes/Phasor_Plot_And_Beyond.pdf%0Ahttps://www.semanticscholar.org/paper/The-Ultimate-Phasor-Plot-and-beyond-Sun-Liao/d55f5f7aac155fbccaa4bbbd1cab89c0816ab011 (04/09/2020).

[187] Clayton, A. H. A. The polarized AB plot for the frequency-domain analysis and representation of fluorophore rotation and resonance energy homotransfer. *J. Microsc.* **232**, 306–312 (2008).

[188] Vallmitjana, A. *et al.* Resolution of 4 components in the same pixel in FLIM images using the phasor approach. *Methods Appl. Fluoresc.* **8**, (2020).

[189] Chen, W. Y. *et al.* A method to quantify FRET stoichiometry with phasor plot analysis and acceptor lifetime ingrowth. *Biophys. J.* **108**, 999–1002 (2015).

[190] Jones, D. C. *et al.* Multidimensional luminescence microscope for imaging defect colour centres in diamond. *Methods Appl. Fluoresc.* **8**, 014004 (2019).

[191] Mohtashami, A. & Femius Koenderink, A. Suitability of nanodiamond nitrogen-vacancy centers for spontaneous emission control experiments. *New J. Phys.* **15**, (2013).

[192] Zhang, J. L. *et al.* Strongly Cavity-Enhanced Spontaneous Emission from Silicon-Vacancy Centers in Diamond. *Nano Lett.* **18**, 1360–1365 (2018).

[193] Turukhin, A., Liu, C., Gorokhovsky, A., Alfano, R. & Phillips, W. Picosecond photoluminescence decay of Si-doped chemical-vapor-deposited diamond films. *Phys. Rev. B - Condens. Matter Mater. Phys.* **54**, 16448–16451 (1996).

[194] Jones, D. C. *et al.* Multidimensional spectroscopy and imaging of defects in synthetic diamond: Excitation-emission-lifetime luminescence measurements with multiexponential fitting and phasor analysis. *J. Phys. D. Appl. Phys.* **54**, (2021).

[195] Tallaire, A. *et al.* Thick CVD diamond films grown on high-quality type IIa HPHT diamond substrates from New Diamond Technology. *Diam. Relat. Mater.* **77**, 146–152 (2017).

[196] Tallaire, A. *et al.* Temperature dependent creation of nitrogen-vacancy centers in single crystal CVD diamond layers. *Diam. Relat. Mater.* **51**, 55–60 (2015).

[197] Gatto Monticone, D. *et al.* Systematic study of defect-related quenching of NV luminescence in diamond with time-correlated single-photon counting spectroscopy. *Phys. Rev. B* **88**, 155201 (2013).

[198] Babich, Y. V, Feigelson, B. N. & Yelisseyev, A. P. Nitrogen aggregation and linear growth rate in HPHT synthetic diamonds. **13**, 1802–1806 (2004).

[199] Private correspondence with Dr Ben Green (Warwick University, 2020)

[200] Rand, S. C. & DeShazer, L. G. Visible color-center laser in diamond. *Opt. Lett.* **10**, 481 (1985).

[201] Eaton-magaña, S. *et al.* Raman and photoluminescence mapping of gem materials. *Minerals* **11**, 1–32 (2021).

[202] Breeding, C. M., Eaton-Magana, S. & Shigley, J. E. Natural-Color Green Diamonds: A Beautiful Conundrum. *Gems Gemol.* 2–27 (2018). doi:10.5741/GEMS.54.1.2

[203] Breeding, C. M., Eaton-Magaña, S. & Shigley, J. E. Naturally colored yellow and orange gem diamonds: The nitrogen factor. *Gems Gemol.* **56**, 194–219 (2020).

[204] Wolleschensky, R., Zimmermann, B. & Kempe, M. High-speed confocal fluorescence imaging with a novel line scanning microscope. *J. Biomed. Opt.* **11**, 064011 (2006).

[205] https://www.princetoninstruments.com/products/isoplane-family/isoplane (04/09/2020)